Characterisation of Photo-Physical Properties of Upconversion Nanocrystals at Ensemble and Single Particle Level

Dissertation
zur Erlangung des akademischen Grades
doctor rerum naturalium
(Dr. rer. nat.)

im Promotionsfach Physik

eingereicht an der
Mathematisch-Naturwissenschaftlichen Fakultät
der Humboldt-Universität zu Berlin

von Diplom Physiker
Florian Stefan Frenzel

Präsidentin der Humboldt-Universität zu Berlin
Prof. Dr.-Ing. Dr. Sabine Kunst

und

Dekan der Mathematisch-Naturwissenschaftlichen Fakultät
Prof. Dr. Elmar Kulke

Gutachter:	1. Prof. Dr. Oliver Benson
	2. PD Dr. Stefan Kirstein
	3. Prof. Dr. Ilko Bald
Tag der mündl. Prüfung:	14. Dezember 2021

Selbstständigkeitserklärung

Ich erkläre, dass ich die Dissertation selbständig und nur unter Verwendung der von mir gemäß § 7 Abs. 3 der Promotionsordnung der Mathematisch-Naturwissenschaftlichen Fakultät, veröffentlicht im Amtlichen Mitteilungsblatt der Humboldt-Universität zu Berlin Nr. 42/2018 am 11.07.2018 angegebenen Hilfsmittel angefertigt habe. Ich habe mich nicht anderwärts um einen Doktorgrad in dem Promotionsfach beworben und besitze keinen entsprechenden Doktorgrad. Die dem Verfahren zugrunde liegende Promotionsordnung der Mathematisch-Naturwissenschaftlichen Fakultät der Humboldt-Universität zu Berlin habe ich zur Kenntnis genommen.

Berlin, 14.12.2021

Florian Frenzel

”... you are looking at an industrial laser,
which emits an extraordinary light, unknown in nature.
It can project a spot on the moon. Or at closer range
cut through solid metal. I will show you....”

Auric Goldfinger in *Goldfinger*

Abstract

Upconversion nanoparticles (UCNPs), such as, $NaYF_4$ crystals co-doped with Yb^{3+} and Er^{3+} ions, emit higher energetic light in the ultraviolet/visible and near-infrared range under lower energetic near infrared excitation. This generates unique optical properties, for example, multi-colour band emissions, reduced background fluorescence, deeper tissue penetration depths and high photostability rendering UCNPs attractive options for bioimaging, medicinal and engineering applications. Although UCNPs are principally ideal candidates for many applications, they suffer from a comparatively low brightness (B). Further optimisation of UCNPs require a broader understanding of their photo-physical properties. This includes examination of non-radiative decay pathways influenced by particle architecture including dopant ion concentration, particle size and surface chemistry. Unlike previous studies, which were largely performed under ensemble conditions and averaged the optical properties of thousands of nanoparticles (NPs) and their interactions, the study of single particles (SPs) provides a deeper insight into photoluminescence (PL) and UC properties of individual UCNPs, particularly useful for future SP applications.

The influence of multi-factor parameters on the photo-physical and spectroscopic properties of UCNPs are investigated under ensemble and single particle condition in this thesis. For this purpose, a confocal laser scanning microscope (CLSM) was designed and constructed to enable the photo-physical characterisation of individual UCNPs. The laser focused down to the diffraction limit enables excitations at high power densities (P) up to MW/cm^2 range, reaching saturation conditions of UCNPs.

In the first part of the thesis, ensemble and single particle studies of core- and core-shell β-$NaYF_4$ crystals co-doped with 20% Yb^{3+} and 1% to 3% Er^{3+} are performed over a P-range of six orders of magnitude. In the ensemble, the addition of an inert $NaYF_4$ shell enhances the upconversion luminescence (UCL) due to effective shielding of surface related quenching effects in water and cyclohexane, whereas on the SP level, the slight increase in Er^{3+} doping provides a strong impact on the UC performance yielding enhanced brightness at high P. With increasing P, the contribution of additional emission bands from high energy Er^{3+} ion levels increases which leads to an overall emission colour change, from green over yellow to white. This provides a deeper insight into the enhanced complex (de)population processes.

The second part of this thesis discusses influences in a wide variation in Yb^{3+}/Er^{3+} ion doping concentration. Three different sample sets of varying size have been studied, using different synthesis approaches. The results of the ensemble and SP study reveal an increase of Er-Er cross-relaxations (CRs) for higher Er content, and more effective energy transfer (ET) and Er-Yb back-energy transfer (BET) processes for higher Yb content. These differences led to significantly different emission spectra for the Yb and Er series. For different P ranges, the brightest UCL were obtained for different Yb/Er doping ratios.

A comparison of the Nd- and Yb-excitation of Nd/Yb/Er triple-doped $NaYF_4$ UCNPs regarding their UCL performance in water is provided in the third section of the thesis. Shifting the excitation wavelength from the high water absorbing range at 980 nm (Yb-excitation) to 808 nm (Nd-excitation), leads to a 25-fold reduction of water absorption and a decreased risk of sample heating. Exceeding a critical penetration depth of the excitation light in water, the Yb→Er sensitized UC efficiency associated with a higher water absorption, can be compensated by less efficient Nd→Yb→Er double sensitized UC processes, thereby leading to higher brightness values.

In further studies, the process of luminescence resonance energy transfer (LRET) from an UCNP to the sulforhodamine B (SRB) dye and the plasmonic interaction of an Au-shelled UCNP have been examined at the SP level. These proof of concept studies are detailed in two reports as is further evidence of our home-built CLSM being a powerful and adaptable instrument for SP studies.

Zusammenfassung

Aufkonvertierungs-Nanokristalle (UCNPs), wie $NaYF_4$ Kristalle, welche mit Yb^{3+} and Er^{3+} Ionen dotiert sind, emittieren höher energetisches Licht im ultravioletten/sichtbaren und nahinfraroten Bereich, nachdem sie mit weniger energiereichem nahinfraroten Licht angeregt wurden. Damit besitzen sie einzigartige optische Eigenschaften, wie verschiedenfarbige Emissionsbanden, verringerte Hintergrundfluoreszenz, größere Eindringtiefen in organisches Probenmaterial und eine hohe Lichtstabilität. Diese Eigenschaften sind besonders in der optischen Bioanalyse, in medizinischen und technischen Anwendungen von Vorteil. Obwohl die UCNPs in vielen Bereichen Anwendung finden, besitzen sie dennoch eine vergleichsweise geringe Helligkeit (B). Für weitere Optimierungsschritte der UCNPs, ist es wichtig die photophysikalischen Eigenschaften besser zu verstehen. Dabei sollten die nicht-strahlenden Auslöschungsprozesse näher untersucht werden, welche stark von der Partikelarchitektur, der Art und Konzentration der Dotierung, sowie Größe und Oberflächenchemie der Partikel beeinflusst werden. Die meisten bisherigen Studien wurden im Ensemble durchgeführt und fassen somit die optischen Ergebnisse vieler tausender Nanopartikel (NPs) und deren Wechselwirkungen auf einmal zusammen, wobei keine Aussage über das homogene und optische Verhalten einzelner NPs getroffen wird, was durch Messungen an Einzelpartikeln (SPs) abgedeckt werden kann. Um die photophysikalischen und spektralen Eigenschaften einzelner UCNPs untersuchen zu können, wurde als Teil dieser Arbeit ein konfokales Mikroskop (CLSM) entwickelt und aufgebaut. Die starke Fokussierung des Laserlichtes ermöglicht sehr hohe Anregungs-Leistungsdichten (P) bis in den MW/cm^2 Bereich, womit Sättigungseffekte der UCNPs erzielt werden können.

Die erste Studie dieser Arbeit umfasst Ensemble- und Einzelpartikelmessungen an Kern und Kern-Schale β-$NaYF_4$ Kristallen, welche mit 20% Yb^{3+} und 1% bis 3% Er^{3+} Ionen dotiert sind, wobei die optischen Eigenschaften P-abhängig über sechs Größenordnungen untersucht wurden. Während im Ensemble die Signalstärke der aufkonvertierten Lumineszenz (UCL) durch die Präsenz der Schale, welche die Löschungseffekte von Wasser und Cyclohexan an der Partikeloberfläche effektiv reduziert, stark erhöht werden konnte, werden bei den Einzelpartikelmessungen die hellsten Partikel durch die Erhöhung der Dotierungskonzentration erreicht. Mit ansteigender P verändern zusätzliche Emissionsbanden von höheren Er^{3+} Energieniveaus das Emissionsspektrum farblich von grün über gelb nach weiß. Dies lässt auch Rückschlüsse auf die zunehmend komplexer werdenden Besetzungs- und Entvölkerungsprozesse der Er^{3+} Niveaus zu.

Die zweite Studie diskutiert die Einflüsse bei starker Änderung der Yb^{3+}/Er^{3+} Ionen Dotierung anhand von drei verschiedenen Probensystemen. Diese unterscheiden sich sowohl in der Partikelgröße als auch in der Synthesevorschrift. Die Messungen am Ensemble und den SPs zeigen mit Erhöhung der Er^{3+} Ionen Konzentration eine Zunahme der Er-Er Wechselwirkungen (CRs) und bei höherem Yb^{3+} Gehalt sowohl effektivere Yb-Er Transferraten (ETs) als auch verstärkte Er-Yb Rücktransferraten. Das führt für die Yb und Er Reihe jeweils zu charakteristischen Emissionsspektren. Die hellsten UCNPs wurden für unterschiedliche Yb/Er Verhältnisse erreicht, abhängig von dem jeweils betrachteten P Bereich.

Bei der dritten Studie wurde die direkte Anregung von Yb^{3+} mit der von Nd^{3+} Ionen an Nd/Yb/Er dotierten $NaYF_4$ Partikeln bezüglich des UCL Verhaltens in Wasser verglichen, wobei durch die Änderung der Anregungswellenlänge von 980 nm (Yb-Anregung) zu 808 nm (Nd-Anregung) die Wasserabsorption um das 25-fache reduziert wird. Diese Verringerung der Wasserabsorption reduziert auch das Risiko der Probenschädigung durch Erhitzen. Ab einer kritischen Wasser-Eindringtiefe

des Anregungslichtes, zeigte die Nd-Anregung (Nd→Yb→Er), trotz zusätzlichem ET, stärkere Helligkeit im Vergleich zu der Yb-Anregung (Yb→Er) mit der höheren Wasserabsorption.
In weiteren Messungen wurde sowohl der Lumineszenz Resonanz Energie Transfer (LRET) ausgehend von einem UCNP zu dem Farbstoff Sulforhodamine B, als auch plasmonische Wechselwirkungen von Au-Schale UCNPs bei Einzelpartikelmessungen untersucht. Auch diese Messungen, welche lediglich als Wirksamkeitsnachweis gemacht wurden, verdeutlichen, dass unser selbst konstruiertes CLSM ein leistungsfähiges und flexibles Gerät zur Einzelpartikelmessung ist.

Keywords Photon upconversion, lanthanide-doped nanocrystals, ensemble and single particle studies, confocal microscopy, high excitation power density, decay kinetics, absolute quantum yield, luminescence quenching, Yb- and Nd-excitation, FRET/LRET process, plasmonic interactions

Schlagwörter Photon-Aufkonvertierung, Lathanoid-dotierte Nanokristalle, Ensemble und Einzelpartikel Messungen, konfokale Mikroskopie, hohe Anregungsleistungsdichten, Zerfallsmessung, absolute Quantenausbeute, lumineszente Auslöschung, Yb- und Nd-Anregungsmessungen, FRET/LRET Prozess, Plasmonische Wechselwirkungen

Contents

List of Abbreviations

AFM	atomic force microscope
Ag	silver
APD	avalanche photon diode
Au	gold
A	acceptor
$BaSO_4$	barium sulfate
BET	back-energy transfer
BP	bandpass
B	brightness
C_6H_{12}	cyclohexane
Ca^{2+}	bivalent Calcium ion
CLSM	confocal laser scanning microscope
co	core-only
CR	cross-relaxation
cs	core-shell
cw	continuous wave
DCL	downconversion luminescence
DC	downconversion
DLS	diffraction light scattering
DMF	dimethylformamide
DM	dichroic mirror
D	donor
EMCCD	electron multiplying charge-coupled device
Er^{3+}	trivalent Erbium ion
ESA	excited state absorption
ETU	energy transfer upconversion
FE	field enhancement
FLIM	fluorescence lifetime imaging
FRET	Förster resonance energy transfer
G/G	green-to-green ratio (I_{521}/I_{541}) of Er^{3+} emission
G/R	green-to-red ratio (I_{541}/I_{654}) of Er^{3+} emission
Gd^{3+}	trivalent Gadolinium ion
G	groundstate
H_2O	water
ICP-OES	inductively coupled plasma-optical emission spectrometry

InGaAs	indium gallium arsenide
IRF	instrument response function
is	inert shell
$\mathbf{LDOS}_{rad}$	local density of states with radiative contribution
LDOS	local density of states
Ln	lanthanide
LP	long pass
LRET	luminescence resonance energy transfer
LSP	localized surface plasmon
$\mathbf{Na}^{3+}$	trivalent Sodium ion
NA	numerical aperture
$\mathbf{Nd}^{3+}$	trivalent Neodymium ion
NIR	near-infrared
NP	nanoparticle
nRP	non-radiative relaxation process
NW	nanowire
n	slope factor
PA	photo-avalanche
PL	photo-luminescent
$\mathbf{Pr}^{3+}$	trivalent Praseodymium ion
PSF	point spread function
QDs	quantum dots
QY	quantum yield
RE	rare earth
ROI	region of interest
SERS	surface-enhanced Raman spectroscopy
SHG	second-harmonic generation
SI	supplementary information
SP filter	short pass filter
SPAD	single-photon avalanche diode
SPP	surface plasmon polariton
SP	single particle
SRB	sulforhodamine B
SWIR	short wavelength infrared
TCSPC	time correlated single photon counting
TEM	transmission electron microscopy
$\mathbf{Tm}^{3+}$	trivalent Thulium ion
TPA	two-photon absorption
UCL	upconversion luminescence
UCNPs	upconversion nanoparticles
UC	upconversion
UPNCs	upconverting nanocrystals

UV	ultraviolet
vis	visible
WI	widefield imaging
XRD	X-ray diffraction
Y^{3+}	trivalent Yttrium ion
Yb^{3+}	trivalent Ytterbium ion
$\overrightarrow{p}$	dipole moment
$\alpha_{abs}(\lambda)$	absorption coefficient at λ
α_{water}	absorbance value of water
ϵ	decadic molar extinction coefficient
η_{LRET}	luminescence resonance energy transfer efficiency
λ	wavelength
λ_{em}	emission wavelength
λ_{ex}	excitation wavelength
Φ_{UC}	upconversion quantum yield
σ_{abs}	absorption cross-section
τ_{ampl}	amplitude weighted lifetime
τ_{int}	intensity weighted lifetime
A	absorbance
c	concentration
d	diameter
I_{λ}	emission intensity at λ
J	spectral overlap integral
n	number of absorbed photons
N_{Ln}	number of Ln^{3+}
n_r	refractive index
P	power density
R	donor-acceptor distance
R_0	Förster radius
T	temperature
t	thickness
V	volume
W_{D-A}	donor-acceptor interaction energy
x_C	crossing-point

1 Introduction

Lanthanide doped spectral shifting upconversion nanoparticles (UCNPs) have the unique capability to produce narrow multi-colour band emission in the UV/vis/NIR spectral range upon multiphotonic absorption of infrared light. This particular feature makes them promising reporters for wide range of applications in bioimaging, medicine and engineering, including bioanalytical sensing [1–3], intracellular photoactivation in optogenetics [4–6], super-resolution nano-spectroscopy [7–9], medical photodynamic therapy [10–12], photovoltaics [13–15] and anti-counter-feiting [16–18]. Importantly, the optical excitation of UCNPs in the NIR range minimises the background signals due to low autofluorescence from auxochromes in biological matrices. Furthermore, the NIR excitation enables deeper penetration depths in biological samples. Moreover, UCNPs show long luminescence lifetimes in the µs range which is favourable for time gated emission in conjunction with a high photostability, chemical inertness and, in contrast to quantum dots (QDs), they do not exhibit any blinking behaviour. Although UCNPs are principally ideal candidates for many chemical and biological sensing and imaging applications, they suffer from a comparatively low brightness due to the low absorption cross-sections of the parity forbidden f-f transitions and low photoluminescence quantum yields (QY_{UC}), particularly in the case of very small nanoparticles with sizes below 50 nm. The rational design of more efficient and brighter UPNCs requires an in-depth understanding of the non-radiative decay pathways in these materials that are influenced by particle architecture including dopant ion concentration and homogeneity of dopant distribution within UCNPs, size/surface-to-volume ratio, surface chemistry and micro-environment.

In contrast to conventional chromophores like semiconductor QDs or organic dyes, where one absorbed higher energy photon results in the emission of a lower energetic one (Stokes shifted emission), the non-linear upconversion emission arises from bi- or multiphotonic absorption processes, leading to excitation power density (P) dependence of luminescence intensities and UC luminescence QY_{UC} values. Hence, for reliable characterisation and performance of different UC materials, P-dependent measurements must be performed. The determination of the QY at a single excitation P is insufficient. However, P-dependent measurements require special instrumentation and the controlled variation of P. Also, other luminescence properties like UC spectra / intensity ratios and the luminescence lifetimes of the different emission bands can be P-dependent and vary in the low and high P regime.

The spectroscopic characterisation of UCNPs, including the characterisation of the surface chemistry and stability tests, are commonly done by ensemble measurements in dispersion. Up to now, only a few studies have focused on the optical behaviour of single UCNPs, by using confocal microscopy determining the brightness and the decay behaviour have been reported [7–9, 19, 20]. In most cases, the correlation with sophisticated ensemble measurements in addition has not been investigated. With confocal fluorescence microscopy, relatively high P with up to MW/cm^2 can be reached due to the strong focusing of the laser down to a small spot. As a result, the luminescence measurements can be performed up to the high P regime reaching the saturation condition of the UC luminescence. These high Ps are typically not reached in ensemble measurements which makes the confocal setup indispensable, and should thus open ways for the detailed analysis of the different energy transfer processes between activator and sensitizer.

The topicality of confocal microscopy on UCNPs has been shown in 2021 by Lee et al. [21], demonstrating the photon-avalanche effect (PA) of Tm^{3+} ion doped single UCNPs at higher P, enabling super-resolution imaging. In the same year, Liu et al. [22] used the lateral point spread function (PSF) of self-interfering single UCNPs with their mirror image for axial sub-diffraction limited localisation and SP tracking. The increasing number of single UCNP studies of the last months highlights the need for such comparative measurements on ensemble and single particle levels, which ultimately, can deepen the knowledge. Here, it is of great importance to understand the influences such as size distribution, dopant concentration, surface chemistry, and P-dependency.

Aim and Outline of the Thesis

The aim of this thesis is to get an in-depth understanding of the optical properties of Yb/Er- and Nd/Yb/Er-doped UCNPs with varying size, dopant concentration, and surface chemistry to optimise the UC performance under ensemble and SP conditions.

- Chapter 2 provides a general introduction to the fundamental optical processes in UC, luminescence resonance energy transfer (LRET) and plasmonic interaction.

- Chapter 3 presents the laboratory setups and sample preparation and experimental methods, including the detailed outline of our home-built CLSM for SP studies.

- Chapter 4 provides a comparative study of the well-known Yb/Er-doped NaYF$_4$ UC system. First, results of the ensemble measurements will be shown and discussed. Second, SP measurements for comparatively low Er ion doping variation and surface passivation (core-shell UCNPs) are discussed. This chapter serves as basis for the subsequent ensemble-SP comparative studies.

- Chapter 5 presents the strong influence of a higher Yb/Er doping variation on the brightness and colour emission. Furthermore, size and doping dependent UCL quenching effects on the ensemble and SP level will be discussed.

- Chapter 6 introduces Nd/Yb/Er-doped UCNPs with Nd^{3+} ion as a sensitizer, which shifts the excitation to shorter wavelength, resulting in a reduced water absorption. In general, this is an approach to optimise UCNPs for bio-applications.
- Chapter 7 gives insight into two further proof of concept studies, using UCNPs as LRET donor for sulforhodamine B. Additionally, the influence of plasmonic effects introduced by an Au-shell is being investigated.

2 Theoretical basis

In this chapter, the theoretical basis for the upconversion (UC) process in general, sensitized UC process, luminescence resonance energy transfer (LRET), plasmonic interactions and relevant measurement parameters will be outlined.

2.1. Upconversion process

UC is a non-linear optical and photo-luminescent process, in which an UC material absorbs photons of energy which is lower than the energy it emits. Usually, the absorption takes place in the NIR spectral range (long wavelength), while the emission is in the UV/vis (shorter wavelength) or NIR regime, leading to an anti-Stokes shifted emission, Figure 2.1. The opposite process with higher energetic absorbed and lower energetic emitted light (Stokes-shift) is named downconversion (DC) which is the typical excitation-emission process of fluorescent and phosphorescent systems like dyes and quantum dots (QDs).

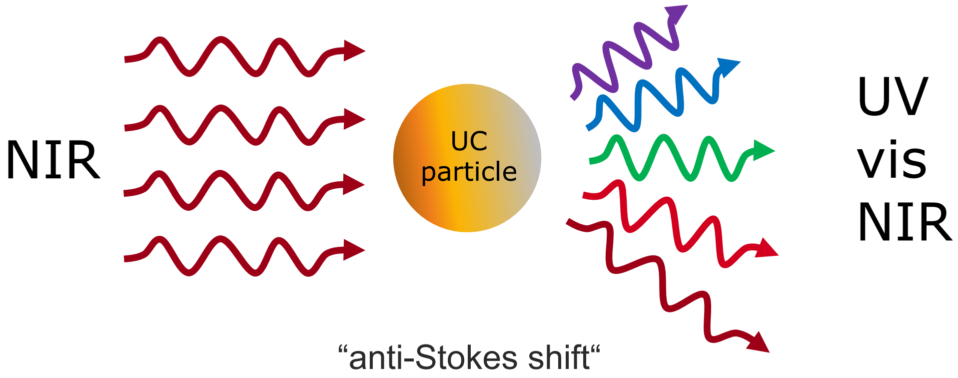

Figure 2.1. Illustration of the UC process of an UC particle with low energy absorbed photons in the NIR and with high energy photons emitted in the UV/vis/NIR with an anti-Stokes shift.

Besides the UC process there are two other common ways of anti-Stokes processes, the two-photon absorption (TPA) and the second-harmonic generation (SHG) [23]. For these processes to occur, two photons are simultaneously combined and virtual intermediate energy levels are needed which results in a limited efficiency and additionally, requires high-intensity coherent excitation, illustrated in 2.2 a), b). In contrast, in UC processes, all intermediate energy levels are real and metastable, making UC a more likely process than TPA and SHG.

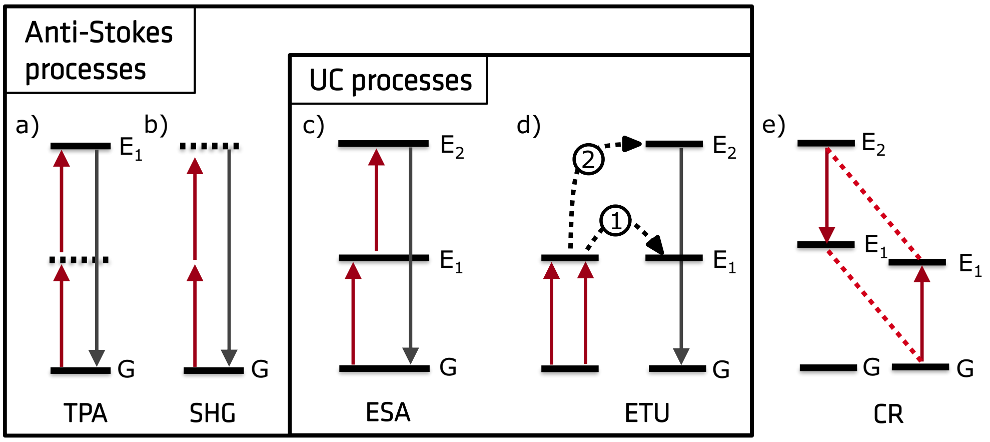

Figure 2.2. Scheme of non-linear optical processes with an anti-Stokes shifted emission (a-d) and illustration of an energy-transfer process (e): a) Two-photon absorption (TPA), b) Second-harmonic generation (SGH) and c)-d) General UC processes with excited state absorption (ESA) and energy transfer UC (ETU). e) Cross relaxation (CR) process as typical energy transfer process between two ions. The horizontal dashed lines of TPA and SHG illustrate virtual intermediate energy levels and the solid lines real energy levels, like the groundstate G and the excited levels E$_1$ and E$_2$.

The general UC process is described by two principal processes, first, the excited state absorption (ESA) and second, the (sensitized) energy transfer upconversion (ETU). However, the UC process of a real system is more complicated and can involve several mechanisms in combination like ESA, ETU and energy-transfer processes like the cross-relaxation process (CR):

Excited-state absorption The ESA is the simplest form of an UC process. Here, the ion is stepwise directly excited, first from groundstate (G) to energy level E$_1$ and second from E$_1$ to the E$_2$ level by using the energy of two subsequently absorbed photons, see Figure 2.2 c). The ladder-like structure and the long-term stability of the intermediate energy levels are requirements for ESA, which are only provided by a few lanthanide ions (see chapter 2.2.1).

(Sensitized) energy transfer upconversion Like the ESA, the ETU also uses the energy of two sequentially absorbed photons to populate the energy levels E$_1$ and E$_2$ of the emitting ion. The photon absorption is previously realised by another neighbouring ion, called sensitizer, which gets excited and transfers the energy sequentially to the emitting ion (acceptor) by relaxing to the groundstate, see Figure 2.2 d). The ETU is a non-radiative energy transfer with Coulomb interactions of van der Waals type between two ions. It is quantum-mechanically described as a dipole-dipole interaction with allowed electric-dipole transitions of both ions [24].

The use of sensitizers with high absorption cross-sections $\sigma_{abs}(\lambda_{ex})$ and a good matching of sensitizer and acceptor energy levels can enhance the UC efficiency significantly. Therefore, the sensitizer-to-acceptor doping ratio and their averaged ion-ion distances must be in an appropriate range, which will be discussed further in chapter 2.3.1.

Cross-relaxation The CR is an ion-ion interaction process of two identical or different ions, in which one excited ion transfers part of its energy to a second ion, which then is excited to an upper level, as illustrated in Figure 2.2 e). The second ion does not have to be in the groundstate before CR takes place. If both ions are from the same type, CR is mainly considered as a detrimental quenching process caused by too high ion concentration which results in a decrease of emission intensity.

The complex UC processes and the appearance of multiple emission bands of a real optical stimulated UC material can be partly explained by the presence of combined ESA, sensitized ETU and CR processes. The fundamental properties and specific requirements for an efficient UCL will be discussed in the next section.

2.2. Upconversion materials

2.2.1. Material requirements

There are two important components of a typical UC material, a highly stable inorganic host material, and the type of efficient doping ions as luminescent centres. By variation of the host lattice and the doping ion type, several UC materials have been developed in the last decades, including transition metal [23], organic [25] and lanthanide-doped upconverters. The most common UC materials contain trivalent rare earth ions as doping components, like the lanthanide ions Pr^{3+}, Nd^{3+}, Er^{3+}, Tm^{3+} or Yb^{3+} and for host lattice material Na^{+}, Ca^{2+} and Y^{3+} based fluorides [26]. But efficient UC only occurs for a few dopant-host combinations with specific properties, as discussed in the following:

Dopant ions

The dopant ions should provide multiple, long-lived metastable energy levels to allow spectroscopically relevant photon absorption and above-mentioned UC energy transfer processes (section 2.2). The inner 4f shells of lanthanide ions (Ln^{3+}) offer such relevant electronic energy levels with ladder-like structures. Particularly, Er^{3+}, Tm^{3+} and Ho^{3+} ions are promising candidates, as shown in Figure 2.3. The outer 5s and 6p shells of Ln^{3+} ions are responsible for stable bonding and embedding in the host lattice. The completely filled 5s and 5p subshells can shield the 4f electrons from host lattice influences, like the exact crystal field and symmetry effects [27]. Consequently, only reduced electron-phonon interactions are present allowing almost undisturbed f-f transitions between the ions [24, 28]. The probability for these f-f transitions is relatively low, as 4 f-f transitions are naturally Laporte-forbidden. This leads to inefficient photon absorption and a limited number of electronically excited states but prolongs the lifetimes of excited levels up to ms.

The improved light absorption is a key factor for a more efficient UC process, and can be realised by increasing the dopant ion concentration up to a critical value where concentration quenching effects become relevant due to enhanced ion-ion interactions. By co-doping the host material with an additional dopant ion as sensitizer, the UC efficiency can be enhanced. Given that, the sensitizer enhances the NP absorption cross-section $\sigma_{abs}(\lambda_{ex})$ for the excitation light and provides effective ETU processes to the emitting ions (activators), cf. Figure 2.2 d). The most common sensitizer for Er^{3+} and Tm^{3+} ions is the Yb^{3+} ion with only one excited 4f level, which can be optically excited in the NIR range at approximately 980 nm.

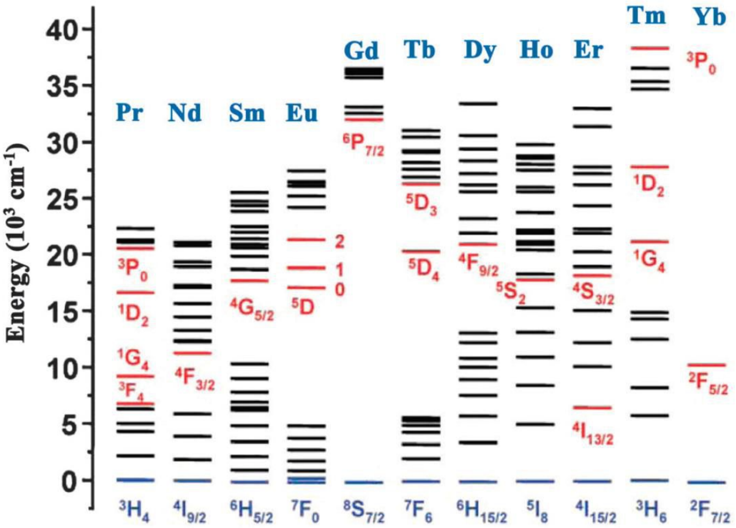

Figure 2.3. Scheme of partial 4f energy diagrams of lanthanide ions, with ground levels in blue and the main luminescent levels in red. Taken from [29]

Host material

The interactions of the host material with the dopant ions have an important impact on the UC process. For the dopant ions the coordination numbers, the relative spatial position, the type of neighbouring ions and their distances to the dopant ions are determined by the chosen host lattice. An ideal host material should meet the following requirements for an efficient UC process: (1) Transparency in the vis and NIR region to avoid (re-)absorption of excitation and emission light. (2) Low phonon energies to minimise non-radiative energy loss caused by electron-phonon coupling. (3) Small lattice mismatch with the dopant ions to enable their homogeneous incorporation with minimised crystal defects and lattice distortion. (4) In the case of Ln ions as dopants, a strong crystal field to partly allow the Laporte-forbidden 4f transitions [28, 30].

These properties are mainly fulfilled by Na^+, Ca^{2+} and Y^{3+}- based fluorides with similar ionic radii of Ln^{3+} dopant ions. Up to now, the most efficient host for UC in the blue and green spectral region is the hexagonal $NaYF_4$ crystal co-doped with Yb as sensitizer and

Tm or Er as activator. The sensitized UC process of $NaYF_4$:Yb,Er is examined in more detail in chapter 2.3.1.

Requirements for bio-applications

The following list sums up the main requirements for applications in bio-technology and medicine, which are aspired to be met from UCNPs [26]:

- high luminescence efficiency for good signal-to-noise ratio to reach the optical detection limits and achieve the therapy effect
- multi-colour emission bands for multiplexing options in imaging, and increased throughput of bio-assays
- monodispersed, uniformly shaped, and small-sized NPs to achieve cellular uptake with identical optical properties for intracellular theranostics
- nano-chemically engineered surface for targeting ligands coupling (like antibodies or peptides), and available phase transfer to allow for dispersion in water
- non-toxicity and biocompatibility to living cells and to the human body

2.2.2. Advantages, drawbacks and optimisation of UC materials

There are several unique optical properties of UC materials providing advantages for optical applications compared to commonly used materials like quantum dots (QDs) or organic dyes. However, UC materials have their limits and sensitive dependencies on several parameters, which partly can be overcome by using optimisation strategies concerning particle composition and architecture.

Advantages

UC materials can be optically excited in the NIR range (mostly between 750 nm - 1000 nm), which has several advantages. Compared to excitation in the UV/vis range with strong autofluorescence emission of organic material, the NIR-excitation causes no autofluorescence background. Furthermore, NIR light has the potential of higher penetration into biological tissue. Consequently, the UCL emission can be enhanced, with high signal-to-noise ratio from UCNPs, which can be either localized deep inside the organic tissue, like in medical applications, or which have organic components attached to their surfaces like ligands. Due to the large anti-Stokes shift, there is nearly no spectral cross-talk between excitation and emission light, and therefore no strong signal re-absorption.
Compared to organic dyes, UC particles are photo-stable without bleaching. In contrast to QDs, they show constant emission intensities and no blinking. The characteristic narrow multi-band emissions of Ln^{3+} ions, arising from optical transitions inside the ladder-like 4f energy levels (cf. Fig. 2.3), offer additional advantages for optical sensing, FRET/LRET applications and multiplexing capabilities [3].

Drawbacks and optimisation techniques

The UC process of Ln doped material is complex and depends on many intrinsic and external parameters, which influence the population and depopulation of the respective radiative energy levels, thereby limiting the UC efficiency and their application ranges. Particularly small UC particles in the nanometer range are affected by surface related effects due to larger surface-to-volume ratio, resulting in large differences in optical behaviour of UCNPs compared to bulk material.

As already mentioned in chapter 2.2.1, a well-chosen composition of Ln-ions with right doping concentrations is one of the key-factors for efficient UC, which increases with the dopant concentration until an optimum is reached. With further rise in dopant concentration, the averaged ion-ion distance is being diminished, resulting in quenching effects which significantly increase due to ion-ion CR processes (cf. Fig. 2.2) [31–33]. Especially for dopant ions of different types, the use of (multi-)shells separately doped with different ions can help to set the range for ion-ion distances and thereby for their interactions [34]. For our study on Nd/Yb/Er co-doped NPs we also used the principle of multi shells to separate Nd from Er ions (cf. chapter 2.3.2 and 6).

The smaller the UC particles are in size, the larger the surface-to-volume ratio becomes, and surface related deactivations increase. For dopant ions close to the surface, surface related quenching processes occur, which are mainly caused by either the small distance to surface lattice defects or the direct contact to the solvent and the surface-ligands with high phonon energies. Particularly, the presence of surface ligands containing O-H, C-H bonds or NH_2 groups show high vibrational modes, which enhance the quenching of the excited levels by multi-phonon relaxations [30]. But also, the dopant ions located in the centre of a NP can be influenced by the surfaces quenching since the energy can migrate long distances (a few μm, [35]) inside the doped crystal and ultimately, reach the surface or the dopants on the surface. The surface related deactivations can be minimised by using a protective shell around the NP, which can largely enhance the UC efficiency. For the shell, the undoped, inert material of the core crystal is typically taken to minimise the lattice mismatch on the core-shell interface. In addition, crystals with similar structures compared to the core are well-suited shell materials, as well as silica and metals. For a β-$NaYF_4$:Yb/Er UCNP, a full closed inert β-$NaLuF_4$ shell of 4-6 nm in thickness can already be sufficient to minimise surface quenching, reaching optimised UCL as reported in [35, 36].

In 2018, the Meijerink group suggested that incorporated OH^- ions on F^--sites in $NaYF_4$ crystals are responsible for additional O-H vibrational based quenching processes of Er^{3+} levels inside the crystal [33].

The above mentioned quenching effects strongly suppress the UCL of small NPs, resulting in relative low quantum yields (QY) and low brightness values (B) compared to UC bulk material. For UCNPs, the QY (QY_{UC}), which is the ratio of emitted photons to absorbed photons, is limited by the properties of bulk material with QY_{UCbulk} of about 0.11 [37], meaning that for about 10 absorbed photons only one photon is emitted.

Due to the non-linear nature of the UC process (see chapter 2.1) both, the UCL I_{UC} and the

QY_{UC} depend on the excitation power density (P) [26, 38–40]:

$$I_{UC} = C \cdot P^n \tag{2.1}$$

and

$$QY_{UC} = \frac{emitted\ photons}{absorbed\ photons} \propto \frac{emitted\ light}{absorbed\ light} = \frac{I_{UC}}{\alpha_{abs}(\lambda_{ex}) \cdot P} \xrightarrow{(2.1)} \propto P^{n-1} \tag{2.2}$$

where C is a coefficient related to material properties, n is the number of absorbed photons needed for a specific radiative UC transition, and $\alpha_{abs}(\lambda_{ex})$ is the absorption coefficient at excitation wavelength λ_{ex}. Hence, for a reliable characterisation and comparison of different UC materials, a single QY_{UC} value is not sufficient but P-dependent measurements must be performed with powers reaching the saturation limit of the studied UC material. With the help of a home-built integrating sphere setup (described in chapter 3.2.2) the QY_{UC} can be determined absolutely.

One of the main goals in last years has been the enhancement of UCL. Several methods have been investigated besides the use of protective shells and the optimisation of the Ln doping concentration. One approach is the addition of a metallic shell to take advantage of plasmonic enhancement effects. Another way of effective tuneable excitation or emission behaviour is the combination of UCNPs with fluorophors (like dyes) as sensitizers or activators for a non-radiative energy transfer process (LRET / FRET). Both, the LRET process as well as plasmonic interactions will be discussed in chapter 7.

2.3. Sensitized upconversion in NPs

In the case of sensitized UC, the excitation light is efficiently absorbed by an ion (sensitizer) in the first step, which transfers the energy to the emitting ion (activator) via non-radiative ETU as described previously in chapter 2.1 and Figure 2.2. The theoretical basis of the sensitized UC processes for Ln co-doped $NaYF_4$ host material will be given in the next sections. Here, the first section focusses on the co-doping with Yb/Er as sensitizer/activator couple ($NaYF_4$:Yb,Er), while the second section discusses triple-doping with Nd/Yb/Er constellation, using Nd as a pre-sensitizer ($NaYF_4$:Nd,Yb,Er).

2.3.1. Yb/Er co-doped systems

Up to now the most efficient UC material is Yb/Er doped (β)-$NaYF_4$, which was firstly presented by Menyuk et al. in 1972 [41]. In the last decades, it has been optimised and downsized to the nm scale. In Figure 2.4 a), the crystal structure of the hexagonal-phase $NaYF_4$ (β-$NaYF_4$) is sketched. Then, Yb and Er are being incorporated by replacing Y sites in the lattice. In contrast, the cubic-phase $NaYF_4$ (α-$NaYF_4$) crystal does not meet the requirements of an efficient host material (cf. section 2.2.1) for Yb/Er dopant ions.

A typical emission spectrum of $NaYF_4$:Yb,Er with the narrow Er emission bands in the UV, vis and NIR range, excited at 980 nm, is plotted in Figure 2.4 b). The spectrum was collected

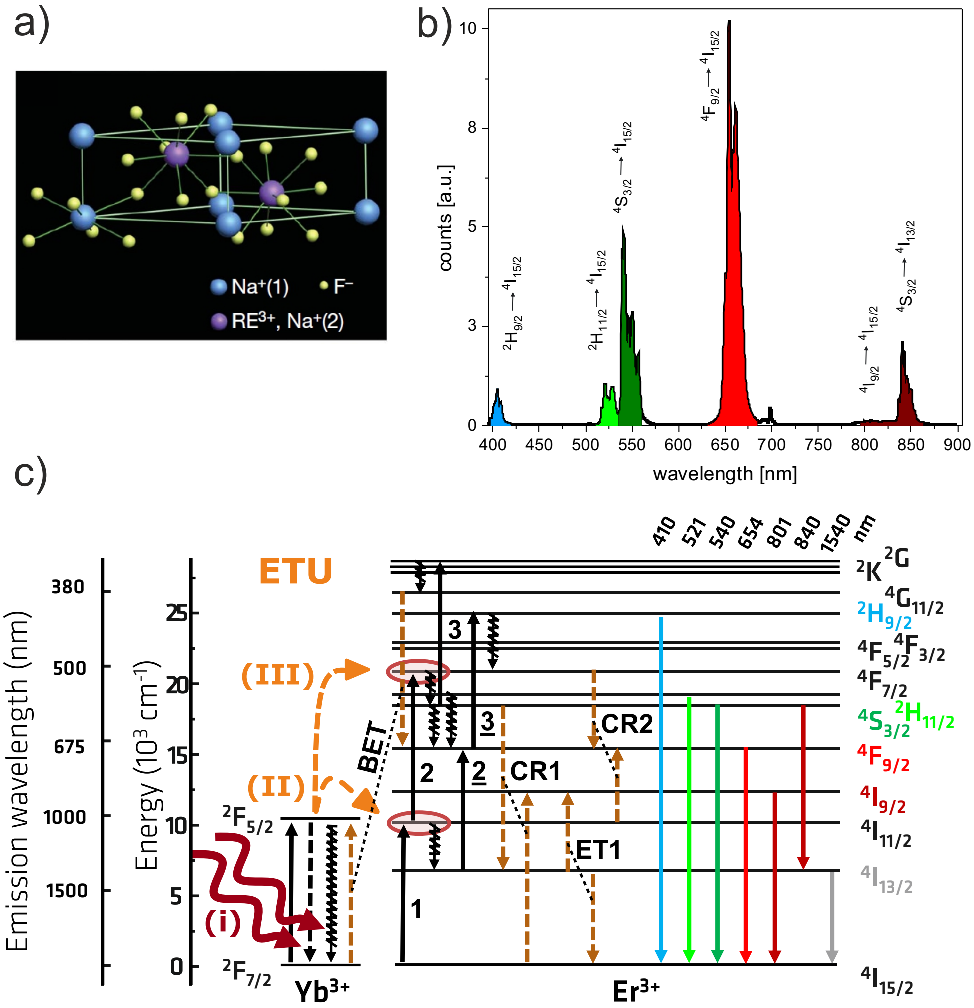

Figure 2.4. Properties of $NaYF_4$:Yb,Er material: a) Hexagonal crystal structure of $NaYF_4$ with an ordered F^- ion array which enables either Na^+ ions or Ln^{3+} /rear earth (RE^{3+}) ions to occupy the cation sites; image taken from [42]. b) Typical spectrum with narrow Er emission bands taken under 980 nm excitation with *P* of 200 W/cm^2 under ensemble condition. For the main 6 UC emissions the specification (start level ⟶ final level) of the radiative transition is labelled. c) ETU between Yb^{3+} ion as sensitizer and Er^{3+} ion as activator, showing the 2 photon absorptions of Yb and population processes of excited Er levels leading to radiative UC emissions at 410, 521, 540, 654, 801, 840 nm and downconversion (DC) at 1540 nm. An additional third absorbed photon is needed for 410 nm emission and for the Er-Yb back-energy transfer (BET) process. The Er-Er interactions are represented by 2 CRs (CR1 and CR2) and one Er-Er ET (ET1). The black wavy arrows denote the multi-phonon relaxations leading to non-radiative depopulation of the higher energetic involved level. The Dieke diagram is based on [43].

under ensemble condition at about 200 W/cm^2. In general, the spectrum is very different to those of single particles with higher laser powers, which will be further discussed in chapter 4.3.

The ETU between the sensitizer Yb^{3+} and the activator Er^{3+} is illustrated in the Dieke diagram in Figure 2.4 c), and can be explained as follows:

(I) Yb absorbs a NIR photon of an approximate wavelength λ_{ex} of 980 nm and gets excited from groundstate $^2F_{7/2}$ to the $^2F_{5/2}$ level. Since $^2F_{5/2}$ is the only higher energy level of Yb, all the absorbed energy is stored there.

(II) The energy is transferred via non-radiative energy transfer (ET) to Er ion, which subsequently changes energetic stated from ground-level to the $^4I_{11/2}$ level (1).

(III) Repeating the photon absorption and ET from Yb to Er, the $^4F_{7/2}$ level of Er can be populated (2). From this energy state the subjacent levels $^2H_{11/2}$, $^4S_{3/2}$, $^4F_{9/2}$ and $^4I_{9/2}$ can be reached via phonon-assisted non-radiative relaxation processes (black wavy arrows).

The depopulation of these levels to subjacent levels or to groundstate results in photon emission with wavelengths of 521 nm, 540 nm ($^2H_{11/2}$, $^4S_{3/2} \longrightarrow {}^4I_{15/2}$), 654 nm ($^4F_{9/2} \longrightarrow {}^4I_{15/2}$) and 801 nm, 840 nm ($^4I_{9/2} \longrightarrow {}^4I_{15/2}$, $^4S_{3/2} \longrightarrow {}^4I_{13/2}$). For blue emission at 410 nm ($^2H_{9/2} \longrightarrow {}^4I_{15/2}$), a minimum of three absorbed photons is needed to populate the $^2H_{9/2}$ level. It can be reached stepwise by overcoming the energy gaps $^4I_{15/2} \longrightarrow {}^2H_{9/2}$ (1), $^2H_{9/2} \longrightarrow {}^4I_{13/2}$ (non-radiative relaxation), $^4I_{13/2} \longrightarrow {}^4F_{9/2}$ ($\underline{2}$) and $^4F_{9/2} \longrightarrow {}^2H_{9/2}$ ($\underline{3}$). Furthermore, with a third absorbed photon the energy gap from $^4S_{3/2}$ to ^2G level can be overcome (3), which is the basis for a following Er-Yb back-energy transfer (**BET**) from the $^4G_{11/2} \longrightarrow {}^4F_{9/2}$ level by simultaneous excitation of Yb ($^2F_{7/2} \longrightarrow {}^2F_{5/2}$). This BET plays an important role, particularly for the red emission intensity of Er^{3+} ions, as the red $^4F_{9/2}$ Er level is excited directly by this process.

The diagram also explains the DC from 980 nm excitation to 1540 nm NIR emission arising from $^4I_{13/2} \longrightarrow {}^4I_{15/2}$ transition. The $^4I_{13/2}$ level can be populated from the $^4I_{11/2}$ level via non-radiative relaxation or after 840 nm emission ($^4S_{3/2} \longrightarrow {}^4I_{13/2}$). The appearing interactions between neighbouring Er ions are described as Er-Er ET and Er-Er CR processes, which depend on the Er^{3+} ion doping concentration and Er-Er distances. The **ET1** Er-Er ET leads to a population of the $^4I_{9/2}$ and $^4I_{15/2}$ level by simultaneous depopulation of the $^4I_{13/2}$ levels of both involved Er^{3+} ions. The **CR1** Er-Er CR populates the $^4I_{13/2}$ and $^4I_{9/2}$ level by depopulation of the green $^4S_{3/2}$ and the $^4I_{15/2}$ level. The **CR2** Er-Er CR enhances the population of the red $^4F_{9/2}$ levels of both participating Er^{3+} ions by depopulation of the $^4F_{7/2}$ and $^4I_{11/2}$ level.

The outlined explanations cover the basic mechanisms of the Yb-Er ET, the level populations, the resulting emission lines and the Er-Er interactions (ET, CR), however, for a complete mechanistic characterisation it is necessary to monitor the P-dependent changes in optical properties. In chapter 4 the P-dependent UCL properties will be discussed for ensemble studies in a low P range (5-400 W/cm^2) and for SPs in the high P range (1 kW/cm^2 - 2.6 MW/cm^2).

2.3.2. Nd/Yb/Er co-doped systems

One drawback of Yb excitation is, especially for bio- or medical applications, the relative high absorption of water at 980 nm, resulting in risky sample overheating and a strong laser light attenuation with reduced penetration ability. In living tissue, the water absorption coefficient shows a local maximum at about 980 nm, whereas at 800 nm the absorption is about 25-fold lower, see Figure 2.5. The use of Nd instead of Yb as a sensitizer enables an excitation of UCNPs at about 800 nm instead of 980 nm due to an intense absorption cross-section of Nd around 800 nm [44].
However, the direct incorporation of Nd into Yb/Er-doped UCNPs has shown much weaker UCL under 800 nm irradiation compared to 980 nm excitation due to quenching via strong Er→Nd ET processes [45]. Exclusively for very low Nd doping concentration (below 1%), this ET quenching can be minimised in Nd/Yb/Er triple-doped systems. Nevertheless, due to the resulting low absorption cross-sections for 800 nm irradiation, only UCNPs with low efficiency have been fabricated. A better solution is offered by core-shell structured UCNPs with spatially confined and high concentrated Nd^{3+} ion doping (up to 20%) inside the shell, and Yb/Er co-doping of the core [46]. Approaches with multi-shell structures have been reported to optimise the Nd sensitized UC, like ($NaYF_4$:Yb,Er@$NaYF_4$:Yb@$NaNdF_4$:Yb) UCNPs with an Nd-free quenching shield layer to eliminate Er-Nd ET and CR processes [47]. In addition, a core-3-shell structure of ($NaGdF_4$:Nd@$NaYF_4$@$NaGdF_4$:Nd,Yb,Er@$NaYF_4$) was used to achieve dual-mode up/down-conversion under 800 nm illumination [48]. Furthermore, the need for onion-layered structures with separated Nd^{3+} ions was questioned by achieving efficient UC luminescence from $NaYF_4$:Yb,Er@$NaYF_4$ NPs with an organic surface capping of cucurbituril coordinated Nd ions [49].

In this thesis, a core-shell Nd/Yb/Er triple-doped system is studied, with Nd as pre-sensitizer co-doped with Yb^{3+} ions in the shell, and a core co-doped with Yb/Er as sensitizer-activator couple. The corresponding energy transfer process is illustrated in the Dieke diagram in Figure 2.6. First, the Nd^{3+} ion gets excited to the $^4F_{3/2}$ level via 808 nm light absorption. From that level, the energy can be transferred to the $^2F_{5/2}$ level of Yb^{3+} ion, and then to the NP core via energy hopping along a chain of neighbouring Yb^{3+} ions. Inside the core, an ET from the excited Yb^{3+} to the Er^{3+} ions can occur, leading to the UC process discussed in the previous section 2.3.1. However, quenching processes may also appear which typically appear at the core-shell interface where Nd^{3+} and Er^{3+} ions are close to each other. These quenching mechanisms involve mainly Nd-Er CR and ET processes (from the $^4F_{9/2}$ Er level to the $^4F_{3/2}$ Nd level).

In chapter 6, the NP efficiencies and UCL performance under different conditions are being compared by determining the QY and the brightness values B_{UC} under both Nd- and Yb-excitation. Therefore, the Nd^{3+}- and Yb^{3+}-absorption cross-sections (per ion and per NP) are precisely measured to avoid misleading assumptions about the sensitizer efficiencies.

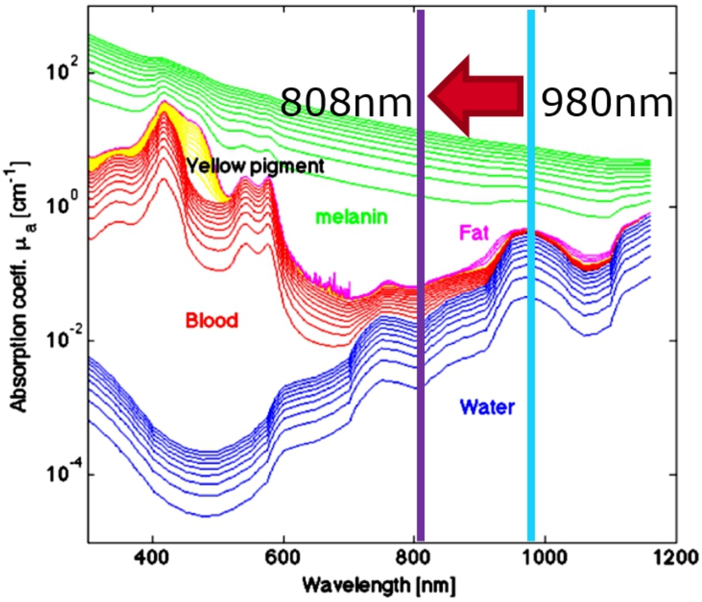

Figure 2.5. Logarithm scaled absorption coefficient of living tissue plotted over excitation wavelength. Water (blue) shows a local maximum at 980 nm and a local minima at 808 nm of light absorption. Modified from [50].

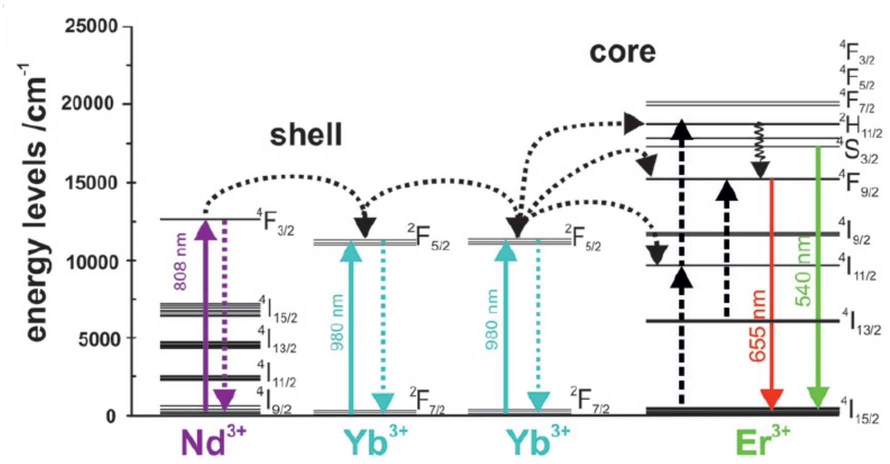

Figure 2.6. Dieke diagram of core-shell UCNP with Nd/Yb co-doped shell and Yb/Er co-doped core. Nd is used as pre-sensitizer, Yb as sensitizer and Er as activator. The 808 nm light is absorbed by Nd, the energy transferred to Yb ions in the shell, from there to Yb ions in the core, where ET from Yb to Er can occur. Taken from own published work [51].

Absorption cross-section of Ln^{3+} ions and Ln^{3+}-doped NPs

For the calculation of the absorption cross-section of Ln^{3+} ions ($\sigma_{Ln}(\lambda_{ex})$) and Ln^{3+}-doped NPs the following theoretical basis was used and described in the supplementary information of own publication [51]:

The Beer-Lambert law describes the intensity reduction of incident light I_0 passing through an absorbing medium with a cross-section σ, a number n of molecules and a thickness t:

$$ln \frac{I_0}{I} = \sigma\ n\ t \tag{2.3}$$

The absorbance $A(\lambda_{ex})$ is defined by the NP concentration c [mol] and the decadic molar extinction coefficient $\varepsilon(\lambda_{ex})$:

$$A(\lambda_{ex}) = log \frac{I_0}{I} = \varepsilon(\lambda_{ex})\ c\ t \tag{2.4}$$

The combination of both equations gives the NP absorption cross-section $\sigma_{NP}(\lambda_{ex})$, with the Avogadro's number N_A:

$$\sigma_{NP}(\lambda_{ex}) = \frac{1}{log\ e} \frac{A(\lambda_{ex})\ 10^3}{N_A\ c\ t} \tag{2.5}$$

$\sigma_{NP}(\lambda_{ex})$ can be used to calculate the brightness B_{UC} and the absorption cross-section of one Ln^{3+} ion:

$$B_{UC} = \sigma_{NP} * QY_{UC} \tag{2.6}$$

$$\sigma_{Ln}(\lambda_{ex}) = \sigma_{NP}(\lambda_{ex})\ /\ N_{Ln} \tag{2.7}$$

with the number of Ln ions per UCNP N_{Ln}. For our study on Nd-doped UCNPs, N_{Ln} (Ln = Nd, Yb, Er) was calculated by considering the number of ions per hexagonal unit cell ($N_{unit,Ln}$), depending on the doping concentration (c_{Ln}) and the number of unit cells per NP (n_{cells}). n_{cells} was calculated by using the ratio of NP volume (V_{NP}) to unit cell volume (V_{cell}). V_{cell} was determined using the procedure reported by Mackenzie et al. [52].

The Table 2.1 lists our own results and different σ_{Ln} values of both, Nd^{3+} and Yb^{3+} ions found in literature for different host materials and excitation wavelengths. This composition illustrates the influences of external parameters on σ_{Ln} and the necessity to determine σ_{Ln} if excitation or host material is being changed.

Ln^{3+}	**host**	**λ_{ex} [nm]**	**σ_{Ln} [cm^2]**	**Ref.**
Nd^{3+}	LaF_3	790	$2.5 \cdot 10^{-20}$	[53]
	$(Gd,Y)VO_4$	808	$2 \cdot 10^{-19}$	[54]
	Nd^{3+}	800	$1.2 \cdot 10^{-19}$	[49]
	Sc_2O_3	825	$7.2 \cdot 10^{-20}$	[55]
	YAG	808	$1.2 \cdot 10^{-19}$	[56]
	-	~ 800	$\sim 10^{-19}$	[54]
	$NaYF_4$	794	$1.3 \cdot 10^{-19}$	our work [51]
	$NaYF_4$	805	$4.9 \cdot 10^{-20}$	our work [51]
Yb^{3+}	$YAlO_3$	980	$2.1 \cdot 10^{-20}$	[55]
	YAG	980	$2.5 \cdot 10^{-20}$	[57]
	Al_2O_3	980	$1.2 \cdot 10^{-20}$	[56]
	-	~ 980	$\sim 10^{-20}$	[54]
	$NaYF_4$	976	$1.8 \cdot 10^{-20}$	our work [51]
	$NaYF_4$	978	$1.4 \cdot 10^{-20}$	our work [51]

Table 2.1. Literature research of absorption cross-section $\sigma_{Ln}(\lambda_{ex})$ values of Nd^{3+} and Yb^{3+} ions for different host materials and excitataion wavelengths, taken from own publication SI [51].

2.4. LRET/FRET of UCNPs

2.4.1. LRET / FRET process

The energy transfer between two molecules, from the electronically excited donor (D) to the acceptor (A) which is located in the groundstate, can occur either radiatively or non-radiatively. In the case of radiative energy transfer, a photon is emitted from the donor and is subsequently absorbed by the acceptor, whereas in the case of non-radiative energy transfer, the energetic depopulation of the donor and the energetic population of the acceptor happen simultaneously without a photon exchange. The theoretical basis of this non-radiative energy transfer is the Coulomb interaction of two resonant oscillating dipoles (”dipole-dipole interaction”), and therefore also called ”luminescence resonance energy transfer” (LRET) or ”Förster resonance energy transfer” (FRET) [58]. In terms of classical electrodynamic, the donor dipole with dipole moment $\overrightarrow{p}_D$ interacts with the electromagnetic field (incident light), and starts oscillating and generating an electrical dipole-field[1]. If the acceptor is located close enough to the donor (distance R), the acceptor dipole (dipole moment $\overrightarrow{p}_A$) starts interacting with the dipole-field, leading to the interaction energy W_{D-A}:

$$W_{D-A} = -\overrightarrow{p}_A \cdot \overrightarrow{E}_D = \frac{\kappa^2 |p_A|\,|p_D|}{n_r^2 R^3} \tag{2.8}$$

with the orientation factor κ^2 and the refractive index n_r of the surrounding medium [59, 60].

A more precise and complete description of the non-radiative energy transfer is offered by quantum mechanics, modelled under first order perturbation theory with the perturbation

---

[1] dipole-field: $\overrightarrow{E}_D = \frac{\overrightarrow{p}_D}{R^3} - \frac{3\overrightarrow{R}(\overrightarrow{R} \cdot \overrightarrow{p}_D)}{R^5}$ with $\frac{\overrightarrow{R}}{R}$ as unit vector. Consequently, $\overrightarrow{E}_D$ scales with $\frac{1}{R^3}$

(here: interaction) term $\widehat{W}_{D-A}$ and Fermi's Golden Rule. The Rule reveals the energy transfer rate k_{ET} as function of the probability $|\langle\psi_1|\widehat{W}|\psi_2\rangle|^2$, that under the interaction $\widehat{W}_{D-A}$ the transition from state $\langle\psi_1| = \langle\psi_{D*}\psi_A|$ to state $\langle\psi_2| = \langle\psi_D\psi_{A*}|$ occurs.

$$k_{ET} = \frac{2\pi}{\hbar^2}|\langle\psi_{D*}\psi_A|\widehat{W}_{D-A}|\psi_D\psi_{A*}\rangle|^2 \tag{2.9}$$

The $*$ marks the corresponding excited status of acceptor and donor. The $\widehat{W}_{D-A}$ is the quantum mechanic operator of W_{D-A} in eq. 2.8 which describes the dipole-dipole transfer interaction for a D-A distance larger than the charge distributions [61]. By replacing $|p_D|$ and $|p_A|$ with the equivalent $\widehat{\mu}_D$ and $\widehat{\mu}_A$ transition dipole operators, it follows for ep. 2.9:

$$k_{ET} = \frac{2\pi}{\hbar^2}\frac{\kappa^2}{n_r^2 R^6}|\langle\psi_{D*}|\widehat{\mu}_D|\psi_D\rangle|^2 \cdot |\langle\psi_A|\widehat{\mu}_A|\psi_{A*}\rangle|^2 \tag{2.10}$$

The donor transition operator $\widehat{\mu}_D$ depends on the emission intensity $\mathrm{F}_D(\lambda)$, the unquenched decay lifetime τ_D and the unquenched QY (ϕ_D) value. $\widehat{\mu}_A$ depends on the extinction coefficient $\epsilon_A(\lambda)$, which together leads to the following relations [60]:

$$|\langle\psi_{D*}|\widehat{\mu}_D|\psi_D\rangle|^2 \propto \int (F_D(\lambda)\cdot\lambda^4)\, d\lambda \cdot \frac{\phi_D}{\tau_D} \tag{2.11}$$

$$|\langle\psi_A|\widehat{\mu}_A|\psi_{A*}\rangle|^2 \propto \int (\epsilon_A(\lambda)\cdot\lambda)\, d\lambda \tag{2.12}$$

Substituting these in eq. 2.10 yields

$$k_{ET} \propto \frac{1}{R^6}\frac{\kappa^2\phi_D J(\lambda)}{n_r^2\tau_D} = \frac{1}{\tau_D}\left(\frac{R_0}{R}\right)^6 \tag{2.13}$$

with the spectral overlap integral $J(\lambda)$ and the Förster radius R_0 defined as:

$$R_0 = 0.02108\left(\kappa^2 \cdot n_r^{-4} \cdot \phi_D \int F_D(\lambda)\cdot\epsilon(\lambda)\cdot\lambda^4\, d\lambda\right)^{1/6} \tag{2.14}$$

with,

$$J(\lambda) = \int F_D(\lambda)\cdot\epsilon(\lambda)_A\cdot\lambda^4\, d\lambda \tag{2.15}$$

The eq. 2.13 reveals a few requirements for a high LRET rate between donor and acceptor. First, a strong overlap of the donor emission and the acceptor absorption spectra (overlap integral $J(\lambda)$), second a short spatial D-A distance R ($\leq$ 10 nm) and third, preferably, a strong donor QY [62]. R_0 represents the distance between donor and acceptor at which the energy transfer efficiency (η_{LRET}) is half of the maximum. Therefore, η_{LRET} can be calculated as follows and scales inversely with the 6^{th} power of R:

$$\eta_{LRET} = \frac{R_0^6}{R_0^6 + R^6} \tag{2.16}$$

The efficiency η_{LRET} also can be calculated from the luminescence of the unquenched donor compared to that of the donor in the presence of the acceptor (DA) by using the QY values (ϕ_D and ϕ_{DA}), the intensities (I_D and I_{DA}), or the decay lifetimes (τ_D and τ_{DA}) [63]:

$$\eta_{LRET} = 1 - \frac{\phi_{DA}}{\phi_D} = 1 - \frac{I_{DA}}{I_D} = 1 - \frac{\tau_{DA}}{\tau_D} \tag{2.17}$$

LRET of UCNPs

As described in the previous sections, the luminescent properties of UCNPs depend mainly on the host material as well as quenching effects inside of the NP or on its surface. Therefore, UCNPs are only marginally influenced by variations in the surrounding, except for the temperature. Consequently, except for temperature, the design of sensors with UCNPs must be combined with an analyte-responsive chromophore (e.g. a dye). Thereby, UCNPs can help to expand the sensitive wavelength range of chromophores to the NIR range, see chapter 8 of [26].
In the last years, a wide range of UCNPs-based LRET nano-sensors have been developed in combination with different energy acceptors (organic dyes, noble metal NPs, MnO_2 and carbon nanomaterials) for biosensing of different species of ions (e.g. Hg^{2+}, Pb^{2+}, Cr^{3+}, Cu^{2+}, Fe^{3+} and K^{+}), gas molecules (e.g. oxygene, carbon dioxide, ammonia) and detection of biomolecules (e.g. proteins, DNA/RNA), see chapter 8 of [26]. Most of these applications use the intensity signal of an emission band, as reference, which is not affected by the LRET [64].

Compared to other classical D-A LRET systems (dye-dye or QD-chromophore pairs [65]), in which the D-A pairs have a fixed distance to each other, the LRET process between an UCNP and dye molecules bound on the surface, is much more complicated. Here, many emitting lanthanide ions, acting as donors, interact with a large number of dyes (acceptors) at different distances. Furthermore, the small Förster radius R_0 (≤ 10 nm) leads to the fact that only surface-near Ln^{3+} ions are significantly involved in the LRET process, while Ln^{3+} ions in the centre are being unaffected. Consequently, η_{LRET} for UCNPs roughly depends on the UCNP diameter. According to Muhr et al. [66], a maximum η_{LRET} of 50-60 % are found for UCNPs with 21-25 nm in size. It is therefore essential to have a sufficiently large diameter to reduce surface related quenching effects, but at the same time, a small enough size to allow for a large number of interacting Er-dye LRET pairs.

In this work, the LRET from UCNPs to the dye sulforhodamine B is discussed as proof of concept at ensemble and SP level. The corresponding results are presented in the section 7.1.
As part of another project, the energy transfer from a NIR-dye to an UCNP, whose absorbance band overlaps with the NIR dye emission band, resulting in a dye-sensitized UC process has been examined and published in [67].

2.4.2. LRET from UCNPs to sulforhodamine B

Using sulforhodamine B (SRB) as an acceptor bound coordinately to the surface of an UCNP, exploits the spectral overlap between the green emission band (520 nm - 560 nm) of Yb/Er-doped UCNPs and the absorption band of the SRB dye molecules, fulfilling a requirement for LRET between UCNPs and SRB dyes, as plotted in Figure 2.7 a). The η_{LRET} can be calculated by using the donor LTs, with and without the presence of the acceptor, cf. equation 2.17. The intrinsic LT of the dye emission (λ_{RSB} = 585 nm) in ethanol is in the ns-range with a lifetime of about 3.6 ns (Fig. 2.7 b)). This mono-exponential decay is much faster compared to the UCNP LTs in the ms range. Due to this huge difference in the donor and acceptor LTs ($\tau_D \gg \tau_A$), the LT of the acceptor dye in the presence of the donor (AD) shows approximately the same value as the LT of the quenched donor (DA): $\tau_{DA} \mathrel{\widehat{=}} \tau_{AD}$. Consequently, for the LRET efficiency [68] follows:

$$\eta_{LRET} = 1 - \frac{\tau_{DA}}{\tau_D} \mathrel{\widehat{=}} 1 - \frac{\tau_{AD}}{\tau_D} \qquad (if\ \ \tau_D \gg \tau_A) \tag{2.18}$$

The LT of the green UC emission of the quenched surface-near Er^{3+} ions (τ_{DA}) is overshadowed by the strong green emission of the unquenched Er^{3+} ions of the NP centre. It is therefore advantageous to take the background free LT of the dye (τ_{AD}) in the presence of UCNPs for the efficiency calculation and as proof for real LRET processes between both contestants [61].

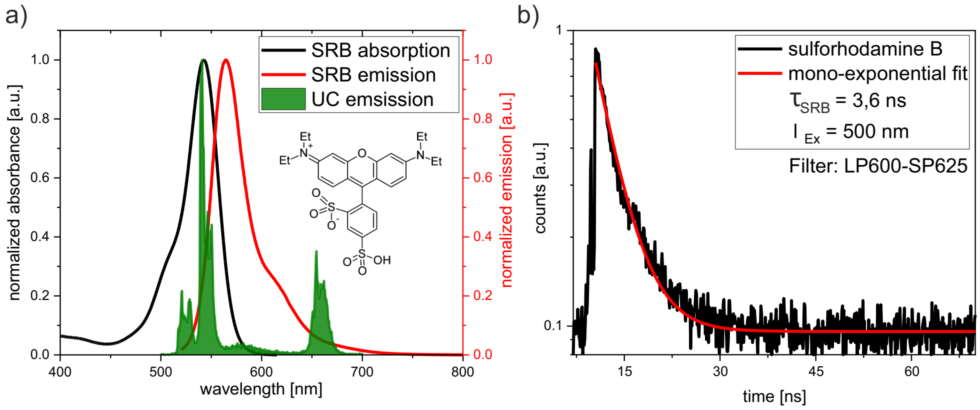

Figure 2.7. LRET/FRET conditions between UCNPs as donor (D) and sulforhodamine B (SRB) as acceptor (A): a) Normalized absorbance and emission spectra of SRB in overlap with the UC emission spectra coloured in green. b) Decay curve of free SRB dyes dispersed in ethanol with a mono-exponential fit revealing an intrinsic decay LT of about 3.6 ns.

2.5. Plasmonic interactions

2.5.1. Plasmonic effects

According to the plasma model, free electrons in a metal start oscillating in the presence of an electromagnetic field, such as (incident) light. These collective oscillations of the electron gas are called plasmons. This effect also occurs at metal-dielectric interfaces, resulting in so-called surface plasmon polaritons (SPPs), which propagate along the interface as longitudinal waves until energy is lost by scattering processes. Perpendicular to the interface, the induced evanescent fields decay exponentially into the metal and the dielectric with different penetration depths, cf. Fig. 2.8 a). SPPs can only be excited by direct light illumination with an additional momentum transfer, as both, the momentum and the energy must be conserved at the interface [69]. Mathematically, the interactions of electromagnetic fields with metal can be fully described by the classical Maxwell equations and the conservation of the field components at the metal-dielectric interface. To overcome the momentum mismatch when using planar wave (or light) excitation, surface coupling techniques and geometries have been implemented, like total internal reflection effects on a prism or like the diffraction effects at a specific grating pattern, cf. chapter 26 in [63].
For metal NPs with dimensions (much) smaller than the incident wavelength, plasmons are no longer propagating but strongly confined to the NP. The so-called localized surface plasmons (LSPs) can only be excited under resonant conditions [70], cf. Fig. 2.8 b). In this case the LSPs enhance the local density of states (LDOS), which in turn also enhances the local electric near-field. The increase in LDOS under resonant condition can enhance the probability for spontaneous emission of a quantised emitter resulting in enhanced luminescence, which is called the ”Purcell effect” [71].

Plasmonic effects are widely used in several opto-analytic applications, like in surface-enhanced Raman spectroscopy (SERS), in which LSPs enhance the near-field resulting in enhanced inelastic photon scattering by the probed matter [72]. In bio-analytic the plasmons are used for luminescence enhancement of fluorophores by placing them in the proximity of a metal. The fluorescence signal can also be quenched by the metal via re-absorption effects and therefore, the geometry and distance between emitter and metal nano-structure have to be determined for optimised condition. Additionally, plasmonics has been also implemented in other areas, such as medical applications [73] and security-coding techniques [74].

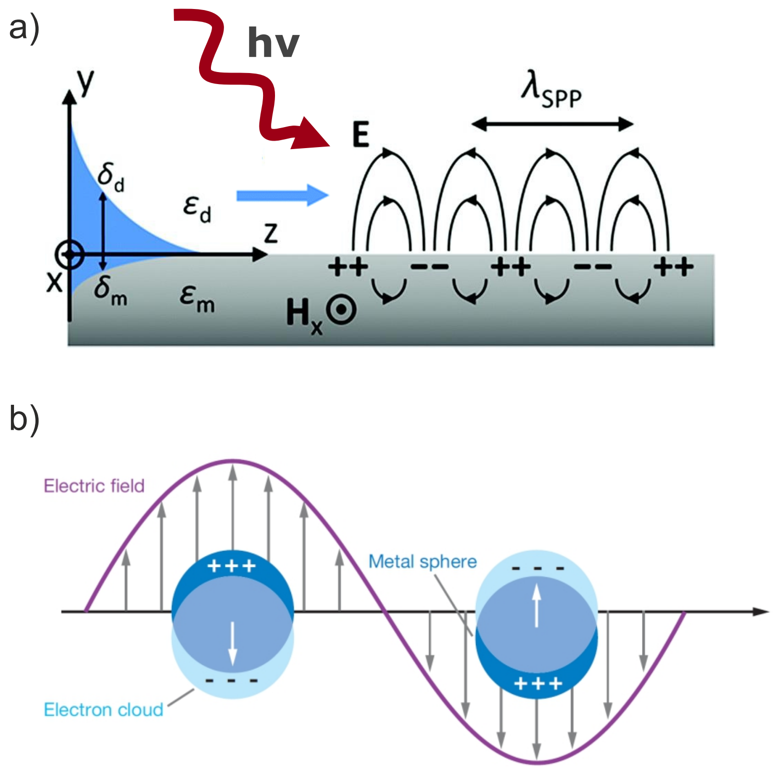

Figure 2.8. Illustration of plasmonics: a) Surface plasmon polariton (SPP) on a dialectic-metal interface arising from light interactions propagating in z-direction with evanescent electric field components in y-directions. Taken and modified from [69]. b) Localised surface plasmon (LSP) originated by interaction of light with metal NPs, which have a diameter smaller than the incident wavelength. Taken from [72].

2.5.2. Plasmonic enhancement of UCNPs

The UCL of RE nanocrystals can be enhanced by using plasmonic resonances in two ways, first matching and enhancing the absorption, and second matching the UC emission (Purcell enhancement). In both cases, the occurrence of non-radiative channels in the metal results in quenching. Therefore, the exact geometry of the metal-UCNP component is crucial to obtain enhanced UC performance [75, 76]. Several studies have been published, focusing on plasmonic UC emission coupling at SP level [77–82]. According to [76], greatest enhancement has been achieved for excitation enhancement at low P, where the NIR absorption scales quadratically. To match the plasmon resonance with the NIR excitation, several shapes and geometries of the appropriate metal system have been shown to be effective like nanopillars [83, 84], holes [85], pyramid arrays [86], nano-grating [87] and using LSPs in Au nanorods [78]. For Er^{3+} ion doped UCNPs, the green and red emission was enhanced by factors of 310 and 100 using an array of Au dots on top of nanopillars [83]. Matching the plasmon resonance to the UC emission is mainly achieved using design engineering with Au or Ag [88]. In previous studies the UC emission were enhanced by factors between 2 and 30 for Au NPs [89–91], and by using Ag NPs, enhancement factors between 1.4 and 17 have been achieved [92–99].

2.5.3. Computational modelling of resonant modes for metal-shelled UCNPs

Our optical studies on metal-shelled UCNPs in chapter 7.2 were part of an European research project, which combined computational modelling, synthesis and the experimental validation aiming to design novel metal-shelled UCNPs with enhanced UCL. The theoretical modelling of the plasmon resonances were performed by our project partner, the group of Prof. García de Abajo (ICFO, Barcelona). They used Mie theory, which is an analytical solution of the Maxwell equations for light scattering, combined with theory about electrodynamic interaction of a dipole E-field on multi-shell systems under fixed incident excitation at 980 nm. A detailed outline of the theoretical work is presented in the PhD thesis of Lijun Meng [100]. The simplified model consists of an incident wave with an E-field in x-direction, which reaches a spherical particle with a dielectric core and an Au-shell (Fig. 2.9 a)). Depending on the dialectic core radius and the metal shell thickness, there are 4 resonant plasmon modes (dipole, quadrupole, hexapole and cavity) enhancing the field intensity $|E|^2$, Figure 2.9 b). The dipole, quadrupole and hexapole modes can be interpreted as stationary waves of LSPs with highest enhancement factors at the metal NP surface (Fig. 2.9 c) (i-iii). Theoretically, they only appear for Au layers thinner than 10 nm, which is difficult to synthesize. The cavity mode arising from plasmon oscillations inside the metal shell leads to field enhancement inside the dielectric/metal core-shell particle. They show highest enhancement for thicker Au-shells, which can be fabricated in the laboratory (Fig. 2.9 c) (iv).

The next step was to calculate the local field enhancement for specific emission bands of a Yb/Er doped UC core, which were theoretical placed in the centre of the dielectric/metal core-shell particle with a diameter of 30 nm. From equation 2.19, the emission intensity (I_{em}) can be calculated taking the field enhancement (FE), the decay rate without metal shell (g_0), the pump intensity (I_0), the saturation intensity (I_S) and the ratio (γ) of density of states with radiative contribution ($LDOS_{rad}$) to density of states in vacuum (LDOS) into account:

$$I_{em} = \frac{\gamma}{\frac{1}{LDOS} + \frac{I_S}{FE \cdot I_0}} \qquad with: \ \gamma = LDOS_{rad}/LDOS \tag{2.19}$$

There are two limiting regimes for the pump intensity, first, **pump saturation** ($I_0 = I_S$) at which the denominator part (1/FE) is ≪ than (1/ LDOS) and therefore follows from eq. 2.19:

$$I_{em} = \frac{\gamma}{\frac{1}{LDOS}} = LDOS_{rad} \qquad (saturation \ \ regime) \tag{2.20}$$

The second regime is the **dimmed pumping** ($I_0 << I_S$), where the denominator part (I_S / FE$\cdot$ I_0) >> (1/LDOS) and eq. 2.19 change to,

$$I_{em} = C \cdot \gamma \cdot FE \qquad (with: \ C = I_0 \cdot \sigma / g_0), \ \ (dimmed \ \ regime) \tag{2.21}$$

Figure 2.10 depicts the calculated emission intensity enhancement factors for green (540 nm) and red (654 nm) Er emission bands of a central UC core inside the Au-shelled dialectic

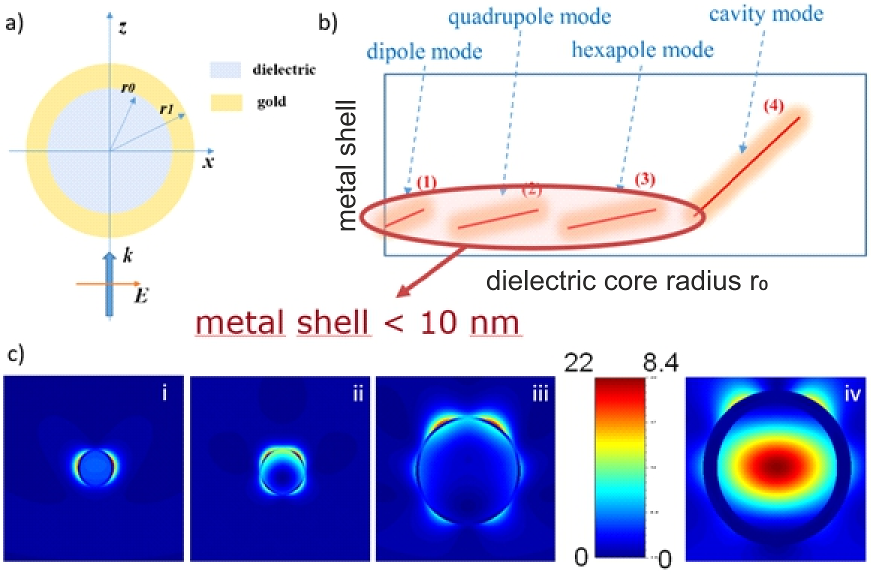

Figure 2.9. Theoretical model of the plasmonic resonance modes of an Au-shell NP in the E-field of an incident light beam: a) Sketch of the Au-shelled NP and the orientation of incoming E-field. b) Expected appearance of resonance modes depending on the metal shell thickness and dialectic core radius. c) Calculated field enhancement due to surface plasmons (dipole, quadrupole and hexapole modes (i-iii)) and the cavity mode (iv). The images were provided from our cooperation partners in Barcelona.

NP. The enhancement of the 654 nm UC emission at 980 nm pump saturation regime (cf. eq. 2.20) is illustrated in Fig. 2.10 a). The red dotted lines and the circles illustrate the tuple (x,y = metal shell, dielectric particle radius) with maximal enhancement factors of the cavity modes written in the black cubes. For a particle with 152 nm in radius (UC core and dialectic shell) the external 51 nm thin Au-shell supports the cavity mode, which results in a theoretically predicted 20-fold enhancement of emission intensity. For the dimmed pumping regime (cf. eq. 2.21), the resulting cavity mode enhancement factors of 11 and 15 are reached for a 252 nm dielectric particle radius and a 35 nm Au-shell for the green and red emission, respectively as shown in Figure 2.10 b) and c). These simulations were the basis for the synthesis procedure, which were performed from our project partner, the group of Prof. Graf (FU Berlin, Germany), with the aim to match the calculated NP radii and shell thicknesses leading to the theoretical predicted UCL enhancement.

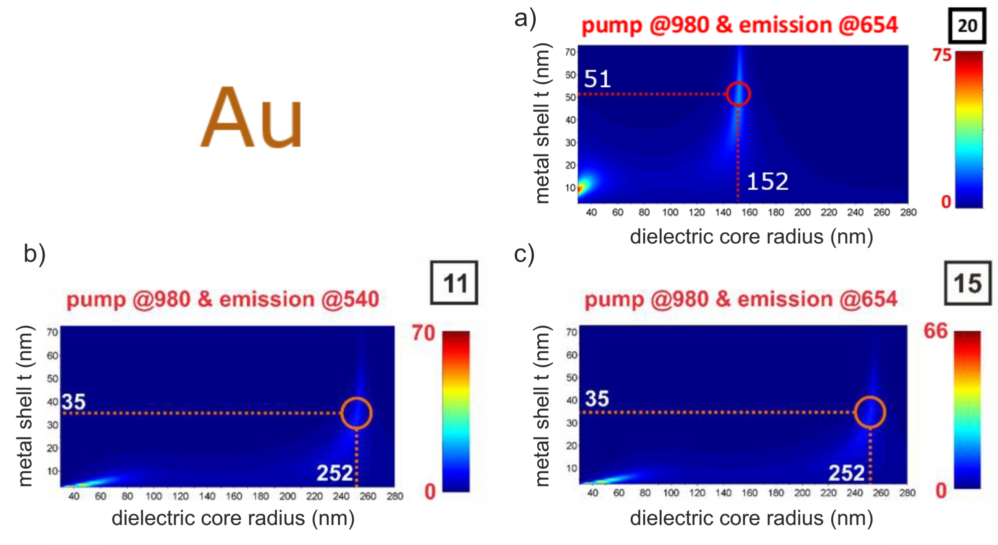

Figure 2.10. Modelling of the plasmonic resonance modes depending on Au-shell thickness and dielectric core diameter at pump saturation and for dimmed pumping: a) Excitation at 980 nm at pump saturation, the cavity mode enhances the red emission theoretically 20 times for 51 nm Au-shell and 152 nm dielectric particle radius. b) and c) The cavity mode for dimmed pimping enhances the 540 nm emission (b) and 654 nm emission (c) about 11- and 15-times for 35 nm Au-shell and 252 nm dielectric particle radius. The calculations have been performed by Lijun Meng [100].

3 Experimental basis: Setups and characterisation methods

This chapter gives an overview of the different sample characterisation methods concerning the chemical structure and the optical characterisation techniques, including sample preparation, handing and measurement conditions. The self-constructed confocal laser scanning microscope (CLSM) is described in more detail at the end of this chapter.

3.1. Structural and chemical analysis

All studied UC samples have been synthesized and provided for our optical studies by several cooperation partners. The structural and chemical analysis were performed by our cooperation partners including the following list of characterisation methods:

- ICP-OES: With inductively coupled plasma-optical emission spectrometry the Ln^{3+} ion doping concentrations are determined for controlling the accuracy of the NP synthesis.

- TEM: Transmission electron microscopy provides with real space images information about the physical dimensions of NPs. By imaging hundreds of NPs with one shot their size distribution can statistically determined leading to averaged NP diameters.

- XRD: X-ray diffraction is a tool to identify the atomic and molecular crystal structure by measuring the intensities and angles of diffracted X-rays. With this technique the crystal phase and therefore the homogeneity of crystal growth during synthesis can be determined. The presence of cubic (α) or hexagonal (β) crystal structure of a $NaYF_4$ crystal can be clarified that way.

- DLS: Diffraction light scattering helps to determine the hydrodynamic diameter of the NPs in solution. Thereby is also captured the mono-dispersity and the colloidal stability of the sample.

The corresponding results of these analysis methods are presented at the beginning of each chapter dealing with a new set of samples.

3.2. Spectroscopic studies at ensemble level

The spectroscopic studies of UCNPs were performed on own setups of the Biophotonic group, BAM Berlin. A complete optical characterisation of UCNPs in ensemble condition includes steady-state and time-resolved measurements possible for powder samples or samples dispersed in solution.

3.2.1. Absorption and emission spectra

Absorption and emission spectra help to get a deeper understanding of what happens when light hits and interacts with an optical active sample. The wavelength dependent light scattering, transmission and absorption behaviour of a sample can be read out from an absorption spectrum. The main absorption peaks give information about material composition with typical absorption lines (e.g. broad 980 nm peak for Yb^{3+}) and at which wavelength the sample can be excited for the emission scan. After correction of scattering and background signal, the absorption spectra can be used for calculation of ion absorption cross-sections σ_{abs}, as it is done in chapter 6.3 for Nd^{3+}-doped UCNPs. For this thesis, the absorption spectra in the UV and vis range were measured either with the Cary5000 from Agilent Technologies or with the Specord200 spectrometer from Jena Zeiss.
For emission spectra in the vis range the photoluminescence spectrometer FLS980 (Edinburgh Instruments) was used and equipped with two 8W laser diodes. One 808 nm diode with variable P values between 25-500 W/cm^2 for Nd-excitation and one 980 nm diode with Ps between 20-120 W/cm^2 for Yb-excitation. A typical emission spectra of a Yb/Er doped $NaYF_4$ crystal is shown in Figure 2.4 b).
For absorption and emission measurements it is essentially to take a blank measurement using the pure solvent for dispersed samples or $BaSO_4$ powder for solid samples.

3.2.2. Upconversion quantum yields

The QY measurements were performed absolutely and P-dependent on a custom-made integrating sphere setup[1] equipped with two 8W laser diodes at 808 nm (RLTMDL-808-8W, Roithner-Laser) and 980 nm (RLTMDL-980-8W, Roithner-Laser) emission wavelength for Yb and Nd excitation. The setup is sketched in Fig. 3.1. The excitation laser-light is focused on the sample by passing a shutter and two density filter wheels, which provides via light-attenuation combined over 15 different excitation Ps covering a range from $4 - 520$ W/cm^2. The sample-holder is positioned on top and places the sample in the centre of the highly reflective sphere. After multiple reflections inside the sphere the emission light is collected at the bottom, send to a monochromator and measured by Si-CCD and InGaAs-CCD for the vis and NIR range, respectively. The measurement settings and the data analyses are controlled using a self-written Labview software tool[1]. For more information about technical details (measurement conditions, calculation of excitation P, component specifications,

---

[1] The integrating sphere setup was mainly built by the colleagues Martin Kaiser and Christian Würth

calibration approaches, signal-correction methods and analyses procedures) read dissertation of Marco Kraft [101] or our published group work [43, 102, 103]. In 2018, this setup and its performance was compared to other integrating sphere setups of two European research groups (in Leiden and Karlsruhe) by measuring the same sample for testing the reliability and comparability of such measurements [104].

For the calculation of the QY, which is defined as ratio of emitted to absorbed photons (see equation 2.2) the comparable emission spectra of sample and blank over the whole vis region including the excitation peak in the NIR range are needed. By subtracting the blank from the sample signal the remaining area segments under the graph are proportional to the absorbed and the emitted photon fluxes in the excitation and the emission range, respectively. By using these area segments after particular correction procedures, the QY values at a certain *P* can be calculated. Since UC samples show a non-linear optical behaviour also the QY values are *P*-dependent. Consequently, the UCL performance needs to be studied *P*-dependently.

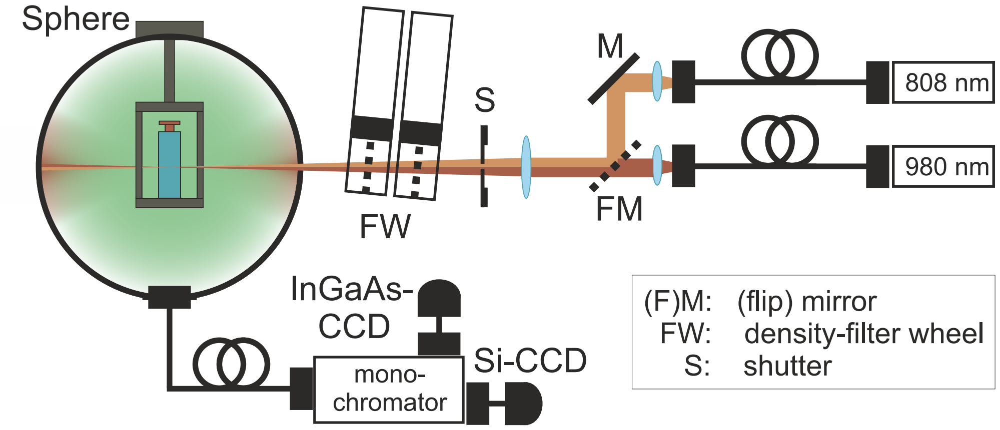

Figure 3.1. Sketch of the home-built integrating sphere setup for QY measurements: Two 8W laser diodes with emission wavelengths at 808 nm and 980 nm are focused onto the sample in the centre of the sphere by passing two density filter wheels for variable adjustment of the excitation *P*. The emission signal is collected at the sphere bottom, send to monochromator and read out by Si-CCD and InGaAs-CCD for the vis and NIR range, respectively.

There are a few critical parameters, which should be chosen well for proper QY measurements with reliable results:

(1) The concentration of absorber ions in the sample (like Yb or Nd ions) should lead to light absorptions of 5-20%, which is both, high enough for effective UC with strong emission and low enough for weak re-absorption effects. For better comparability of different measurements it is useful to keep the light absorption values constant.

(2) The sample temperature should be held constantly low since thermal energy can influence the UC process and distort the QY results. Especially, samples dispersed in high absorbing solvents can overheat and be damaged easily under long and intensive light irradiation, as it is the case for samples dispersed in water under 980 nm excitation.

(3) The laser intensity should be stable with a minimal variation of ±1% during both the

blank and the sample scans. Even small changes in excitation power can have great impact on results due to the non-linear nature of UC processes and their P-dependency.
This setup was used for both, Yb and Nd sensitized particle systems, which are discussed in this work in chapter 4 and chapter 6. To get more reliable QY results the scans were several times repeated and the individual results averaged.

3.2.3. Time-resolved measurements

The study of UC process on time scale opens a deep insight about the intrinsic energetic population and de-population processes of the involved fluorescent levels. The idea is to excite the sample in a short time-frame with a single laser pulse and detect time-resolved the fluorescent respond of a fluorescent level at the specific wavelength over a certain period of time. By multiple repeating of this sequence of short excitation with following detection procedure, the time-resolved trend of fluorescent emission can be plotted in an intensity over time histogram.
The technical implementation, which is called time correlated single photon counting (TC-SPC), is realised with a periodic pulsed laser excitation including variable laser pulse power P_{puls}, pulse length t$_{pulse}$, for detection a monochromator with an APD (Avalanche Photon Diode) and for the computations a fast electronic readout technique device. The basis is the repeating and precise time registry of single photon signals referenced in time to the corresponding excitation pulse (start-stop-time: t_1, t_2) [63][105], as it is illustrated in Fig. 3.2 a). The accumulation of time-dependent photon-signals in a histogram as shown in 3.2 b) gives the typical decreasing trend of PL signal intensity with time following the exponential decay behaviour of fluorescent systems. The intensity $I(t)$ drops exponentially with time from the maximum value a (= I(t=0)), the lifetime τ is the reciprocal of the total decay rate, which is the sum of the emissive rate Γ and the non radiative decay rate k_{nr}, as follows [63]:

$$I(t) \approx a \cdot exp\left(-\frac{t}{\tau}\right) \qquad with \quad \frac{1}{\tau} = (\Gamma + k_{nr}) \tag{3.1}$$

Compared to fluorescent dyes or quantum dots (QDs) with lifetimes in the ns-range and mono-exponential decay behaviour, UCNPs show mono- and bi-exponential decays with significantly longer lifetimes from the μs up to ms-range. This is caused by the long-lived Laporte-forbidden 4 f-f transitions of lanthanides, as explained in chapter 2.2.1. The bi-exponential decay behaviour of UCNPs can be attributed to ion emissions which can originate either from the NP core or from the NP surface, where local surface quenching effects can occur [106]. The calculation of an average lifetime (eq. 3.2) can be done in two ways, by tail-fitting of the bi-exponential decay curve and weighting the components either by intensity (τ_{int}) or amplitude (τ_{ampl}), eq. 3.3.

$$I(t) = a_1 \cdot exp\left(-\frac{t}{\tau_1}\right) + a_2 \cdot exp\left(-\frac{t}{\tau_2}\right) \tag{3.2}$$

$$\tau_{ampl} = \frac{a_1 \cdot \tau_1 + a_2 \cdot \tau_2}{a_1 + a_2} \qquad \tau_{int} = \frac{a_1\tau_1 \cdot \tau_1 + a_2\tau_2 \cdot \tau_2}{a_1\tau_1 + a_2\tau_2} \tag{3.3}$$

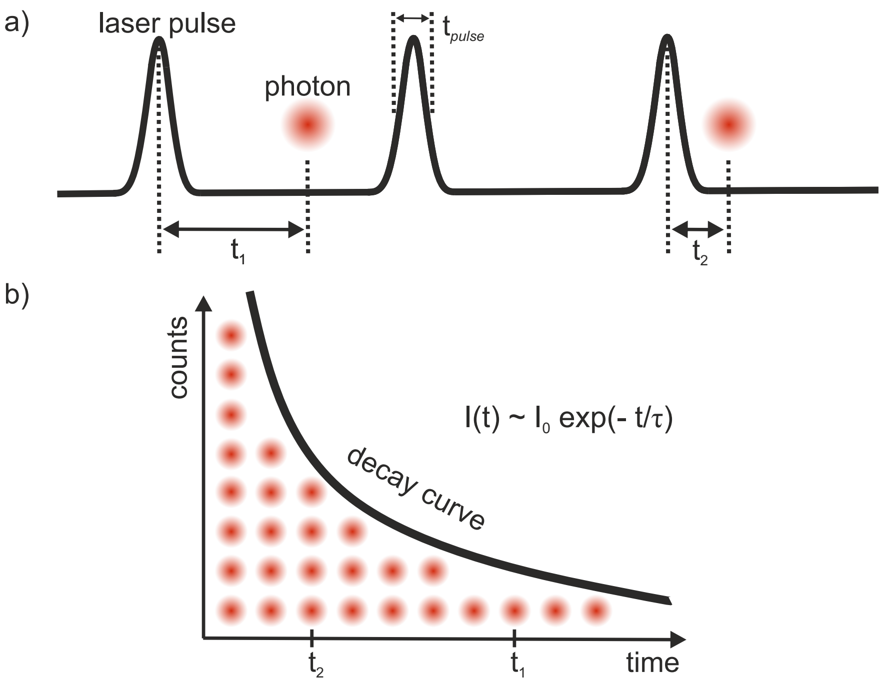

Figure 3.2. Principle of time-resolved fluorescent decay measurements: a) Time correlated single photon counting (TCSPC) caused by periodic laser pulse excitation sequences. The time intervals t_1, t_2 are defined as differences in time between a laser pulse and a detected photon. b) The time-resolved photons detected after multiple excitation circles are summed up in a histogram, plotted over time and show the typical exponential decreasing decay behaviour of fluorescent systems.

The amplitude weighted lifetime τ_{ampl} is proportional to the total steady-state intensity and used for comparison of processes which are quantified by the fluorescence intensities. In contrast, the intensity weighted lifetime τ_{int} is equivalent to the classical mean value of $I(t)$ over time (time average) and usefully for direct comparison of different lifetime values without having to focus single LT components [63].

For the lifetime-measurements of UCNPs on ensemble level the photoluminescence spectrometer FLS980 (Edinburgh Instruments) was used, which was equipped with a pulsed 980 nm laser diode variable in pulse lengths (40-410 μs) and pulse repetition rate (50-200 Hz). The decay curves were fitted using the software FAST from Edinburgh Instruments.

3.3. Studies of single particles

The single particle (SP) measurements have been performed with a home-built confocal laser scanning microscope (CLSM), which was designed and constructed[1] to record the steady-state and time-dependent luminescent behaviour of a broad range of different sample systems - like quantum dots (QDs), fluorescent dyes and UCNPs on SP level. Furthermore, the optional implementation of an AFM-head on top of the microscope body enabled correlated AFM-PL measurements. In the following sections the operating principle of the

---

[1] The CLSM was designed and constructed together with the two colleagues Florian Weigert and Christian Würth.

CLSM, detailed component specifications, data correction principle, sample preparation measurements techniques and data evaluation are described in detail.

3.3.1. Confocal laser scanning microscope

Figure 3.3 shows a sketch of our home-built CLSM with several laser sources for excitation at 405, 808 and 980 nm and a supercontinuum white-light laser covering the spectral range from 480 to 850 nm. For imaging and detection of the steady-state and time-dependent PL emission signal two cameras (CMOS and EMCCD) and two avalanche photo diodes (APDs) are available. The CLSM enables two microscopy measurement techniques - widefield imaging (WI) and confocal scanning - which will be described in the next sections by reference to Fig. 3.3.

Widefield imaging The 405 nm or 980 nm excitation light could be coupled into the microscope via an optical fiber and a dichroic mirror on demand. A concave was inserted in to the beam path to widen the beam diameter, which leads to a broad sample illumination with a $20 - 50\ \mu$m spot size, when using an high NA objective lens. Simultaneously, the sample can be illuminated from the top with a white Xe-lamp. Imaging was carried by with a monochrome CMOS camera at the emission port of the microscope body. A widefield image taken under combined laser and white-light illumination is an easy way to get quickly a quantitative overview of the sample and to check the presence of luminescent NPs.

Confocal scanning For confocal imaging, excitation light (white-light, 405 nm, 980 nm or 808 nm; blue and red in Fig. 3.3) is guided to the microscope from the fiber-coupled diode lasers, passing through a beam splitter (BS), a chopper, density filter (DF) and a dichroic mirror (DM) on its way. In the microscope the excitation laser light is focused onto the sample from the bottom (epifluorescence geometry) via an oil- immersion object lens with high NA. The sample emission (marked green in the sketch) is collected via the same objective lens and directed to the two avalanche-photodiodes (APDs) (PDM series, PicoQuant, Germany) by passing the DM in the transmissive range (F73-877SG, AHF, Germany), a DF for blocking the laser light and a pinhole to discard out-of-focus light (confocal condition). A 50/50 Pellicle-beam-splitter is used to split the emission light into two equal parts for both APDs (Fig. 3.3), in front of which an appropriate fluorescent filter (FF) can be placed to suppress the contributions of certain spectral ranges to the emission signal. This was done for UCNP studies with a green (545 ± 12.5 nm; F49-546) and a red (655 ± 20 nm; F39-655) bandpass filter (AHF Analysetechnik AG, Germany). Beside the sample emission, laser light is reflected at the glass/air interface and is collected by the objective lens as well and guided back in the direction of the laser diodes by the DM and send via a 90/10 Pellicle-beam-splitter (BS) to a CCD camera. This was used to control the laser focus position.

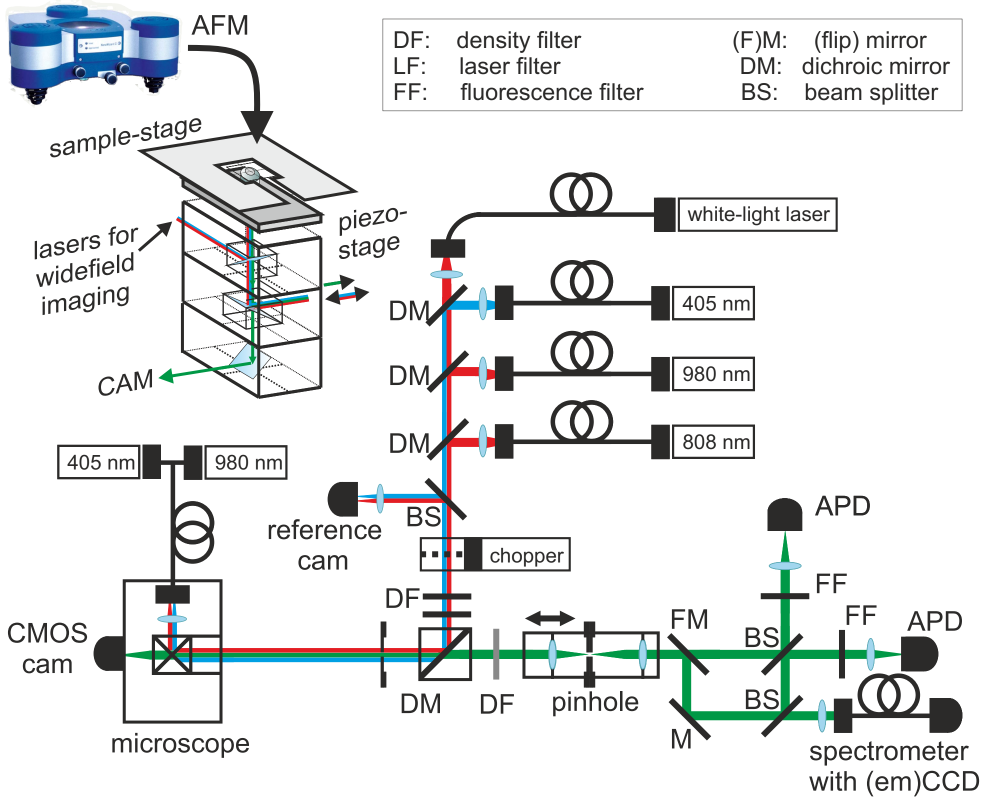

Figure 3.3. Sketch of the home-built CLSM-AFM setup for imaging vis/NIR photo-luminescence of SPs like UCNPs with temporal and spatial resolution (ability to measure steady- and time-resolved spectra) and perform time correlated single photon counting (TCSPC) measurements. For confocal laser scanning microscopy, 4 different laser sources can be used (405 nm, white-light laser (480-850 nm), 808 nm and 980 nm laser diodes) for excitation in cw or pulsed mode with variable laser power and repetition rates for lifetime measurements in the ns to s range. Widefield imaging can be done with 405 nm and 980 nm laser diodes. Sample emission can be read out with a CCD or two avalanche photodiodes (APDs) (for lifetime and antibunching studies) or with an EMCCD (for measuring spectra). Taken and modified from own publication [107].

In contrast to WI where a large area of the sample is illuminated and can be simultaneously observed, in confocal imaging only a small sample volume is excited by using objectives with high magnification and large numerical aperture (NA > 1). The use of point-like illumination is one strategy to enhance the local resolution, which is limited by the diffraction barrier. By focusing an optical planar wave of excitation light with such an objective results in an intensity distribution described by a main Airy pattern[1] $I(x, y, z)_{ex}$ and can be approximated by a Gaussian distribution [108]. The Rayleigh criterion defines the local resolution of an optical microscope by the minimal distance of two separated emitters, which can be individually detected by separating their generated Airy patterns. This is guaranteed if the first emitter maximum spot is located at the first minimum spot of the second emitter diffraction pattern. For the lateral distance Δ_r of the laser focus follows according

---

[1] Airy pattern/disk names the diffraction pattern of light on a circular aperture under uniform, central illumination.

to [109]:

$$\Delta r = \frac{0.61 \cdot \lambda_{ex}}{(NA)} \tag{3.4}$$

depending on the excitation wavelength λ_{ex} and the NA of the objective.

The resolution of the detection signal $I(x,y,z)_{em}$ can be enhanced by guiding the emission signal through a pinhole, which enables only photons from the focal plane to reach the detector [110]. This can enhance the resolution especially in 3D samples due to less blurring effect caused by scattering, background and autofluorescence light [111]. If the size of the pinhole is adjusted to the maximal spot diameter of the $I(x,y,z)_{ex}$ Airy disk, the resolution is enhanced without loosing too much signal intensity of the central peak. Consequently, the point-like characteristics of the illumination and detection can be described by $I(x,y,z)_{ex} \cdot I(x,y,z)_{em} \approx I(x,y,z)^2 = I(x,y,z)_{total}$[1] [110], whereas the squaring decreases the spot size by about $\sqrt{2}$ leading to a confocal resolution of

$$\Delta r_{confocal} = \frac{0.43 \cdot \lambda_{ex}}{(NA)} \tag{3.5}$$

These values are only theoretical limits, which can only be reached by a perfectly aligned setup, with optimized optical components. Furthermore, the real $\Delta r_{confocal}$ is also affected from the finite detection pixel sizes.

In case of SPs on a glass substrate, which are aligned in a sparse monolayer and can thus be approximated as a 2D structure - there is no need for a pinhole as contribution from out-of-plane fluorescence is expected to be minimal and the resolution scales directly with the excitation volume. The lateral resolutions of our setup is determined by detection and characterisation (FWHM of Gaussian fit) of the point spread function (PSF), which represents the $I(x,y,z)_{total}$ intensity distribution of a small ($\ll \lambda_{ex}$) NP emitter, as outlined in the setup specification.

For a quantitative study of single UCNPs it is necessary to have a constant local P of the excitation laser spot. Under confocal condition this can be realised with a diffraction limited (highly focused) laser spot by using an objective lens with high numerical aperture and by choosing the size of scanning pixels less than half of the expected diffraction limit to get a high resolved image. The choice of sufficient small pixel sizes can be attributed to the strongly recommended adjustment of the scanning frequency by the Nyquist theorem, which suggests a scanning frequency more than twice as high as the maximal frequency of the sample signal to guarantee the recording of all sample information.

For WI a constant excitation condition requires high accuracy of the laser spot alignment after beam expansion with subsequent cutting out of the edges for getting an excitation P as homogeneous as possible over the whole image. This explains why in the widefield image in figure 3.4 the single UCNPs in the centre appear brighter than the NPs on the edge of the image. Whereas comparing the same region of interest (ROI, here white dashed box) under confocal scanning all UCNPs show the same emission intensities of the red channel,

---

[1] Instead of λ_{ex} and λ_{em} the averaged wavelength $\bar{\lambda} \approx \sqrt{2}\frac{\lambda_{ex}\lambda_{em}}{\sqrt{\lambda_{ex}^2+\lambda_{em}^2}}$ is defined in this approximation [112].

as all NPs are excited with the same highly focused laser spot. Therefore, WI is only used to get a fast overview over the sample and confocal scanning is used for further quantitative studies of selected single NPs.

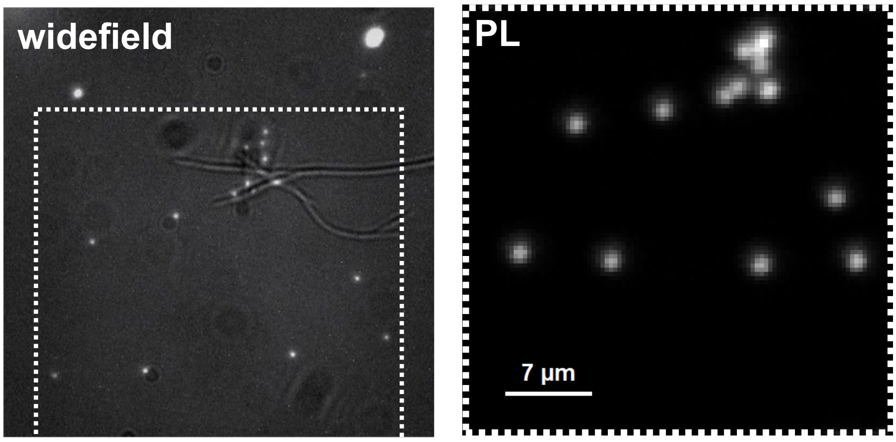

Figure 3.4. Comparison of widefield imaging (WI) and confocal scanning of the same ROI (white dashed box). The full illumination of the WI shows the UCNPs (bright spots) besides the CdSe nanowires, which serve as markers. The photoluminescence (PL) scan was recorded with an APD and shows the brightness information of the red UC channel using a 655 ± 40nm filter in front of the APD.

Setup specification

Excitation sources

The laser diodes producing the excitation light were fiber coupled to the collimators, and a combination of various dichroic mirrors with reflective properties in the specific wavelength ranges was used to align their light beams to the optical axis of the other components. This combined beam alignment makes it possible to switch easily between excitation light or to use more than one light source for excitation. For white-light excitation, 405 nm and 980 nm excitation the super-continuum laser SOLEA-R, the LDH-D-C-405 and LDH-D-F-980 diodes from PicoQuant are used. The spectral output of the SOLEA laser is plotted in appendix Fig. A.1. The SOLEA laser operates only in pulsed-mode, whereas the other two diodes can be used in pulsed- and *cw*-mode. For the laser pulses with a single pulse length of 12.5 ns, a repetition rate between 0.25 and 80 MHz can be adjusted by triggering the Sepia PDL 828 laser driver with the PicoQuant oscillator module SOM 828. Using the implemented burst-mode generator, any number of pulses between 1 and 16.7 million can be achieved as one combined output of multiple pulses (”controlled burst”) and in the same way any time gap without laser signal can be created. The combined use of two trigger output channels - one for laser signal ”on” and the other for signal ”off” - enables the flexible generation of any excitation pulse pattern needed for decay kinetic studies on UCNPs, like a 400 μs to 4 ms laser on/off burst ratio per rotary sequence.

For the Nd studies a 808 nm laser diode (RLTMDL-808-2W) from Roithner-Laser was added. The cw-laser light of both, the 808 nm laser and the super-continuum laser can be subsequently modified to act as pulsed excitation source by using a chopper-wheel to modulate the laser intensity over time.

To measure the diffraction limited laser spot size, the point spread function (PSF) of a single UCNP with a diameter of about 30 nm was taken with excitation at 980 nm and 808 nm. The PSF, which is the spread intensity distribution of a light point source after passing all diffractive optical elements, can be approximated by the FWHM of a Gaussian intensity distribution. The PSFs based on Gaussian fits of both PL images are plotted in Figure 3.5 and reveal an optical resolution of about 757 nm for the 808 nm (RLTMDL-808-2W) diode (a) and of about 745 nm for 980 nm (LDH-D-F-980) excitation (b).

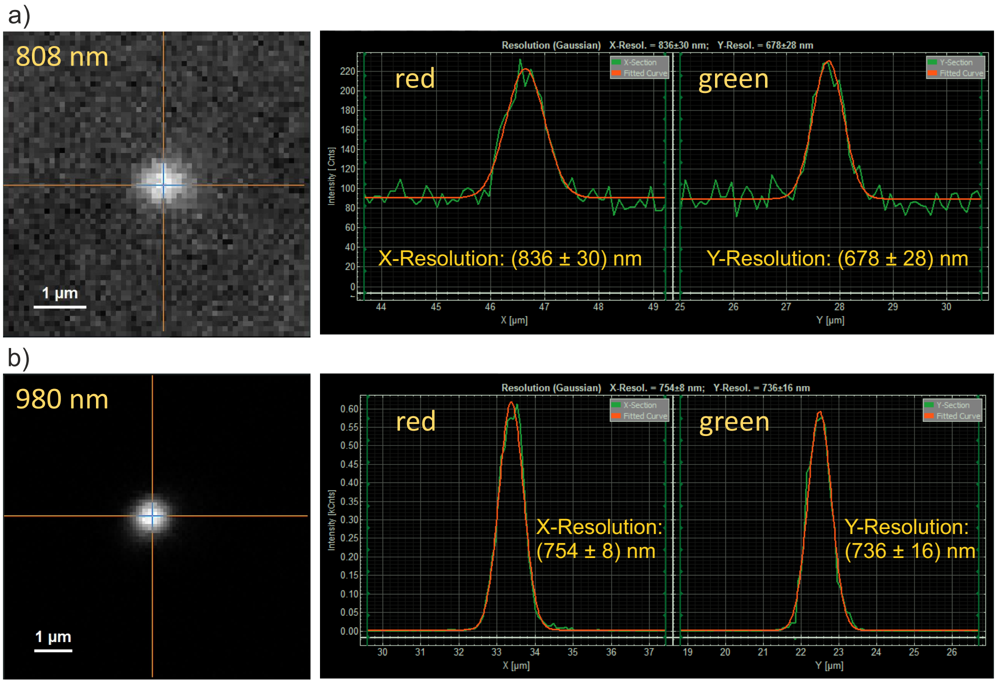

Figure 3.5. Determination of the lateral resolution by measuring the PSF of a single UCNPs with diameters (about 25 nm) smaller than the diffraction limited resolution, which is about ($\lambda_{ex}/2$): a) under 808 nm excitation of a Nd^{3+} co-doped UCNP and b) under 980 nm excitation of a Yb^{3+} sensitized UCNP.

The beam power was measured directly in front of the objective and multiplied with the λ-dependent objective transmission rate, cf. appendix Fig. A.2. Using the laser spot sizes from the PSF analyses, the power density (P) was calculated for various control settings at the laser spot in the focal plane as described in Table 3.1.

Chopper-wheel The chopper-wheel MC2000B from Thorlabs can be brought into the optical path directly after the laser sources (cf. Fig. 3.3). Its chopping frequency (4 Hz – 10 kHz) and phase relative to a reference signal can be controlled manually. Two different blades from Thorlabs were used for setting the duty cycle and frequency ranges, the MC1F2P10 (duty cycle of 10%, frequency of 4 - 200 Hz) and the MC1F10A (adjustable duty cycle from 0 - 50%, frequency of 20 - 1000 Hz) blade. For decay kinetic studies with the super-continuum and the 808 nm laser diodes, we connected the chopper controller to the

excitation	mode	settings	power density [W/cm^2]
808 nm	cw	OD 3 filter	21 k
	cw	OD 2 filter	28 k
	cw	OD 1 filter	170 k
	cw	OD 0.6 filter	304 k
	cw	OD 0.4 filter	441 k
	cw	OD 0.2 filter	802 k
	cw	no filter	2 M
980 nm	pulsed	30% power, 0.5 MHz	1.3 k
	pulsed	40% power, 0.25 MHz	1.4 k
	pulsed	40% power, 0.5 MHz	2.9 k
	pulsed	40 power, 1 MHz	5.8 k
	pulsed	40% power, 2 MHz	11.7 k
	pulsed	40% power, 4 MHz	23.5 k
	pulsed	40% power, 8 MHz	46.9 k
	pulsed	40% power, 16 MHz	91.8 k
	pulsed	40% power, 32 MHz	160 k
	pulsed	40% power, 64 MHz	200 k
	pulsed	40% power, 80 MHz	230 k
	cw	28% power	29 k
	cw	29% power	108 k
	cw	30% power	190 k
	cw	32% power	450 k
	cw	35% power	870 k
	cw	40% power	1.6 M
	cw	50% power	2.3 M
	cw	60% power	2.4 M
	cw	80% power	2.5 M
	cw	100% power	2.6 M

Table 3.1. Local *P*s at the focal plane at the CLSM for 808 nm and 980 nm laser excitation. For the pulsed mode of the 980 nm diode the burst mode generator was used to set the pulse rate between 0.25 and 80 MHz.

Sepia PLD laser controller by using the SIA 400 adapter from PicoQuant. The TTL signal output of the chopper shutter controller is send to the AUX-in of the PDL oscillator SOM 828 and the sequencer in the control software is set on "running on AUX IN high". Thereby, the chopper TTL signal is used as external oscillator and sync-signal, which triggers the start pulses of the rotary sequences at TCSPC measurements.

Sample and scanning stage The sample is placed on top of the inverted microscope body (Olympus Axiovert IX73) on a piezo-controlled XYZ-sample stage (TAO stage from JPK) with a 100x100x10 μm^3 scanning range. The TAO stage enables sample-scanning for AFM and correlated AFM-PL measurements.

Objectives The objective is mounted on a XY-scanner module from PI for XY-objective scanning with a 80x80 μm^2 scanning area. The scanner is controlled by the SymPhotime64 software from PicoQuant. For the SP measurements a 100× oil-immersion objective with a numerical aperture of 1.4 (UPLSAPO100XO/1.4) from Olympus is used. The transmission of this objective in the vis (400 to 700 nm) range is over 80%, whereas at 808 nm only 70% and at 980 nm only 44% of the incoming (laser) light is transmitted, as plotted in appendix Fig. A.2.

Filters and dichroic mirrors For coupling the 405 and 980 nm laser light into the beam-path, the dichroic mirrors *F48-403* (R:355-409 nm > 95%; T:420-850 nm > 95%) and *F73-877SG* (T:450-850 nm > 95%; R:900-1800 nm > 95%) from AHF (Germany) were used, respectively. In the filter wheel the dichroic mirrors were used to direct the excitation light to the microscope and for passing the sample signal to the detection part (APDs, EMCCD) of the CLSM via transmission. In order to suppress the laser light efficiently for the further signal detection, the long-pass filter F47-522 (OD 6: 300-415 nm) and F37-842 (OD 5: 842-1000 nm) were adjusted directly behind the filter-wheel at 405 and 980 nm laser excitation. In front of the APDs the bandpass filters *F49-546* (T: 545/25; blocking OD 6) and *F39-655* (T: 655/40; blocking OD 6) from AHF for detection of the green and red UC emission bands are used.

Pinhole Between the filter-wheel and the detectors, pinholes with 20 and 30 μm diameter can be inserted to ensure the confocal imaging of the spatial confined emitting part of the laser focus. The pinhole was not used for NPs drop-casted and dried on glass-substrate, since the quasi 2D-alignment of all NPs naturally limits the area of emission to this layer.

Detectors and cameras Under WI, the emission signal can be detected via a monochrome CMOS-camera (UI-3370CP Rev. 2) from Imaging Development Systems (IDS), which has a resolution of 2048x2048 pixels and is directly mounted to the microscope camera port. Whereas, the PL emission achieved under confocal condition can be read out using either two APDs for single photon counting or one spectral CCD camera. The APDs (MPD-100-CTB) are part of the PDM series from Micro Photon Devices (MPD) with an active area diameter of 100 μm and dark count level below 25 cps. The spectral efficiency (wavelength-dependent quantum efficiency) of the APDs is plotted in appendix Fig. A.3.
The spectra were recorded with a monochromator with two selectable gratings 1200 and 600 lines/mm leading to spectral resolutions of 0.1 nm and 0.43 nm, respectively and a CCD Camera iDus420 from ANDOR. In February 2019 the iDus420 was replaced by an EMCCD camera (DU970P-BVF, Andor Ltd) with the selectable gratings with 600 and 300 lines/mm.

TCSPC electronics For the recording and processing of the sync and APD signal the very fast electronic device ”TimeHarp 260 PICO Dual” from PicoQuant is used. This device offers TCSPS and Multi-Channel Scaling (MCS) for count rates up to 40 million cps with a time-resolution of 25 ps to generate histograms with up to 32768 channels. The additional ”long range mode” enables LT measurements up to the ms-range with a resolution down to 2.5 ns.

Calibration and data correction

Before the CLSM could be used for SP studies, a calibration and validation of the measurement conditions regarding the spatial and temporal domain was performed and corrections for the spectral sensitivity were applied.

Spatial domain For validation of spatial correctness of the X-Y scanning piezo elements a commercially resolution test target (a glass plate with 10 μm line distances) were used with the backscattered excitation light. The dimension differences between the test-target and its scanned image could be corrected by adjusting the parameters of the piezo controller.

Temporal domain The accuracy of the time-resolved measurements on this CLSM setup were tested by comparing PL decay results and the instrument response function (IRF) of well-known samples with the appropriate results achieved on accredited photoluminescence spectrometers in our group. The IRF takes into account the influences on the temporal laser pulse shape by all optical and electronic components involved at time-resolved PL decay measurements and is acquired from the backscattering signal of excitation light from a non-luminescent sample. This response function is needed for data reconvolution and PL decay curve fitting.

Spectral correction For the (EM)CCD camera a spectral correction was performed manually for each measurement condition with a fixed spectral range, EM-factor and, filters using an accredited reference lamp (BN-9701 SDS 10 W by Gigaherz-Optik GmbH) to correct the spectral sensitivity of the sensor. In Figure 3.6 an uncorrected and a spectral corrected single UC emission spectrum are plotted revealing the differences in the signal counts of both spectra. In addition, the fluorescence background and dark counts are in general subtracted using a blank spectrum.

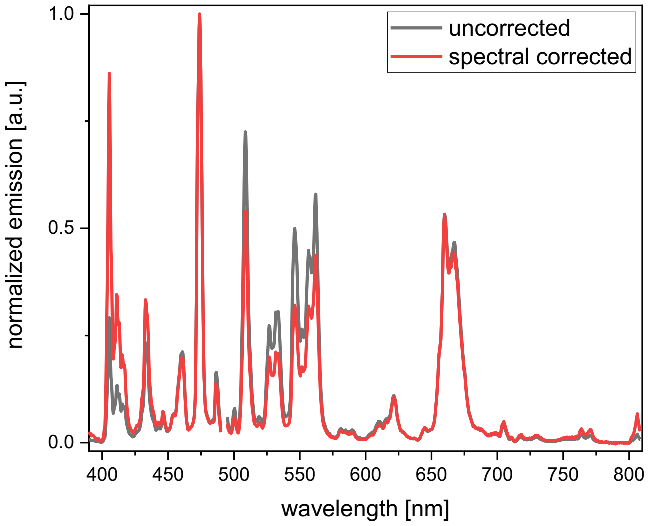

Figure 3.6. Comparison of uncorrected and spectral corrected normalized UC emission spectra taken with the EMCCD of our CLSM setup.

Particle preparation and measuring procedure

Single UCNPs dried on glass The most UC samples were provided in high concentration and dispersed either in cyclohexane, water, DMF or hexane. As substrates for the CLSM, the cover glasses from SCHOTT (D 263® M, 0.175 mm thickness) are used and placed in the sample holder of the microscope body. The focal distance, the objective to substrate distance is adjusted manually and is optimized by setting the laser light back-reflex of the glass-surface to a minimal spot on the reference camera image guaranteeing the highest focusing on the sample plane. For most of the samples a dilution series were performed with concentrations of 1/10, 1/100 down to $1/10^6$ of the stock-solution. Then, 3 to 5 μl of the most diluted solution were brought via ”drop-and-dry method” on the glass substrate. The presence of UCNPs is verified by a fast PL scan at 980 nm excitation. This procedure is repeated with the next higher concentrated solution until the proper NP density with clearly separated SPs is found on the glass substrate. The drop-and-dry method is especially favourable for samples dispersed in fast evaporating solvents like hexane and cyclohexane. Alternatively spin-coating can be used for sample preparation.

Single UCNPs in solution For the UCNP measurements in solution the μ-slide wells (”μ-slide 8 wells, glass bottom”) from IBIDI with a volume of 300 μl per well were used instead of glass cover slips. The sample solution was either directly dropped into the well or as described in the latter paragraph the NPs were transferred via ”drop and dry” method onto the glass bottom of the well until the appropriate NP distribution is reached and got subsequently re-dispersed with the adequate solvent. Using the latter procedure with re-dispersion, sedimentation and clustering of NPs during the measurements can be avoided.

3.3.2. AFM and correlated measurements

The AFM-head ”NanoWizard® NanoOptics AFM (880nm)” from JPK/BRUKER Germany can be used either with the TOA-stage on top of the CLSM for correlated measurements or separately on an additionally stage in stand-alone configuration.

The AFM was used to prove the SP nature of the chosen UCNPs, which were used for the optical studies in this work, and to exclude aggregates and NP clusters, which could not be clearly categorised optically due to the diffraction limit (about half the excitation wavelengths). The correlated PL-AFM measurement offers a powerful tool to detect NPs, to determine their sizes and to separate the luminescent NPs from unwanted objects like dust, substrate impurities or chemical remains.

To demonstrate the broad range of applications of our CLS-AFM setup, a sample with three very different materials consisting of CdSe nanowires (CdSe-NW), $NaYF_4$(Yb,Er) UCNPs and CdSe QDs were prepared and tested together with my colleague Florian Weigert, who also presented parts of this study in his PhD thesis [113]. In Figure 3.7 a) and b) the PL images of the same ROI reveal the luminescent signals of the CdSe-NWs and CdSe QDs under 405 nm excitation using a 600 LP and a 750 SP filter (a), and the UC luminescence of three UCNPs under 980 nm excitation using a 655/40 BP filter (b).

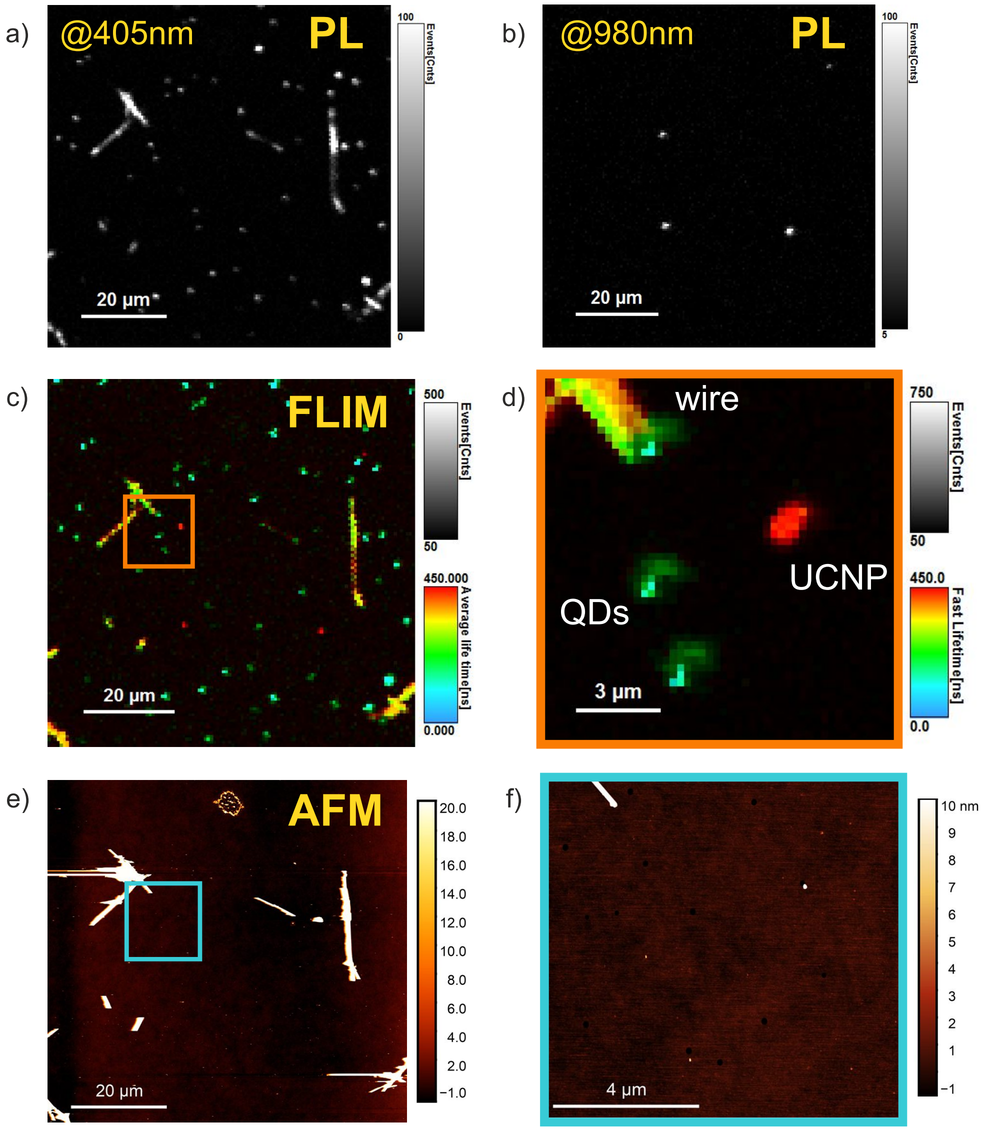

Figure 3.7. PL, FLIM and correlated AFM scans of a sample with three different material systems - CaSe nanowires (NW), UCNPs and QDs: a) and b) PL scans of the same ROI under 405 and 980 nm excitation. c) and d) FLIM images under combined 405 and 980 nm excitation (pulsed at 1 MHz) of the three different materials, which can be easily distinguished by their different fluorescent decay behaviour. The used dichroic mirror has to be reflective for both excitation wavelengths (405 and 980 nm) and transmissive in the emission region of all three NP systems. e) and f) Corresponding AFM topographic scan and close-up used for height profiles and structural sample information. Taken and varied from [113].

Since the emission signals of the three material systems are all situated in the vis range and partly overlapping, a clear separation by the PL brightness information was not possible, even under simultaneous 405 and 980 nm excitation. Using the PL decays and LTs instead of brightness information solved this problem. Therefore, fluorescence lifetime imaging (FLIM) was performed under combined 405 and 980 nm pulsed excitation (pulse rate of 1 MHz) as pictured in Fig. 3.7 c) for the same ROI. From the colour-coded LT information a clear differentiation of the NWs (yellow/orange), the UCNPs (red) and QDs (blue/green) is possible. The close-up image (Fig. 3.7 d)) includes all three material systems. The smearing (ghosting) of NP images can be attributed to reflections of the laser spots on the backside of the dichroic mirror (DM), whose front side is not perfectly reflective for both excitation ranges, leading to phantom images of the emissive NPs.
The corresponding AFM scan in Fig. 3.7 e) shows the topography of all objects, including the non-emissive or quenched particles. The AFM close-up image (Fig. 3.7 f)) features all three particle systems (part of CdSe NW, 1 UCNP and 2 QDs). Their height profiles are plotted in appendix Figure A.4 and reveals the real sizes of the three different material systems and their dimensions, which can not be provided by the PL images.

3.4. Comparison of ensemble and SP measurement conditions

There are a few differences in the measurement conditions and parameters of ensemble and SP studies making a direct comparison of the obtained results challenging. In following the relevant issues, requirements and differences of the two measurement methods are listed and discussed in general and partly with reference to our used setups.

- Sample quality: The mono-dispersity of the sample, especially concerning to doping and size distributions is important for the reliable interpretation of the results for both methods and it is necessary to quantify the degree of the mono-dispersity in advance with ICP-OES and TEM. Here, widefield imaging can also contribute as a third tool to check the mono-dispersity on SP level on a limited number of NPs.

- Sample condition: The ensemble measurements are performed either on UCNPs in powder or dispersed in aqueous or organic solvent, whereas for SP measurements the NPs were dried on glass-substrates and measured on air or re-dispersed in solvent after fixation.

- Number of particles: In ensemble the results are averaged over thousands of NPs and sufficient statistic can be achieved with repeated measurements or long integration times, whereas in SP studies just a limited number of NPs are picked for specific studies and used for statistical analysis, due to the time consuming measurements.

- NP interaction: The NP-to-NP interaction can be minimised in SP studies, if the particle concentration is chosen low enough, the NPs are sparsely spread and well isolated on the glass-substrate and aggregates are excluded from measurements. In ensemble the NP interaction, including re-absorption effects and surface quenching by NP clustering can be limited with a reduction of NP concentration in the solvent. NP aggregation/clustering can be avoided by using ultrasonic bathing in advance.

- Detecting methods: Using different setups with different equipment, only standardised calibration methods and reference measurements can guarantee the output of comparable results. In our studies this is especially tricky for LT measurements, for which in ensemble a monochromator and for SP studies bandpass-filters are used for the wavelength selection.

- Excitation power density: The P-dependent measurements in ensemble are performed in a range between 5 to 400 W/cm^2 by using a lens with a focal length f of 10 cm. In contrast the working P range in the SP studies is between 1 kW/cm^2 to 2.6 MW/cm^2 under high focused laser excitation (f of 0.2 mm). Therefore, even small variations in the laser position (z-axis) can change the local P significantly and should be avoided. Furthermore, the high photon flux can cause thermal heating effects, which influence the optical behaviour of our samples and should be recorded (e.g. via green-to-green UC band ratio of Er^{3+} emission).

4 Ensemble vs. SP studies: Yb/Er UC material

In this chapter the optical behaviour and upconversion performance of Yb/Er co-doped nanoparticles will be discussed and compared under both conditions, first in ensemble and second on single particle level. The influences of an additional inert shell and the variation in Er^{3+} doping concentration from 1% to 3% Er^{3+} are discussed. Furthermore, in the ensemble measurements the impact of the organic solvent cyclohexane and of water on the UC efficiency is studied. At the end of this chapter based on SP results, the energetic population pathways of highly excited Er^{3+} ions and their photoluminescence are discussed.
Parts of this chapter includes data and results, which have been published in *Nano Research* [107] under my own first authorship. The respective sections are labelled in each case.

4.1. Preparation and chemical analysis

For this study the Hirsch group (University of Regensburg, Germany) synthesized a set of 12 samples containing 3 core-only and 3 core-shell $NaYF_4$(20% Yb, x% Er, with $x = 1, 2, 3$) with oleate ligands dispersed in cyclohexane and additional the same 6 core-only/core-shell particles with an amphiphilic polymer poly(isobutylene-alt-maleic anhydride) coating (PIBMAD) modified with dodecyl amine side chains dispersed in water. The synthesis and the coating of the NPs with the oleate surface modification have been performed following previously reported protocols [114]. For the water dispersible UCNPs an additional coating process with PIBMAD was done as described in the PhD thesis of Verena Muhr [115].
The NPs have been structural and chemical analysed by our cooperation partner using DLS, XRD, ICP-OES and TEM measurements. The DLS and the XRD measurements revealed that the dispersions were colloidally stable without aggregations and that the crystal structures are hexagonal (β-$NaYF_4$). The ICP-OES data and the mean diameter determined from TEM images are listed in Table 4.1. The real lanthanide concentrations of 1.0%, 2.0% and 2.9% Er^{3+} are very close to the theoretical concentrations. From the NP diameters the following shell thicknesses of (4.35 ± 1.6) nm, (4.7 ± 0.8) nm and (5.3 ± 1.2) nm were determined for the 1%, 2% and 3% Er^{3+} doped NPs. The NP concentration in both solvents cyclohexane and water was about 10 mg/mL and 3 mg/mL, respectively.

theoretical composition	**diameter** [nm]	**Yb^{3+} content [%]**	**Er^{3+} content [%]**
NaYF$_4$(20% Yb, **1% Er**)	28.7 ± 1.1	17.5	1.0
NaYF$_4$(20% Yb, **2% Er**)	27.4 ± 0.8	19.5	2.0
NaYF$_4$(20% Yb, **3% Er**)	28.3 ± 0.8	19.6	2.9
NaYF$_4$(20% Yb, **1% Er**)@NaYF$_4$	37.4 ± 2.2		
NaYF$_4$(20% Yb, **2% Er**)@NaYF$_4$	36.8 ± 1.1		
NaYF$_4$(20% Yb, **3% Er**)@NaYF$_4$	38.9 ± 1.5		

Table 4.1. Mean particle diameter of core-only and core-shell NPs determined from TEM images and lanthanide contents of Yb/Er UCNPs containing varying amounts of Er^{3+} determined by inductively coupled plasma-optical emission spectroscopy.

4.2. Ensemble studies

The spectroscopic analysis of the dispersed samples includes *P*-dependent UCL spectra, the calculations of QYs, emission band ratios, slope-factors (n) in the *P* range from 5 to 400 W/cm^2 and decay kinetics of specific Er and Yb bands under 980 nm excitation. For the *P*-dependent studies the integrating sphere setup (section 3.2.2) and for the decay kinetics the spectrometer FLS980 was used as described in section 3.2.3.

UCL colour influenced by solvent, Er doping and shell

The *P*-dependent luminescence studies of the oleate ligand stabilized UCNPs in cyclohexane and in water reveal the impact of the shell and the variation in Er doping on the relative spectral contribution of emission bands and therefore on the UCL colour. In Figure 4.1 a) the relative emissions are shown for the 410 nm (blue range: 394-430 nm), the 520 nm and 541 nm (green: 510-570 nm), the 654 nm (red: 630-685 nm), the 810 nm (brown: 783-833 nm) and the 840 nm (grey: 833-880 nm) Er emission bands for all 12 samples. The *P*-dependent differences in emission band contributions reveals the influences of the competing processes from Yb → Er ions (ETU) and inversely from Er → Yb (BET), the population and depopulation processes of intermediate Er levels and the non-radiative decay pathways.

Influence of the solvent By comparing the UC performance in cyclohexane and in water, the direct quenching influences of the C-H and O-H vibrational bonds on surface near Ln^{3+} ions are revealed. For the core-only UCNPs in cyclohexane the green band shows the strongest intensity at low *P* but decreases with *P*, whereas the red emission intensity increases with *P* and gets the most intensive band for higher *P*, cf. Fig. 4.1 a). In water the red emission dominates the UCL over the whole *P* range revealing a strong population of the $^4F_{9/2}$ level intensified from relaxation processes from the $^4S_{3/2}$ level caused by O-H vibrations of water at the UCNP surface. The $^4F_{9/2}$ level is populated by a mix of bi- and tri-photonic absorption steps as illustrated in the Dieke diagram in Fig. 2.4 c): With two subsequently absorbed photons from the $^4I_{15/2}$ (1) via ETU and the $^4I_{13/2}$ ($\underline{2}$) level including a non-radiative relaxation process from $^4I_{11/2}$ to $^4I_{13/2}$ enhanced by O-H vibrations, the red emissive $^4F_{9/2}$ level can be populated via ESA. The latter transition ($\underline{2}$) is also enhanced by

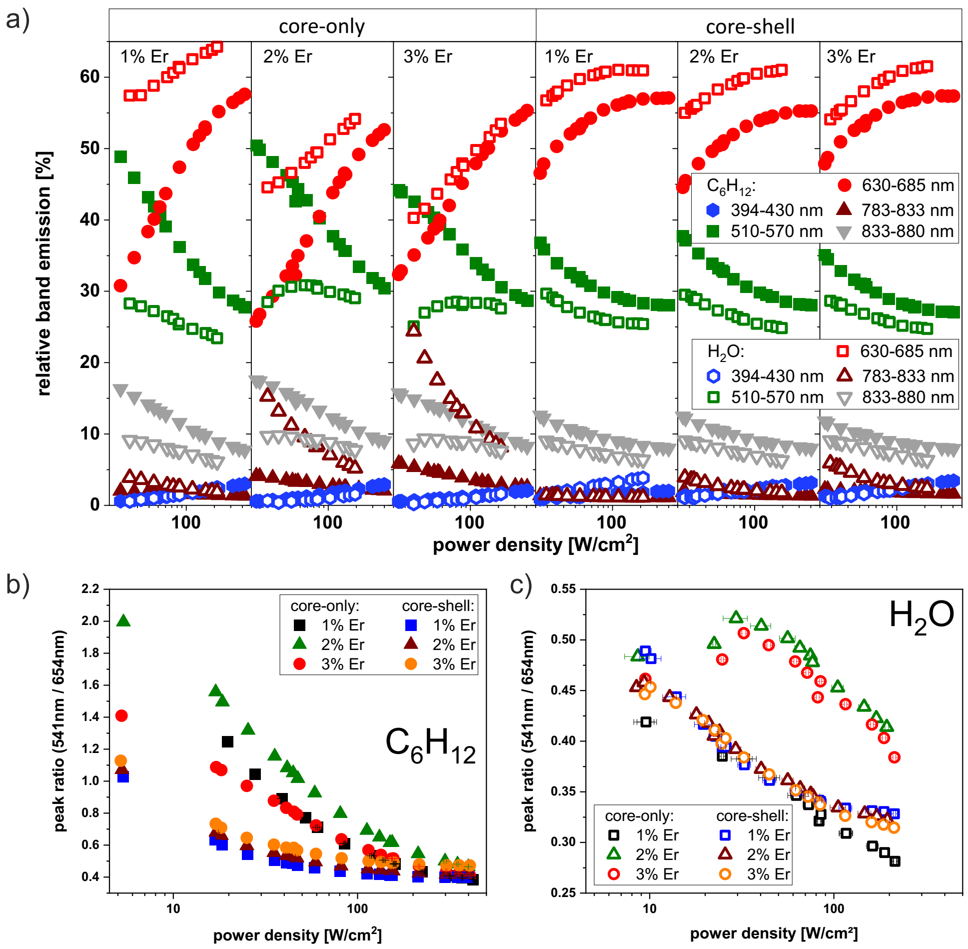

Figure 4.1. *P*-dependent spectroscopic studies on the core-only/core-shell UCNPs varied in Er doping concentration dispersed in the solvents cyclohexane (C_6H_{12}, filled symbols) and water (H_2O, open symbols): a) Relative band emission ratios of the 410 nm (blue), 520 nm and 541 nm (green), 654 nm (red), 810 nm (brown) and 840 nm (grey) emissions to overall UCL. b) and c) The green-to-red (G/R) emission ratio of the 541 nm and 654 nm peaks are plotted *P*-dependent for NPs in cyclohexane (b) and in water (c).

the increased population of the $^4I_{13/2}$ level via Er-Er CR (CR1) from the $^4S_{3/2}$ to $^4I_{13/2}$ and $^4I_{9/2}$ levels. Further $^4F_{9/2}$ population pathways based on 2 absorbed photons appear via non-radiative relaxation from the green levels ($^2H_{11/2}$, $^4S_{3/2}$) leading to increased red at the cost of green emission [103]. Additionally, the Er-Er CR (CR2) from the $^4F_{7/2}$ and $^4I_{13/12}$ to the $^4F_{9/2}$ level can feed the red emissive level directly, but is more unlikely due to a short intrinsic LT of the $^4F_{7/2}$ level [116]. From the ^4G Er levels following a 3 photonic absorption process (1+2+3) to the ^2G level at higher P, the $^4F_{9/2}$ can be reached by a back-energy process (BET) between Er and Yb. The trend of the green-to-red (G/R) peak (I_{541}/I_{654}) ratios in Figure 4.1 b,c) illustrates the strong influence of the solvent on the two emission bands and reveals their competition behaviour. In cyclohexane all G/R ratios decrease with higher P and converge to about 0.45 (Fig. 4.1 b)). Whereas in water the unprotected core-only samples (2% and 3% Er^{3+}) show a rise in G/R for $P < 40\ W/cm^2$ (Fig. 4.1 c)), which marks a higher probability for green level population until the G/R ratio decreases for higher P due to favoured red level population [103]. The 1% Er doped core-only sample shows unexpectedly the same behaviour as the core-shell samples, which indicates a reduced influence of the water molecules on the NP surfaces, probably caused by particle aggregation[1]. The behaviour of the 1% Er doped core-only sample will be discussed in the following sections in more detail.

The 810 nm emission (brown) shows enhanced contribution in water mainly caused by Er-Er ET (ET1) from the $^4I_{13/2}$ ($^4I_{13/2} \longrightarrow {}^4I_{9/2}$, $^4I_{15/2}$) levels after non-radiative decay from the overlying $^4I_{11/2}$ level induced by O-H vibrations [43]. Furthermore, the CR1 leads to population of 810 nm emitting $^4I_{9/2}$ level by simultaneous depopulation of the green $^4S_{3/2}$ level. In contrast, the 840 nm emission (grey) is reduced in water for the same reason as the green emission, as both originate from the $^4S_{3/2}$ level.

The contribution of the 410 nm emission from the $^2H_{9/2}$ level (blue) is not strongly affected by the solvents and reaches maximal 3% of total UCL. The increase of the blue light reflects the enhancement of the 3 photonic population processes with P, which are needed for the $^2H_{9/2}$ population.

Influence of the varied Er doping concentration The change in Er doping concentration from 1% to 2% to 3% has relatively small effects on the UCL band ratios and the overall emission colour. For the core-shell systems the two most intensive bands, the green and red emissions show the same trends in cyclohexane and water in Figure 4.1 a). Only the 810 nm emission increases at the expense of red emission with higher Er content, which is significant in case of water dispersed core-only NPs at low P. The 3% Er core-only sample shows a maximal contribution of about 24% at $P = 25\ W/cm^2$ in water. The change in 810 nm emission is attributed to enhanced ET1 (Fig. 2.4 c)), which scales with reduced Er-Er distances for higher doping rates and is a competing process to the red level feeding ETU process (2) from the $^4I_{13/2}$ level following a O-H related relaxation process. In [116], the changes in averaged Er-Er distances of the 2% and 3% compared to the 1% Er doped $NaYF_4$ crystals were calculated to 0.79 and 0.69. For our subsequent discussion, the core-only 1% sample in water is excluded due to the unexpected shielding effect in water probably caused by NP aggregation.

Influence of the shell The presence of an additional inert shell with an average thickness of about 5 nm has a strong impact on the UCL performance in the different solvents due to the shielding effect and the reduced influence of C-H and O-H vibrations on the surface located ions. In cyclohexane the crossing point of green and red emission ratio (G/R = 1) is shifted from about 60 W/cm^2 of the core-only samples to P below 15 W/cm^2, Figure 4.1 a). This shift reflects the compensation of surface related quenching effects with higher excitation P. In water the green emission bands and the G/R peak ratio (Fig. 4.1 c)) of the core-only samples (only 2% and 3% Er doped) increase in intensity for low P, which illustrates a higher contribution of 2 photonic than 3 photonic absorption processes for P

---

[1] In SP studies, NP aggregation was detected for the water dispersed samples.

< 30 W/cm^2 [43]. The green and the red emission bands converge for higher P to ratios between 25-30% and 55-60%, showing a constant balance between population and depopulation processes of the respective Er^{3+} ion levels, which is termed as saturation of the UC process. Comparing band ratios of the 1% Er doped core and core-shell systems, the same P-dependent decrease of the green emission band and even higher red emission contributions are present for the core-only sample in Fig. 4.1 a), which indicates a better water protection without the additional shell. One explanation is unintentional aggregation of the NPs with a shielding effect of the 30 to 50 nm long dodecyl amine chains of PIBMAD coating around clustered NPs. Consequently, a 5 nm thick inert shell does not guarantee full protection of solvent related surface quenching effects. Furthermore, the reduced Yb content of 17.5% instead of about 19.5% (the case for 2% and 3% Er samples), also reduces the quenching effect of O-H bonds on surface located Yb^{3+} ions.

n(P) influenced by solvent, Er doping and shell

The slope factor n(P) indicates the number of absorbed photons involved in the population of a respective emissive energy level at a certain P and is meaningful for low P below the saturation range. The n(P) values are determined from the slope of a double logarithm plot of the respective band emission intensity I_{UC} over P. In Figure 4.2 a) the slope factors of the 410 nm, 541 nm and 654 nm are shown via cubic polynomial fitting for the varied Er concentrations in the different solvents.

Lets focus first on the core-only sample series in cyclohexane. The n values of the three emission bands are largest at low P and represent the number of needed absorbed photons (3, 2-3 and 2) for the generated respective bands (blue, green and red). The slopes decrease with higher P due to the increased population and the beginning of Er level saturation processes. The onset of the saturation (P_{sat}) can be correlated to the maxima of the red band slopes at about 25/30/35 W/cm^2 of the 1%/2%/3% Er samples, which represents the rise in bi-photonic population processes of the red ($^4F_{9/2}$) via the green ($^4S_{3/2}/^2H_{11/2}$) levels [116]. The Yb-Er BET, which accounts as a ”1-photon-re-excitation” [43] for the red level, leads for higher P to additional population of the red level, which in turn decreases the slope factor of the red emission band.

The presence of water molecules on the unprotected NP surfaces leads to non-radiative relaxation processes (cf. Fig. 2.4 c)), which limits the efficiency of the multi-photon absorption processes and reduces tri-photonic activations of the red level with simultaneous enhanced bi-photonic feeding processes from the green levels resulting in lower slopes of the red band and in a shift of the green slope to higher P. For the blue band emission there is nearly no change of the slope in water compared to cyclohexane.

For the three core-shell samples in cyclohexane the slopes are lower in comparison to the unshelled NPs due to reduced surface quenching and more efficient Yb-Er ETU processes at even lower P values. Consequently, the onset of saturation processes and the also the slope factors of the three emission bands are shifted to lower P values in presence of a shell. In case of water, in which quenching influences are not fully shielded by the inert shells (as discussed in the section above), the slopes are shifted to higher P values compared to the shelled NPs dispersed in cyclohexane.

The variation in Er doping only affects significantly the blue emission in presence of water. For lower Er content the full available energy is bundled to a lower number of Er ions, which in return can get easier excited to higher levels, like the blue emitting $^2H_{9/2}$ level via 3 photon absorption processes. Consequently, the samples with lower Er content reach the highest slope factors of the blue emission already for lower P and therefore, an increase in Er doping leads to a shift of the slope curves to higher P values.

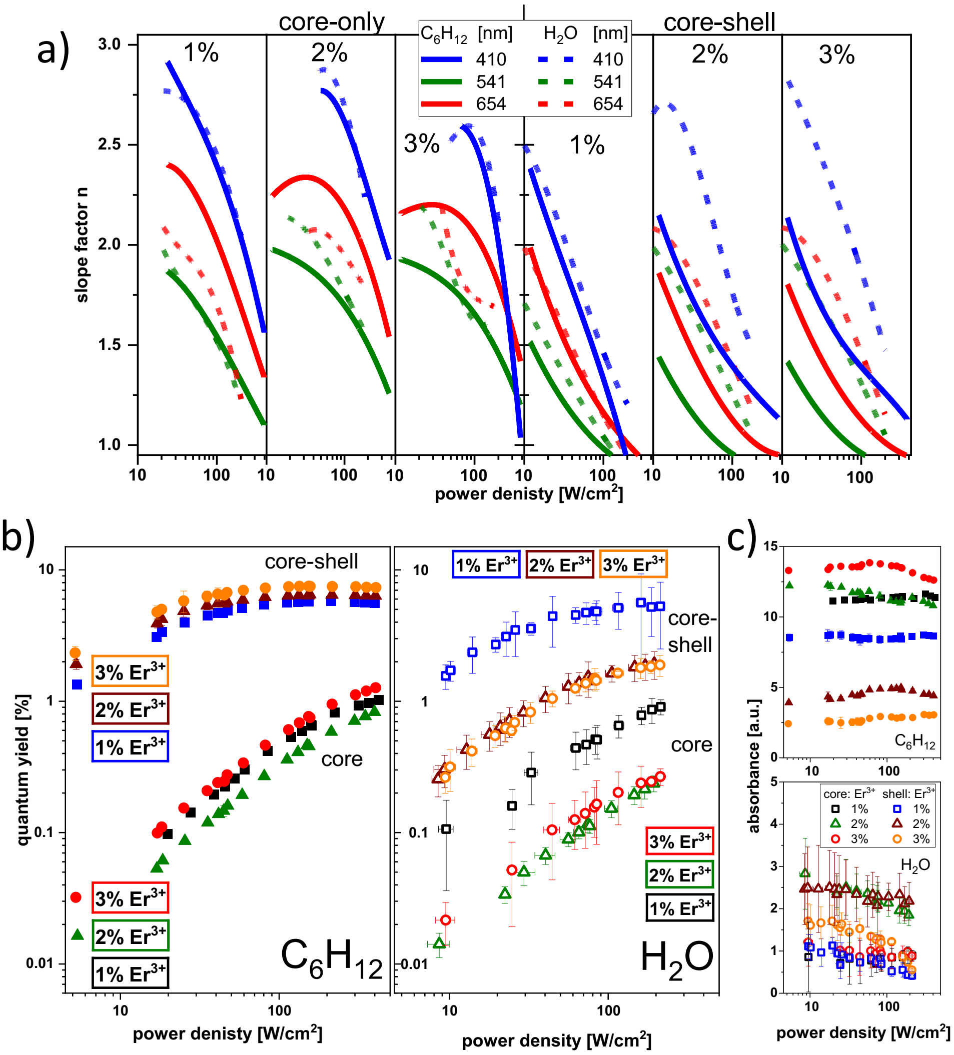

Figure 4.2. P-dependent photoluminescence behaviour of the core/core-shell UCNPs with varied Er^{3+} ion content: a) Slope factors n(P) of the blue (410 nm), green (541 nm) and the red (654 nm) emission bands. b) Quantum yields (QYs) of the 6 samples in cyclohexane (left panel) and in water (right panel). c) Appropriate absorption values of the NIR light during the integrating sphere measurements needed for QY calculations in cyclohexane (upper panel) and in water (bottom panel).

QYs influenced by solvent, Er doping and shell

In Figure 4.2 b) the double logarithmic P-dependent QYs are plotted for all 6 samples in cyclohexane (left panel) and in water (right panel) with their light absorbance values in Figure 4.2 c). In cyclohexane, the P-dependent QYs are strongly increased for the presence of an additional inert shell. The shell of the 3% Er doped sample enhances the QY about 70-fold from 0.032% to 2.33% at $P = 5\ W/cm^2$ and at $P = 400\ W/cm^2$ about 6-fold from 1.26% to 7.34%, whereas, the variation in Er^{3+} doping concentration from 1% to 3% increases the QYs only marginal about 1.3-fold. The core-shell NPs reach an equilibrium condition at $P > 100$ W/cm^2 with nearly constant QYs with maximal values of about 7.5% for the 3% Er-doped sample, while the QYs of the core-only NPs increase over the whole P range with decreasing slopes. The presence of the shell leads to reduced surface quenching of C-H bonds in the organic solvent [43, 117, 118]. With QY values of about 7.5% (at 150 W/cm^2), the 3% core-shell sample shows already a high efficiency, which is not too far away from the QY values of 10.3% measured for bulk material [37].

The presence of water reduces the QYs of the 2% and 3% Er^{3+} doped NPs by 70 - 75% compared to the shelled NPs in cyclohexane. At 200 W/cm^2, QYs of 0.27% and 1.9% were measured for the 3% Er doped sample without and with shell, respectively. The extremely high QY values of the 1% Er doped sample, which nearly matches the results reached in cyclohexane are tentatively ascribed to NP aggregation in water leading to a better shielding of O-H quenching influences. Furthermore, the lower Yb content, of about 2% by weight, of the 1% Er sample leads to smaller absorbance with values in the range from 0.5 to 1%, which is close to noise level of the spectrometer, see also section 3.2.2. The suggested NP aggregation, the difference in Yb content and the resulting critically low absorbance values of the 1% Er sample does not guarantee a fully reliable measurement condition and QY results in water.

The decreasing trend of absorption values in water with higher P in Figure 4.2 c), indicates unwanted sample heating, which can be ascribed to enhanced NIR light absorption of water with higher P.

UCL decay kinetics influenced by solvent, Er doping and shell

In Figure 4.3 a) the decay curves of all 6 samples are plotted for the green (541 nm), the red (654 nm) Er^{3+} emission bands and the NIR emission band (940 nm) of Yb^{3+} in cyclohexane (upper row) and in water (bottom row) excited under 980 nm light irradiation (Yb-excitation). From the 940 nm decay curve the intrinsic LT of the $^2F_{5/2}$ Yb level can be derived, whereas from the decay curves of the green and red Er emission bands an overall LT is given, including the Yb-excitation and Yb-Er ET processes, as the Er levels are not directly excited under 980 nm excitation. Using bi-exponential fitting, the short and the long decay components were determined and the intensity weighted lifetimes ($\tau_{intensity}$) were calculated and plotted for all decay curves in Fig. 4.3 b).

Influence of solvent and shell The core NPs show the same decay kinetics for the three emission bands and revealed comparable LT values in cyclohexane and in water. The values vary from 50 - 150 μs, 180 - 280 μs and 140 - 200 μs for the 541 nm, 654 nm and 940 nm bands of the samples varied in Er doping, respectively. In contrast, the core-shell NPs revealed a different behaviour depending on the influence of the solvent, cf. Fig. 4.3 b).

In cyclohexane, the LTs of the 541 nm (540 - 600 μs) and the 940 nm (640 - 780 μs) Er bands under Yb-excitation (980 nm) of the samples doped with varying Er content are about 4-folds longer compared to the core-only samples, which indicates an effective shell and good protection against surface related C-H vibrational quenching of the green and NIR emission bands. At the same time, the red emission LTs are only about doubled to around 450 μs, which reveals a stronger impact of the C-H bonds on the red emission level.

In water the LTs of the 3 emission bands are significantly shorter as in cyclohexane, which reveals a stronger quenching impact of O-H compared to C-H vibrational bonds. This indicates the need of thicker shells in water for more effective UC performance. Especially the green and NIR bands are stronger affected by the O-H vibrational quenching and only reaching LT values between 120 - 160 μs (541 nm) and 250 - 280 μs (940 nm) for the 2 and 3% Er samples with a shell. The red emission is not that strongly influenced by the O-H vibrations with the additional shell and its LTs are longer as for the green and NIR bands. The only exception is given by the 1% Er core-shell sample with longer green and NIR LTs, which is supposedly ascribed to NP aggregation resulting in a better protection against water induced quenching effects.

Influence of Er doping According to a rate-equation model from Kaiser et al. [116], the increase from 1% to 4% in Er content leads to faster decays of all three emission bands, which are explained by enhanced non-radiative quenching of the 980 nm $^2F_{5/2}$ Yb and $^4I_{11/2}$ Er levels with higher Er ion content. With a larger number of Er ions in the proximity of Yb, more energy is lost by non-radiative quenching of the $^4I_{11/2}$ Er level, which is especially pronounced for Er ions close to the NP surface. The smaller energy gap[1] of the 980 nm $^4I_{11/2}$ Er level to its subjacent ($^4I_{13/2}$) level enhances the probability for non-radiative quenching compared to Yb ion with its larger gap between the $^2F_{5/2}$ level and the ground state [116]. In Fig. 4.3 b) the LT decrease with higher Er content is mostly present for the 940 nm LTs of the core-only and core-shell particles in cyclohexane and for the green emission of the core-only particles in water.

The red emission of the 3% Er doped sample show longer LTs than the 1 and 2% Er samples, which might be explained by a slightly higher BET activity, which provides an additional feeding process for the red emissive $^4F_{9/2}$ level and is enhanced due to reduced Yb-Er ion distances for higher Er content.

For the 1% Er doped sample the unintended 2% smaller Yb doping content (17.5% instead of 19.5% Yb^{3+}) might contribute to longer LTs of the 940 nm Yb emission and in consequence both LTs of Er emissions. This is explained by the fact, that at lower Yb concentration

---

[1] $\Delta E_{Er}(^4I_{11/2} - {}^4I_{13/2}) < \Delta E_{Yb}(^2F_{5/2} - {}^2F_{7/2})$

the energy migration to the NP surface and the number of Yb^{3+} ions near the surface is decreased, resulting in a reduced quenching impact of the solvent and surface ligands [116].

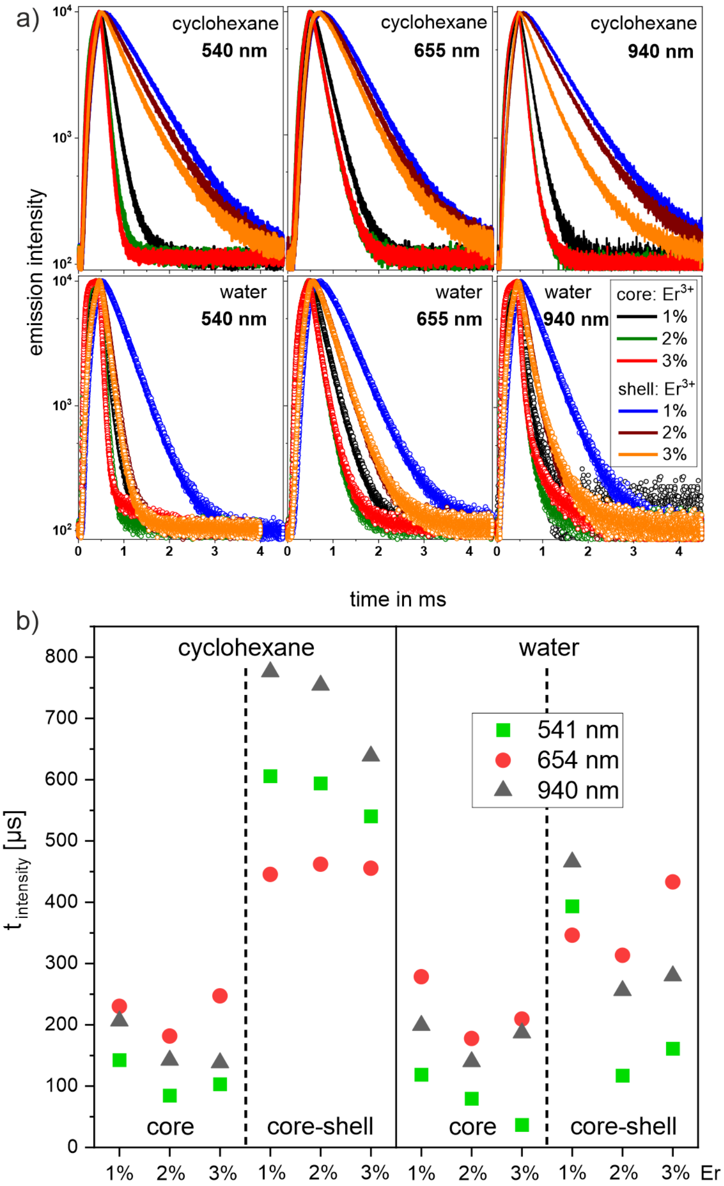

Figure 4.3. Measured decay kinetics of the 541 nm, 654 nm and 940 nm Er^{3+} ion emissions under 980 nm excitation of all 6 samples: a) Decay curves of all 6 samples measured in cyclohexane (upper plots) and in water (bottom plots). b) Calculated intensity weighted lifetimes (LTs) using bi-exponential fitting of the decay curves for determination of the short and long decay components.

4.3. Single particle studies

The most results in this chapter have been published under my own first authorship in *Nano Research* 2021 [107].

The single UCNP measurements with excitation Ps up to the MW/cm^2 range enable not only information on the variation of UCL features between different particles synthesized within one batch, but more importantly allow to explore the nonlinear UCL properties of UCNPs at high P ($\geq$ MW/cm^2) without influencing NP-NP interactions. The SP study were run on two of the three Yb-Er systems varied in Er doping discussed above, namely the 1% and the 3% Er doped core-only (co) and core-shell (cs) particles, as illustrated in Fig. 4.4. This allows a measure of the shell and the Er doping influence on the UC process at higher excitation Ps. All the measurements have been performed on our home-built CLSM (described in section 3.3.1) by my own, except the brightness-distribution study, which has been run by our cooperation partner (Mély group in Strasbourg) at their SP setup.

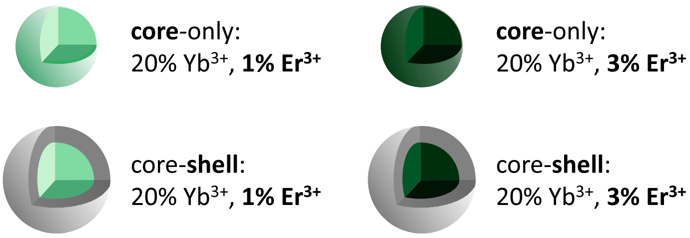

Figure 4.4. Set of hexagonal β-NaYF$_4$:x% Er^{3+}, 20% Yb^{3+} core/core–shell UCNPs (x = 1 and 3) used for the SP study.

Correlated AFM-PL measurements on SPs

The fist step of the SP study is to ensure that only real SPs are chosen and that NP clusters and aggregates are excluded for further tests. By using widefield imaging (WI) under combined white-light and 980 nm excitation, the region of interest (ROI) was chosen containing bright UC emissive spots and a characteristic cluster of CdSe nano-wires as alignment marker, cf. Fig. 4.5 i). Due to the diffraction limited optical imaging we used an AFM to confirm particle sizes and to identify single UCNPs. To prove SP nature, a correlated imaging of PL and AFM scans (Fig. 4.5 ii) and iii)) was used to get an AFM-PL overlay as shown in Fig. 4.5 iv). Here, the single UCNPs (dashed white circles) and the larger aggregates (dashed black squares) were identified and confirmed by AFM close-up images as exemplary illustrated in Fig. 4.5 v) and vi). In case of a high monodisperse sample, the PL information of a handful AFM-proved SPs can be taken as reliable comparative parameter for determining further SPs without time consuming correlated AFM-PL measurements.

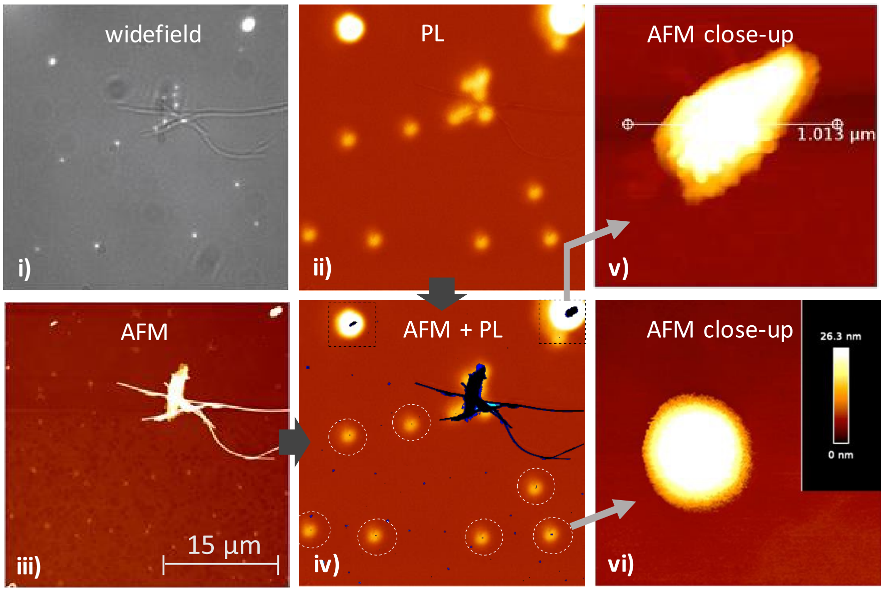

Figure 4.5. Using different detection methods on the same ROI to prove SP nature of core-shell UCNPs: i) Widefied imaging under combined white-light and 980 nm excitation taken by an CCD camera with pixel size of 0.03 μm. ii) Photoluminescence (PL) scan under 980 nm excitation detected with a SPAD (pixel size of 0.4 μm). iii) AFM-scan revealing detailed the CdSe-nanowire cluster (bright object) and iv) overlay of PL and AFM (blue) images. Single UCNPs are indicated by white circles and aggregates by black squares. v) and vi) AFM close-up scans of an UCNP cluster and a single core-shell NP to confirm shape and size of the luminescent objects. Taken and modified from own publication [107].

Particle-to-particle variation using WI

From the brightness distributions, conclusions about the NP homogeneity in doping and their emissive behaviour can be drawn and used as measure for the NP quality provided by the synthesis and the sample preparation. The monodispersity of our samples have been studied by measuring the brightness distributions of the green and red Er^{3+} emissions using WI of a statistically representative number of SPs. The WI measurement were run by our cooperation partner in Strasbourg as described in [107].

In Figure 4.6, the Gaussian-like brightness distributions of the 4 samples including expected value (μ_λ), standard deviations (σ_λ) and number of considered NPs (n_{SP}) are summarized by the UCL histograms taken at P of about 8 kW/cm^2. Besides only a few outliers, the histograms show mainly the emission signal of the least bright NPs, which originates from SPs. The red emission of both core-only systems reveals a wider distribution compared to the green signal, for 1% Er^{3+} $\sigma_r^{co,1\%} \sim 1.4\cdot\ \sigma_g^{co,1\%}$ and for 3% Er^{3+} $\sigma_r^{co,3\%} \sim 1.2\cdot\ \sigma_g^{co,3\%}$. This can be explained by the additional 3-photonic absorption pathway of the red emission and by local differences of the excitation power due to high laser focusing. The change from 1% to 3% in Er^{3+} doping leads to a 2.3 times higher green and 1.8 times higher red emission of the co NPs, shown in Fig. 4.6 i) and ii). The addition of the 5 nm inactive shell enhances the green and the red emission intensity of the 1% Er^{3+} sample by about 2.5- and 1.3-times (cf. Fig. 4.6 i) and iii)). The 3% Er^{3+}-doped NPs showed the brightest green and red UC emission, cf. Fig. 4.6 iv).

This homogeneity study is based on the detected emission intensity and hence, contains also small contributions from variations or fluctuations in the excitation *P*. Furthermore, a direct comparison of the 4 histograms is tricky as the different statistics must be considered, the higher numbers of studied 1% Er^{3+} doped co (n = 259) and 3% Er^{3+} doped cs NPs (n = 233) lead to a better statistic and a Gaussian behaviour compared to the other two NP systems (42 < n < 73).

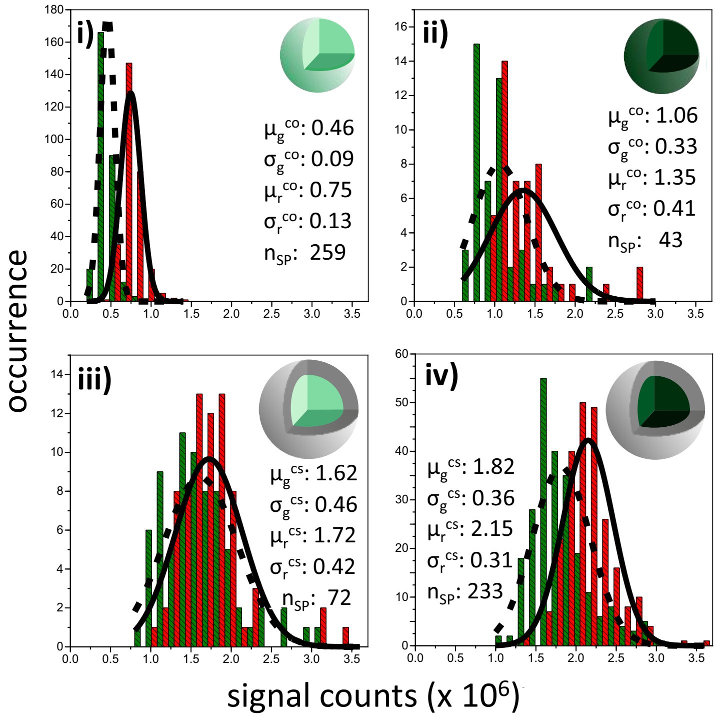

Figure 4.6. Brightness distribution histograms of the green and red emission bands including expected value (μ_λ), standard deviations (σ_λ) and number of considered NPs (n_{SP}): i) - iv) The black dotted and solid lines are Gaussian fits of the occurrence-over-signal distributions of the green (g) and red (r) emissions of the core-only (co) and core-shell (cs) systems. These measurements were performed by our cooperation partners in Strasbourg as described in SI [107].

P-dependent spectra and overall colour emission of single UCNPs

After proving the SP status, the *P*-dependent UCL spectra were taken for the 4 NP systems in the range from 390 nm to 810 nm. In Figure 4.7 a) the emission spectra of the 3% Er^{3+}-doped NP system is plotted for 17 different *P*-values covering a range from 1 kW/cm^2 up to 2.6 MW/cm^2. Besides the typical UC emission peaks known from ensemble studies at **410 nm**, **521 nm**, **541 nm**, **654 nm**, and **840 nm** (cf. chapter 2.3.1), this spectrum reveals a lot of new emission bands, which appear with increasing *P* at **400 nm**, **427 nm**, **440 nm**, **454 nm**, **468 nm**, **481 nm**, **495 nm**, **503 nm**, **506 nm**, **556 nm**, **575 nm**, **585 nm**, **616 nm**, **639 nm**, **699 nm**, **765 nm** and **801 nm**. Additionally, the high spectral resolution of 0.43 nm allowed the detection of further sharp peaks at **405 nm**, **527 nm**, **610 nm**, **662 nm**,

712 nm, **724 nm**, and **750 nm**. A sophisticated explanation for the main emission bands and their *P*-dependency will be given in the next chapter in more detail.

The additional emission bands lead to a change of total UCL emission colour from green

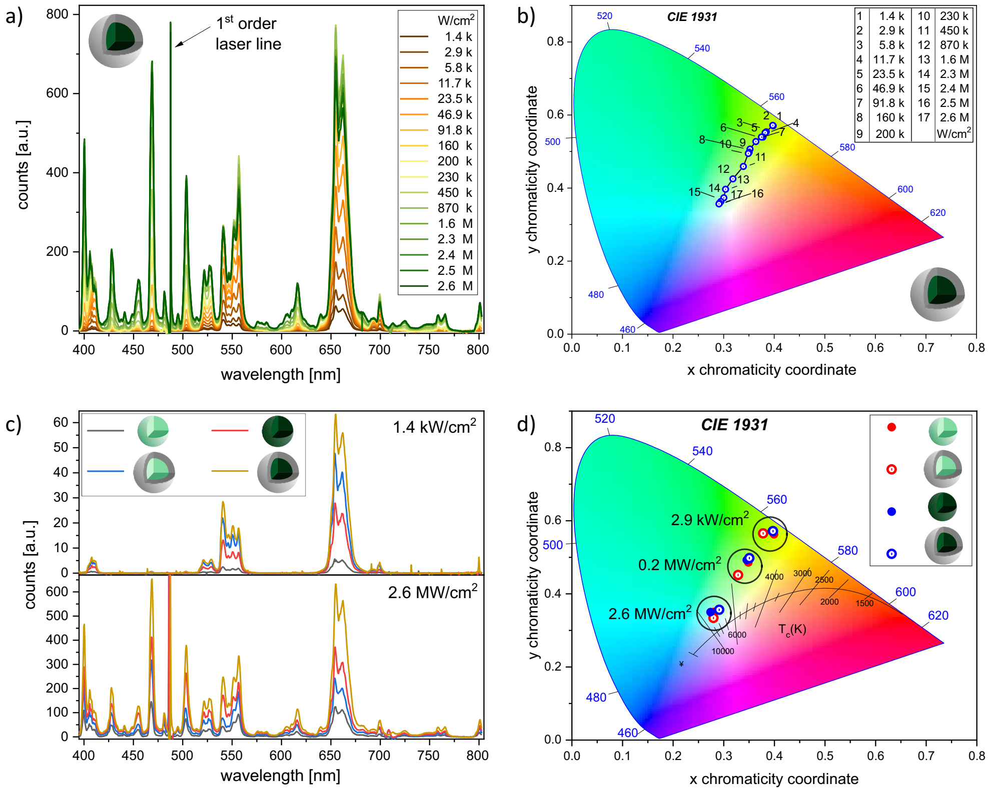

Figure 4.7. *P*-dependent UC emission spectra and CIE chromaticity diagrams covering the *P* range from 1.4 kW/cm^2 to 2.6 MW/cm^2: a) Spectrum of 3% Er^{3+} doped core-shell NP sample taken at 17 different *P* values showing large number of newly detected emission bands. b) CIE diagram of 3% Er^{3+} doped core-shell illustrating the colour change from green over yellow to white with increasing *P*. c) Spectra of the 4 NP systems at lowest *P* (upper plot) and highest *P* (bottom plot). d) CIE diagram with colour coordinates for the 4 NP systems at three different *P* vales (2.9 kW/cm^2, 0.2 MW/cm^2 and 2.6 MW/cm^2). Taken and modified from own publication [107].

over yellow to white with increasing *P*, as exemplarily illustrated in the CIE diagram in Figure 4.7 b) for the 3% Er^{3+}-doped sample.

Comparing the spectra of the 4 different NP systems at two specific, the lowest and highest *P* values (1.4 kW/cm^2 and 2.6 MW/cm^2) clarifies that for all samples the same emission bands are present, but varied in UCL intensity, see Fig. 4.7 c). At both *P* values the 3% Er^{3+} doped core-shell sample shows the highest UCL intensity of the 4 samples. The second highest emission signal is provided by different NP systems, for low *P* (1.4 kW/cm^2) by the 1% Er^{3+} doped core-shell sample and for high *P* (2.6 MW/cm^2) by the 3% Er^{3+} doped core-only sample. This change in emission intensity reveals that for low *P* the influence of the protective shell and for high *P* the Er^{3+} doping rate has a stronger impact on the UCL performance. This finding will be confirmed by following measurements.

The *P*-dependent overall emission colour is not significantly changed by the influence of

varied Er doping or the presence of the shell and shows for the 4 sample types the previously mentioned change from green over yellow to white with higher *P*, as illustrated in Fig. 4.7 d) at the three *P* values of 2.9 kW/cm^2, 0.2 MW/cm^2 and 2.6 MW/cm^2.
Before the comparison of SP and ensemble results (in chapter 4.5) will be outlined, the *P*-dependent appearing of the newly detected Er^{3+} ion emission bands needs to be explained.

4.4. High energetic UC transitions

In this chapter, the origin and the *P*-dependent behaviour of the most prominent and partly new observed Er-emission bands will be discussed based on literature research and on measured SP emission spectra taken at different *P*s. Like for the previous chapter, the results of this chapter is already published in *Nano Research* [107] under my own first authorship. We used the averaged SP spectra derived from 5 core-shell NaYF$_4$: 20% Yb^{3+}, 3% Er^{3+} NPs in the *P* range of 1.4 kW/cm^2 to 2.6 MW/cm^2, plotted in Figure 4.8 a). For this detailed study only the main peaks were taken into account, which were clearly separable from neighbouring peaks without strong overlapping. Thereby, the need for complex and error-prone spectral deconvolution for signal separation, as it was presented by Berry group for the green emission bands [119], was avoided here.

Categorising of *P*-dependent band emission and processes

The chosen peaks were then categorised into three groups on the basis of their *P*-dependent PL emission signals, as presented in Figure 4.8 b), c), d). To explain the complex (de)population processes of Yb^{3+} -Er^{3+} system, a Dieke diagram based on Judd-Ofelt analyses [120–124] was used, as illustrated in Figure 4.8 e). Part of the complex (de)population processes are excited state absorption (ESA) from Er^{3+}, energy transfer (ET), Er^{3+} – Yb^{3+} back-energy transfer (BET), cross-relaxation (CR) and non-radiative relaxation processes (nRP).

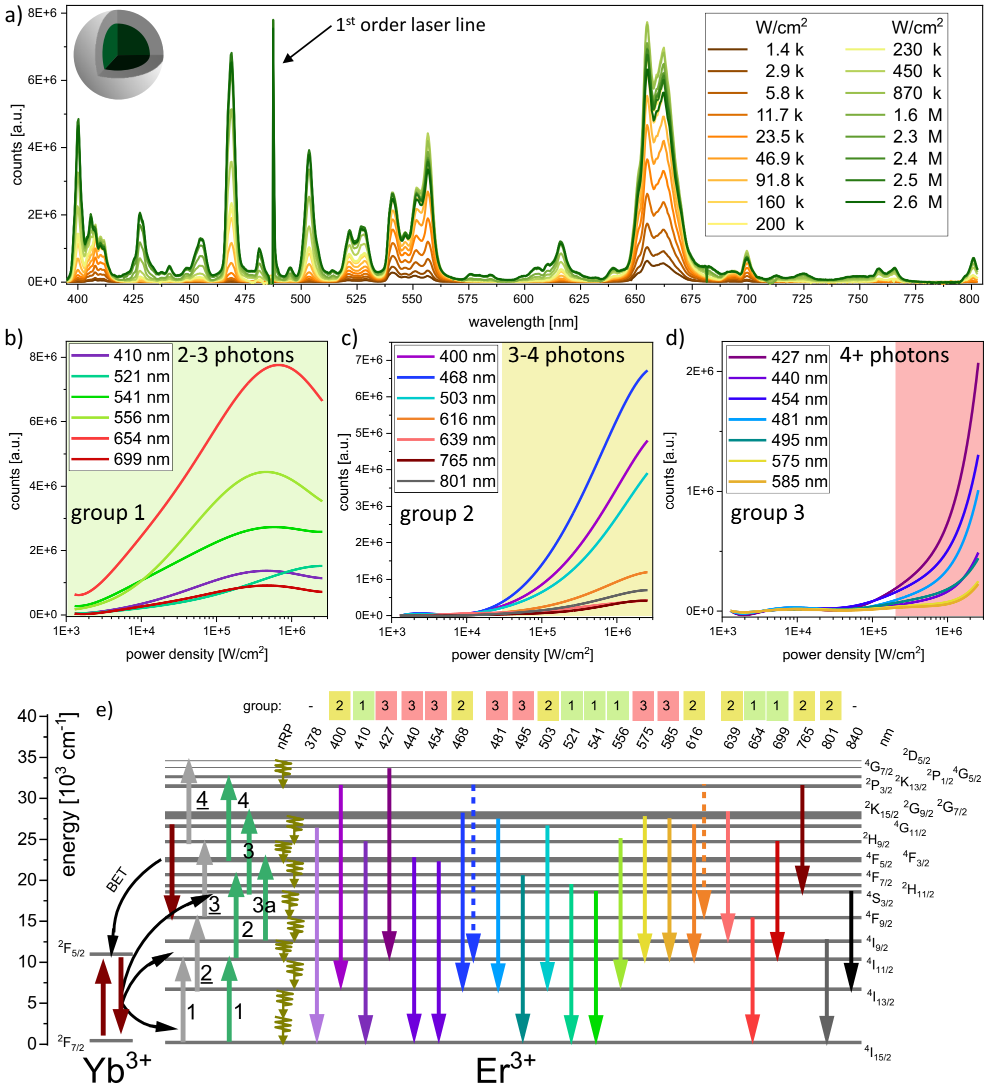

Figure 4.8. *P*-dependent UCL behaviour of 3% Er^{3+} doped core-shell (cs) NPs covering the *P* range from 1.4 kW/cm^2 to 2.6 MW/cm^2: a) *P*-dependent UC spectra achieved and averaged from 5 individual SP measurements per adjusted *P*. b), c), d) *P*-dependent UC intensity trends of the strong emission bands categorised in 3 groups with *P*-activated emission at low, medium and high *P*, associated to 2-3, 3-4 and 4 photonic processes. e) Dieke diagram of Yb-Er system based on Judd-Ofelt analyses illustrating the (de)population of the energy states with the most prominent emission bands in the range between 370 - 850 nm under 980 nm excitation. Taken and modified from own publication [107].

Group 1: 2 - 3 photonic processes The first group contains the emission bands well-known from ensemble studies at lower *P* (< 1000 W/cm^2) with the peaks at **410 nm** ($^2H_{9/2} \rightarrow {}^4I_{15/2}$), **521 nm** ($^2H_{11/2} \rightarrow {}^4I_{15/2}$), **541 nm** ($^4S_{3/2} \rightarrow {}^4I_{15/2}$), **556 nm** ($^2H_{9/2} \rightarrow {}^4I_{13/2}$), **654 nm** ($^4F_{9/2} \rightarrow {}^4I_{15/2}$), and **699 nm** ($^2H_{9/2} \rightarrow {}^4I_{11/2}$). The general origin of these emission bands is explained in the theoretical basis section 2.3.1 and will therefore here only be repeated shortly regarding their *P*-dependency for $P > 1$ kW/cm^2. The emission bands increase in intensity with *P* and show a maximum at about 600 kW/cm^2, see Fig. 4.9. For the population of these emissive energy levels, the absorption of 2 or 3 NIR-photons are involved. The first ET from Yb^{3+} ($^2F_{5/2}$) to Er^{3+} populates the $^4I_{11/2}$ Er level (grey/green arrow 1, Fig. 4.9). Via a 2nd Yb → Er ET, the $^4F_{7/2}$ level can be populated from $^4I_{11/2}$ (green bars, 1+2) leading to 521 nm and 541 nm emission bands after nRP from $^4F_{7/2}$ to $^2H_{11/2}$ and $^4S_{3/2}$ levels. The two green Er^{3+} emission bands show a moderately different *P*-dependent trend, as the 521 nm band follows the *P*-dependent behaviour of the 541 nm emission, but shifted to higher *P*. This can be explained by the thermal Boltzmann coupling of the two green emissive $^4S_{3/2}$ and $^2H_{11/2}$ levels. Thereby, the population of the lower to the higher energy level is enhanced with increasing *P* [125, 126].

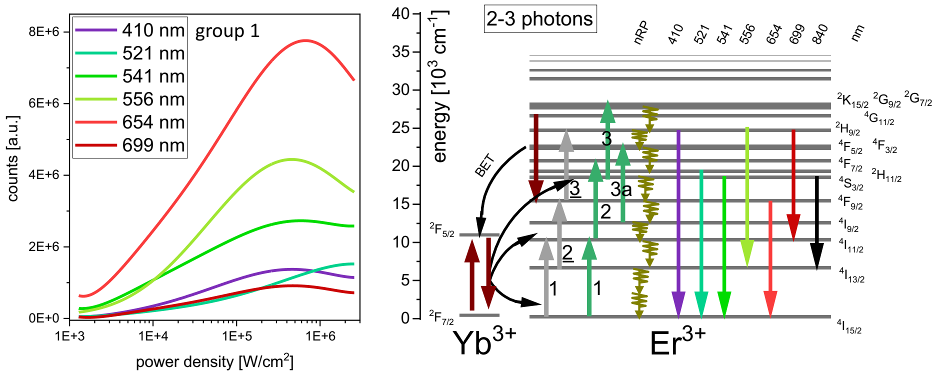

Figure 4.9. Left: *P*-dependent UC trends of the low *P* activated Er^{3+} ion emission bands (group 1) corresponding to 2-3 photonic absorption processes (left) and the appropriate Yb-Er Dieke diagram (right). Taken and modified from own publication [107].

The red emissive level ($^4F_{9/2}$) is known for being populated by a mix of 2 and 3 photonic absorption processes for lower *P* (section 2.3.1), but for higher *P*, the BET process seems to gain more importance. Via the BET process from the Er^{3+} ion ^{4}G/^{2}K manifolds ($^2G_{7/2}$, $^2G_{9/2}$, $^2K_{15/2}$, $^4G_{11/2}$) to Yb^{3+} ($^2F_{7/2} \rightarrow {}^2F_{5/2}$) [127] the $^4F_{9/2}$ level is populated following a 3 photon absorption process (green arrows 1-3 + BET), cf. Fig. 4.9. The strong increase of the 654 nm emission up to *P* of 600 kW/cm^2 can mainly be attributed to an enhanced Yb-Er BET occurrence, which boosts the Yb-excitation [116, 127].

The $^2H_{9/2}$ starting level is responsible for the emissions at 410 nm ($\rightarrow {}^4I_{15/2}$), 556 nm ($\rightarrow {}^4I_{13/2}$) and 699 nm ($\rightarrow {}^4I_{11/2}$) and its population is also based on a 3 photonic process, either excited directly with a 3rd Yb-Er ET from $^4F_{9/2}$ (grey arrow 3) or via nRP from higher lying ^{4}G/^{2}K levels [128, 129].

It seems, that the P-dependent trend - the intensity rise maximised at P of about 600 kW/cm^2 with following signal decrease - is directly related to the 2 and/or 3 photonic processes of the respective emission bands. The signal drop for $P > 600$ kW/cm^2 will be explained in the following discussion on the photonic processes with higher order.

Group 2: 3 - 4 photonic processes The second group of emission bands showing same P-dependent trend includes the peaks at **400 nm** ($^2P_{3/2} \rightarrow {}^4I_{13/2}$), **468 nm** ($^2G_{7/2} \rightarrow {}^4I_{13/2}$) & ($^2P_{3/2} \rightarrow {}^4I_{11/2}$), **503 nm** ($^4G_{11/2} \rightarrow {}^4I_{13/2}$), **616 nm** ($^4G_{11/2} \rightarrow {}^4I_{11/2}$) & ($^2P_{3/2} \rightarrow {}^4F_{9/2}$), **639 nm** ($^2G_{7/2} \rightarrow {}^4I_{9/2}$), **765 nm** ($^2P_{3/2} \rightarrow {}^4S_{3/2}$), and **801 nm** ($^4I_{9/2} \rightarrow {}^4I_{15/2}$). They all have in common to appear at $P > 100$ kW/cm^2 and to start saturation for $P > 600$ kW/cm^2, cf. Fig. 4.10.

To populate the $^4G_{11/2}$, $^2G_{7/2}$ and the $^2P_{3/2}$ Er^{3+} energy levels a minimum of 3 to 4 NIR-photons are needed. Via ET processes and ESA starting from the $^4S_{3/2}$ level (green arrow 3), the $^2G_{7/2}$ level can be reached leading to the 468 nm and 639 nm emission bands. Therefore, the population of $^2G_{7/2}$ is on the cost of the green $^4S_{3/2}$ level occupation, which explains the decrease of the 541 nm luminescent intensity for higher P (Fig. 4.9).

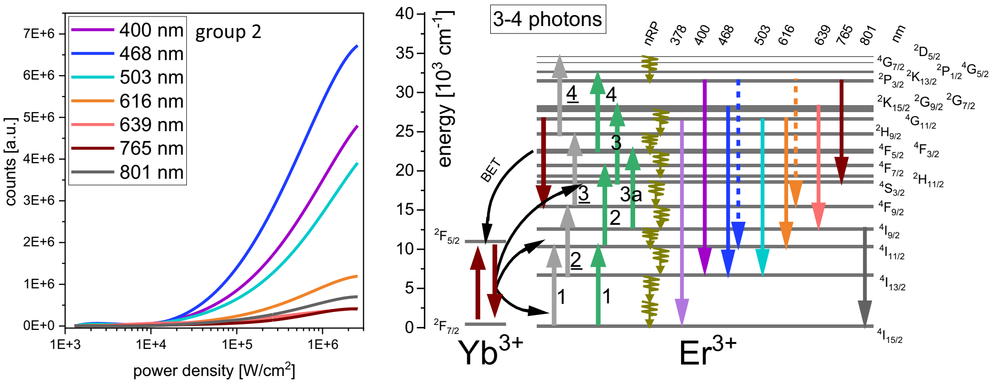

Figure 4.10. Left: P-dependent UC trends of the medium P activated Er^{3+} ion emission bands (group 2) corresponding to 3-4 photonic absorption processes (left) and the appropriate Yb-Er Dieke diagram (right). Taken and modified from own publication [107].

The emissions at 503 nm and 616 nm arise from the $^4G_{11/2}$ level, which can be populated via nRP from the energetically overlying $^2K_{15/2}$ level. According to O'Shea et al. [122] the 468 nm and 616 nm luminescence can also have radiative contributions from the higher lying $^2P_{3/2}$ energy level (dashed arrows), for which at least 4 absorbed photons are needed for population. The $^2P_{3/2}$ energy level is also responsible for the 400 nm and 765 nm emissions [121, 123] and can get excited by ET and ESA from $^4F_{5/2}$ / $^4F_{3/2}$ to $^2K_{13/2}$ (green arrow 4) [122] or by ESA from $^2H_{9/2}$ to $^2D_{5/2}$ (grey arrow $\underline{4}$) [107]. The last-mentioned ESA works as a non-radiative depopulation pathway of the $^2H_{9/2}$ level and provides an explanation for the intensity decrease of the 410 nm, 566 nm and 699 nm bands for P exceeding 600 kW/cm^2, cf. Fig. 4.8 and Fig. 4.9.

The P-dependent emission trend of the 801 nm, originating from the comparably low energetic $^4I_{9/2}$ level, can be explained by a mix of processes. Namely, an increased Er-Er CR1 (donor transition: $^2H_{11/2}$ / $^4S_{3/2} \rightarrow {}^4I_{9/2}$ and acceptor transition: $^4I_{15/2} \rightarrow {}^4I_{13/2}$) [130], or via a nRP from the energetically above lying $^4F_{9/2}$ level or by the radiative depopulation of the $^2G_{7/2}$ into the $^4I_{9/2}$ level under 639 nm emission.

The band emissions of the 2nd group are favoured by the already high population of the Er^{3+} energy levels. Furthermore, the increasing contributions of ESA and reduced Er–Yb BET processes due to the already high number of excited Yb^{3+} ions seem to play a significant role with higher P and will be even more relevant for the 3rd group of emission bands [107].

Group 3: 4+ photonic processes The 3rd group of emission bands starts to grow at $P >$ 100 kW/cm^2 and contains the peaks at **427 nm** ($^4G_{7/2} \rightarrow {}^4I_{11/2}$), **440 nm** ($^4F_{3/2} \rightarrow {}^4I_{15/2}$), **454 nm** ($^4F_{5/2} \rightarrow {}^4I_{15/2}$), **481 nm** ($^2K_{15/2} \rightarrow {}^4I_{13/2}$), **495 nm** ($^4F_{7/2} \rightarrow {}^4I_{15/2}$), **575 nm** ($^2G_{9/2} \rightarrow {}^4I_{11/2}$), and **585 nm** ($^2K_{15/2} \rightarrow {}^4I_{11/2}$), cf. Fig. 4.11. The higher P gets and therefore the population density of Er^{3+} ions increases, the more difficult it becomes to explain and to distinguish the different underlying (de)population processes, like Er-Yb ET, Er-Er ET1 and ESA.

Following a 3 photon absorption process containing an Er-Er, Er-Yb and ESA process (green arrows 1-3), the $^2G_{7/2}$ is excited and from there via mutli-phonon relaxation processes (mpR) the $^2G_{9/2}$ and $^2K_{15/2}$ energy levels can be populated, which are the emitting levels for the 481 nm, 575 nm, and 585 nm luminescence [131, 132]. Unfortunately, the 1. order laser line overlaps with the 481 nm emission peak, so that this band cannot be analysed in detail, cf. Fig. 4.8 a).

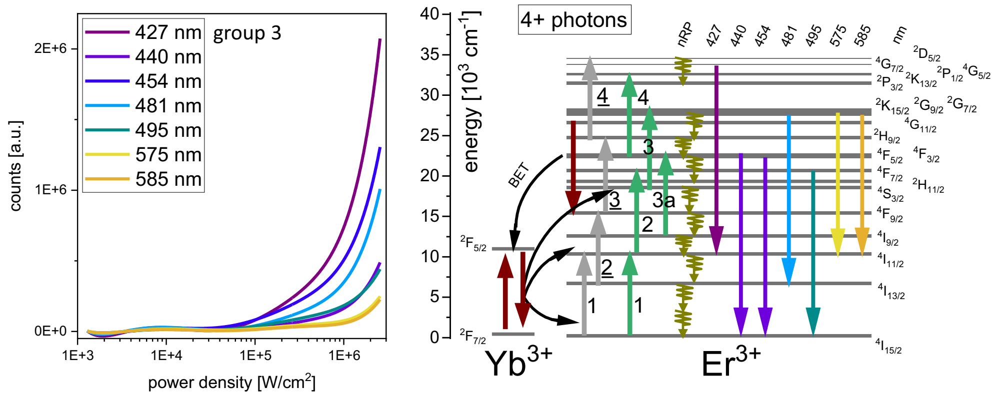

Figure 4.11. Left: P-dependent UC trends of the high P activated Er^{3+} ion emission bands (group 3) corresponding to 4 or more photonic absorption processes (left) and the appropriate Yb-Er Dieke diagram (right). Taken and modified from own publication [107].

The intensity rise of the 440 nm, 454 nm and 495 nm emission bands, which arise for high P from the comparable low energetic ^4F states ($^4F_{3/2}$ / $^4F_{5/2}$ / $^4F_{7/2}$) could be explained with a high P-activated further ESA (green arrow 3a) bridging the energy gap between $^4I_{9/2}$ and $^4F_{3/2}$. This ESA acting as non-radiative depopulation pathway from the $^4I_{9/2}$ can explain the flattening increase of the 801 nm emission and was reported before by Lyapin et al. [133].

In general, the described ESA and ET processes (arrows: green 3, 3a, 4 and grey $\underline{4}$) seems to play bigger role with higher P leading to population of higher Er^{3+} levels, which is consistent with the enhanced depopulation of lower lying Er^{3+} ion level (group 1, Fig. 4.9) revealed by their luminescence emission intensities. Consequently, the energy levels of the 3rd group emission bands are populated partly on the cost of the energetic lower lying levels (group 1 and 2). The emissions show a strong intensity increase at the P of about 2.6 MW/cm^2, which seems far away from saturation behaviour, cf. Fig. 4.11.

The strongest P-dependent increase is given by the 427 nm emission originating from the $^4G_{7/2}$ level, which can be reached via ET and ESA processes (grey arrow $\underline{4}$) involving 4 or more absorbed NIR-photons.

For some of the above-mentioned emission peaks the assignment is not uniquely identifiable and more than one energy level can be responsible, as it was already discussed for 468 nm and 616 nm in Fig. 4.10. In 2003 the Meijerink group experimentally found a bunch of additional emission lines at **378 / 405 / 481 nm** and at **433 / 466 / 505 nm** originating from the much higher lying $^4D_{1/2}$ ($47.2 \cdot 10^3$ cm^{-1}) and $^2F(2)_{7/2}$ ($54.7 \cdot 10^3$ cm^{-1}) energy states, respectively [121]. Since the 405 / 481 nm (from $^4D_{1/2}$) would closely match the above-mentioned 400 nm ($^2P_{3/2} \rightarrow {}^4I_{13/2}$) and the 481 nm ($^2K_{15/2} \rightarrow {}^4I_{13/2}$) emission bands, and the 433 / 466 / 505 nm (from $^2F(2)_{7/2}$) would be in overlap with the previously discussed 427 nm ($^4G_{7/2} \rightarrow {}^4I_{11/2}$), 468 nm ($^2G_{7/2} \rightarrow {}^4I_{13/2}$) & ($^2P_{3/2} \rightarrow {}^4I_{11/2}$) and 503 nm ($^4G_{11/2} \rightarrow {}^4I_{13/2}$), we could not simple exclude the possibility that our results show contributions from theses high $^4D_{1/2}$ and $^2F(2)_{7/2}$ energy levels. To populate these two states via ET and ESA processes, the absorption of at least 7 or 8 photons would be needed theoretically. At this point we suggested an alternative but (in our opinion) more realistic assumption of an Er^{3+} - Er^{3+} ET consisting of one ET from a higher to lower Er state with a simultaneous ET from a lower to a higher Er energy level [107]. That means, instead of being spontaneously emitted, the energies of certain transitions could help to overcome large energy gaps, therefore the energies of the 378 nm and 410 nm emission bands would be sufficient to populate the $^2F(2)_{7/2}$ state, as shown in Fig. 4.12. The energy amounts of the 521 nm, 541 nm, 556 nm, 616 nm, 654 nm, and 699 nm radiative transitions would be enough to reach and excite the $^4D_{1/2}$ level, as suggested in Fig. 4.12. Such a bunch of Er-Er ETs would also be an explanation for the intensity drop of the 1st and 2nd group bands at P exceeding 600 kW/cm^2 by simultaneous enhancement of the 3rd group emission band intensities.

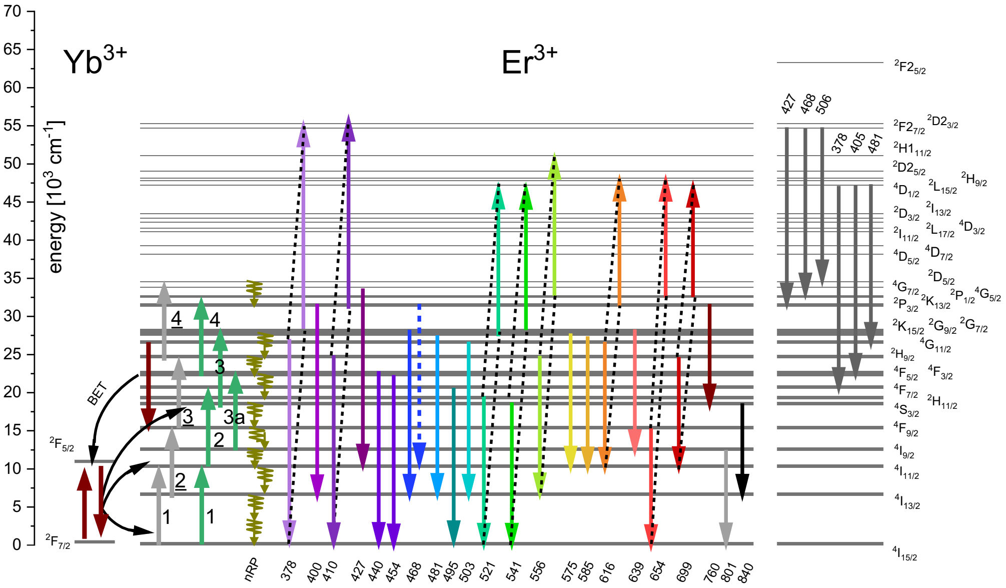

Figure 4.12. Dieke diagram of Yb-Er system based on Judd-Ofelt analyses illustrating the (de)population of the energy states with the most prominent emission bands in the range between 370 - 850 nm under 980 nm excitation. Here, a suggestion of a bunch of additional Er-Er ET processes is offered to explain the high Er level populations and their emission behaviour: Instead of being spontaneously emitted at 378 nm, 410 nm, 521 nm, 541 nm, 556 nm, 616 nm, 654 nm and 699 nm, higher states like $^2F(2)_{7/2}$ and $^4D_{1/2}$ could be populated via the proposed Er-Er ET processes (dashed black lines). According to Wegh et al. [121] the emission bands at about 427 nm, 468 nm, 506 nm and 378 nm, 405 nm, 481 nm are emitted from the $^2F(2)_{7/2}$ and $^4D_{1/2}$ states, respectively. The image is redesigned from own publication [107].

P-dependent emission trends of the 4 NP systems

Besides the (de)population pathways and ion-ion interactions, also external temperature (T) effects like laser-induced heating can be partly responsible for the increased populations of energetic higher Er^{3+} states by increasing the likelihood for transitions with an energetic mismatch. The thermal impact on UC process can be read out by checking the intensity ratio of green emissions at 521 nm ($^2H_{11/2}$) and 541 nm ($^4S_{3/2}$), which are coupled in a Boltzmann equilibrium and can be used for temperature sensing [134]. With higher T, the energetic higher $^2H_{11/2}$ level gets populated via depopulation of the underneath lying $^4S_{3/2}$ level. In our measurements this energy transfer was revealed by an increased 521 to 541 nm ratio (G/G) with increasing *P*, as illustrated for the 4 NP systems in Fig. 4.13 a) [107]. Using the $T = T(\frac{I_{521}}{I_{541}})$ dependency[1] derived under ensemble condition by Vetrone et al. [134], T values of up to 280 °C would be reached for the 1% Er doped core-shell sample with a maximal G/G ratio of about 0.9 at *P* of 2.6 MW/cm^2. From our own study on SPs with high Yb and Er doping variation in chapter 5, we learned, that the G/G ratio is both, dependent on *P* and on the doping ratio of Yb^{3+} and Er^{3+} ions (cf. appendix Fig. A.13 b)). Consequently, there is no generally valid use of G/G ratios for T-sensing, in fact the T-dependency of the

---

[1] Linear dependency of Emission ratio ($\frac{I_{521}}{I_{541}}$) and (1/T), according to [134]: $ln(\frac{I_{521}}{I_{541}}) = 1.74 - 1028 \cdot (1/T)$

G/G ratio has to be measured and calibrated for each specific NP-system with a variation in ion doping and host matrix, and for a specific P-range.

A comparison of the integrated UCL of the 4 NP systems revealed for P below 10 kW/cm^2 clearly higher total luminescence intensities of the core-shell compared to the core-only UCNPs, cf. Fig. 4.13 b). With increasing P (> 20 kW/cm^2), the influence of surface effects and hence the passivation by a protective shell levels off more and more. At higher P, a higher number of Er^{3+} ions per NP leads to more efficient UC emission as obtained by the comparison of UCNPs doped with 1 and 3 Er^{3+}.

The P-dependent UCL emission bands of the four UCNP systems (see Fig. 4.13 c), d), e)) reveal the same trends for the 3 groups of UCL emission bands and their dependencies on the Er doping concentration as previously detailed for the core-shell UCNPs doped with 3% Er^{3+}, cf. Fig. 4.8. The corresponding P-dependent emission spectra of the 4 NP systems, which were averaged from the results of individual SPs, are plotted in the appendix Fig. A.5.

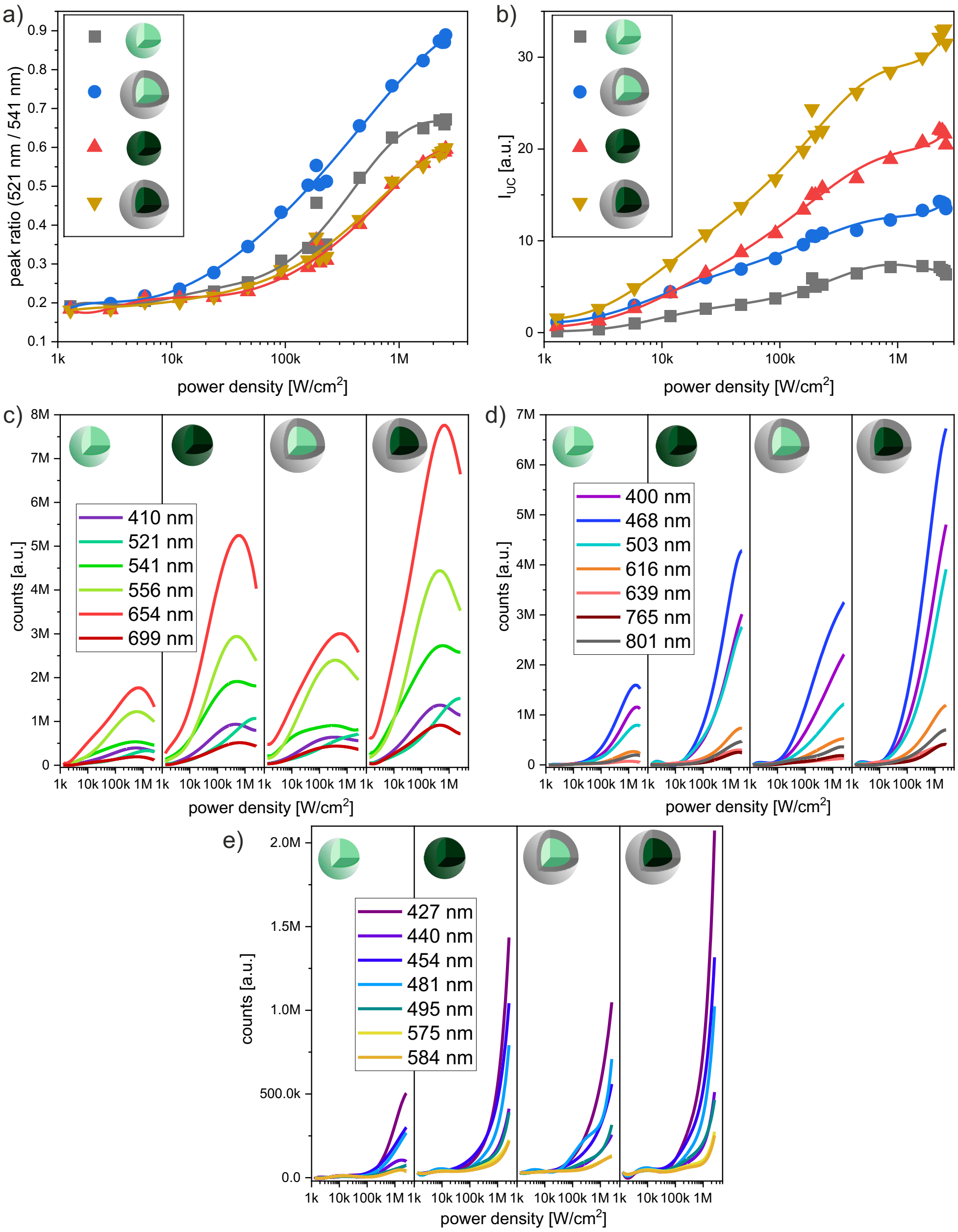

Figure 4.13. Comparison of the P-dependent SP luminescence behaviour of the 4 NP systems covering a P range from 1.4 kW/cm^2 to 2.6 MW/cm^2: a) Green-to-green (521 to 541 nm) peak ratio of the two, $^2H_{11/2}$ and $^4S_{3/2}$ levels linked by thermal Boltzmann coupling. b) Integrated overall emission intensities showing the different impacts of the shell and of Er^{3+} ion doping at low and high P-ranges. c), d), e) Grouping of the most prominent and clear detectable bands in low, medium and high P activated emissions, respectively. The band intensities scale with Er concentration and show stronger signal with the higher 3% Er^{3+} ion doping. Taken and modified from own publication [107].

4.5. Comparison of ensemble and SP studies

The number of variables which are measurable at both conditions, in ensemble and on SP level, is limited, which also makes a direct comparison of both measurement conditions tricky. To enable comparison, we focused on emission bands, which are present in ensemble and SP condition, took their maximum peak signals for ratio calculations and measured their decay behaviour. From the ensemble studies, which were performed in cyclohexane and water, and are outlined in previous chapter 4.2, only the results achieved in cyclohexane with reduced surface quenching effects were taken for the following comparisons to approach closest the measurement conditions of dried SPs.

P-dependent peak ratios

In Figure 4.14, the peak intensity ratios of the green-to-green (G/G) and the green-to-red (G/R) emissions are plotted for both, the ensemble and SP measurement condition covering over 5 orders of magnitude of *P*. The ratios reveal the impact of the shell and the doping at different *P* ranges.

The G/G peak ratio is calculated by the 541 nm emission ($^4S_{3/2} \rightarrow {}^4I_{15/2}$) divided by the 556 nm ($^2H_{9/2} \rightarrow {}^4I_{15/2}$) emission and therefore, represents the ratio between 2 and 3 photonic processes. In the low *P* range in ensemble condition the G/G ratios are different for the core-only (black, red) and the core-shell (blue, orange) NPs, cf. Fig. 4.14 a). With higher *P*, this difference in G/G ratio decreases and in SP condition at *P* higher than 100 kW/cm^2 the 1% Er^{3+} and 3% Er^{3+} doped samples show different ratios and converge to values of 0.4 and 0.65, respectively. This highlights the strong influence of a protective shell in ensemble condition, which decreases with higher *P* due to enhanced population rates of the Er^{3+} and Yb^{3+} energy levels compensating for quenching effects [107]. In SP studies the peak ratio is nearly independent of the NP architecture and mainly influenced by the Er^{3+} ion doping rate.

The G/R ratio (541 nm over 654 nm ($^4F_{9/2} \rightarrow {}^4I_{15/2}$)) shows similar trends compared to the G/G ratios for the ensemble and SP *P* ranges depending on the presence of a shell and doping influences. The saddle point at medium *P* (about 5 kW/cm^2) and the following local minima at about 600 kW/cm^2 can be attributed to the influence of enhanced BET processes until Yb^{3+} ion saturation occurs for higher *P* [107].

The peak ratios provide an approach to connect both spectra results achieved from ensemble and SP studies of the same samples measured under different conditions. Therefore, the SP studies can be used as an extrapolation of the conventional ensemble studies up to the MW/cm^2 *P* range.

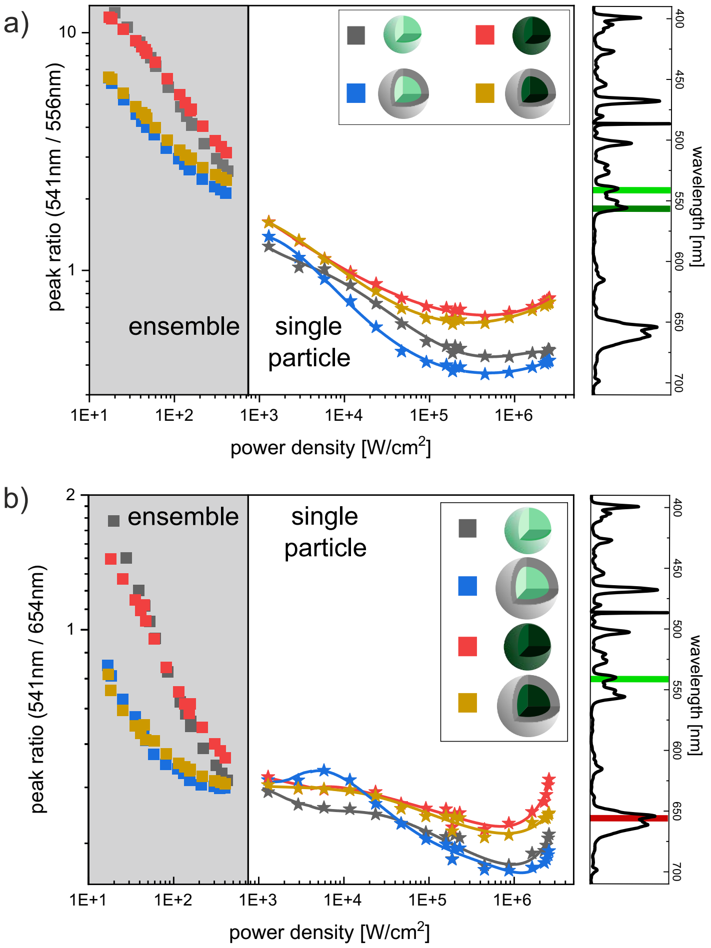

Figure 4.14. *P*-dependent peak ratios combined from ensemble studies in the *P* range from 5 to 400 W/cm^2 (grey area) and SP studies from 1.4 kW/cm^2 to 2.6 MW/cm^2 of the 4 core-only and core-shell NP systems: a) Green-to-green (G/G) ratio of the 541 nm and 556 nm emission peaks. b) Green-to-red (G/R) ratio of the 541 nm and 654 nm emission peaks. Taken and modified from own publication [107].

Decay kinetics

The decay behaviour of the green (541 nm) and red (654 nm) emission band was measured on SP level to get a better understanding of the UCL (de)population processes of these levels at higher *P*. In Fig. 4.15, the calculated intensity weighted lifetimes (LTs) of the 4 NP systems are plotted for the green and red emission under 4 different excitation *P* conditions.

Decay kinetics from SPs

As part of the decay kinetic studies on SPs the impact of the laser excitation parameters like pulse length and pulse power was tested. Therefore, the repetition rates and the electronically setted laser power outputs were varied to generate 4 different laser-excitation pulses by using the burst-generator[1]. The following averaged laser-excitation pulse powers of specific lengths had been adjusted by setting 2k or 80k

---

[1] The burst-generator from PicoQuant forms an excitation laser pulse of a length in the *μs* to *ms* range by the repetition of a finite number of single ns-laser pulses with a certain pulse power and a variable repetition rate

single ns-pulses by an repetition rate of either 16 or 80 MHz: 0.5 W/cm^2 / 125 µs pulse (2k ns-pulses, 16 MHz, in blue), 20 W/cm^2 / 5 ms pulses (80k ns-pulses, 16 MHz, in orange), 5.8 W/cm^2 / 25 µs pulse (2k ns-pulses, 80 MHz, in grey) and 230 W/cm^2 / 1 ms pulse (80k ns-pulses, 80 MHz, in yellow), cf. Fig. 4.15.

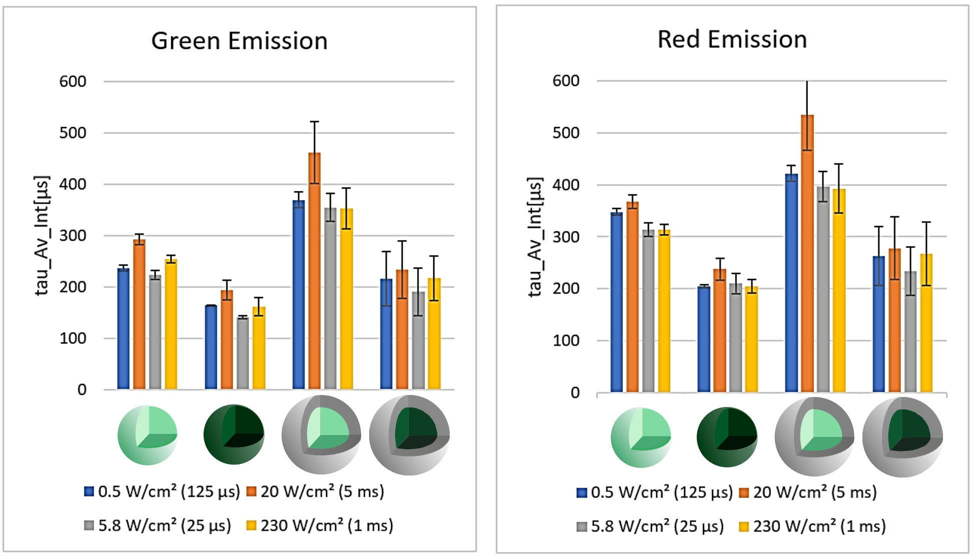

Figure 4.15. Intensity weighted lifetimes (LTs) of the green (left) and red (right) emission bands of the 4 NP systems for different excitation conditions varied in pulse length and pulse power at the wavelength of 976 nm. The laser pulses consists of a finite number n of ns-laser pulses (2k or 80k pulses) with a specific repetition rate (16 or 80 MHz) and a specific electronically controlled pulse intensity. Specifically, low and high laser pulse powers were combined with short and long pulse lengths leading to the 4 specific excitation conditions: 0.5 W/cm^2 / 125 µs pulse (2k ns-pulses, 16 MHz, in blue), 20 W/cm^2 / 5 ms pulses (80k ns-pulses, 16 MHz, in orange), 5.8 W/cm^2 / 25 µs pulse (2k ns-pulse, 80 MHz, in grey) and 230 W/cm^2 / 1 ms pulse (80k ns-pulses, 80 MHz, in yellow). The laser excitation pulses have been generated using the burst-generator tool from PicoQuant. Taken and modified from own publication [107].

For longer pulse lengths, longer decays and increased LTs of the green and the red emissions of all 4 NP systems were measured for both low and high laser pulse powers, as shown in Fig. 4.15. The influences of the pulse lengths are more pronounced for the green emission. Even if the trends are in total comparably small, it highlights the problem of the general comparability of UCL data received under different conditions or at different setups and therefore, underlines the need for correctly determined excitation conditions.

As expected, the addition of the protective shell enhances the LTs of both emission bands significantly due to reduced surface quenching effects for all 4 excitation conditions. The change in Er^{3+} ion content from 1% to 3% leads to shorter LTs and faster decays for the green and the red emission band. This is related mainly to the Yb:Er ion ratio, which changes from 20:1 to about 7:1 by enhancing the Er content from 1% to 3% Er^{3+} [135]. A larger number of Er^{3+} ions in the direct proximity of the excited Yb^{3+} ions enhances the relative amount of

Yb^{3+} ions involved in Yb-Er ET processes, which reduces the intrinsic Yb-LT and therefore the overall temporal response of green and red emissions for the higher Er doped sample. According to Kaiser et al. [116], the relative small changes in Er doping (1% to 3%) should not lead to a significant enhancement of Er-Er CRs related quenching.

Comparing decay kinetics from ensemble and SP studies The intensity weighted LTs derived from ensemble measurements of cyclohexane-dispersed UCNPs at low P (63 W/cm² per 400 µs pulse; blue) are compared to the LTs obtained in SP studies of dried UCNPs at high P (230 W/cm² per 1 ms pulse; black) for the green and red emission bands of all four UCNP systems in Fig. 4.16 a) and c). The corresponding decay curves of the 3% Er^{3+} core-shell NPs are exemplarily plotted in Fig. 4.16 b) and d).

The decay kinetics on SP level reveal changes in LTs compared to them obtained in ensemble condition. For the green emission the unshelled NPs show shorter LTs in ensemble compared to single NPs, whereas with presence of shell the opposite trend occurs, see Fig. 4.16 a). This can be explained by the different measurement conditions regarding the strong variations in P and the detection systems used in ensemble and single NP studies. The higher P values at SP level lead to more populated energy states and saturation effects, which enlarges the LTs by surpassing quenching effects in case of unshelled NPs. Furthermore, via multiphoton absorption processes (3 or 4 photons) the high P enables populations of higher energy levels with additional and overlapping emission bands in the observed spectral ranges. A total separation and an isolated decay measurement of a specific energy transition is not possible due to overlapping and thermal broadening of the closely lying emission bands. This is especially challenging for the SP kinetic studies, since bandpass filters have been used for single-photon counting of the green and the red emission bands with transmissive windows from 533-557 nm and 635-675 nm, cf. Fig. A.6. In consequence, the 556 nm emission ($^2H_{9/2} \rightarrow {}^4I_{13/2}$) contributes to the green 541 nm measured decay. The short intrinsic decay rate of about 19.5 μs of the $^2H_{9/2}$ level [102] can explain the faster decays in the green channel of single core-shell NPs compared to the decays found in ensemble. The decay behaviour of the red emission shows the same trends as the green UCL, except for the core UCNPs doped with 3% Er^{3+}, for which slightly longer LTs are obtained in the ensemble studies. The longer red LTs of the core-shell SP decays, can be attributed to the contribution of the overlapping 639 nm emission ($^2K_{15/2} \rightarrow {}^4I_{9/2}$). For the ensemble measurements a monochromator was used to cut out the green emission line at 541±1 nm and the red at 654 ±1 nm.

To test the influence of cyclohexane under SP condition, the decay kinetics of the 3% Er^{3+} doped core-only and core-shell systems were exemplarily measured, first dried on glass-substrate and then re-dispersed in cyclohexane (orange bars). Only marginal differences in the LTs were found for the green and red emissions, consequently, the influence of cyclohexane on the UCL decay behaviour can be neglected at higher P on SP level [107].

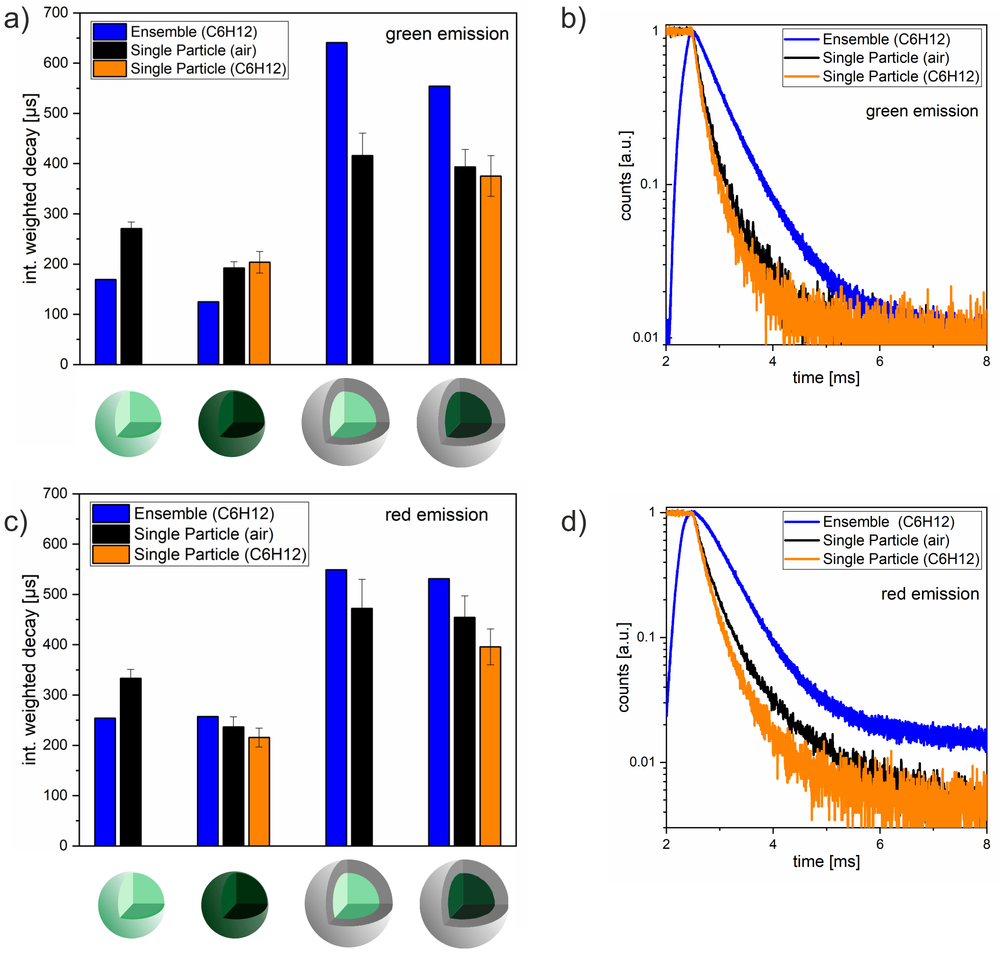

Figure 4.16. Comparison of the decay kinetics of the 4 NP systems obtained in ensemble condition (in cyclohexane; 63 W/cm² per 400 µs pulse; blue) and in SP condition (230 W/cm² per 1 ms pulse) ones dried on glass-substrate (black) and ones for the 3% Er doped samples exemplary re-dispersed in cyclohexane (orange): a) and c) Intensity weighted LTs of the green and red emission bands. b) and d) Decay curves of the 3 measurement conditions exemplary for the 3% Er^{3+} doped core-shell UCNPs for the green and red emission bands. Taken and modified from own publication [107].

4.6. Conclusion

In this chapter, the optical properties of core-only and core-shell β-$NaYF_4$:Yb,Er UCNPs with 20% Yb^{3+} have been tested, first on ensemble level with a variation of 1%, 2% and 3% Er^{3+} doping concentration and on SP level with 1% and 3% Er^{3+} doping. The P-range of the ensemble measurements (5 to 400 W/cm^2) was expanded by the SP studies with the P range from 1.4 kW/cm^2 to 2.6 MW/cm^2 performed on the CLSM. The several newly detected Er^{3+} emission bands at high P, changing the total emission colour from green to yellow to white, have been grouped depending on their P-dependency and the order of photonic processes, meaning 2-3, 3-4 or 4+ absorbed photons.

With the G/G (541 nm / 556 nm) and the G/R (541 nm / 654 nm) ratios the results from ensemble and SP studies have been combined and illustrated the strong influence of the protective shell at low and medium P and the strong impact of the Er^{3+} doping concentration at high *P*. The decay kinetic studies highlighted the difficulties of a direct comparison of the ensemble and SP results obtained under such different measurement conditions. The additional contributions from emission bands, arising from higher Er^{3+} transitions can lead to effectively accelerated decay kinetics for the SP studies at high *P*. Therefore, especially closely lying and overlapping emission bands need to be exactly considered before they are taken for UCL LT measurements.

Since the comparably small variation in Er^{3+} ion doping concentration from 1% to 3% of this sample series got already apparent in this study, a higher variation in Yb^{3+} and Er^{3+} doping ratios should even show stronger effects. This issue will be discussed in the next chapter.

5 High variation in Yb and Er doping

In the last chapter, the ensemble and SP studies on one of the most widely used UC system, $NaYF_4$ crystal co-doped with 20% Yb^{3+} and a low Er^{3+} concentration of about 2% revealed the strong dependence of UCL on the excitation P, the surface protection, and the Ln^{3+} doping concentration. Since already the relatively small doping variation from 1% to 3% Er^{3+} showed an impact on UCL performance and a significant influence on NP brightness under SP condition, in this chapter the effect of a broad variation in Ln^{3+} doping concentration on UCL will be discussed under ensemble and SP condition.

The variation of Ln^{3+} doping concentration causes a change of the total number of absorbing Ln^{3+} ions and therefore, the absorption cross-section of a NP. Also, it changes the ion-ion distances and their interactions. A high number of dopant ions is essential for efficient ETU between neighbouring Ln^{3+} ions. An increase of the dopant ion concentration, especially of the sensitizer ions enhances light absorption and probably also the NP brightness if QY_{UC} is not considerably decreased. A high density of dopant ions can lead to enhanced lattice distortions and to enhanced concentration quenching and non-radiative energy loss via localised ion-ion CR and long distance energy migration to the surface or lattice defects [32, 136, 137]. This concentration based energy loss can be compensated by the combination of enhanced absorption (related to higher c) and increased excitation P [31, 138].
For Yb/Er doped UCNPs, there is not the one unique Yb/Er doping ratio, which leads under all conditions to brightest UCL. We will see, that for the different P regimes and for different NP diameters, the variation in Yb and/or Er doping will lead to a different optical behaviour. Since the positive effect of a protective shell was already presented in the previous section and also confirmed for higher Yb/Er doping ratios by other research groups [31, 33, 139], in this chapter we only used NPs with an inert protective shell of $NaYF_4$ or $NaYF_4$ co-doped with Lu^{3+} ions.

In this study, 2 different set of core-shell samples were used, first sub-10 nm UCNPs synthesized by the Hirsch group (University of Regensburg) and second sub-30 nm UCNPs synthesized by the Haase group (University of Osnabrück). In addition, the sub-10 nm β-$NaYF_4$: 20% Yb^{3+} / 2% Er^{3+} sample will be compared to μm-sized β-$NaYF_4$: 18% Yb^{3+} / 2% Er^{3+} UCNCs to study the impact of size and volume effects on the UCL behaviour at ensemble and SP level.

5.1. Sub-10 nm UCNPs: ensemble and SP studies

Preparation, chemical and experimental analysis

The set of sample consist of 3 different core-shell UC systems, first the ”standard” configuration of 20% Yb^{3+} / 2% Er^{3+} ($NaYF_4$(20% Yb, 2% Er)@$NaYF_4$), second 80% Yb^{3+} / 20% Er^{3+} ($NaYbF_4$(20% Er)@$NaYF_4$) and third 100% Er^{3+} ($NaErF_4$@$NaYF_4$). The synthesis was performed by Alexandra Schroter (University of Regensburg) based on the procedure presented in the last section and published in [51, 107]. The core and core-shell diameters are listed in Table 5.1 based on TEM images, cf. Fig. A.7.

label	th. Yb/Er ratio [%]	core diameter [nm]	core-shell diameter [nm]
$NaYF_4$(20% Yb, 2% Er)@$NaYF_4$	20/02	8.5 ± 0.8	12.3 ± 1.2
$NaYbF_4$(20% Er)@$NaYF_4$	80/20	8.4 ± 0.5	12.8 ± 0.9
$NaErF_4$@$NaYF_4$	0/100	6.0 ± 0.4	11.2 ± 1.4

Table 5.1. Overview of core and core-shell diameters based on TEM data analysis of the 3 samples synthesized by the Hirsch group (Regensburg).

Please note, that the core diameter of the 100% Er doped sample does not match the core diameters of the two Yb/Er doped samples, which only differ marginally. For such small NPs, the difference of about 2.5 nm in diameter d causes a large difference in the total number of Ln^{3+} ions (N_{Ln}) and in the NP volume, which scales with $(d/2)^3$. Taking the diameter uncertainties into account, the volume and N_{Ln} of the Er samples is only between 24% to 53% of the Yb/Er doped samples, making only limited comparisons between these samples possible. In the following discussion the reduced number of N_{Ln} inside the 100% Er doped sample must be kept in mind.

The time-resolved ensemble measurements have been performed on the FLS980 setup (cf. section 3.2.3) by my colleague Monica Pons (Master student under the supervision of Prof. Oliver Benson from HU Berlin) and the steady-state measurements were done by myself on the integrating sphere setup (Fig. 3.1). All samples were dispersed in cyclohexane with a NP concentration of $3.5 \cdot 10^{15}$ particles per mL. All SP studies have been done by myself on the CLSM (setup in section 3.3.1).

At the end of this section, the 20/02 Yb/Er samples will be compared to powdered bulk-like UCNCs with 18/02 Yb/Er doping ratio provided by K. Krämer (University of Bern), which was produced via a high temperature synthesis and is therefore ligand-free. The ensemble measurement on the powdered sample was performed by my colleague Bettina Grauel and the single particle measurements by myself. For the latter, a thin layer of the powdered sample was dropped on the glass-slide, covered by a second slide and μm flakes / bulk-like UCNCs were selected for the subsequent CLSM measurements.

Decay behaviour under ensemble condition

From the decay behaviour in Figure 5.1 the impact of increased Er and/or Yb doping concentration on the rise and decay kinetics of the 541, 654 and 1000 nm emitting levels can be examined under 980 nm excitation and will be explained in comparison to the ”standard” 20/02 Yb/Er sample. Figure 5.1 a) shows the decays of the 1000 nm emission, which arises of transitions inside Yb ions ($^2F_{5/2} \rightarrow {}^2F_{7/2}$) and additionally inside Er ions ($^4I_{11/2} \rightarrow {}^4I_{15/2}$) at high Er doping. The decay curve of the 80/20 Yb/Er sample (red) shows a bi-exponential behaviour, with a shortened τ_1 and an increased τ_2 component compared to the 20/02 Yb/Er sample (black). The 4 times higher Yb content enhances the energy migration to lattice and surface defects, leading to enhanced non-radiative quenching and therefore, to a faster τ_1 component. An additionally increased energy migration to OH^- centres inside the cores was suggested from Meijerink group [31], which also measured a strong decrease in LTs for single Yb doped $NaYF_4$ particles with Yb content ≥60%.

The parallel tenfold increase of Er content also leads to faster decays (τ_1 component) caused by enhanced concentration quenching (Er-Er CRs), thereby the CR2 ($^4I_{11/2} \rightarrow {}^4F_{9/2}$ and $^4F_{7/2} \rightarrow {}^4F_{9/2}$, cf. Fig. 2.4 c)) depopulates the $^4I_{11/2}$ level, which either interacts with the $^2F_{5/2}$ Yb level or contributes radiatively to the 1000 nm emission band. As we have seen for a smaller increase in Er doping in chapter 4.2, a higher Er^{3+} ion content leads to a faster decay of the $^2F_{5/2}$ Yb level. It is explained mainly for the near-surface Yb/Er ions by an enhanced surface related non-radiative quenching rate of the $^4I_{11/2}$ Er level compared to the $^2F_{5/2}$ Yb level due to a smaller energy gap to the respective subjacent energy level[1] [116]. Thereby, the enhanced non-radiative pathway of the $^4I_{11/2}$ Er level leads to an enhanced quenching rate of the interacting $^2F_{5/2}$ Yb level, resulting in shorter decays.

In contrast to the 20/02 sample, whose crystal contains about 78% Y^{3+} ions, for the 80/20 sample all Y^{3+} ions are replaced by absorbing Yb^{3+}/Er^{3+} ions, resulting in enhanced transfer rates between Yb-Er and Er-Er ions due to reduced ion-ion distances. Especially in the centre of the NP, at which surface related quenching is reduced, the undisturbed Yb^{3+} ion emissions [140] and the appearing of multiple Er-Er transfers between the long-lived $^4I_{11/2}$ Er levels of different ions might explain the extended τ_2 component of the 1000 nm decay curve in Fig. 5.1 a). Additionally, the increase of the τ_2 component might arise from possible Yb-cluster formations at high Yb doping concentrations, resulting in a reduction of the energy migration to quenching centres due to enhanced intra cluster energy migration as described in [141].

The 1000 nm decay curve of the 100% Er^{3+} doped sample (blue) revealed a much faster decay of the $^4I_{11/2}$ Er level with shorter τ_1 and τ_2 components compared to the 20/02 Yb/Er sample. This is mainly caused by an increased concentration quenching, enhanced CR2 Er-Er-ET processes and the lack of Yb involved interactions (Yb-Er ET and BET), which are only present for the 20/02 and 80/20 Yb/Er samples.

---

[1] $\Delta E_{Er}(^4I_{11/2} - {}^4I_{13/2}) < \Delta E_{Yb}(^2F_{5/2} - {}^2F_{7/2})$

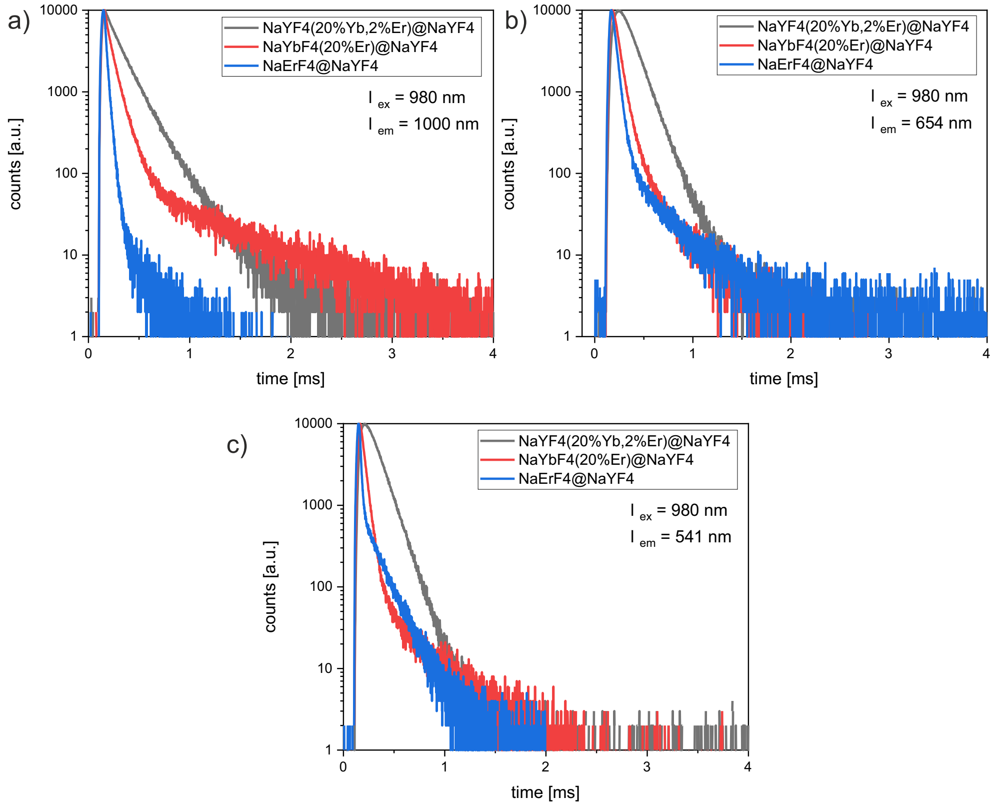

Figure 5.1. Decay behaviour of the 20/02 Yb/Er (NaYF$_4$(20% Yb, 2% Er)@NaYF$_4$), 80/20 Yb/Er (NaYbF$_4$ (20% Er)@NaYF$_4$) and 100% Er (NaErF$_4$@NaYF$_4$) doped particles under 980 nm excitation: a) 1000 nm emission with radiative contributions from $^2F_{5/2}$ Yb and $^4I_{11/2}$ Er levels. b) 654 nm emission from $^4F_{9/2}$ Er level. c) 541 nm emission from the $^4S_{3/2}$ Er level.

The decay kinetics of the green and red Er^{3+} emissions under 980 nm excitation (Fig. 5.1 b) and c)) are strongly influenced of the preceding and underlying Yb sensitizing (Fig. 5.1 a)) and the previously discussed concentration quenching processes for all 3 particle systems. The missing rise behaviour of green and red emissive levels of both 80/20 Yb/Er and 100% Er particles compared to the 20/02 system can be explained by increased direct excitation and more efficient ET processes at higher Yb and Er ion concentrations [142]. The 80/20 Yb/Er and 100% Er samples show nearly similar decays of the red emissive level, even if different processes are mainly responsible for the population of the $^4F_{9/2}$ Er level for both NP systems. The red emissive level of the Yb/Er particles are mainly populated by enhanced BET processes, whereas, for the Er-only doped particles the Er-Er CR2 ($^4F_{7/2} \rightarrow {}^4F_{9/2}$ and $^4I_{11/2} \rightarrow {}^4F_{9/2}$) [143] and direct excitation processes are relevant. The green decay is more affected by the concentration quenching effects than the red emission and is therefore faster, especially for higher Er content [31].

P-dependent changes in ensemble: QYs and band ratios

In Figure 5.2 a) the spectra under 980 nm excitation are plotted for low (6 W/cm^2) and high (400 W/cm^2) P for the different samples. At 6 W/cm^2 the 80% Yb^{3+} / 20% Er^{3+} (80/20, red) sample outperforms significantly the commonly used 20% Yb^{3+} / 2% Er^{3+} (20/02, black), especially with higher intensities of the red (630-670 nm) and the NIR (790-860 nm) emission bands. This is also affirmed in Fig. 5.2 b) by the minimal higher QY value of about 0.043% for the 80/20 sample compared to the 20/02 sample at 6 W/cm^2. The higher light absorption of the 80/20 sample with about 14.9% compared to the 3.7% absorption of 20/02 sample leads to brighter UCL even if the 80/20 sample shows lower QYs for $P > 10$ W/cm^2. The QY value of the 100% Er sample is about 27-fold lower than that of the 20/02 sample at 90 W/cm^2, even if the overall NIR light absorption by Er ions with about 5.4% is higher compared to the absorption of 20/02 Yb/Er sample with about 3.7%. As the NP concentration of all three samples equals about $3.5 \cdot 10^{15}$ particles per mL, higher absorption values represent higher NP absorption cross-sections. In consequence, the combination of higher NP absorption cross-section and simultaneously lower QY values of the 100% Er sample compared to the 20/02 sample reveals the inefficient UC performance of fully Er doped NPs due to strong energy loss via Er-Er CR processes [32].

As mentioned before, the volume of the Er-only core is much smaller and reaches only between 24% to 53% of the other Yb/Er doped core volumes. Hypothetically, a larger Er-only sample with the size of the Yb/Er sample would have a 2- to 4- times higher NP cross-section and brightness, which would still not be sufficient to reach the signal intensities of the Yb/Er samples at P = 400 W/cm^2, cf. bottom panel of Fig. 5.2 a). In consequence, even if we can not directly compare the QYs of the Er-doped and Yb/Er-doped samples, the results show at least the minimum limit of the QY values of the Er-only sample.

In Figure 5.2 c) the relative band emissions are plotted as a function of P from 5 to 460 W/cm^2. The 20/02 Yb/Er sample (left panel) shows dominating green (541 nm) contribution from the $^4S_{3/2}$ Er level for the whole P-range, which is typical for shelled particles with that doping ratio and a core-size smaller than 10 nm [144]. The relative intensity of the 808 nm emission from the $^4I_{9/2}$ level can be taken as an indicator for enhanced Er-Er interactions, like Er-Er CR1 ($^4S_{3/2} \rightarrow {}^4I_{13/2}$ and $^4I_{15/2} \rightarrow {}^4I_{9/2}$) and the Er-Er ET1 ($^4I_{13/2} \rightarrow {}^4I_{9/2}$ and $^4I_{13/2} \rightarrow {}^4I_{15/2}$] [145], cf. Fig. 2.4 c). These Er-Er interactions enhance the population of the $^4I_{9/2}$ level. Furthermore, the ET1 Er-Er process leads to a depopulation of the $^4I_{13/2}$ level, which is a competing process to the ESA from the $^4I_{13/2}$ to the $^4F_{9/2}$ level and reduces indirectly the red $^4F_{9/2}$ emission intensity. These competitive processes are clearly obtained for both samples, the 80/20 Yb/Er and the Er-only (middle and right panel in Fig. 2.4 c)), showing a dominant 808 nm band for low P, which indicates a strong presence of ET1 and CR1 processes. For increasing P, a decease of the 808 nm band by a simultaneous increase of the red band is obtained for both samples, reflecting a more efficient population and enhanced UC activity. In contrast to the Er-only sample, the strong increase of the 654 nm emission of the 80/20 Yb/Er sample with increasing P can be additionally attributed to a higher NP cross-section, more efficient population and to enhanced Er-Yb BET processes, which directly populates the $^4F_{9/2}$ from the higher lying $^4G_{11/2}$ level.

In conclusion, Figure 5.2 c) gives a good overview of the P-dependent optical emission ratios of small UC particles, first the behaviour of the commonly used 20/02 Yb/Er sample

[103], second the competitive processes of Er-Er interactions and efficient Yb-excitation and third the Yb-free Er-excitation with Er-Er interactions.

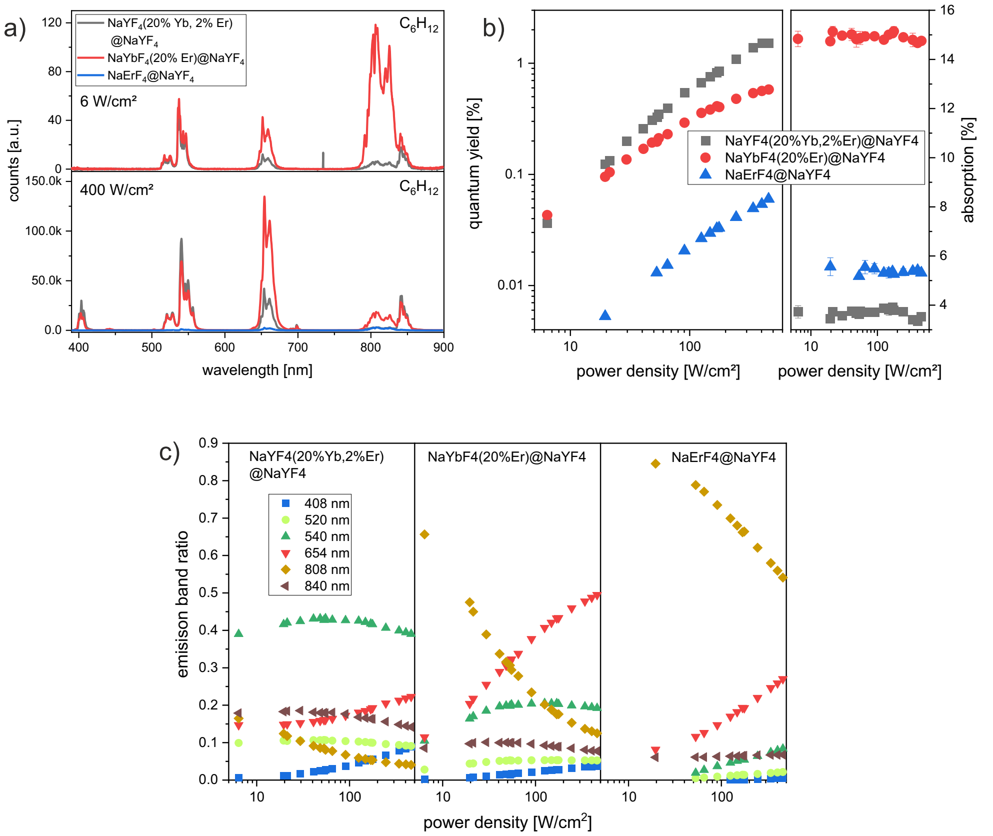

Figure 5.2. P-dependent optical results taken from integrating sphere measurements of the 3 samples dispersed in cyclohexane with varied Yb/Er ratios of 20/02, 80/20 and 0/100, measured in the P range from 5 to 460 W/cm^2: a) Spectra comparison at 6 W/cm^2 (top) and 400 W/cm^2 (bottom). b) QY values (left) and corresponding absorption values (right). c) Relative band ratio of the 408, 520, 540, 654, 808 and 840 nm emissions.

P-dependent changes of sub-10 nm NPs at SP level

The spectra taken from SPs are plotted in Fig. 5.3 at different P values in the range from 190 kW/cm^2 to 2.6 MW/cm^2. In contrast to the 20/02 Yb/Er sample with increasing multi-band emissions over the whole spectral range (Fig. 5.3 a)), including the UV range, the 80/20 Yb/Er and Er-only samples show increasing UCL intensities mainly restricted to the red and green spectral ranges. The poor presence of the 400 nm peak emission ($^2P_{3/2} \rightarrow {}^4I_{13/2}$) for both higher doped particle systems (Fig. 5.3 b,c)), reveals even for very high P values only a small proportion of 4 photonic absorption processes, which would be needed to populate the $^2P_{3/2}$ Er level. In addition, even 3 photonic processes are limited for the higher Ln^{3+} doped samples compared to the 20/02 Yb/Er system, stated by the relatively poor 556 nm peak emission following 3 photon absorptions. This indicates, that even the high Ps (MW/cm^2) can not compensate the concentration related quenching effects. Fur-

thermore, a saturation of the lower Er^{3+} energy levels is not reached, which would lead to favoured population of the higher Er energy states and to strong multitude emission bands, as described in the previous chapter 4.3. Changing the Yb/Er from 20/02 to 80/20 decreases the Yb:Er ratio from 10:1 to 4:1 and therefore, less Yb^{3+} per Er^{3+} ions are available in case of the 80/20 Yb/Er sample. This decreased Yb:Er ratio explains the reduced high energetic population via 3 or 4 photon absorption processes. Consequently, for the Yb-free Er-only sample the opportunity for efficient population of high energetic Er levels is even lower.
In Figure 5.3 d) the comparison of the 3 NP spectra at low (190 kW/cm^2), medium (1.6 MW/cm^2) and high (2.6 MW/cm^2) SP *P*s are illustrated. The 80/20 Yb/Er sample (red) clearly reaches the highest intensity with a massive red emission and shows similar intensities of the green band as the Er-only doped sample (blue). Since the core volume of the Er-only doped sample is only between 24% to 53% of the Yb/Er doped core volume, it can be expected, that same sized Er-only doped core would top the 80/20 sample in the green range in intensity.

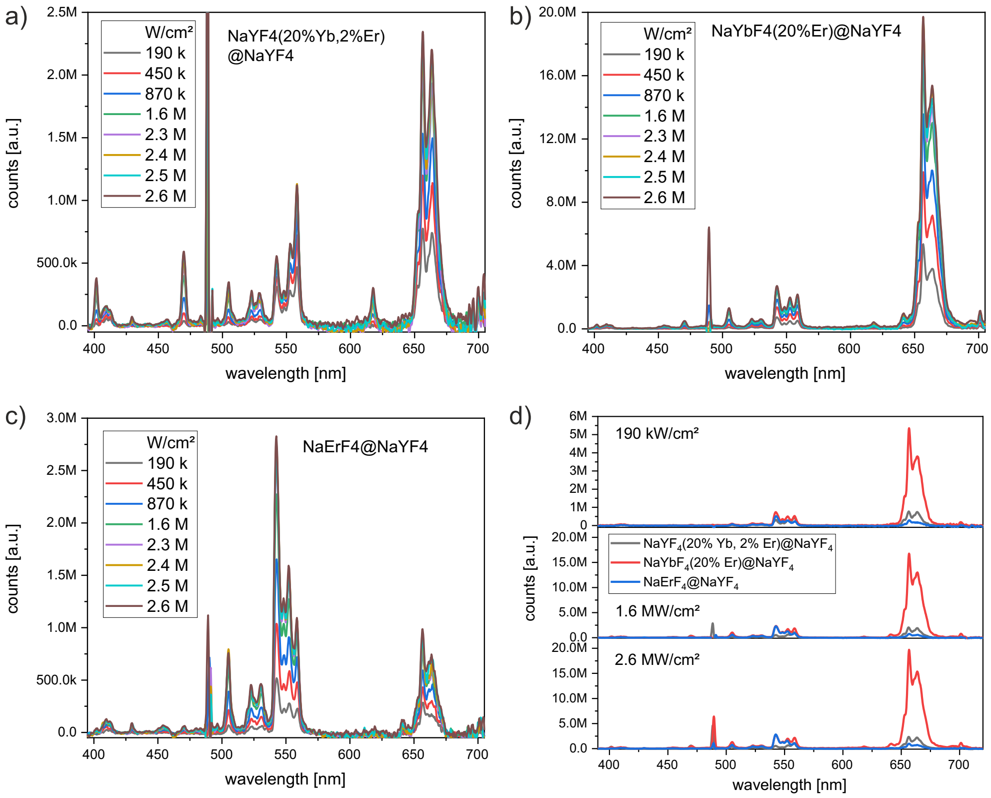

Figure 5.3. *P*-dependent SP studies of the 3 samples with varied Yb/Er ratios: a)-c) Spectra of the 20/02, 80/20 and 0/100 Yb/Er doped samples at different *P* values in the range from 190 kW/cm^2 to 2.6 MW/cm^2. d) Direct comparison of the spectra at 3 different *P*s (190 kW/cm^2, 1.6 MW/cm^2 and 2.6 MW/cm^2).

The *P*-dependent band emission trends at SP level in Figure 5.4 a) and b) reveal for the most intense peaks an increase in intensity over the whole *P* range (190 kW/cm^2 to 2.6 MW/cm^2) for all 3 samples. The strong increase of the 654 nm peak signal of the 80/20 Yb/Er sample is related to a continuing strong presence of BET processes without any indication for saturation of the excited $^2F_{5/2}$ Yb level. The strong increase of the 503 nm peak intensity of the 80/20 Yb/Er and Er-only doped samples in Fig. 5.4 b) indicates a continuous increase of 3 photonic absorption processes with higher *P*.

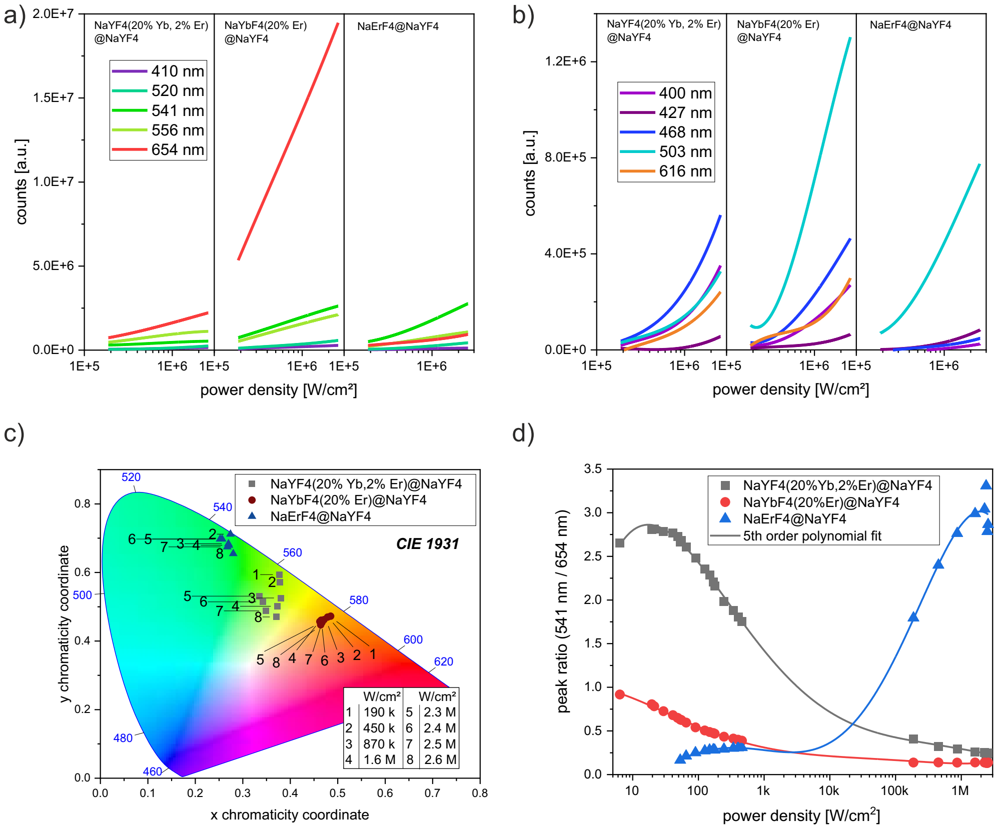

Figure 5.4. SP results of the 20/02, 80/20 and 0/100 Yb/Er doped samples in the range from 190 kW/cm^2 to 2.6 MW/cm^2: a) and b) *P*-dependent band emission trends of 410, 520, 541, 556 and 654 nm (a) and 400, 427, 468, 503, 616 nm (b) peak signals plotted with 4th order polynomial fits over mono-logarithmic *P* scale. c) CIE diagram for illustration of *P*-dependent overall emission colour. d) Green to red (G/R) peak ratios of the ensemble and SP studies combined by using 5th order polynomial fits.

The different impact of Yb^{3+} and Er^{3+} ion doping on the total emission colour is presented in the CIE diagram in Figure 5.4 c), covering clearly separated the yellow, the orange and the green colour space by the 20/02, 80/20 Yb/Er and Er-only samples, respectively. A notable *P*-dependent colour change is only present for 20/02 Yb/Er sample with an enhanced blue colour content for increasing *P*.

Combining the ensemble and SP studies by plotting the green to red (G/R: 541 nm / 654 nm) peak ratio *P*-dependently from 5 W/cm^2 to 2.6 MW/cm^2 in Figure 5.4 d) illustrates the strong differences of Ln^{3+} doping variation at different *P* regimes. Nearly opposite G/R ratios were measured for the 20/02 Yb/Er and Er-only samples. A polynomial fit of 5th order was used to bridge the large gap between ensemble and SP data, illustrating a suggested possible peak ratio behaviour.

Comparing sub-10 nm SPs to μm-sized UCNCs at ensemble and SP level

By comparing the P-dependent emission spectra of bulk-like / μm-sized UCNC flakes with 18/02 Yb/Er (from K. Kramer) and 0/02 Yb/Er (from Th. Jüstl) ratios, the impact of Yb^{3+} ions on the presence of specific Er^{3+} ion emission bands and direct Er excitation effects can be studied with higher signal-to-noise ratios and negligible surface quenching effects. The P-dependent spectra of the 18/02 (Yb/Er-NC) and 0/02 (Er-NC) Yb/Er μm-sized NCs are plotted for the P-range from 1 kW/cm^2 up to 2.6 MW/cm^2 in appendix Figs. A.8 a), b) and illustrate the strong impact of Yb on the red emission via Er-Yb BET processes. The relative changes of normalized spectra, the P-dependent G/R emission ratios and the CIE diagram are plotted in appendix Figs. A.8 c)-e). The P-dependent emission band intensity trends are described in appendix Fig. A.9.

In Fig. 5.5 the powdered bulk-like 18/02 Yb/Er UCNCs from Kramer are compared to the sub-10 nm sized 20/02 Yb/Er sample from the Hirsch group first, under ensemble condition (dispersed in cyclohexane) at 50 W/cm^2 and second, under SP condition at 2.6 MW/cm^2 dried on glass. The slight variation in Yb^{3+} ion concentration of 2% can be neglected. The emission spectra normalized to the 541 nm peak emission reveals at ensemble level large differences of the emission band ratios ascribed to the different surface condition and the enormous volume difference. Contrary, the normalized spectra measured at the CLSM (Fig. 5.5 b)) showed only few differences of the emission band intensities at 2.6 MW/cm^2, a P value at which surface quenching influences are expected to be strongly minimised, as shown in chapter 4.5. The small spectral differences of the nm-NPs and the μm-NCs do not strongly affect the overall emission colour of both systems, comparing CIE diagrams in Figs. 5.4 c) and A.8 e). This indicates that besides reduced quenching even the number of emitters per NP and the NP volume impact become nearly negligible at high P studies.

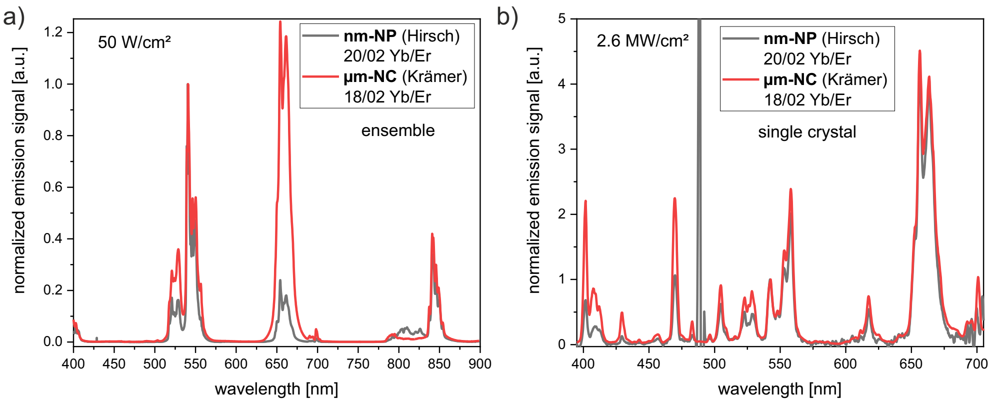

Figure 5.5. Comparison of emission spectra normalized at 541 nm emission of 20/02 nm-sized core-shell NPs from the Hirsch group (Regensburg) and powdered μm-sized 18/02 Yb/Er UCNCs from K. Kramer (Bern) at ensemble and SP level: a) Ensemble measurements taken at 50 W/cm^2 of the nm-sized particles dispersed in cyclohexane and the powdered UCNCs. b) SP condition on dried nm-sized NPs and μm-sized powdered UCNCs taken at 2.6 MW/cm^2.

5.2. Sub-30 nm UCNPs: SP studies

In this section only the results of the SP studies will be discussed, since the ensemble measurements were performed by my colleague Bettina Grauel and the results discussed in her PhD thesis [146].

Preparation, chemical analysis and experimental

The second set of core-shell samples was synthesized by the Haase group (University of Osnabrück) following a special developed, water-free synthesis approach, leading to optimised UCNPs with enhanced QYs as published 2018 in cooperation with our group [37]. The sample cores consist of a $NaYF_4$ host crystal co-doped with Yb^{3+} and Er^{3+} ions in such ratios resulting in a Yb and a Er series. The Yb series has a fixed 2% Er^{3+} ion concentration and varies in Yb^{3+} ion concentration from 20, 40, 60 and 98%, whereas the Er series has a fixed 60% Yb^{3+} ion concentration and varies in Er^{3+} ion concentration from 2, 10, 20 and 40%, as described in Fig. 5.6 a). The 60/02 Yb/Er sample is part of both series. All samples have a thick protective inert $NaYF_4$ shell around the core with different amounts of co-doped Lu^{3+} ions to compensate lattice mismatch at the core-shell interface due to similar ionic radii of about 0.98 $\mathring{A}$ and 0.97 $\mathring{A}$ of Yb^{3+} and Lu^{3+} ions, respectively [147]. The Lu^{3+} ratio is equal to the sum of Yb^{3+} and Er^{3+} ion content inside the respective core. Table 5.2 summarises the core and shell doped Ln^{3+} concentrations and the diameters of the core and the core-shell NPs based on TEM measurements run by Hennig Eickmeier (University of Osnabrück). The particle size determinations were performed by Monica Pons (Master student at BAM, HU Berlin) using the software JImage.

Since the 60/10 Yb/Er sample is much larger in diameter, leading to about 3 times higher NP Volume compared to the other samples of Er series (with averaged diameter of about 18.2 nm), making a direct comparison of absolute signal values difficult.

label	Yb/Er core, Lu in shell [%]	core diameter [nm]	core-shell diameter [nm]
KR519	20/02, 22	21.0 ± 1.2	39.8 ± 4.4
KR522	40/02, 42	19.9 ± 0.8	43.0 ± 3.6
KR500	60/02, 62	18.8 ± 0.8	38.4 ± 2.1
KR505	98/02, 100	18.5 ± 2.2	41.5 ± 3.4
KR527	60/10, 70	25.9 ± 1.0	49.6 ± 2.7
KR530	60/20, 80	18.5 ± 0.9	38.8 ± 1.7
KR533	60/40, 100	17.4 ± 0.8	37.6 ± 1.4

Table 5.2. Overview of core and core-shell diameters based on TEM data analysis of the 7 samples synthesized by the Haase group (Osnabrück). NP size determinations were performed by Monica Pons. Modified from [146].

All SP measurements were conducted on the CLSM (cf. section 3.3.1) by myself. For the decay studies at 980 nm a repetition rate of 80 MHz, a sequence period of 127 Hz and a averaged P of 29 kW/cm^2 was selected. The SP spectra have been taken at varied P values between 2.9 kW/cm^2 and 2.6 MW/cm^2.

Decay behaviour at SP level

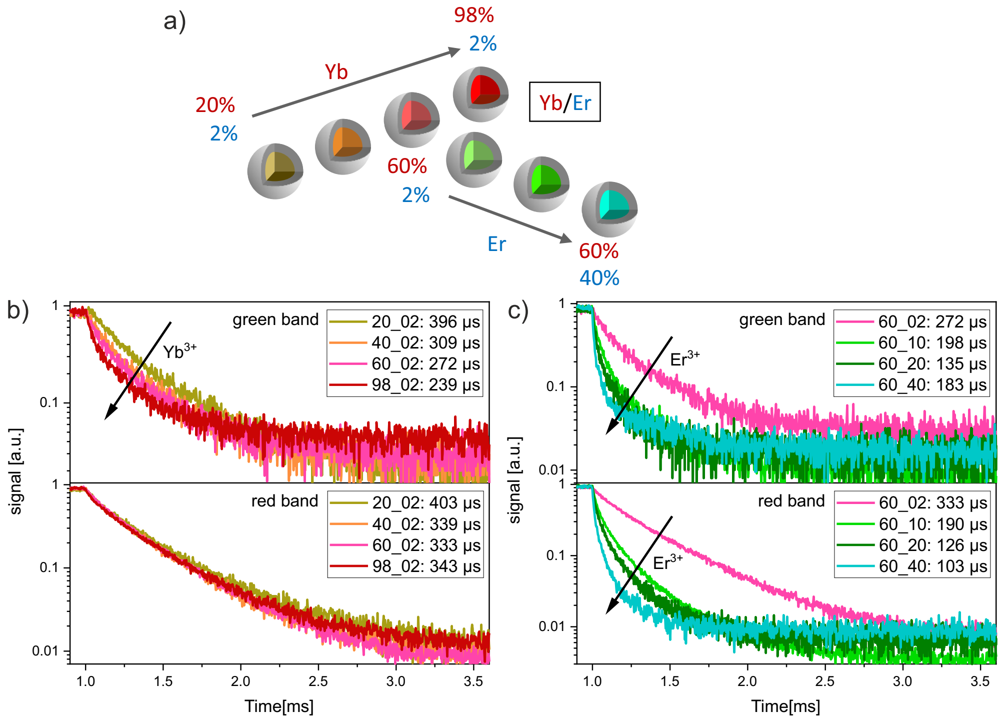

Figure 5.6. Yb^{3+} and Er^{3+} series of sub-30 nm NPs: a) Overview of the NP systems varied in Yb/Er ratio. b) and c) Decay curves of the green (545 ± 12.5 nm, upper panel) and red (655 ± 20 nm, bottom panel) band emissions of the Yb series (b) and of the Er series (c). The bi-exponential fitted intensity weighted LTs are listed for all decays averaged from 2 single measurements.

Yb series The decay curves of the Yb series under 980 nm excitation are plotted in Fig. 5.6 b) for the green (545 ± 12.5 nm) and red (655 ± 20 nm) band emissions representing the total Yb-Er ETU and ESA processes and not intrinsic decay rates of the green or red Er levels. The corresponding decay measurements on ensemble level[1] did not show significant changes of the green and red decays under NIR-excitation in cyclohexane mainly caused by the Yb-concentration independent behaviour of the Yb^{3+} decay rate due to the high shell-quality and reduced surface quenching [146].

For SP studies the surface-related quenching influences can be expected to be reduced, which was discussed in section 4.5. Therefore, an Yb content independent behaviour of the green and red Er^{3+} decay kinetics - scaled and dominated by the Yb decay rate - can also be expected for the SP studies. This is the case for the red emission (cf. Fig. 5.6 b), bottom panel). The relatively small change of the red band decays indicates two things, first a low

---

[1] The ensemble measurements were performed by my colleague Bettina Grauel and discussed in her PhD thesis [146]

impact of concentration quenching effects via energy migration to lattice or surface defects, which demonstrates the high quality of the thick and Lu^{3+} ion co-doped protective shells. Secondly, a very pronounced BET process from the Er $^4G/^2K$ manifolds to Yb^{3+} ($^2F_{7/2} \rightarrow {}^2F_{5/2}$), which is mainly responsible at SP condition with high P for the red emissive $^4F_{9/2}$ level population and already pronounced for the sample with only 20% Yb content.

Unexpectedly, the green band LTs are shortened from 395 μs to 239 μs with a variation from 20 to 98% Yb $^{3+}$ ions, which is a direct contradiction to the intrinsic green decay trends under direct UV-excitation in ensemble condition [146].

The decrease of the green LTs with higher Yb content can not be explained by enhanced energy migration quenching or by the Yb-Er ET, which would also affect the red emission. Therefore, an other quenching or ET process regarding the green emission band scaling with Yb content might be revealed. A new "green BET" from Er to Yb might explain the Yb content dependent depopulation of the $^4S_{3/2}$ Er level including a simultaneous population of $^4I_{13/2}$ Er level and an excitation of Yb ($^2F_{7/2} \rightarrow {}^2F_{5/2}$). This "green BET" was previously suggested by Wang et al. [141] for a $NaYbF_4$:2% Er sample and is illustrated in a Dieke diagram in appendix Fig. A.10. The probability for the green BET despite the energy mismatch of about $0.7{\cdot}10^3 cm^{-1}$ of the involved intra-transitions in Yb ($11.2{\cdot}10^3 cm^{-1}$) and Er ($11.9{\cdot}10^3 cm^{-1}$), seems to increase with higher Yb concentration due to minimal Yb-Er ion distances in $NaYF_4$ crystal. The green BET could be verified by measuring for higher Yb concentrations an increase in the radiative depopulation of the $^4I_{13/2}$ level at 1540 nm, which is not technically feasible with our CLSM up to now.

Furthermore, a temperature increase and stronger phonon activity due to higher absorption cross-sections for higher Yb content could contribute as well to faster decays of the green band, whose non-radiative depopulation rate ($^4S_{3/2} \rightarrow {}^4F_{9/2}$) is more sensitive to phonons as it is for the red band.

As already discussed in chapter 4.4, the additional contribution of 556 nm emission band from the energetic higher lying $^2H_{9/2}$ Er level ($\rightarrow {}^4I_{13/2}$) with fast intrinsic decay rates (about 19.5 μs) could lead to faster measured LTs of the green band, cf. appendix Fig. A.6 a). Looking at the 556 to 541 nm peak ratio in Figure A.13 a), reveals a decreasing contribution of the 556 nm emission with higher Yb concentration and therefore a decreasing contribution of the faster intrinsic decay rate of the $^2H_{9/2}$ Er level for the decay measurements. Consequently, the decreasing trend of the green band LTs with higher Yb content could be underestimated and might be even more pronounced for the $^4S_{3/2}$ Er level.

Er series The decay curves of both, the green and the red emission bands show faster rates and shorter LTs with increase of Er^{3+} content in Figure 5.6 c) and include the Yb-decay rate, the Yb-Er ETs and ESA processes of Er. From the fact that the decays of both bands show similar trends with higher Er^{3+} content, and that the NIR-excitation includes the Yb-decay rate, Yb-Er ETs and ESA processes of Er, follows, that the Yb decay rates[1] are

---

[1] The measurement of the Yb decay ($^2F_{5/2} \rightarrow {}^2F_{5/2}$) includes also the Er emission ($^4I_{11/2} \rightarrow {}^4I_{15/2}$)

overshadowing and dominating in both plots. This is in accordance with the corresponding ensemble measurements of the Yb^{3+} emission, obtaining the same decreasing LT trend for higher Er content [146]. The increase in Er^{3+} content leads to shorter Yb-Er ion distances, which enhances the ET transfer rates from Yb to Er ions. In addition, with higher Er doping, the ratio of direct NIR-excited Er^{3+} ions ($^4I_{15/2} \rightarrow {}^4I_{11/2}$) increases, which should accelerate the population of both, the green and red emissive Er levels.

As discussed previously, for the sub-10 nm NPs from the Hirsch group, the shortened green LTs of the Er series with higher Er^{3+} ion concentration can be additionally explained by enhanced presence of Er-Er CRs, like the CR1 involving the green Er level ($^4S_{3/2} \rightarrow {}^4I_{13/2}$ and $^4I_{15/2} \rightarrow {}^4I_{9/2}$) and the Er-Er CR2 ($^4F_{7/2} \rightarrow {}^4F_{9/2}$ and $^4I_{11/2} \rightarrow {}^4F_{9/2}$) [143] providing simultaneously an enhanced feeding path for the red emissive $^4F_{9/2}$ Er level with higher Er concentration, cf. Fig. 2.4.

P-dependent changes on sub-30 nm NPs: spectra, peak ratios and overall colour

Spectra and integrated intensities The spectra of the Yb and Er series are shown in Figure 5.7 a) at low, medium and high P (24 kW/cm^2, 200 kW/cm^2 and 2.5 MW/cm^2) and reveal the surpassing role of the red band emission and the low contributions from the remaining transitions. In the appendix in Figs. A.11 and A.12 the P-dependent spectra are plotted for each sample of the Yb and Er series, respectively.

The P-dependent integrated intensities I_{total}, which are proportional to the brightness of the NPs, are plotted in Fig. 5.7 b), left for the Yb and right for the Er series. For the Yb series the brightest sample is the 60/02 for $P < 2.4$ MW/cm^2 and is outperformed for higher P by the 98/02 Yb/Er sample, which does not reach saturation. The 20/02 Yb/Er sample reaches its maximal brightness at about 1 MW/cm^2, whereas I_{total} of the 40/02 and 60/02 Yb/Er samples increases in the P range from 100 - 300 kW/cm^2, followed by a decrease. The intensity drop can be associated with increased sample heating at high P, which is supported by the increasing 521 to 541 nm peak ratios of the Boltzmann coupled $^2H_{11/2}$ and $^4S_{3/2}$ Er levels with higher P, plotted in Fig. 5.7 d).

The increase in Er^{3+} content from 2% to 10%, roughly doubles the maximal achieved integrated intensity for $P > 100$ kW/cm^2 and tops the whole Yb series in that P range, cf. right panel in Fig. 5.7 b). The outstanding high brightness of the 60/10 Yb/Er sample needs to be examined critically due to the larger, about 3 times bigger NP volume compared to the rest of the Er series. A hypothetical volume correction of the 60/10 Yb/Er sample - dividing the emission signal by a factor of 3 - would lead to intensity values in the range of the other samples, higher as for the 60/02 but lower as for the 60/20 Yb/Er sample. In this case, the Er series would show higher brightness values for low Er content (2%) for $P < 100$ kW/cm^2 and for $P > 100$ kW/cm^2, dominating brightnesses for the 10% and 20% Er samples. The increasing intensities of the 60/10 and 60/20 Yb/Er samples with higher P reflect the compensation of Er concentration quenching by enhanced photon flux, resulting in more efficient UC performance.

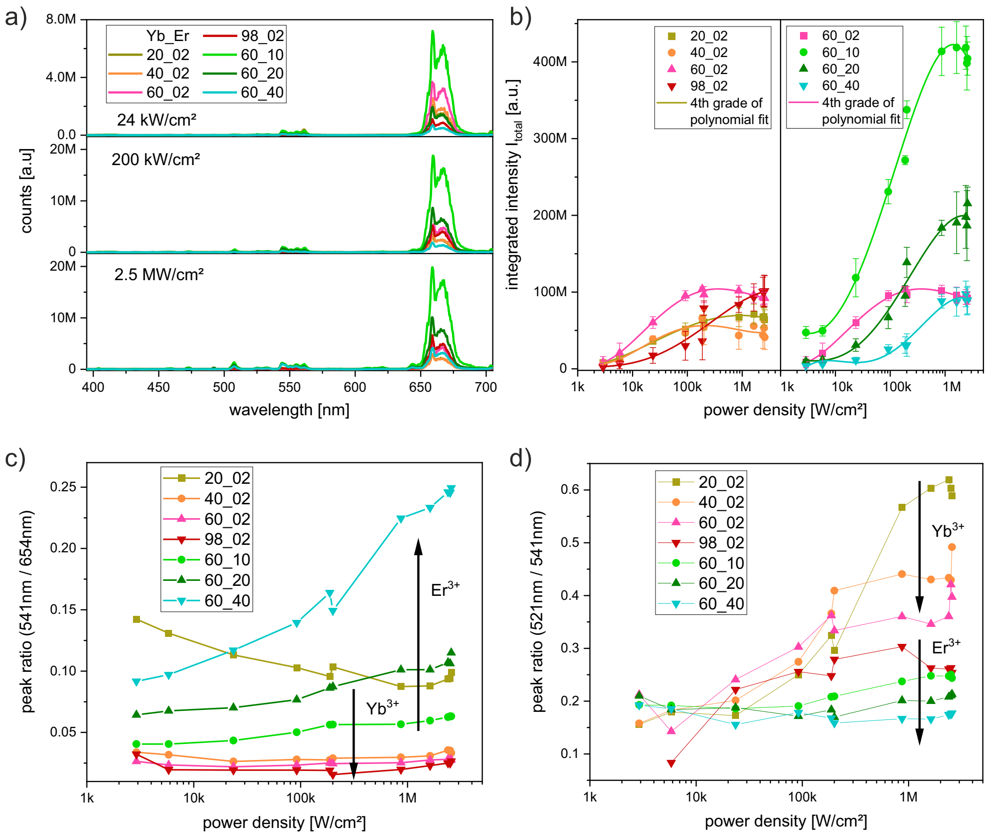

Figure 5.7. *P*-dependent UCL behaviour of the Yb and Er series: a) SP spectra of all samples averaged respectively from 2 or 3 single NP spectra, plotted for low (24 kW/cm^2), medium (200 kW/cm^2) and high (2.5 MW/cm^2) *P*. The *P*-dependent spectra of each sample are plotted in appendix in Figs. A.11 and A.12. b) Integrated intensities of the Yb (left) and Er series (right) plotted with 4th grade polynomial fits. Taken and modified from own publication [148]. c) Green-to-red (G/R) ratios of the 541 nm and 654 nm peaks emitting from the $^4S_{3/2}$ and $^4F_{9/2}$ Er levels. d) 521 nm to 541 nm (G/G) peak ratios of the Boltzmann coupled $^2H_{11/2}$ and $^4S_{3/2}$ Er levels.

Plotting I_{total}/P over P, provides an indicator for the P-dependent intensity growths per P unit and can be taken as QY-related value for SP studies. I_{total}/P decreases for samples of both series with increasing P and shows constant behaviour for $P > 1$ MW/cm^2, marking a saturation regime for the UC processes as it is plotted in appendix Fig. A.13 b).

The P-dependent band emission trends of both series are plotted in appendix Figs. A.14 and are not discussed here in more detail, since the other bands beside the red emission show relatively low contributions. Therefore, the above discussed I_{total} covers the P-dependent trend of the dominating red band sufficiently good.

Peak ratios and overall emission colour

The 541 to 654 nm peak (G/R) ratios in Figure 5.7 c) show for both series small values below 0.25, reflecting the intensive 654 nm emission. The decreasing trend of the G/R ratio of the 20/02 Yb/Er sample, followed by a flattening at $P > 1$ MW/cm^2 is in accordance to the results discussed in chapter 4.5 for the 20/01 and 20/03 Yb/Er samples from the Hirsch group.

With higher Yb concentrations, an enhanced red-level-feeding Yb-Er BET activity can explain the lower G/R ratios, which are nearly *P*-independent over the whole *P* range. With enhanced *P*, the Er series show higher G/R ratios with higher Er content due to enhanced direct Er-excitation processes and enhanced Yb-Er ET rates caused by the larger Er:Yb ion ratio. Particularly, the 60/40 Yb/Er sample with an Er:Yb ratio of 2:3 shows an increasing G/R trend with higher *P*, cf. Fig. 5.7 c).

The G/G ratio (521 nm / 541 nm) of the Boltzmann coupled $^2H_{11/2}$ and $^4S_{3/2}$ Er levels is plotted in Fig. 5.7 d) for the Yb and Er series. As previously mentioned, an increase of the G/G ratio with higher *P* reflects a temperature (T) increase of the sample caused by laser heating. For $P \geq 0.5$ MW/cm^2, this ratio decreases with higher Yb and higher Er ion concentration, which results in reduced sensitivity for T-sensing. Additionally, for the Er series with Er^{3+} concentrations ≥ 10%, the G/G ratios show a nearly constant behaviour over the whole *P* range. These results are contrary to expectations, as a higher Ln^{3+} ion doping enhances the absorption cross-sections of the NPs, which leads to higher energy uptake and therefore, T and the G/G peak-ratios should increase. In consequence, the G/G peak ratio cannot generally be taken as T-sensor for samples with high Ln^{3+} doping concentrations at high *P*. This should be taken into account, for the development of bright and sensitive T-sensors at high *P*.

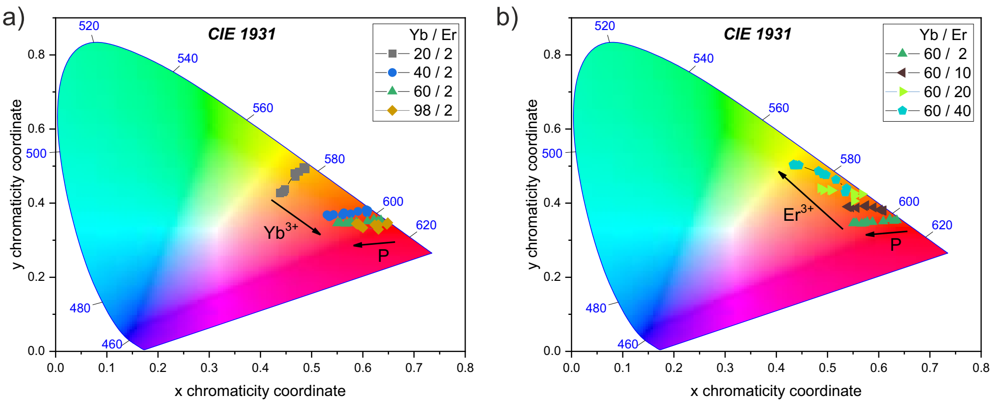

Figure 5.8. *P*-dependent total emission colours illustrated in CIE diagrams for the Yb series (a) and Er series (b).

The *P*-dependent total emission colours for both Ln^{3+} series are illustrated in the CIE diagrams in Fig. 5.8, covering only the orange and red colour ranges. With enhanced Yb^{3+} ion content the overall UCL shifts from orange to intensive red colour and show only slightly colour change with increasing *P*. For the Er series the total emission colour is shifted from red to yellow with both, higher Er concentration and with higher *P*.

5.3. Conclusion

This chapter illustrates the strong impact of high Ln^{3+} ion doping on the UCNP performance, regarding the level decay rates, the UCL band emission ratios, the total emission intensity and overall colour. The optical response of ensemble and SP measurements on high Ln^{3+} doped UCNPs varies largely, as indicated from the results of lower Yb/Er ratios in chapter 4.5. Particularly reflected by the opposite trends of the G/R emission band ratios, which decreases for high Yb and increases for high Er content with increasing P. The comparison of the sub-10 nm NPs with the larger μm-sized NCs revealed only few differences of the normalized spectral emission behaviour at high $P \geq$ MW/cm^2. That implies, that surface-related quenching effects of the small NPs with high surface-to-volume ratios have been partly compensated by effective shells and by intense photon fluxes at high P. Additionally, at high P, there was no significant impact detected of the sample size and of the number of Ln^{3+} per NP on the population behaviour of the Er^{3+} ions.

The total emission colour can be tuned using higher Er doping for a green and higher Yb doping for a red shift. The important role of Yb^{3+} ions for a strong red emission band can be explained by intense Er-Yb BET processes, which are mainly responsible for the population of red emissive $^4F_{9/2}$ Er level manifested by the low intense red band of Yb-free, pure Er-doped NPs and NCs. An increase in Er^{3+} concentration leads to poor UC efficiencies in ensemble condition caused by enhanced concentration quenching, which can be to some extent compensated in SP condition at high P. With Er^{3+} content also the amount of Er-Er interactions increases, like CR1, CR2 and ET1 processes. In addition, for higher Er content the ”green Yb-Er BET” [141] was found as explanation for decreased green and stable red LTs at SP condition and should be experimentally validated in forthcoming studies. With increasing Yb and Er doping concentration the population of higher Er energy levels are strongly reduced, resulting in low intensities of emission bands based on 3-4 and 4+ photon absorption processes.

The G/G peak ratios of the Boltzmann coupled $^2H_{11/2}$ and $^4S_{3/2}$ Er levels showed at high P an unexpected decrease with increase of Yb and Er concentrations, which revealed the limited usability of the G/G ratio for T-sensing at high P.

It was shown that for the different P regimes, different Yb/Er doping ratios should be used to guarantee strong brightnesses and efficient UCL with tunable colour. The brightest UCL was found for combined high Yb and Er concentrations with Yb:Er ratios of 6:1 and 3:1 (60/10 and 60/20 samples) with a dominatting red emission band. However, further fine-tuning of the ratios might lead to even higher UCL. The specially adapted optimisation of highly doped UCNPs enables the use of such particles for wide range of applications like in Biosensing as adjusted FRET-donor, in multiplexing, and in high-resolution microscopy like STED technique.

6 Yb vs. Nd excitation

In the last years, the benefits of using Nd^{3+} instead of Yb^{3+} as (pre-)sensitizer in UCNPs, which shifts the excitation wavelength from 980 nm (Yb-excitation) to about 808 nm (Nd-excitation) with lower absorption of water and reduced laser-induced overheating, have been studied on different Nd^{3+} co-doped UCNPs varying in structure, design and host matrix. Nevertheless, a systematic study of the performance and UC efficiencies of comparable Nd-doped and Nd-free NPs based on UC QY measurements at different excitation wavelengths were missing and the following questions unanswered so far: Is there any impact of Nd ions on the Yb → Er energy transfer under the direct Yb-excitation? What is the impact of the solvent on the UCL involving Nd ions? Does the higher absorption coefficient of Nd (compared to Yb) automatically lead to higher UCL via Nd-excitation? Under which conditions Nd- or Yb-excitation is favourable and what does that mean for optimised NP architecture? How efficient are the Nd-doped NPs compared to commonly Yb/Er doped NPs of the same size? How does Nd/Yb/Er triple-doped NPs behave at higher excitation P on SP level?

This motivated us to study the influence of Nd^{3+} as substitute and pre-sensitizer in commonly employed Yb/Er sensitizer/activator systems for potentially enhanced UC efficiencies in different environments on ensemble and SP level. In ensemble condition, the P-dependent QYs and the calculated particle brightness (B_{UC}) were used as measure for the UCNP efficiency and for derivation the condition under which Nd- tops Yb-excitation. At the end of the chapter, SP studies show the influence of high power Nd-/Yb-excitation on the UC performance.

Most of the ensemble measurements in this chapter have been already published 2019 in Nanoscale [51] under my own shared first authorship. All QY measurements, calculations of absorption cross-sections, brightness values and theoretical optimisation parameters were done by my own. The time-resolved measurements have been performed by my colleague Bettina Grauel.

6.1. Set of samples, preparation and chemical analysis

The set of particles has been synthesized by the Hirsch group (University of Regensburg, Germany) consisting of 4 different core-shell-shell (css) NP systems with hexagonal $NaYF_4$ crystal (cf. Fig. 6.1), all with a total diameter of about 35 nm, a 25 nm thick 20% Yb / 2% Er co-doped core (green) and an external inert shell (*is*) of about 2 nm (*is*2). The systems differ in the doping combination and concentration of the 4 nm thick $NaYF_4$ shell covering the core, as illustrated in Fig. 6.1: (1) active shell co-doped with 10% Yb / 10% Nd: $(Yb@Yb,Nd)^{is}$, (2) co-doped with 10% Yb: $(Yb@Yb)^{is}$, (3) active shell containing the Yb/Er core material: $(Yb)^{is2}$ and (4) consisting of inert $NaYF_4$ crystal: $(Yb)^{is5}$.

As a basis for this study, our cooperation partners have tested in the first place different Yb/Nd doping ratios of the active shell with 5, 10 and 15% content of both sensitizer ions and found the highest UC intensities for the doping ratios of 10% Yb and 10% Nd, which were then used.

The synthesis, the surface coating, the ligand exchange from organic to aqueous phase (from oleate to PAA ligands) and the chemical analyses (DLS, XRD, ICP-OES and TEM) of the NPs have been performed by the Hirsch group and are precisely reported in our publication and the related SI [51].

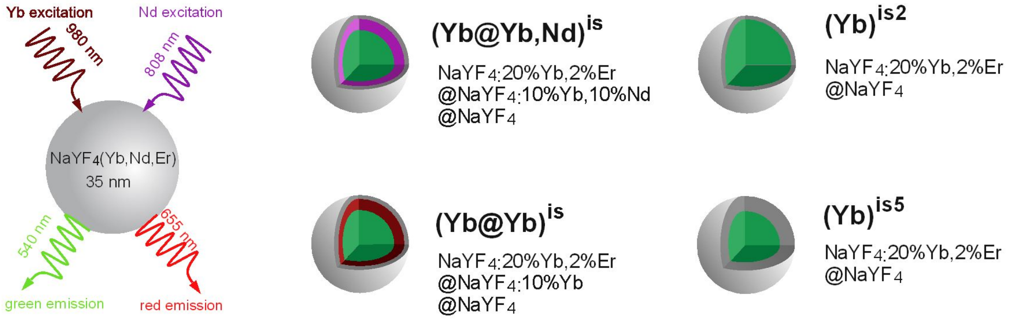

Figure 6.1. Overview of the sample systems and sketch with acronyms of the four 35 nm thick core-shell-shell $NaYF_4$ NPs with same Yb/Er cores (25 nm) and protecting inert shell (is) of 2 nm ($is2$), but different types of intermediate shell (4 nm): with Yb/Nd $(Yb@Yb,Nd)^{is}$, with Yb $(Yb@Yb)^{is}$, with core material $(Yb)^{is2}$ and with inert shell material $(Yb)^{is5}$. Taken and modified from own publication [51].

6.2. Ensemble studies

In ensemble condition, steady state and time-resolved optical behaviour of Nd/Yb/Er-doped UCNPs in water, cyclohexane and lipid phantom tissue are compared to appropriate Nd-free Yb/Er UCNPs under 980 nm and 808 nm excitation. Furthermore, the Nd^{3+} and Yb^{3+}-absorption cross-sections are determined for a clear assumption about the UC efficiency.

Influence of Nd on Yb-excitation in Cyclohexane and Water

By comparing the UC emission spectra at normalized NP concentration, the relative band emissions, the QYs, and decay kinetics of both NP systems, $(Yb@Yb,Nd)^{is}$ and $(Yb@Yb)^{is}$ under 980 nm (Yb-excitation), the impact of Nd with its energy level scheme on the Yb-Er UC process is tested, as shown in Fig. 6.2. In cyclohexane the Nd-doped NPs show reduced emission intensities compared to their Nd-free counterparts, whereas in water only minimal differences of the UC spectra taken at about 20 W/cm^2 are present, cf. Fig. 6.2 a).

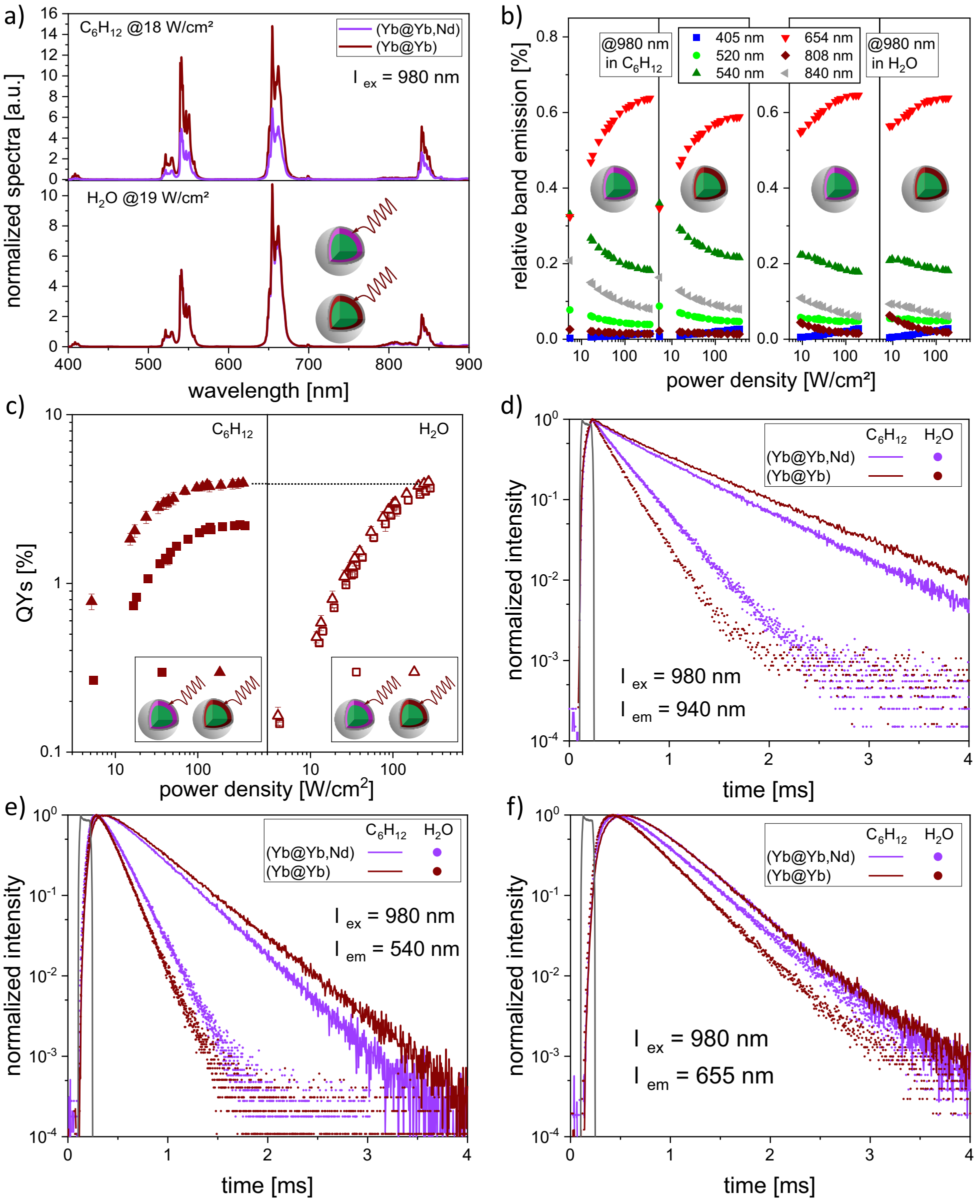

Figure 6.2. Steady state and time-resolved optical behaviour of (Yb@Yb,Nd)^{is} and (Yb@Yb)^{is} NP systems in cyclohexane (C_6H_{12}) and in water under Yb-excitation: a) Emission spectra of both NP systems at low *P* of about 18-19 W/cm^2 in C_6H_{12} (top) and in water (bottom). b) *P*-dependent relative band emission at 405, 520, 540, 654, 808 and 840 nm in C_6H_{12} (left) and water (right). c) *P*-dependent quantum yields, left in C_6H_{12} and right in water. d), e) and f) Decay curves of the 940 nm, 540 nm and 655 nm emission of both NP systems in both solvents. Taken and modified from own publication [51].

The relative band ratios in Fig. 6.2 b) reveal a slightly higher green (520 and 540 nm) and lower red ratios of the Nd-free NPs compared to the Nd containing NPs dissolved in cyclohexane. Whereas, in water both NP systems show similar band ratios. It seems that the presence of Nd^{3+} ions in the active shell in combination with the solvent cyclohexane affects negatively the Yb-Er energy transfer and its efficiency. This is clearly confirmed by lower QY values of the $(Yb@Yb,Nd)^{is}$ NPs, which show same P-dependent trend but with a reduction of about 66% at 5 W/cm^2 and about 43% at 190 W/cm^2 compared to the $(Yb@Yb)^{is}$ NPs in case of cyclohexane, as shown in Fig. 6.2 c)). In water the Nd-doped NPs show nearly same QYs with about 8% lower values compared to Nd-free NPs and reach nearly same QYs as $(Yb@Yb)^{is}$ in cyclohexane at about 300 W/cm^2.

The decay kinetic studies of the direct Yb emission (940 nm), the green (540 nm) and red (655 nm) Er bands under 980 nm reveal changes in the decay behaviour caused by the Nd ions. Whereas, for the different solvents different trends of the decay kinetics are present, as shown in Fig. 6.2 d)-f). In cyclohexane the decays of the $(Yb@Yb,Nd)^{is}$ (purple coloured) are shortened, slightly for the red (655 nm) Er emission and significantly for the green (540 nm) Er emission, but also the direct populated Yb level (940 nm emission) is affected by the presence of Nd. As the Yb-excitation is the first step of the Yb → Er ET, the faster decay of the excited Yb level directly affects further the measured green and red decays.

In water an opposite trend appears for all three emission bands, showing longer decays of the $(Yb@Yb,Nd)^{is}$ system (brown) compared to the Nd-free sample (purple). To explain this opposite impact of Nd^{3+} ions on decay behaviour in the two solvents, the differences in quenching impact and quenching radius of O-H vibrations (water) and C-H vibrations (cyclohexane) should be taken into account [149]. Furthermore, the volume ratio of the active shell to the core ($V_{a-shell}$ / V_{core}), which is about 1.3 should be considered. As C-H vibrations have a stronger quenching impact on Er^{3+} than on Yb^{3+} ions (cf. [43] and results in chapter 4.2), the $(Yb@Yb)^{is}$ sample in cyclohexane with 10% Yb co-doped active shell is not strongly affected by surface related quenching and therefore, Yb-excitation takes place in both volumes, the active shell and the Yb/Er-doped core. An effective energy migration via energy hopping from Yb→Yb from the shell to the core-shell interface can be expected, which provides one explanation for the comparable long LTs of Yb emission at 940 nm. In case of the $(Yb@Yb,Nd)^{is}$ sample dispersed in cyclohexane with its additional 10% Nd^{3+} doped active shell, Nd-Er ETs can be expected at the core-shell interface. The Nd-Er ETs lead to depopulations of Er^{3+} levels, affecting the $^4I_{11/2}$ Er level would explain the shortening of the Yb LT[1], as presented in Figure 6.2 d). The presence of Nd-Er ET/quenching processes also provides the answer for the sharp fall of QYs in presence of Nd^{3+} ions in cyclohexane, cf. Fig. 6.2 c).

The quenching impact of O-H vibrations in water is shielded less effective by an outer shell (here 1.5 nm thick) as it is for the C-H vibrations [43] and therefore, water quenching can be expected to be active in the 4.5 nm thick inner shell and even in the Yb/Er co-doped core.

---

[1] The Yb-decay and LTs are an overlay of radiative depopulations from the $^2F_{5/2}$ Yb^{3+} and $^4I_{11/2}$ Er^{3+} levels to the groundstates.

In consequence, the Yb^{3+} ions and Yb-Yb energy migration processes inside the active inner shell are strongly reduced, which explains the clearly shorter Yb decay in water compared to cyclohexane. It follows, that the light absorption relevant for UCL can be expected to occur mostly in the Yb/Er co-doped core volume (V_{core}). The additional presence of Nd in the active shell enables an additional energy loop from Yb→Er→Nd→Yb ions at the core-shell interface, which can explain the longer Yb LTs measured for the $(Yb@Yb,Nd)^{is}$ sample in water. Compared to the strong water quenching, the Nd-Er CRs make only a small contribution, leading to the slightly smaller QYs of the $(Yb@Yb,Nd)^{is}$ sample compared to the Nd-free sample in Figure 6.2 c). In contrast, the additional energy loop (Yb→Er→Nd→Yb) might be of no consequences for the already long Yb LTs based on Yb-Yb migrations in cyclohexane.
Other possible explanations like an additional direct Yb→Nd BET or re-absorption processes from Nd^{3+} ions can be assessed as very unlikely due to comparable large energy level mismatches and low absorption cross-sections of Nd^{3+} in the relevant spectral ranges.

Under 980 nm excitation both solvents - cyclohexane and water - have strong impact on the Nd-involved energy transfers, but since only the samples in water showed comparable results regarding the UC efficiency, in the following comparisons the NPs dissolved in cyclohexane are excluded. The effects of a bigger inert protective shell on the total UCL efficiency and Nd^{3+} related ion-ion quenching effects should be considered in forthcoming studies in water. Furthermore, the $(Yb@Yb)^{is}$ did not show any emission signal at low P under Nd-excitation (808 nm), so that ESA processes of Er^{3+} ions can be neglected for the following experimental conditions in ensemble.

Efficiency of Nd-/Yb-excitation in water

According to literature [45, 46, 49], Nd^{3+} have about 10-fold higher absorption cross-section as Yb^{3+} and the water absorption at 808 nm (Nd-excitation) is about 25-fold lower compared to Yb-excitation at 980 nm. The lower water absorption at 808 nm leads to minimised heating effects and to higher penetration depths, which are both advantages for bio-applications. On the other hand the shorter wavelength of 808 nm causes higher scattering especially in tissue compared to 980 nm, which will be discussed in the next section. The light absorption values of sensitizer ions and of the surrounding water have an influence on the UC emission signal and therefore, must be taken into account for the comparison of Nd- and Yb-excitation. As a basic measure for particle-related UC performance, the particle brightness $B_{UC}(\lambda_{ex})$ was chosen, which is determined by the product of NP absorption cross-section $\sigma_{UCNP}(\lambda_{ex})$ (given in $[cm^2]$) and the P-dependent $QY_{UC}(\lambda_{ex})$:

$$B_{UC}(\lambda_{ex}) = \sigma_{UCNP}(\lambda_{ex}) * QY_{UC}(\lambda_{ex}) \tag{6.1}$$

The absorption cross-section The σ of one UCNP ($\sigma_{UCNP}(\lambda_{ex})$) can be derived in two ways: First by using Beer-Lambert law (eq. 2.3) and the definition of absorbance $A(\lambda_{ex})$ (eq.

2.4) as described in theory chapter 2.3.2. Secondly, by using the total number of absorbing Ln^{3+} ions per NP and the absorption cross-section of a single Ln^{3+} ion from literature: $\sigma_{UCNP}(\lambda_{ex}) = N_{Ln} * \sigma_{Ln}(\lambda_{ex})$. Since the latter method is based on the assumption, that the Ln^{3+} properties are only minimal influenced by the host crystal, we chosen the first way determining the σ_{UCNP} for the specific $(Yb@Yb,Nd)^{is}$ system and using this results and N_{Ln} to determine $\sigma_{Ln}(\lambda_{ex})$ per Ln ion. Thereby, the symmetry and crystal field influences of the host matrix on the Stark splitting are considered, which in turn affects the distribution of the absorption band and therefore, the absorption cross-sections.

The absorbance values at the specific Nd- and Yb-excitation wavelengths were taken from the absorbance scan of the $(Yb@Yb,Nd)^{is}$ system dispersed in cyclohexane at 10 mg mL^{-1}, as shown in Figure 6.3 a). The Nd-doped NPs show a 1.3 times higher absorbance at 805 nm (Nd-excitation) compared to Yb-excitation at 978 nm by matching the laser lines (real). Looking at the respective absorbance maxima of both ions (ideal), the absorbance value of Nd^{3+} would be about 2.6 times higher that that of Yb under ideal excitation.

The $\sigma_{Ln}(\lambda_{ex})$ were calculated as described in chapter 2.3.2 and revealed under real excitation for σ_{Nd}(805 nm) and σ_{Yb}(978 nm) values of about $4.93 \cdot 10^{-20} cm^2$ and $1.44 \cdot 10^{-20} cm^2$. In case of an ideal excitation, σ_{Nd}(794 nm) is about $1.25 \cdot 10^{-19} cm^2$ and σ_{Yb}(976 nm) about $1.77 \cdot 10^{-20} cm^2$.

In Table 2.1 our results are compared and listed with other σ_{Ln} values of Nd^{3+} and Yb^{3+} ions found in literature for different host materials and excitation wavelengths. The different values illustrate the strong influences of the host matrix and the necessity to calculate the σ_{Ln} for the specific NP system for a well-founded discussion. In addition, the spectral profile and the exact excitation wavelength of the laser diode should be measured and mentioned (upper panel Fig. 6.2 a)), since the match between the narrow ion absorption bands and the laser lines can strongly influence the UC efficiency. As Nd has a narrower absorption band compared to Yb, even a slightly change of the excitation wavelength would affect strongly the light absorption.

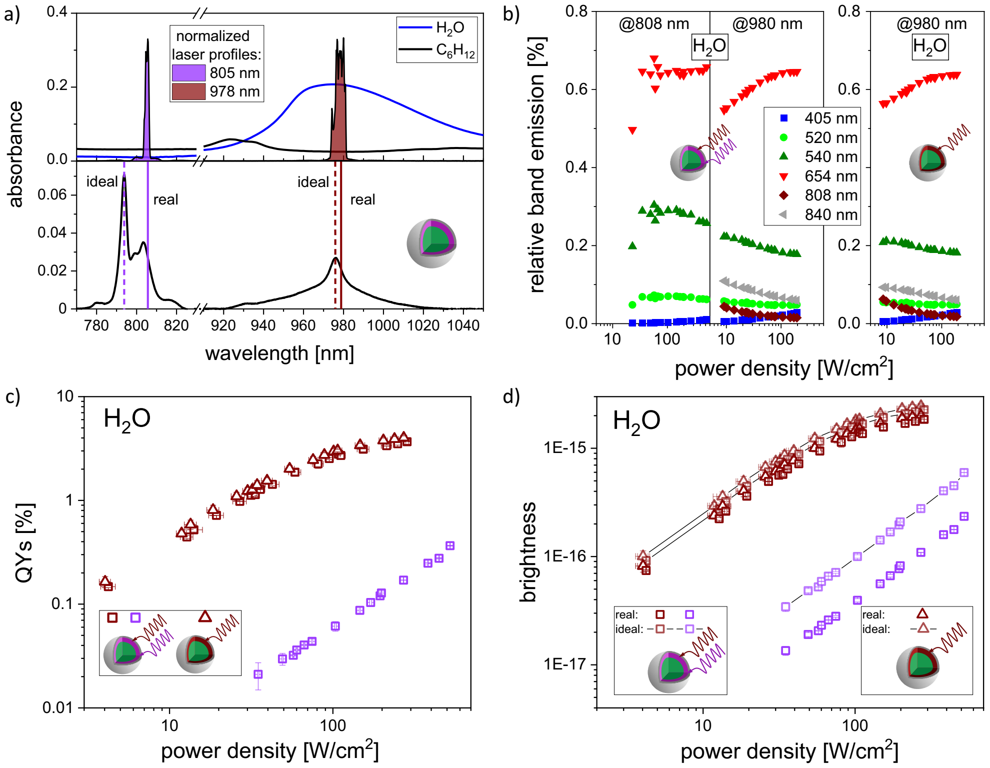

Figure 6.3. Comparison of Nd- and Yb-excitation on the (Yb@Yb,Nd)^{is} and (Yb@Yb)^{is} NP systems in water: a) Absorbance spectra of the solvents C_6H_{12} and water with the real and normalized laser profiles at 805 nm and 978 nm (top) and the absorbance spectra of (Yb@Yb,Nd)^{is} system with the Nd (780 - 820 nm) and Yb (940 - 1000 nm) absorption bands (bottom). The dashed lines mark the ideal excitation wavelengths, matching the maximal absorption peaks. b) *P*-dependent relative emission bands under Nd- and Yb-excitation for the (Yb@Yb,Nd)^{is} NPs and under Yb-excitation for the (Yb@Yb)^{is} NP systems in water. c) *P*-dependent quantum yields of both NP systems for Nd-excitation (purple) and Yb-excitation (brown). d) *P*-dependent brightness values calculated for the real (no lines) and the ideal (lines) Nd- and Yb-excitation wavelengths. Taken and modified from own publication [51].

Relative band emission, QYs and brightness values of (Yb@Yb,Nd)^{is} and (Yb@Yb)^{is} The *P*-dependent relative band emissions of (Yb@Yb,Nd)^{is} under Nd-excitation show nearly constant green (540 nm) and red (654 nm) band contributions of about 28% and 65% for *P* higher than 30 W/cm^2, as described in the left panel Fig. 6.3 b). Compared to the Yb-excitation of the same NP system and the reference sample, under Nd-excitation the green band shows a higher contribution and the red band reaches already at lower *P* the saturation condition, comparing the left to the middle and right panel in Fig. 6.3 b).

The *P*-dependent QY measurements of both systems, with and without Nd in water in Fig. 6.3 c) provide clearly that Yb-excitation leads to much higher QYs. At 60 W/cm^2 the QY values are about 50-times higher under Yb-excitation with 1.869% compared to 0.036% under Nd excitation. There are different explanations, the first is the different number of sensitizers with about 13 200 Nd^{3+} ions and about 34 5000 Yb^{3+} ions per (Yb@Yb,Nd)^{is} sys-

tem, which is not considered by QY data and is not compensated by the higher absorption cross-section of all Nd ions inside this NP system (Fig. 6.3 a)). An additional explanation might be the higher Yb^{3+} ion doping rate of 20% in the core, where Yb → Er ET occurs, compared to 10% doping rate of Nd^{3+} in the active shell. So, Yb^{3+} ions in the core got excited at 978 nm and then transfer directly the energy to the Er^{3+} ions, whereas the Nd^{3+} ions excited at in the shell are surrounded by a lower Yb^{3+} ion rate of 10%, which in turn are spatial separated from the Er^{3+} ions in the core, leading possibly to reduced Yb-Er ET rates. The most conclusive reason for lower QYs under Nd-excitation is the additional and preceding ET step from Nd → Yb prior to the Yb → Er ET.
Since the brightness values B_{UC} (eq. 6.1) were calculated with the QY values under 805 nm and 978 nm excitation (real), B_{UC} values show the same P-dependent trends but in consideration of the specific absorption cross-sections $\sigma_{UCNP}(\lambda_{ex})$, Fig. 6.3 d). At P of about 60 W/cm^2, the Yb-excitation of $(Yb@Yb,Nd)^{is}$ NPs leads to B_{UC} of $9.42{\cdot}10^{-16}$ which exceeds the brightness values under Nd-excitation about 40-times ($2.32 \cdot 10^{-17}$ @ 805 nm and $9.42 \cdot 10^{-16}$ @ 978 nm). In other words, the maximal brightness value of $2.3 \cdot 10^{-16}$ under Nd-excitation at P of 522 W/cm^2 can be reached already at P of 15 W/cm^2 using Yb-excitation. Under ideal excitation at about 60 W/cm^2, the brightness values would be increased, resulting in about 20 times higher brightness under Yb-excitation compared to Nd-excitation ($5.88 \cdot 10^{-17}$ @ 794 nm and $1.16 \cdot 10^{-15}$ @ 976 nm). The reference sample $(Yb@Yb)^{is}$ show only marginal higher B_{UC} values under both real and ideal Yb-excitation in Fig. 6.3 d). For a complete comparison, in appendix Figure A.15 the QYs and brightness values are plotted for both NP systems dispersed in cyclohexane and in water.

Influence of NP architecture For a better understanding of the UC performance of our core-shell-shell $(Yb@Yb,Nd)^{is}$ particles, two other reference NP systems with same total diameter of about 35 nm representing the most common core-shell structured UCNPs with an active core and an inactive shell have been examined. As sketched in Fig. 6.1, the $(Yb)^{is2}$ and $(Yb)^{is5}$ particles have different inert shell thicknesses (2 nm and 5 nm) and therefore differ in the amount of core material. For $(Yb)^{is2}$ system, the previously active shell was replaced by a shell with chemical composition as the core, whereas for $(Yb)^{is5}$ the active shell was superseded by inert protective shell ($NaYF_4$).
The QY values of $(Yb)^{is5}$ particles in water are about 6 times higher compared to those of $(Yb)^{is2}$ and about 65 times higher then those of $(Yb@Yb,Nd)^{is}$ at 60 W/cm^2, as plotted in Figure 6.4 a). The calculated B_{UC} values of $(Yb)^{is5}$, which takes the number of sensitizer ions into account, still exceed those of $(Yb)^{is2}$ and $(Yb@Yb,Nd)^{is}$ systems under real excitation condition by about 2.6 times and 35 times, respectively. Therefore the lower QYs of $(Yb)^{is2}$ is not compensated by the higher number of Yb^{3+} ions (52100±4200 in $(Yb)^{is2}$ and 23400±1700 in $(Yb)^{is5}$), which indicates that the 2 nm thick inert shell does not fully protect the core from water quenching. Under ideal Yb- and Nd-excitation, the B_{UC} values of $(Yb)^{is5}$ are about 18-times higher than that of $(Yb@Yb,Nd)^{is}$ at 60 W/cm^2.

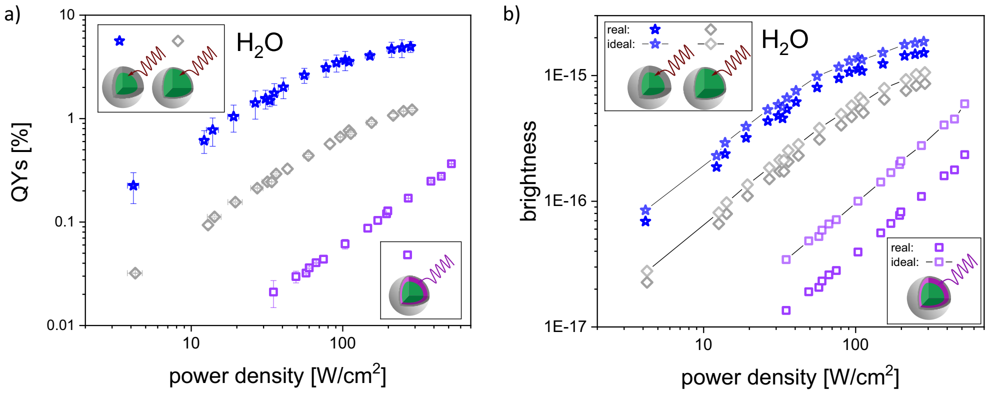

Figure 6.4. Comparing the optical efficiency of the (Yb)^{is2} and (Yb)^{is5} under Yb-excitation with the (Yb@Yb,Nd)^{is} NPs under Nd-excitation: a) P-dependent quantum yields of the three NP systems. b) P-dependent brightness values calculated for the real (no lines) at 805 and 978 nm excitation and the ideal (lines) Nd- and Yb-excitation at 794 and 976 nm. Taken and modified from own publication [51].

The significant lower QYs and brightness values of Nd-excited (Yb@Yb,Nd)^{is} NPs compared to the Yb-excited reference systems ((Yb@Yb)^{is}, (Yb)^{is2} and (Yb)^{is5}) lead apparently to the impression that Nd-excitation is not favourable at all and can nowhere near top Yb-excitation in efficiency. Before this assumption can be finally confirmed, the influences of scatting and solvent related absorption processes should be taken into account, as done in the next two paragraphs.

Penetration depth into water and phantom tissue

Penetration depth into water As shown in Figure 6.2 a), water has a higher absorption coefficient α_{water} at 980 nm compared to 805 nm. Therefore, with deeper penetration (x) into water the power density P of Yb-excitation light is stronger reduced than that of Nd-excitation. Since the QY is strongly P-dependent, a reduction of the local excitation P leads automatically to a decrease of the QYs and the brightness values. That means, at a certain penetration depth (crossing-point x_C) the previously lower emission intensity of Nd-excited NPs show same signal as the Yb-excited systems and for deeper penetration ($x > x_C$) Nd-excitation leads to brighter emission signal in water. In our publication we discussed that in the supporting information [51].

Th UC emission intensity $I_{UC,Ln}$ depends on the local power density P_{ex}(x), the number of Ln^{3+} absorbers (N_{Ln}), the absorption cross-section $\sigma_{Ln}(\lambda_{ex})$ and the QY value:

$$I_{UC,Ln}(x) \approx P_{ex}(x) \cdot N_{Ln} \cdot \sigma_{Ln}(\lambda_{ex}) \cdot QY(P_{ex}(x)) \qquad (6.2)$$

Using the Beer-Lambert law for light passing an absorbing medium (α_{water}), the P_{ex}(x) is reduced as followed with $P_0 = P_{ex}(x = 0)$:

$$P_{ex}(x) \approx P_0 \cdot e^{-\alpha_{water}(\lambda_{ex})\cdot x} \qquad (6.3)$$

Combining eq. 6.2 and 6.3 and using ($A_{Ln} \sim N_{Ln} \cdot \sigma_{Ln}$), it follows for UC emission intensity $I_{UC,Ln}$:

$$I_{UC,Ln}(x) \;\approx\; P_0 \;\cdot\; e^{-\alpha_{water}(\lambda_{ex})\cdot x} \;\cdot\; A_{Ln} \;\cdot\; QY(P_{ex}(x)) \tag{6.4}$$

The decreasing emission intensities of the $(\mathrm{Yb@Yb,Nd})^{is}$ NPs, depending on the penetration depth into water are plotted in Figure 6.5 a) for the real and ideal Yb- and Nd-excitations using eq. 6.4 at $P_0 = 50W/cm^2$. The crossing points reveal higher emission signals under Nd-excitation for penetration depths exceeding ~ 6 cm and ~ 9.5 cm for ideal and real conditions, respectively.

In Figure 6.5 b) the crossing points are shown for both real and ideal excitation at 6 different initial power densities ($P_0 = P_{ex}(x = 0) = 5, 50, 100, 200, 300$ and 400 W/cm^2). With increasing P, the crossing points decrease and the Nd-doped NPs start to top the Yb-doped systems at shorter penetration depths, which is more pronounced under ideal conditions, where x_C^{ideal} is about 2.3 cm at 400 W/cm^2. This underlines that the match of the laser lines with the absorbing ions have a huge impact on the luminescence outcome at high penetration depths in water and therefore, also for deep-tissue imaging and theranostic applications.

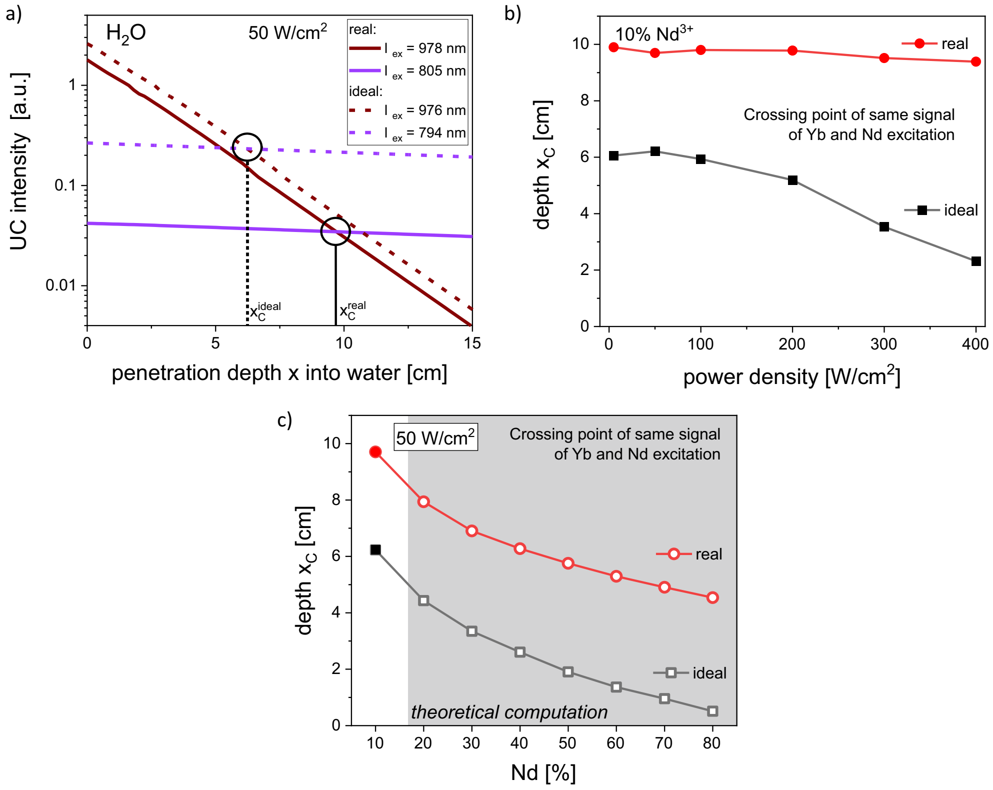

Figure 6.5. Penetration depth into water: a) Calculated intensity decrease of UC emissions under ideal and real Nd- and Yb-excitation with penetration into water at P of about 50 W/cm^2. b) P-dependent calculated crossing points, meaning the penetration depths of same UC intensities under Nd- and Yb- excitation for real and ideal conditions. c) Calculated crossing points for theoretically higher Nd-content of 20, 30, 40, 50, 60, 70 and 80% in the active shell of $(\mathrm{Yb@Yb,Nd})^{is}$ NPs under real and ideal excitations. Taken and modified from own publication [51].

Next, the influence of the Nd doping concentration on the competition of Nd- and Yb-excitation was examined, regarding the UC efficiency in water. Therefore, the number of Nd ions N_{Nd} was theoretically varied and the crossing points were calculated for Nd contents of 20%, 30%, 40%, 50%, 60%, 70% and 80% in the active shell of $(\mathrm{Yb@Yb,Nd})^{is}$ NPs using eq. 6.4. In Figure 6.5 c) the decreasing trends of the crossing points x_C with theoretical higher Nd content are plotted for the real and ideal excitation conditions at P_0 of 50 W/cm^2. These calculations reveal that systems with higher Nd doping theoretically start to outperform the efficiency of the Yb-doped particles at penetration depths below 1 cm and therefore provide the basis for further optimising of Nd-doped systems in future studies.

It must be mentioned that this estimation exclude influences like cross-relaxations, which are possibly enhanced by the shorter ion-ion distances, and like crystal lattice strain arising from different Nd^{3+} and Y^{3+} ionic radii possibly leading to enhanced defect formations.

Penetration depth into phantom tissue At the end of the ensemble studies our cooperation partners (Hirsch group from Regensburg) run some measurements on the $(\mathrm{Yb@Yb,Nd})^{is}$ NPs in phantom tissue, a turbid emulsion of phospholipid micelles of polydisperse nature and water referred to as intralipid [51]. The use of intralipid as solvent helps to simulate sample tissue by combining water absorption and strong scattering influences. The wavelength dependent transmission spectra in Figure 6.6 c) compares the light penetration passing 1 cm of 0.01% intralipid emulsion and water, revealing massive light scattering of the phantom tissue. The high light scattering in such a medium makes the determination of exact power densities of the propagating laser light really difficult. For that reason only relative intensity changes were measured from that point on. Measuring the relative laser intensities in 0.1 cm penetration steps into intralipid emulsion (1%), shows that after 20 mm less than 10% of the initial Yb-excitation and less than 30% of Nd-excitation are left, as shown in Fig. 6.6 a). The initial laser powers were chosen at about 150 mW, which is recommended for medical applications. This clearly illustrates the benefits of Nd-excitation in tissue regarding the excitation laser power, resulting also in higher UC emission intensities as shown in Fig. 6.6 b) taken under 90-degree configuration in 1 cm cuvettes.

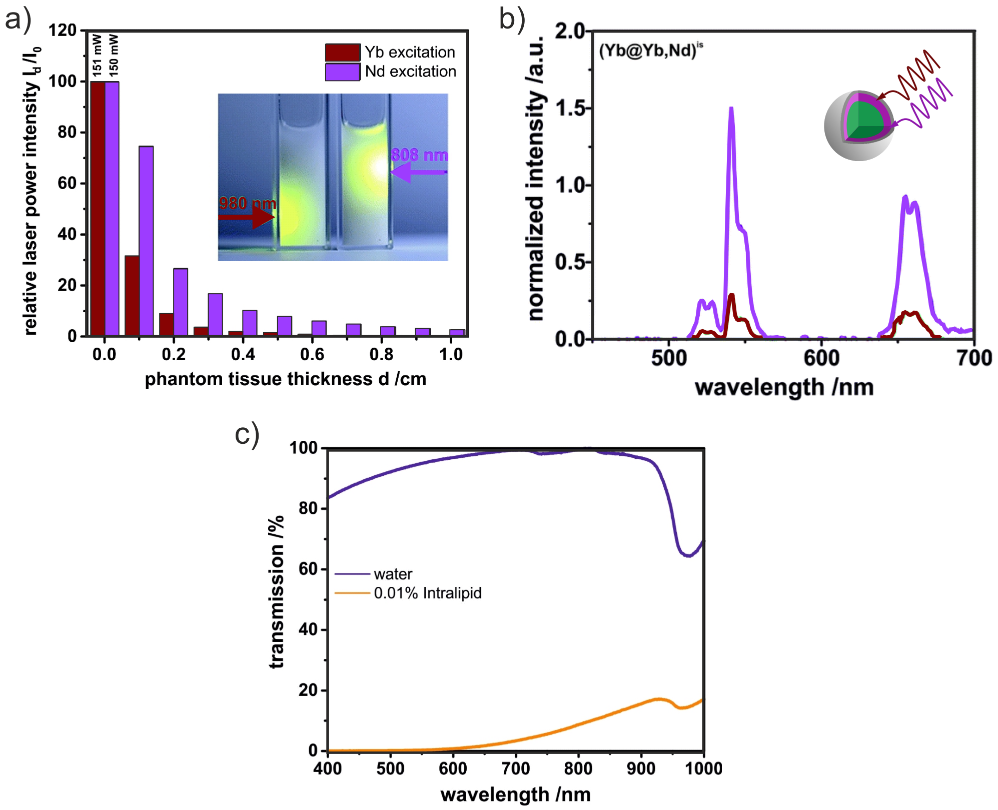

Figure 6.6. Penetration depth into phantom tissue (Intralipid emulsion): a) Relative power decrease of a 808 nm and a 980 nm laser diode depending on the penetration depth into phantom tissue (1 mg/mL). b) Normalized UC emission spectra of (Yb@Yb,Nd)^{is} NPs under Nd- and Yb-excitation acquired in 90° configuration with 1 cm cuvettes. c) Transmission measurements of water and a diluted intralipid emulsion (0.01%) covering the range from 400 to 1000 nm. Taken and modified from own publication [51].

6.3. Single Particle studies on Nd co-doped UCNPs

On the SP level, the decay behaviour and the P-dependent spectra, band emissions and characteristic band ratios have been performed under direct Nd- and Yb-excitation (808 nm and 980 nm) on the (Yb@Yb,Nd)^{is} and (Yb@Yb)^{is} NP systems (Fig. 6.1) using our CLSM (chapter 3.3.1). The Nd-excitation with the CLSM setup was realised using a 2W, 808 nm laser operated in cw-mode for steady-state and in combination with a chopper system (MC2000B, Thorlabs) for time-resolved measurements. The samples dispersed in cyclohexane have been taken for the SP preparation on the glass-substrate.

Decay behaviour at 808 nm and 980 nm

In Figure 6.7 the decay curves of the green (a) and the red (b) band emissions are plotted for the (Yb@Yb)^{is} sample at 980 nm and for the (Yb@Yb,Nd)^{is} for 808 nm and 980 nm. The intensity-weighted LTs were calculated and averaged from the bi-exponential fits of 10 single NPs, respectively.

The direct Nd-excitation of (Yb@Yb,Nd)^{is} at 808 nm (blue) shows the longest green and red LTs with 390 μs and 450 μs, which is not surprising due to the additional ET step from Nd → Yb. The Yb-excitation at 980 nm reveals longer LTs of the Nd-free (red) samples at the green (385 μs) and the red (420 μs) bands compared to the Nd-containing (grey) samples with green and red LTs of 330 μs and 393 μs. The same trends were observed for the 940, 540 and 665 nm emissions of the samples dispersed in cyclohexane at ensemble condition, cf. Fig. 6.2 d)-f) and can be associated to Nd-Er ion CR effects at the core-shell interface of the SPs dried on glass-substrate with reduced surface-related quenching effects.

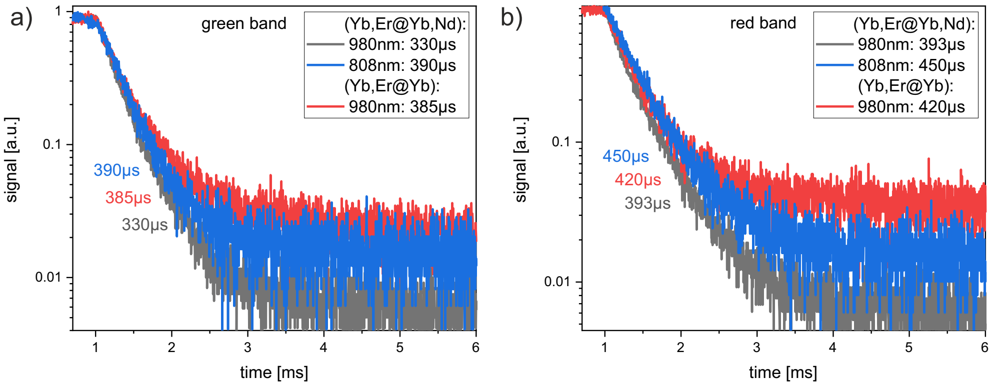

Figure 6.7. Decay kinetic of the (Yb@Yb,Nd)^{is}) SPs under Nd-and Yb-excitation and of the (Yb@Yb)^{is}) SPs under Yb-excitation with corresponding calculated LTs based on bi-exponential fitting: a) Decays of green band emission covering spectra range 533-557 nm. b) Time-resolved red band emission of the spectral region 635-675 nm.

P-dependent emission trends at 808 nm and 980 nm

A direct comparison of UCL intensities obtained under Nd- and Yb-excitation on both samples is not possible due to different filter sets and spectral correction curves used for the two measurement conditions. This explains the higher signal counts under Nd-excitation in the following plots, which does not reflect reality.

In appendix Figs. A.16 a) and b), the *P*-dependent spectra of (Yb@Yb,Nd)^{is} and (Yb@Yb)^{is} NPs are presented for both excitation wavelengths covering *P* over 3 orders of magnitude. In Figure 6.8 a) and b) the spectra of the two samples are compared directly for low (21 kW/cm^2) and high (2 MW/cm^2) *P* values under Nd-excitation (a) and Yb-excitation (b). Under 808 nm excitation the UCL intensity of (Yb@Yb,Nd)^{is} NPs are about double as high compared to the (Yb@Yb)^{is} sample in Fig. 6.8 a). The UCL of the (Yb@Yb)^{is} sample under Nd-excitation indicates a strong direct light absorption by Er^{3+} ions, which also boosts the UCL of the (Yb@Yb,Nd)^{is} NPs and was not detected in ensemble measurement condition. Excited at 980 nm, the Nd-containing sample shows about 30% reduced luminescent intensity compared to the Nd-free sample, illustrating the presence of quenching influences of Nd-Er CRs at *P* of 21 kW/cm^2, which are compensated by higher *P* at 2 MW/cm^2 in Fig. 6.8 b). The presence of the additional 404, 471, 503 nm peak emissions, which are missing under 808 nm excitation and arise from higher Er energy levels (cf. section 4.4), demonstrates more efficient populations and UC processes under Yb- compared to Nd-excitation.

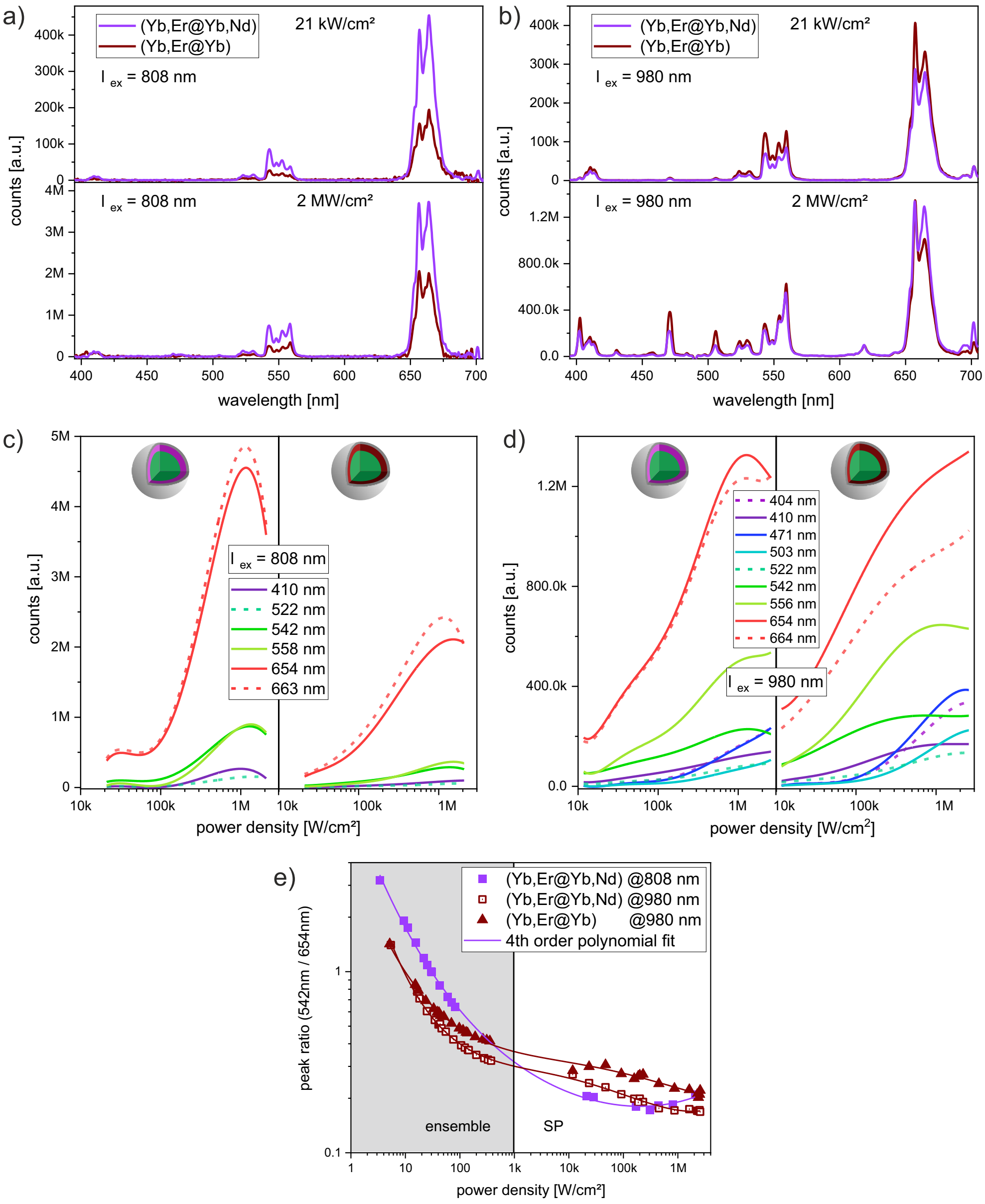

Figure 6.8. *P*-dependent spectra, band emission trends and peak ratios of the (Yb@Yb,Nd)^{is} and (Yb@Yb)^{is} SPs: a) and b) Spectra of both samples at low (21 kW/cm^2) and high (2 MW/cm^2) *P* under 808 nm (Nd-excitation) (a) and under 980 nm (Yb-excitation). c) and d) Band emission trends of both SP samples under 808 nm (c) and under 980 nm excitation (d). Combined G/R (541nm / 654nm) peak ratios of ensemble and SP measurements of both samples excited under Nd- and Yb-excitation.

The P-dependent emission trends of the main peaks in Figure 6.8 c) show for both NP systems similar behaviour under 808 nm excitation. The trends under 980 nm excitation (Fig. 6.8 d)) reveal no significantly Nd^{3+} ion influence on the band emissions for $P < 1$ MW/cm^2. For higher P, the red band of the Nd-free sample shows ongoing intensity increase, whereas the (Yb@Yb,Nd)^{is} NPs reach maxima at 1.2 MW/cm^2. This effect implies a higher rate of red level-feeding Er-Yb BET processes if the quenching influences of Nd^{3+} are missing at the core-shell interface. Furthermore, the increasing red emission intensity indicates the maximal brightness values of the (Yb@Yb)^{is} NPs in the P range > MW/cm^2, which is not covered by our CLSM (so far).

In appendix Figs. A.16 c) and d), the green-to-red (G/R = 541 nm / 654 nm) and the green-to-green (G/G = 520 nm / 541 nm) peak ratios are plotted for both excitations, revealing under Nd-excitation lower G/R ratios of the Nd-free sample due to poor green emissions compared to Nd-containing NPs with their slightly higher and constant ratios. Under 980 nm excitation both samples show same decreasing trends of G/R ratios nearly unaffected by the additional Nd^{3+} ions. The rise of the G/G peak ratios - the Boltzmann coupled $^4S_{3/2}$ / $^2H_{11/2}$ Er^{3+} levels - with higher P clearly marks the laser induced sample heating under 980 nm excitation. In comparison, under 808 nm excitation, the constant G/G ratios reveal no strong sample heating even in the MW range and reflect the comparative lower and less efficient light absorptions in case of Nd-excitation and ESA processes of Er^{3+} ions.

The combined G/R peak ratios of the ensemble and SP measurements in Figure 6.8 e) converge for the Nd-excited (Yb@Yb,Nd)^{is} NPs to about 0.2 at high P. For the Yb-excitation slightly smaller ratio values of the (Yb@Yb,Nd)^{is} compared to the Nd-free NPs are present at $P > 100$ kW/cm^2, reporting a quite continuous quenching influence of Nd^{3+} on the Yb-excitation processes for the P range covering over 4 orders of magnitude.

6.4. Conclusion

In this chapter, a set of similarly sized (Nd^{3+})/Yb^{3+}/Er^{3+}-doped core-shell-shell NPs with different particle architecture were optically characterised dispersed in cyclohexane and in water under ensemble condition and dried on glass-substrate in SP condition. The P was broadly varied using Yb-excitation and Nd-excitation. The spatial separation of Nd ions in the active shell and Er ions in the core reduces ion-ion quenching effects.

In response to the questions raised at the beginning of this chapter, there is a negative impact of Nd^{3+} ions on the Yb $\rightarrow$ Er ET at Yb-excitation. The reduction of UC rates and QYs were attributed to Nd-Er quenching processes at the core-shell interface. The fact that this Nd-related quenching effects only appeared for samples in cyclohexane and on the SP level suggests that in water a higher extent of surface related quenching from O-H bonds is overshadowing the UC processes in the core-shell interface, and therefore a thicker inert shell should further enhance UC efficiencies of Nd-doped samples in water. Furthermore, the use of the ideal excitation wavelengths, matching the sensitizer absorption maxima can enhance the particle brightnesses, especially for Nd-excitation with its sharp absorption peak.

In addition, our results underline that a higher absorption cross-section and a lower water absorption of Nd-excitation compared to Yb-excitation does not necessarily lead to a brighter UCL emission due to the additional ET step from Nd to Yb. Nd-excitation can top Yb-excitation under certain measurement conditions including the local P and the properties of the absorbing medium with its extend of light scatting and the light penetration depth into it. In this respect, a first proof of concept study in phantom tissue revealed the need for more accurate studies of the influence of tissue impact on photo-physical behaviour of UCNPs used for bio-applications.

Our SP studies showed that higher P values (up to MW/cm^2) of Nd-excitation do not lead to significantly enhanced population of higher Er-levels and therefore, Nd-excitation cannot compensate efficiently the non-radiative quenching channels as it is the case for high P Yb-excitation.

According to our calculations, higher Nd^{3+} ion concentrations could lead to enhanced UC signals, whereby in particular the particle architecture and the ion-ion distances should be taken into account. Especially at SP condition with higher P, the impact of higher Nd^{3+} concentrations could lead to more efficient UC performance as it was already exhibited for higher Yb and Er ion concentrations in chapter 5, providing a basis for further studies on varied and optimised Nd-sensitized UCNPs.

7 | Further studies: LRET and plasmonic interactions

7.1. LRET between UCNPs and sulforhodamine B

In this section, the energy transfer process between Er^{3+}-dopded UCNPs and the dye sulforhodamine B (SRB) is discussed on different samples under ensemble and under SP condition. In addition, the proof for LRET and the resulting LRET efficiencies are outlined. The theoretical background about FRET/LRET processes is given in chapter 2.4.

7.1.1. Preparation and chemical analysis

The sulforhodamine B (SRB)-loaded UCNPs have been synthesized by the Hirsch group (University of Regensburg, Germany) consisting of 2 $NaYF_4$:20% Yb/ 2% Er NP systems with different size and surface-modification. The first system consist of a 25.5 ± 0.9 nm thick core with a thin inert shell around leading to a total diameter of 26.2 ± 1.3 nm made by Markus Buchner following a protocol described in [51]. For the subsequent dye-loading preparation, the surface was modified via ligand exchange with $NOBF_4$ and the particles were coated with PVP (K25) for stabilisation in ethanol and finally 500 μg of SRB were brought on 5 mg NPs leading to a NP concentration of 2.5 mg/mL. The PL and decay kinetics of these particles were measured under both conditions, on the ensemble and the SP level. The TEM images and appropriate size distributions are plotted in appendix Fig. A.17.
The 2nd SRB-loaded NP system was only studied on SP level and was synthesized by John Galligan and is a core-only NP with 19.3 ± 0.5 nm in diameter, surface modified with BF_4 and dispersed in DMF. In the next step, these Yb/Er doped UCNPs were mixed in a ratio 1:100 with undoped $NaYF_4$ NPs of the same size. Drops of this NP mixture were then brought on a silanized glass-substrate forming a monolayer on top. Finally, the SRB was brought on top of the NP mixture following the protocol in [66] and bound to the surface with the sulfonate group of the SRB.

7.1.2. LRET at ensemble level

In contrast to the reference sample without a dye, the SRB-loaded NPs (blue curve) clearly show a dye emission in the range from 565 to 670 nm with a maximum peak at 585 nm and a simultaneous reduction of the green emission band in the emission spectra under 980 nm excitation in Figure 7.1 a). This indicates an energy transfer from the UCNPs to the dye molecules. It is a common procedure to readout the LRET intensities by normalizing the spectra of both samples (with and without dye) to an UC emission band, which seems not to be directly involved in the LRET process. Commonly, the red UC emission band is chosen [66, 150], which should be critically questioned. The spectra in Fig. 7.1 a) were taken at the same NP concentration of 2.5 mg/mL and show that taking the red band as reference can lead to biases, since the FRET-based SRB emission (565-670 nm) overlaps with the red band (650-675 nm). Furthermore, the green donor emission is connected to the red emission band, since the red ($^4F_{9/2}$) Er^{3+} ion energy level can be energetically fed by the overlying green ($^4S_{3/2}$) level via non-radiative relaxation processes or indirectly via Er-Er CR (CR2, cf. Fig. 2.4 c)) and therefore, a quenched green band can also affect the red band emission intensity. These two issues should be taken into account for SRB-UCNPs LRET particles to prevent misleading LRET intensity ratios and can be avoided by using time-resolved studies for LRET efficiency measures instead.

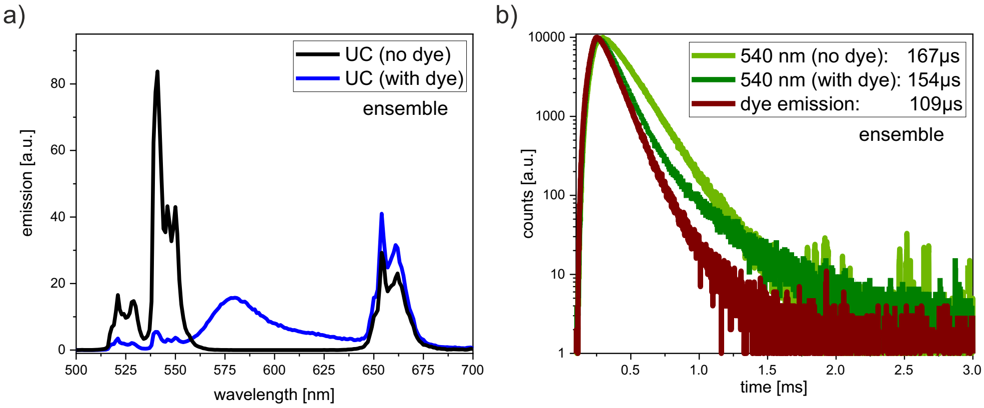

Figure 7.1. LRET measurements in ensemble condition of 26.2 nm thick core-shell UCNPs with and without SRB dye molecules as LRET acceptors: a) Emission spectra of UCNPs with and without dye taken at the same NP concentration of 2.5 mg/mL in ethanol. b) Decays of the green UC emissions (540 nm) with and without SRB and of the SRB emission (585 nm). The intensity weighted LTs were calculated from bi-exponential fits.

To further prove the presence of a non-radiative energy transfer / LRET process, the LTs of the dye emission at 585 nm and the green emission band (540 nm) at presence and absence of the dye have been calculated from bi-exponential fitting, cf. Fig. 7.1 b). The short component of the 540 nm with dye is quenched and overlaps with the decay curve of the dye, whereas the long component overlaps with the 540 nm decay curve of the reference sample. This clearly confirms LRET from the UCNPs to the SRB molecules with an LRET efficiency $\eta_{LRET,UCensemble}$ of about 35% using the equation 2.18. This equation excludes the contribution of the unquenched green emission arising from the centre of the NPs as described in the theoretical section 2.4.1. The next step is to measure this NP system on the SP level.

7.1.3. LRET at SP level

For the SP studies, the SRB channel was measured with a bandpass filter (F39-085 from AHF, Germany) covering the range of 585 ± 6.5 nm and a 6 OD blocking characteristic for the rest of the spectra between 320 - 1120 nm, cf. appendix Fig. A.18 c).

In Figure 7.2 a) the dye-loaded UCNPs described in the previous section was drop-casted via drop-and-dry process on a glass-substrate and the emission spectra were taken at different time points (30, 90, 150, 330 and 630 seconds) under non-stop 980 nm excitation at 5 kW/cm^2. With time the SRB emission intensity decreases by simultaneous increase of the green donor UC emission band. This illustrates the fast reduction of the energy transfer between the UCNP and the surface bound SRB molecules and obtains that after about 10 min all SRB molecules on the surface or their linkers are damaged or photo-bleached by high thermal energy caused by the laser illumination. Besides the green also the red emission band increases in intensity with longer illumination times at this high *P*. This clearly demonstrates the strong connection of the green and red emissive Er^{3+} energy levels ($^4F_{9/2}$ and $^4S_{3/2}$) and therefore the red band is indirectly involved to this specific energy transfer process and should not be used as reference band like it is common practice [66, 150]. In contrast to ensemble studies with lower excitation *P*, on the SP level even the comparable low *P* of 5 kW/cm^2 damages the LRET system over time, so that only short laser exposures should be used, which makes LT measurements of a few minutes on a fixed NP impossible. This explains, why both decay curves of the green bands with and without dye do not differ much, which makes the proof for real LRET on SP level difficult. The shortening of the SRB LT could also originate from a radiative energy transfer (no LRET) between the surface near Er^{3+} ions, which suffer from surface-related quenching effects, to the dye molecules. Even if surface-related quenching effects are decreased in SP studies, as shown in chapter 4.16, it cannot totally be ruled out that the shorter LTs of the SRB molecules appear partly

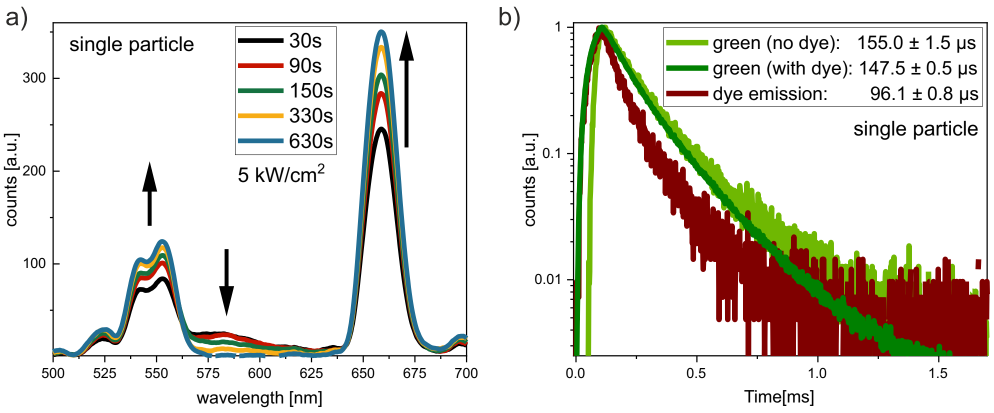

Figure 7.2. LRET measurements in SP condition of 26.2 nm thick core-shell UCNPs with and without SRB molecules as LRET acceptors: a) Emission spectra of a single UCNP taken after certain times (30, 90, 150, 330, 630s) under continuous 980 nm illumination. b) Decays of the green UC emission band (545 ± 12.5 nm) with and without SRB and of the SRB emission band (585 ± 6.5 nm). The intensity weighted LTs were fitted bi-exponentially.

from a radiative transfer component from the surface near Er^{3+} ions.
Using equation 2.18 with the unquenched D and dye LTs (Fig. 7.2 b)) an LRET efficiency $\eta_{LRET,SP}$ of about 38% is achieved, which is comparable to the 35% efficiency of the ensemble.
Comparing ensemble and SP studies, the LT of the SRB dye is slightly shorter on SP level (96 μs) as measured in ensemble (109 μs, Fig. 7.1 b)), which can be explained by the additional and strong green Er^{3+} emission band at about 560 nm, which results from the $^2H_{9/2}$ level with a short intrinsic decay rate of about 19.5 μs [102]. With higher excitation P, more additional Er emission bands appear with increased emission intensity as described in chapter 4.5. Those, which are in overlap with the SRB absorption band contribute to the energy transfer and could result in enhanced LRET efficiency.

To overcome long laser exposure times focused on single NPs during LT measurements, FLIM scans were used as a second approach for LRET proving and efficiency calculation. Therefore, the UCNPs provided by John Galligan (University of Regensburg) were used consisting of a mixture of Yb/Er-doped and undoped $NaYF_4$ NPs ("SP array") covered completely with SRB molecules. In Figure 7.3 a) the FLIM scans show the green (545 ± 12.5 nm), the SRB dye (585 ± 6.5 nm) and the red (655 ± 20 nm) emission bands of about 8 UCNPs. The emission intensity is represented by the pixel brightness and the intensity weighted LT ($\tau_{Av,Int}$) by the pixel colour increasing from blue to red. The luminescent spots in the three channels show different diameters due to various signal distributions. The largest spots with a smoother signal distribution were obtained in the SRB channel, marking a lower dye emission signal on the surface of the doped UCNPs. Whereas, the signal from the red band is stronger and more localized representing the emission of the NP centres. The smearing of the luminescent spots in the green channel may be explained by the small fraction of SRB emission which overlaps with green channel, cf. Fig. 2.7 a).
The averaged LTs of the SRB channel are shorter compared to those detected in the green channel, indicating an energy-transfer from the UCNPs to the SRB molecules. In Figure 7.3 b) the τ_{Av_Int} distributions and the corresponding Lorentz fits of the green and SRB FLIM scans with averaged decay times of 170 and 109 μs are plotted. According to equation 2.18, an LRET efficiency $\eta_{LRET,SParray}$ of about 36% is achieved for this NP system with a core diameter of about 19.3 ± 0.5 nm, which is comparable with the 35% LRET efficiencies of the larger core-shell NP system (26.2 ± 1.3 nm) calculated in ensemble and SP condition. Consequently, in SP condition neither the core-size nor the presence of an additional thin shell seams to influence the LRET efficiency significantly. This can be explained by the generally reduced influences of surface-related effects in SP compared to ensemble studies as shown in chapter 4.5.
The difference in the fitted LTs of the green UC channel on the NPs with the dye (155.8 ± 2.6 μs) and without the dye (161.3 ± 2.8 μs) in Figure 7.3 b) show also only small differences. This is in accordance to the decay studies of the larger core-shell NPs (cf. Fig. 7.2 b)), even if the dye-free condition was generated by 30 min of strong laser exposure using photobleaching to destroy the SRB molecules on the surface. The quenching influence of the SRB

molecules on the green donor band seems reduced in SP studies and is harder measurable due to additional green emissions with fast intrinsic decay rates and the destroying effect of the laser light on the dye molecules.

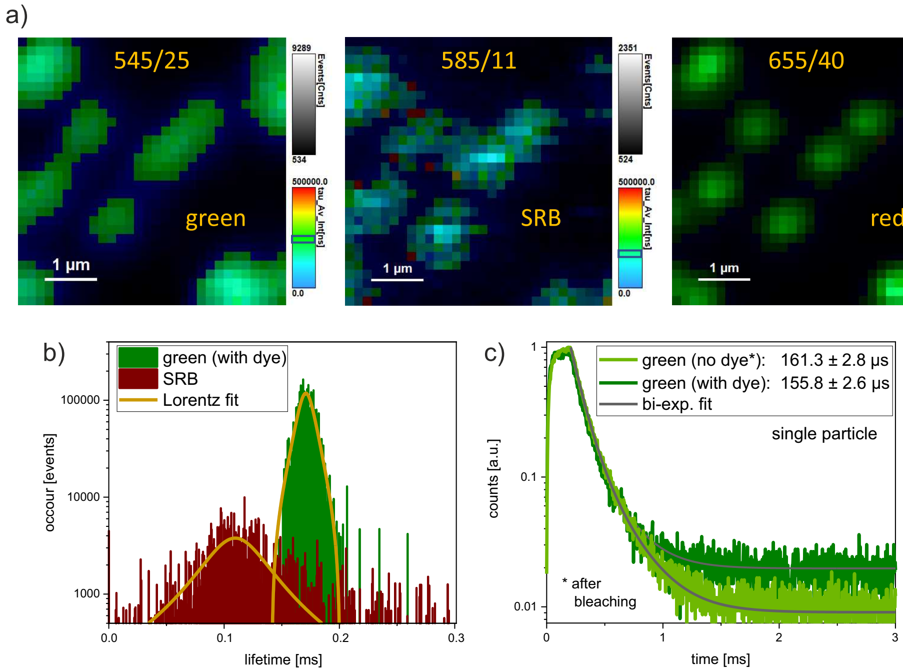

Figure 7.3. SP LRET studies on 19.3 nm thick core UCNPs with surface bound SRB molecules: a) FLIM scans of 8 UCNPs at the green (545 ± 12.5 nm), the SRB (585 ± 6.5 nm) and the red (655 ± 20 nm) channels colour coded for emission signal and intensity-weighted LTs. b) LT distributions with corresponding Lorentz fits of the green and the SRB decays. c) Decay curves of the green UC band with and without SRB.

Conclusion

The LRET process involving UCNPs is a complex process and in contrast to well-studied FRET/LRET systems of single donor-acceptor couples, for dye-loaded UCNPs, multi emitters are interacting with various Förster distances. To prove the presence of LRET and to calculate its efficiency the decay kinetic rates of the donor and the acceptor energy levels should be used instead of the changed donor emission intensities, which contains UCL from emitters at the NP centre not involved in the LRET process. Furthermore, the SP studies revealed, that the red emission band can not be used as reference band, since it is intrinsically connected and scales with the green donor emission band. Particularly, for the use of SRB dyes as acceptors, the overlap of the SRB emission with the red Er^{3+} band additionally disqualifies the red band as reference, as presented in ensemble condition.

In SP studies, the higher excitation P leads to additional emission bands (e.g. 560 nm), which makes the LRET process even more complex, if they matching the acceptor absorbance band and contribute to the LRET process. To avoid strong damage and photobleaching of the SRB dye, the laser power has to be kept low and the exposure time as short as possible. The evidence of LRET on SP level was not completely provided in our study. In a prospective resumption of this study, the influence of surface-related quenching effects on surface-near Er^{3+} should be considered regarding the donor emission and the impact on the LRET process. Furthermore, P-dependent LT measurements and spectral emission scans in the low P-range ($< 1\ \mathrm{kW/cm^2}$) should be performed in the future on SP level to be able to calculate P-dependent LRET efficiencies and to study the influence of additional emission bands for getting a deeper insight on the LRET processes of UCNPs.

7.2. Plasmonic interaction of Au-shelled single UCNPs

Sample preparation and chemical properties

The samples were prepared by our cooperation partners, the group of Prof. Christina Graf at FU Berlin. The syntheses of the Yb/Er co-doped UC core, the spacer layer made of silica (SiO_2) and the metal shell have been synthesized by Cynthia Kembuan and Maysoon Saleh. The sample and shell preparation are described in detail in their PhD theses [151, 152].

Single particle studies of Au-shelled UCNPs

The optical measurement on SP level have been performed on different set of samples based on the theoretical calculations described in section 2.5.2. Representative for both the saturation and the dimmed pumping theoretically calculated cases one set will be present here in more detail.

7.2.1. Saturation pumping regime

The following system was synthesized to match the pumped saturation regime with enhanced red emission, cf. Figure 2.10 a) in the theoretical section. NP System:

- UC@SiO_2: 317 nm diameter
- UC@SiO_2@Au: 317 nm diameter + 10-20 nm Au-shell

SP studies on both systems were performed and confirmed via AFM measurements. As shown in Fig. 7.4 a), the P-dependent spectra show significant lower intensity in presence of the Au-shell under 980 nm excitation in the P range between 50 $\mathrm{kW/cm^2}$ to 2.5 $\mathrm{MW/cm^2}$. The UC luminescence is strongly quenched by light absorption and non-radiative channels of the Au-shell. The competing effect of plasmonic interaction surpassing the quenching, resulting in enhanced emission intensities can not be detected in Fig. 7.4 a). Furthermore, a shortened lifetime of the green and the red emission bands for the Au-shelled system can be observed which is in agreement with the aforementioned quenching. The corresponding decays are shown in Figures 7.4 c) and d). Imperfections in the Au-shell, such as percolation, as well as particle parameters not perfectly matching the calculated parameters might strongly affect the optical properties. To prove the above-mentioned theory (cf. section 2.5.3), further NP syntheses are needed.

For the *P*-dependent emission trends of the green and red bands in Figure 7.4 b), a clear increase in intensity occurs for the Au-shelled NP especially at high *P*, whereas the unshelled system shows a maximum followed by reduced intensities, as it was detected for NaYF$_4$:20% Yb^{3+}/ 1-3% Er^{3+} samples in chapter 4.3. The differences in the emission performance of the Au-shelled NP system reveal the direct influence of the metal on the population behaviour of emissive bands, which can be evaluated even more clearly from normalized emission spectra at 2.5 MW/cm^2 in Figure A.19 a). There, the Au-shell NP shows relatively lower contributions from higher energy levels with emissions at 400, 476 and 503 nm to the overall emission. Thermal effects caused by high focused laser *P* can be considered using the band ratio of the thermal-energetic coupled $^4S_{3/2}$ (543 nm) and $^2H_{11/2}$ (524 nm) levels presented in Figure A.19 b). With increasing *P*, an increased population of the higher energetic level ($^2H_{11/2}$) originating from the subjacent level ($^4S_{3/2}$) is present, proving the enforced influence of thermal energy on the UC process at high *P*.

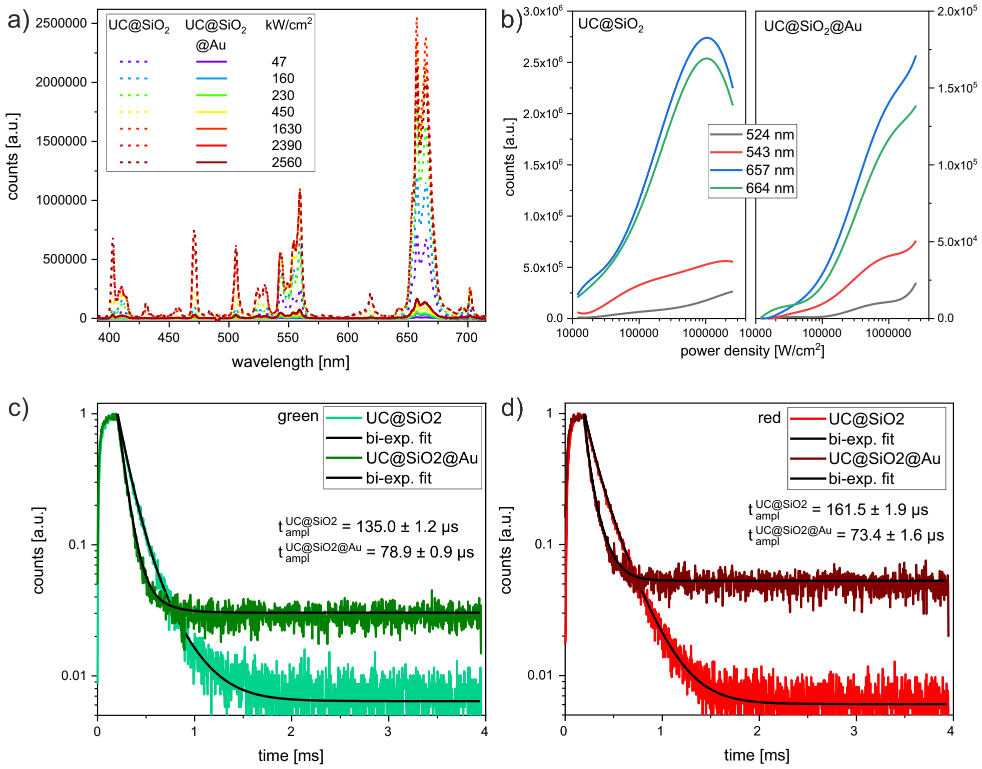

Figure 7.4. Saturation *P*-regime of UC@SiO$_2$ with and without Au-shell: a) *P*-dependent spectra of both systems. b) *P*-dependent emission trends of the 524, 543, 657 and 664 nm bands. c) and d) Decay curves of the green and the red emission bands with bi-exponential tail-fitting to get the amplitude weighted LT values.

7.2.2. Dimmed pumping regime

The following systems have been synthesized to match the NP parameters for the maximal enhancement at dimmed pumping regime, cf. Figure 2.10 b) and c) in the theoretical section 2.5.3:

- UC@SiO_2: 472 nm diameter

- UC@SiO_2@Au: 472 nm diameter + 21 nm Au-shell (mainly closed)

Confocal NPs studies including time traces and SP spectra at different *P*s have been performed. The time traces over 100s under 980 nm illumination reveal for both red and green channel constant behaviour for metal free NP (Fig A.20 a)) and decreasing trends for the Au-shelled system (Fig. A.20 b)). This intensity loss can be explained by laser induced heating processes of the metal shell. It points out that measurement duration and *P* strongly influence the results. Therefore, faster measurements and low *P* are desirable. However, decay studies and low-counts accumulations of SP spectra are difficult to collect at these conditions.

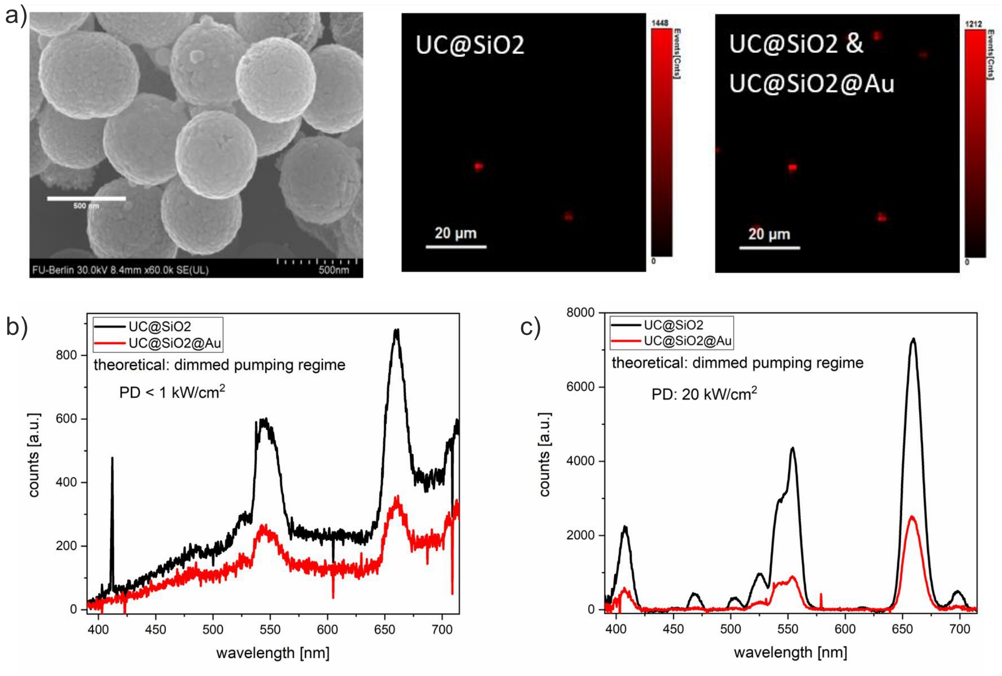

Figure 7.5. Dimmed *P*-regime: a) TEM image of the UC@SiO_2 with a 21 nm thick Au-shell (left image), PL scans of the same ROI with UC@SiO_2 NPs (middle scan) and in a 2nd step with additive Au-shelled UC@SiO_2 NPs (right scan) for keeping the scan conditions for both NP systems as comparable as possible. b) and c) Spectra of both single NP systems under 980 nm excitation below 1 kW/cm^2 and at about 20 kW/cm^2.

From SP spectra taken at low *P*, smaller than 1 kW/cm^2 (Fig. 7.5 b)), and at high *P* of about 20 kW/cm^2 (Fig. 7.5 c)) only reduced UC luminescence is detected and there is no enhancement by adding an Au-shell. The absence of certain emission bands at higher *P* for the Au-shelled system (red curve in Fig. 7.5 c)) demonstrates the strong quenching impact of the Au-shell, leading to diminished population of high energetic Er-ion levels and consequently reduced UCL.

Conclusion

For both measurement conditions, the saturated and the dimmed *P*-regimes, no enhancements of the UC luminescence were measured in the presence of an additional Au-shell compared to the metal-free UCNPs. In contrast, a strong reduction of the UC performance was detected, arising from metal-induced absorption and quenching effects, which are neither counterbalanced nor surpassed by the theoretically predicted plasmon-induced enhancements. However, our results do not automatically disprove the theoretical calculations of the plasmon resonances. The theoretical predictions of luminescence enhancement were only calculated for very specific NP geometries. Particularly the synthesis of the SiO_2 spacer layer with precise thickness is difficult to accomplish, which is a requirement for the resonant condition of the cavity mode. Another challenge is the synthesis of an Au-shell with a thickness which is thin enough to minimise metal-induced re-absorption effects but at the same time thick enough to be fully closed. Both requirements for the spacer and the Au layer were not precisely accomplished by the syntheses of our samples.

Furthermore, the saturation and dimmed pumping conditions, which were used to calculate the enhancement factors for low and high *P* as theoretical approximations, can only be adjusted to a limited extend. The *P*-range of the NIR-laser at the CLSM is limited from kW/cm^2 to MW/cm^2. Therefore, the slightly discrepancy in NP architecture and experimental *P* conditions compared to the theoretical calculations might explain the contrary results of reduced instead of enhanced UC intensities.

For further studies, the NP synthesis needs improvement as well as reproducibility to comply with the theoretical optimised NP geometry. Additionally, the development of a surface coating procedure for thin metal shells (≤ 10 nm) would enable NP geometries with smaller radius, fulfilling the theoretical conditions for dipole surface resonance modes with much higher local field enhancement. This would ultimately lead to broader field of applications due to the smaller size of metal-shelled UCNPs.

8 Summary and conclusion

In this thesis, the photo-physical properties of β-NaYF$_4$(Yb,Er) and β-NaYF$_4$(Nd,Yb,Er) UC nanomaterials, varying in size, doping composition and structural design, have been investigated at ensemble and single particle (SP) level. For the latter experiments, a confocal laser scanning microscope (CLSM) setup was designed, constructed and equipped with several lasers in the UV/vis/NIR range, two fast avalanche photo diodes (APDs) and a sensitive electron multiplying charge-coupled device (EMCCD) spectrograph. This setup was a crucial addition as it enables to measure the PL decay kinetics as well as to study PL intensity/brightness (B) and to acquire PL spectra of single UC particles with high spatial and spectral resolution. Additionally, the CLSM allows to study the strongly P-dependent behaviour of UCNPs over a large range from 1 kW/cm^2 up to 2.6 MW/cm^2, extending greatly the P range (5 - 400 W/cm^2) of our ensemble studies. Furthermore, to allow for precise localisation and verification of SPs rather than aggregated and clustered particles, an AFM was additionally installed in combination with the confocal microscope.

Influence of solvent, shell and small variation in Er^{3+} doping on the optical nature of NaYF$_4$(Yb,Er) UCNPs at ensemble and SP level

In an ensemble, the quantum yield (QY) and decay studies on β-NaYF$_4$: 20% Yb, x% Er (x = 1,2,3) under 980 nm excitation revealed a strong surface quenching by O-H vibrations in water and C-H vibrations in cyclohexane. As a result, a reduced upconversion luminescence (UCL) efficiency and accelerated decay kinetics of Yb and Er emissions have been found. However, an additional 5 nm inert surface passivation shell resulted in a significant increase of the UC QYs with an up to 70-fold enhancement at 5 W/cm^2, and about 12-times higher QYs at 100 W/cm^2 in cyclohexane. In water, a lower QY enhancement, at 100 W/cm^2, of approximately 8 was achieved, indicating the need for thicker shells. Furthermore, an increase in Er^{3+} doping from 1% to 3% only marginally enhanced the UC efficiency. A maximal QY of about 7.5% at 150 W/cm^2 for the 3% Er doped sample has been found. A comparison of the decay behaviour of the Yb (940 nm) and Er (540 and 655 nm) emission bands revealed that the 940 nm and the 540 nm emissions are more strongly quenched by water, while the 655 nm red emission is more quenched by cyclohexane. The ensemble studies show that the presence of a protective and thick enough shell is essential to achieve efficient UCL in both cyclohexane and water.

Moreover, SP studies have been performed with core- and core-shell 1% and 3% Er^{3+} ion doped samples. Several additional Er^{3+} ion emission bands have been observed and attributed to higher Er^{3+} energy levels, which can be amplified by increasing P. As a result, the overall emission colour has been changed from green to yellow to white with increasing P. Due to their different P-dependent emission behaviour, the UCL bands could be classified into three groups depending on the number of absorbed photons which are needed for the underlying UC process, like 2-3, 3-4 or 4+ photons. With increasing P, the complexity of the (de)population processes was also increased. The origin of the newly detected Er^{3+} emission bands and their P-dependency have been illustrated and explained using a Dieke diagram including Yb-Er energy transfers (ETs), excited state absorption (ESA), Er-Er cross-relaxations (CRs), Er-Yb back-energy transfer (BET) processes and non-radiative relaxation processes (nRPs).

The comparison of ensemble (dispersed in cyclohexane) and SP studies (dried on glass) has been realised by combining the P-dependent green-to-green (G/G) (541 nm / 556 nm) and green-to-red (G/R) (541 nm / 654 nm) peak ratios of the ensemble and SP studies, covering P over six orders of magnitude. These ratios indicate that at low and medium P, the protective shell is mainly responsible for an efficient UCL performance. For higher P, the shell becomes less relevant, while in contrast, the Er^{3+} ion doping content gains impact and influences mainly the UCL behaviour. These findings demonstrate that the surface quenching effects in SPs become less relevant at higher P, which was also confirmed by decay studies, showing the same lifetimes as that of the 3% Er doped NPs under different conditions (first dried on glass-substrate and then re-dispersed in cyclohexane). At the SP level, the additional contributions of higher energetic transitions result in faster decays of the green and the red emission bands. At higher P, the lifetimes of overlapping and closely lying emission bands cannot be sufficiently separated anymore. The decay studies, in particular, demonstrated that a reliable comparison of results achieved in ensemble and SP measurements varying in P and sample preparation, is difficult and limited to only a few measurement parameters, like P-dependent peak ratios and normalized PL spectra. These findings underline the importance of performing both, ensemble and SP measurements. In the future, a better comparability could be achieved by studying the photo-physical behaviour of the sensitizer Yb^{3+} ion not only at ensemble but also on SP level.

Influences of highly varying Er^{3+} and Yb^{3+} doping ratio on the optical properties of $NaYF_4$(Yb,Er) UCNPs at ensemble and SP level

The impact on the UC performance for strongly varying Yb^{3+} and Er^{3+} ion doping concentrations has been studied for sub-10 nm particles and sub-30 nm core-shell particles. It has been shown that an increase in Ln^{3+} ion doping concentration enhances the absorption cross-section of the nanoparticle (NP) and reduces the Ln-Ln distance, leading to enhanced ion-ion interactions (ETs, CRs) and concentration quenching. Furthermore, changing the Yb/Er ratio of sub-10 nm particles from 20/02 to 80/20 resulted in an enhanced emission intensity due to higher absorption cross-section, despite smaller QYs, as well as enhanced surface quenching effects. The latter have been confirmed by accelerated decay kinetics and a strong 808 nm emission band for $P < 200\ \mathrm{W/cm^2}$. In contrast, the 100% Er sample showed a significantly reduced UCL intensity which has been attributed to dominating Er-Er CRs and surface related quenching, that is not compensated by the 1.5 times higher absorption cross-section compared to the 20/02 Yb/Er sample. SPs with 80/20 Yb/Er ratio excited with high P, reached the highest intensity with a dominating red band. For the 100% Er doped sample, a stronger green emission intensity has been revealed in comparison to the 20/02 Yb/Er sample. The emission behaviour observed in ensemble and SP measurements varies largely at high Ln^{3+} doping, reflected by the G/R emission band ratios. An opposite trend for higher Yb and Er concentration with increasing P has been observed. For SPs, the surface-related quenching effects become less significantly at high P. The three samples gives a good overview of the P-dependent optical properties of sub-10 nm samples, first of the commonly used 20/02 Yb/Er sample as reference, second the competitive processes of efficient Yb-excitation and Er-Er interactions of the 80/20 Yb/Er sample, and third the impact of Er-Er interactions and direct Er-excitation of the 100% Er ion sample.

The comparison of the normalized PL spectra of the sub-10 nm 20/02 Yb/Er sample to μm-sized 18/02 Yb/Er doped $NaYF_4$ NCs revealed under ensemble condition different UCL behaviour, while at SP measurement condition with high P, an approximately equal emission behaviour of both samples was obtained. It can be concluded that at high P, not only quenching effects, but also the NP volume effect and the number of emitters per NP have strongly reduced influence on the optical properties of UCNPs.

Furthermore, the systematic change in Yb and Er concentration has been studied at the SP level for the sub-30 nm sized Yb series (Yb/Er: 20,40,60,98/02) and Er series (Yb/Er: 60/02,10,20,30). The key findings are variations in the emission colours, the band ratios, and the UCL efficiencies. The emission colour was found to change with doping concentration, whereas with higher Yb^{3+} ion content, the total emission colour changed to red due to higher ET rates and enhanced red-level feeding BET processes. A higher Er^{3+} ion content shifted the overall emission colour to the green. Furthermore, the reduced spectral contribution of the blue and green emission bands arising from 3 and 4+ photon absorption processes indicated a reduced population of high Er energy levels with higher Yb and Er concentration. This can be attributed to the enhanced depopulation of the energy levels of Er^{3+} ions via enhanced Er-Yb BET processes with higher Yb content and less efficient Yb-Er ETs per Er^{3+} ion with higher Er content.

The unexpected decrease of the Boltzmann coupled G/G (521 nm / 541 nm) ratio with higher Yb and Er concentration at high P limits the feasibility of a temperature sensor with both, high sensitivity and bright UCL. The maximum UCL intensity was achieved for the 60/02 and 60/10 Yb/Er samples with $P < 100$ kW/cm^2, and for the 60/10 and 60/20 Yb/Er samples at higher P. It can be concluded that at high P the brightest UCNPs are achieved by a dominating red emission band, realised by high Yb^{3+} ion doping. A further fine-tuning of the Yb/Er doping concentrations with ratios of 60/4,8,12,16 might help to find one even higher efficient UC particle system.

Comparison of Yb- and Nd-excitation impact on the optical properties of $NaYF_4$(Nd,Yb,Er) UCNPs at ensemble and SP level

The additional use of Nd^{3+} ions as sensitizers into a Yb^{3+}/Er^{3+}-doped $NaYF_4$ UCNP enables a shift from 980 nm (Yb-excitation) to 808 nm (Nd-excitation) with about 25-times lower absorption by water, and therefore, a reduced risk of sample overheating. These properties make Nd-sensitized UCNPs well-suited candidates for bio-applications. The differences of Yb- and Nd-excitation on the UCL performance of equally sized (Nd^{3+})/Yb^{3+}/Er^{3+}-doped core-shell-shell NPs with Nd^{3+} ions incorporated in the inner shell have been investigated P-dependently in water and cyclohexane at both, ensemble and SP level. For the NPs dispersed in cyclohexane, a negative impact of Nd^{3+} ions on the Yb-excitation was revealed by reduced QYs and faster decays of the Yb, and both, green and red Er emissions. This indicates a quenching process between Nd and Er ions at the core-shell interface. The absence of measurable Nd-Er interactions in water could be explained by more intense water-induced surface quenching, overshadowing the Nd-Er quenching effects at the core-shell interface. This can potentially be minimised by a thicker protective shell. In addition, the absorption cross-sections of the NP systems $\sigma_{UCNP}(\lambda)$ and the Nd^{3+} and Yb^{3+} ions $\sigma_{Ln}(\lambda)$ have been calculated and used to determine the NP brightness $B_{UC}(\lambda)$, which equals the product of $\sigma_{UCNP}(\lambda_{ex})$ and the QY. The absorption cross-sections of the ideal Nd- and Yb-excitation wavelengths matching the sensitizer absorption maxima at 794 nm and 976 nm have theoretically been determined. Using the ideal excitation wavelengths would lead to an enhancement of particle B_{UC}, particularly for the excitation of Nd with its sharp absorption peak. However, the higher absorption cross-section and lower water absorption of Nd^{3+} ions compared to Yb^{3+} ions, does not automatically lead to higher B_{UC} values under Nd-excitation (Nd→Yb→Er ETs) compared to Yb-excitation (Yb→Er ET). This can be explained by the additional ET from Nd→Yb which reduces the efficiency of the Nd-excitation. The higher absorption of 980 nm light by water compared to 808 nm light leads to more strongly reduced B_{UC} values with deeper penetration depth in water under Yb-excitation. Therefore, exceeding a certain penetration depth x_C, brighter UCL is expected under Nd-excitation. Calculations have revealed that x_C can be reduced by using the ideal excitation wavelengths, higher P values, or by an increase of Nd^{3+} ion content. However, in case of higher Nd^{3+} ion doping, the Nd-concentration quenching must be considered. Furthermore, the combined influence of light absorption and scattering on the UCL has been studied as proof of concept in a phantom tissue.

At the SP level, the emission spectra of Nd-doped NPs did not exhibit any visible contributions from highly energetic Er levels under Nd-excitation. This is indicative of the fact that the high P (up to 2 MW/cm^2) is not sufficient to compensate the strong non-radiative quenching channels arising from Nd-Er interactions. As was revealed for higher Yb/Er doping in chapter 5, an additional increase in Nd^{3+} ion doping concentration might enhance the Nd-sensitized UC efficiency at higher P. Besides the Ln^{3+} doping concentrations, also the particle architecture needs to be considered in further development to optimise

Nd/Yb/Er-doped samples. Possible designs could include complex multi-shell structures and controlled Ln-Ln separation.

LRET and plasmonic proof of concept studies

The luminescence resonance energy transfer (LRET) process between Er^{3+} ions of Yb/Er doped $NaYF_4$ UCNPs and sulforhodamine B (SRB) dyes, bound on the UCNP acting as donors and acceptors, has been studied in an ensemble as well as under SP condition. The main methods used throughout this study were emission spectroscopy, time-dependent PL, and fluorescence lifetime imaging (FLIM). Compared to the classical single donor-acceptor LRET process, the UCNP-based LRET is more complex, as a high number of donors interact with multiple acceptors at various Förster distances and LRET efficiencies (η_{LRET}). In an ensemble, a strong SRB emission has been observed and associated with a strongly reduced green UCL and a slightly enhanced red Er emission band. The increase of the red band is associated with a spectral contribution of the SRB dye emission overlapping with the red Er level. The results clearly show that the red Er band is indirectly affected by the LRET process. Consequently, the red band should not be taken as reference band, although being common practice. Additionally, by intended SRB photo-bleaching, the SP studies have revealed an intrinsic coupling between the red and green emissive Er energy levels. Both bands increased in intensity by simultaneous decrease of the SRB emission intensity. This disqualifies the red Er band as a reference for spectrum normalisation. Therefore, the LRET efficiency was calculated using the decay kinetics of acceptor and donor energy levels instead of the donor intensity reduction, which avoids the spectral contribution of unaffected emitters from the NP centre leading to a bias of the η_{LRET}. For ensemble and SP measurements, the same η_{LRET} of about 35% have been calculated for NPs with slight variation in size.
At the SP level with higher P, the additional Er emission bands arising from higher Er energy levels increase the LRET complexity, if they match the acceptor absorption band. However, to avoid photo-bleaching of the dye, a low laser P is required in conjunction with a short laser exposure time. In further studies, the P-dependent LRET efficiencies and the influence of additional Er emission bands on the LRET process should be determined based on P-dependent LT measurements and spectral emission scans in the low P-range ($\ll 1\,\mathrm{kW/cm^2}$). This, then, provides a deeper insight into the LRET processes of UCNPs and related applications.

Moreover, comparative studies of Au-shelled and metal-free UCNPs have been performed at the CLSM, attempting to confirm the theoretically predicted improvement of UCL performance caused by plasmonic field enhancement of a resonant cavity mode. The theoretical modelling was customised for saturated and dimmed P-regimes and predicted enhanced UCL only for very specific NP architectures which match the plasmonic resonance conditions. For both P conditions, which could be realised at our CLSM (lowest and highest P available), only reduced instead of enhanced UCL intensities were measured in the presence of an additional Au-shell. This reduction indicates a strong metal-induced absorption as well as quenching effects. However, these results do not necessarily disprove the calculations, as the geometry of the UCNPs did not perfectly match the required resonance conditions of the cavity modes. Particularly, the required nm-precise thickness of the SiO_2 spacer layers and the need for fully sealed Au-surfaces were difficult to be synthetically realised. Therefore, the contradictory results of theory and experiments can most likely be attributed to the discrepancies in NP architecture and experimental P conditions.

In further studies, an overall improved synthesis is necessary, together with the development of a synthesis strategy for thin metal shells (sub-10 nm) to meet the theoretical requirements for strong plasmonic dipole resonances. Ultimately, these small Au-shelled UCNPs could have a wide range of possible applications in enhanced UCL.

In conclusion, our home-built CLSM enables P-dependent UCL studies on SPs extending the P-range of ensemble measurements about several orders of magnitude up to the MW/cm^2 range. As shown throughout my thesis, high P values are imperative to investigate UCNPs in the SP regime where surface-related quenching effects and even volume effects of UCNPs are nearly negligible. This increases the comparability of mechanistic studies on Ln-Ln interactions, and their (de)population behaviour, and furthermore, enables a relative comparison of differently doped UCNP systems.

The use of specific peak ratios and normalized emission spectra realises the P-dependent comparison of ensemble and SP studies. Moreover, at high P, maximum brightness was achieved for highly Yb^{3+} ion doped UCNPs, resulting in a strong and dominating red emission band. For an enhanced contribution of blue and green Er^{3+} ion emission bands with strong intensities, both a high Er^{3+} ion content as well as a high Yb-to-Er ratio are needed at the same time, leading necessarily in search of a compromise.

These results show that a profound understanding of the complex mechanistic processes involved in UC processes is needed to design bright and efficient UCNPs for different application-relevant P-ranges with precise colour control and colour tuning. In the future, a better comparability of ensemble and SP measurements could be achieved by studying besides the UC process, as well the downconversion process, allowing a complete investigation of the mechanistic processes.

9 | Perspective

9.1. Low *P* and NIR-SWIR studies of single UCNPs

Low *P* studies for bio-applications

In this thesis, the SP research has been performed in the P range from 1 kW/cm^2 upto 2.6 MW/cm^2 as part of a mechanistic (de)population study. A future aim is to run SP studies at much lower P values as needed for bio-applications, like advanced LRET studies without dye bleaching or like single UCNP detection in organic cells for condition controlling or drug release. For the cell studies, the P value of an 980 nm excitation source should be at about 100 mW/cm^2 to guarantee comparable high signal-to-noise ratios, but also to prevent tissue damage through overheating [153, 154]. The installation of the electron multiplying CCD camera with increased sensitivity is one step to realise such sensitive measurements, furthermore a wheel with varied optical density filters should be installed to enable further attenuation of the excitation light. To keep the integration and accumulation times low, only optimised and bright UNCPs with specific adjusted doping concentrations (cf. high doping NPs, as discussed in section 5) should be used to allow for low P studies.

PL studies in the NIR-SWIR range

The extension of the detection range opens new opportunities for a detailed study of the UCNPs, especially Yb-sensitized systems and the measurement of DCL. Therefore, next upgrade of the CLSM setup (cf. section 3.3.1) is the installation of an additional InGaAs-SPAD (PDM-IR from MPD), which can be used for single photon detection in the NIR-SWIR spectral range (900 - 1600 nm).

The measurement of the time-resolved (de)population behaviour of the direct excited $^2F_{5/2}$ Yb energy level under 980 nm excitation is already part of the fundamental UCNP screening in ensemble condition to reveal the Yb^{3+}-related surface quenching effects, and energy-loss pathways, which generally needs to be minimised for optimised UC performance. Furthermore, the influence of Yb-to-Yb energy hopping and Yb^{3+} clustering effects of high Yb-doped NPs can be detected using the decay behaviour of the excited Yb energy level. To guarantee a high signal-to-noise ratio, a sharp BP filter should be used to cut out the excitation laser line at 980 nm and to let the Yb emission pass, either at shorter wavelength (940 - 950 nm range) or at longer wavelength (1000 - 1020 nm). Studying these direct Yb-induced effects on single UCNPs with varying excitation P (up to 2.6 MW/cm^2) would contribute to a deeper insight into the P-dependent (de)population processes and would also allow for comparison of the results to the corresponding ensemble studies.

In addition, the NIR-APD also enables the time-resolved study of the DC luminescent bands of UC materials on a SP level. In contrast to the UC processes, the DC transitions are more likely and more effective leading to relatively higher QYs and stronger luminescence intensities. The Yb/Er co-doped NaYF$_4$ crystals show a strong DC band at about 1540 nm ($^4I_{13/2} \rightarrow {}^4I_{15/2}$) and Tm co-doped systems reveal a NIR band at about 1450 nm ($^3H_4 \rightarrow {}^3F_4$) [155]. All of them are inside of the detection range (-1600 nm). The study of NIR emission bands is of high importance for several applications in the fields of telemetry, optical lasers and medical diagnostics.

9.2. Double-line excitations of single UCNPs

To gain further insight into the (de)population processes of the Ln^{3+} activators, the NIR excitation can be extended by an additional UV/vis/NIR excitation, matching the absorption lines of the relevant Ln^{3+} ions. After ETU by the NIR excitation, the excited Ln energy levels can be used as start levels for ESA with a second excitation source for direct excitation of higher Ln^{3+} ion energy levels, which cannot be directly reached with the NIR excitation. By using this double-line excitation processes, the (de)population rates of specific energy levels can vary strongly, and non-radiative pathways can be bridged. These processes might result in an altered luminescence behaviour, an potentially even lead to new emission bands. Thereby, the P-dependent change of both excitation sources should be included as part of a future study. In addition, using pulsed excitation sources, the time-dependent changes of both pulse lengths and relative pulse-timing should be part of varying parameters to investigate the time-dependent optical response.

In the case of Yb/Er doped UCNPs, the Er^{3+} shows many options to either excite specific energy levels (cf. Fig. 4.8 e)), or to measure the time-dependency of certain levels by stimulated depopulation, realised with pump-probe experiments. If, for instance, an additional excitation at 470 nm is used next to the typical 980 nm, several emission bands (like 400, 427, 556, 575, 585, 639 nm) and the Er-Yb BET process should show enhanced emission intensities and activity due to ESA processes: $^4I_{13/2} \rightarrow {}^4G_{7/2}$, $^4I_{11/2} \rightarrow {}^2P_{3/2}$ and $^4I_{9/2} \rightarrow {}^2D_{5/2}$.

In the case of Nd/Yb/Er triple-doped UCNPs, the simultaneous Nd- and Yb-excitation at 808 nm and 980 nm should, ideally lead to an enhanced UC emission intensity. In water, an additional Yb-excitation might intensify the UC emission. Nevertheless, the laser power must be below a certain threshold to avoid sample heating.

At our CLSM, the supercontinuum laser covers the vis range from 480 nm to 850 nm. However, the choice of an additional excitation wavelength is not only limited by the available laser but also the optical components. E.g., appropriate filters and dichroic mirrors must be found which fit both excitation wavelengths equally well. Furthermore, the separated wavelengths lead to different focal points due to diffraction behaviour of the objective. If the foci of the two wavelengths show a large difference, as expected for simultaneous UV and NIR excitation, an appropriate correction is required.

9.3. Temperature-sensing in high *P* microscopy

In ensemble condition at low *P*, the G/G (521 nm to 541 nm) band ratio is commonly used for T-sensing, since both levels are thermally coupled and their populations follow the Boltzmann distribution [156, 157]. In contrast, on the SP level with *P* values up to $\mathrm{MW/cm^2}$, the linear T-dependency of the G/G ratio cannot be expected anymore, as with higher *P* the (de)population processes (ESA, nRP, CRs) become much more complex and might even affect the population of the higher-lying green level. The presented results have shown that T values of about 280°C are expected for the sample in the laser focus, assuming a linear T-dependency, cf. section 4.4. Given that the estimated temperature can be assumed to be realistic, there are additional limitations of this method proposed for T-sensing: It has been shown that there was a decrease of the G/G peak ratio with higher $\mathrm{Yb^{3+}}$ ion concentration (cf. Fig. A.13 b)), rather than an increase which was expected.

In conclusion, at high *P*, the G/G ratio must be either newly calibrated or additionally peak ratios have to be taken into account for T-sensing. One suggestion is to use the 440 nm to 454 nm peak ratio, as it has a smaller energy gap ($\Delta(^4F_{3/2}$ - $^4F_{5/2}) \approx 350\ \mathrm{cm^{-1}}$) than the G/G levels ($\Delta(^2H_{11/2}$ - $^4S_{3/2}) \approx 750\ \mathrm{cm^{-1}}$), however, these emission bands are only relevant for high *P*. Furthermore, the 454 nm to 495 nm peak ratio seems promising due to the larger energy shift ($\Delta(^4F_{5/2}$ - $^4F_{7/2}) \approx 1650\ \mathrm{cm^{-1}}$), having the potential to cover higher T values. Runowski et al. [158] has proven, that even T values of up to 1000 K can be sensed, using the sensitive T-dependency of ($\mathrm{Tm^{3+}/Tm^{3+}}$) and ($\mathrm{Yb^{3+}/Tm^{3+}}$) peak ratios of Yb/Tm co-doped $\mathrm{YVO_4}$ UCNPs. If this approach could be applied for the Yb/Er UCNPs, the thermal energy uptake by laser radiation and the local T could be screened simultaneously during the measurements. Ultimately, this method would allow to unravel the direct T influences on the optical processes in SP studies.

Bibliography

[1] S. Gai, C. Li, P. Yang, and J. Lin. Recent progress in rare earth micro/nanocrystals: Soft chemical synthesis, luminescent properties, and biomedical applications. *Chemical reviews*, 114, 12 2013.

[2] Z. Zhang, S. Shikha, J. Liu, J.and Zhang, and Q. Mei. Upconversion nanoprobes: Recent advances in sensing applications. *Analytical Chemistry*, 91, 09 2018.

[3] U. Resch-Genger and H. Gorris. Perspectives and challenges of photon-upconversion nanoparticles - Part I: routes to brighter particles and quantitative spectroscopic studies. *Analytical and bioanalytical chemistry*, 409, 07 2017.

[4] X. Lin, Y. Wang, X. Chen, R. Yang, Z. Wang, J. Feng, H. Wang, K. W. C. Lai, J. He, F. Wang, and P. Shi. Multiplexed optogenetic stimulation of neurons with spectrum-selective upconversion nanoparticles. *Advanced Healthcare Materials*, 6(17):1700446, 2017.

[5] S. Chen, A. Weitemier, X. Zeng, L. He, X. Wang, Y. Tao, A. Huang, Y. Hashimotodani, M. Kano, H. Iwasaki, L. Parajuli, S. Okabe, D. Teh, A. All, I. Tsutsui-Kimura, K. Tanaka, X. Liu, and T. Mchugh. Near-infrared deep brain stimulation via upconversion nanoparticle–mediated optogenetics. *Science*, 359:679–684, 02 2018.

[6] K. Ao, Y.and Zeng, B. Yu, Y. Miao, W. Hung, Z. Yu, Y. Xue, T. Tan, T. Xu, M. Zhen, X. Yang, Y. Zhang, and S. Gao. An upconversion nanoparticle enables near infrared-optogenetic manipulation of the c. elegans motor circuit. *ACS Nano*, 13, 01 2019.

[7] Y. Liu, Y. Lu, X. Yang, X. Zheng, S. Wen, F. Wang, X. Vidal, J. Zhao, D. Liu, Z. Zhou, C. Ma, J. Zhou, J. Piper, P. Xi, and D.-Y. Jin. Amplified stimulated emission in upconversion nanoparticles for super resolution nanoscopy. *Nature*, 543, 01 2017.

[8] Q. Zhan, H. Liu, B. Wang, Q. Wu, R. Pu, C. Zhou, B. Huang, X. Peng, H. Agren, and S. He. Achieving high-efficiency emission depletion nanoscopy by employing cross relaxation in upconversion nanoparticles. *Nature Communications*, 8:1058, 10 2017.

[9] X. Qin, J. Xu, Y. Wu, and X. Liu. Energy-transfer editing in lanthanide-activated upconversion nanocrystals: A toolbox for emerging applications. *ACS Central Science*, 5, 01 2019.

[10] N. Idris, M. Jayakumar, and A. Bansal. Upconversion nanoparticles as versatile light nanotransducers for photoactivation applications. *Chemical Society reviews*, 44, 06 2014.

[11] Y. Liu, X. Meng, and W. Bu. Upconversion-based photodynamic cancer therapy. *Coordination Chemistry Reviews*, 379:82–98, 2019. Novel and Smart Photosensitizers from Molecule to Nanoparticle.

[12] M. Hamblin. Upconversion in photodynamic therapy: Plumbing the depths. *Dalton Transactions*, 47, 02 2018.

[13] J. C. Goldschmidt and S. Fischer. Upconversion for photovoltaics – a review of materials, devices and concepts for performance enhancement. *Advanced Optical Materials*, 3, 04 2015.

[14] S. Han, W. Huang, and X. Liu. Cheminform abstract: Enhancing solar cell efficiency: The search for luminescent materials as spectral converters. *Chemical Society reviews*, 42, 10 2012.

[15] R. Martín-Rodríguez, S. Fischer, A. Ivaturi, B. Fröhlich, K. Krämer, J. C. Goldschmidt, B. Richards, and A. Meijerink. Highly efficient IR to NIR upconversion in Gd_2O_2s: Er^{3+} for photovoltaic applications. *Chemistry of Materials*, 25:1912–1921, 05 2013.

[16] L. Mackenzie and R. Pal. Circularly polarized lanthanide luminescence for advanced security inks. *Nature Reviews Chemistry*, 5, 12 2020.

[17] P. Kumar, S. Singh, and B. Gupta. Future prospects of luminescent nanomaterial based security inks: From synthesis to anti-counterfeiting applications. *Nanoscale*, 8, 07 2016.

[18] S. Shikha, T. Salafi, and J. Cheng. Versatile design and synthesis of nano-barcodes. *Chem. Soc. Rev.*, 46, 10 2017.

[19] J. Zhou, S. Xu, J. Zhang, and J. Qiu. Upconversion luminescence behavior of single nanoparticles. *Nanoscale*, 7, 06 2015.

[20] O. Dukhno, V. Przybilla, F.and Muhr, M. Buchner, T. Hirsch, and Y. Mély. Time-dependent luminescence loss of individual upconversion nanoparticles upon dilution in aqueous solutions. *Nanoscale*, 10, 07 2018.

[21] C. Lee, E. Xu, Y. Liu, A. Teitelboim, K. Yao, A. F Bravo, A. Kotulska, S. Nam, Y. Suh, A. Bednarkiewicz, B. Cohen, E. Chan, and P. Schuck. Giant nonlinear optical responses from photon-avalanching nanoparticles. *Nature*, 589:230–235, 01 2021.

[22] Y. Liu, Z. Zhou, F. Wang, G. Kewes, S. Wen, S. Burger, M. Wakiani, P. Xi, J. Yang, X. Yang, O. Benson, and D.-Y. Jin. Axial localization and tracking of self-interference nanoparticles by lateral point spread functions. *Nature Communications*, 12:2019, 04 2021.

[23] D. R. Gamelin and H. U. Güdel. Design of luminescent inorganic materials: new photophysical processes studied by optical spectroscopy. *Accounts of Chemical Research*, 33(4):235–242, 2000. PMID: 10775316.

[24] F. Auzel. Upconversion and anti-stokes processes with f and d ions in solids. *Chemical Reviews*, 104(1):139–174, 2004. PMID: 14719973.

[25] G. Zhou, D Wang, X. Wang, Z. Shao, and M. Jiang. Two-photon absorption and excited state absorption properties of an organic dye PSPI. *Optics Communications*, 241(1):215 – 219, 2004.

[26] F. Zhang. *General Introduction to Upconversion Luminescence Materials*, pages 1–20. Springer Berlin Heidelberg, Berlin, Heidelberg, 2015.

[27] X. Li, F. Zhang, and D. Zhao. Highly efficient lanthanide upconverting nanomaterials: Progresses and challenges. *Nano Today*, 8(6):643 – 676, 2013.

[28] F. Wang and X. Liu. Recent advances in the chemistry of lanthanide-doped upconversion nanocrystals. *Chem. Soc. Rev.*, 38:976–989, 2009.

[29] Y. Liu, D. Tu, H. Zhu, and X. Chen. Lanthanide-doped luminescent nanoprobes: controlled synthesis, optical spectroscopy, and bioapplications. *Chem. Soc. Rev.*, 42:6924–6958, 2013.

[30] M. Haase and H. Schäfer. Upconverting nanoparticles. *Angewandte Chemie (International ed. in English)*, 50:5808–29, 06 2011.

[31] Z. Wang and A. Meijerink. Concentration quenching in upconversion nanocrystals. *The Journal of Physical Chemistry C*, 122(45):26298–26306, 2018.

[32] R. Martín-Rodríguez, F. T. Rabouw, M. Trevisani, M. Bettinelli, and A. Meijerink. Upconversion dynamics in Er^{3+}-doped Gd_2O_2S: Influence of excitation power, Er^{3+} concentration, and defects. *Advanced Optical Materials*, 3(4):558–567, 2015.

[33] F. T. Rabouw, P. T. Prins, P. Villanueva-Delgado, M. Castelijns, R. G. Geitenbeek, and A. Meijerink. Quenching pathways in $NaYF_4$:Er^{3+},Yb^{3+} upconversion nanocrystals. *ACS Nano*, 12(5):4812–4823, 2018. PMID: 29648802.

[34] G. Chen, H. Ågren, T. Y. Ohulchanskyy, and P. N. Prasad. Light upconverting core–shell nanostructures: nanophotonic control for emerging applications. *Chem. Soc. Rev.*, 44:1680–1713, 2015.

[35] S. Fischer, N. Bronstein, J. K. Swabeck, E. M. Chan, and A. P. Alivisatos. Precise tuning of surface quenching for luminescence enhancement in core–shell lanthanide-doped nanocrystals. *Nano Letters*, 16(11):7241–7247, 2016. PMID: 27726405.

[36] J. Zuo, D. Sun, L. Tu, Y. Wu, Y. Cao, B. Xue, Y. Zhang, Y. Chang, X. Liu, X. Kong, W. J. Buma, E. J. Meijer, and H. Zhang. Precisely tailoring upconversion dynamics via energy migration in core–shell nanostructures. *Angewandte Chemie International Edition*, 57(12):3054–3058, 2018.

[37] C. Homann, L. Krukewitt, F. Frenzel, B. Grauel, C. Würth, U. Resch-Genger, and M. Haase. $NaYF_4$:Yb,Er/$NaYF_4$ core/shell nanocrystals with high upconversion luminescence quantum yield. *Angewandte Chemie International Edition*, 57(28):8765–8769, 2018.

[38] G. Chen, H. Qiu, P. N. Prasad, and X. Chen. Upconversion nanoparticles: Design, nanochemistry, and applications in theranostics. *Chemical Reviews*, 114(10):5161–5214, 2014. PMID: 24605868.

[39] M. Pollnau, D. R. Gamelin, S. R. Lüthi, H. U. Güdel, and M. P. Hehlen. Power dependence of upconversion luminescence in lanthanide and transition-metal-ion systems. *Phys. Rev. B*, 61:3337–3346, Feb 2000.

[40] G. Chen, G. Somesfalean, Y. Liu, Z. Zhang, Q. Sun, and F. Wang. Upconversion mechanism for two-color emission in rare-earth-ion-doped ZrO_2 nanocrystals. *Phys. Rev. B*, 75:195204, May 2007.

[41] N. Menyuk, K. Dwight, and J.W. Pierce. $NaYF_4$: Yb,Er — an efficient upconversion phosphor. *Applied Physics Letters*, 21(4):159–161, 1972.

[42] F. Wang, Y. Han, C. Lim, Y. Lu, J. Wang, J. Xu, H. Chen, C. Zhang, M. Hong, and X. Liu. Simultaneous phase and size control of upconversion nanocrystals through lanthanide doping. *Nature*, 463:1061–5, 02 2010.

[43] C. Würth, M. Kaiser, S. Wilhelm, B. Grauel, T. Hirsch, and U. Resch-Genger. Excitation power dependent population pathways and absolute quantum yields of upconversion nanoparticles in different solvents. *Nanoscale*, 9:4283–4294, 2017.

[44] Y. Wang, G. Liu, L. Sun, J. Xiao, Ji. Zhou, and C. Yan. Nd^{3+}-sensitized upconversion nanophosphors: Efficient in vivo bioimaging probes with minimized heating effect. *ACS Nano*, 7(8):7200–7206, 2013. PMID: 23869772.

[45] J. Shen, G. Chen, A. Vu, W. Fan, O. S. Bilsel, C.h Chang, and G. Han. Engineering the upconversion nanoparticle excitation wavelength: Cascade sensitization of tri-doped upconversion colloidal nanoparticles at 800 nm. *Advanced Optical Materials*, 1(9):644–650, 2013.

[46] X. Xie, N. Gao, R. Deng, Q. Sun, Q. Xu, and X. Liu. Mechanistic investigation of photon upconversion in Nd^{3+}-sensitized core–shell nanoparticles. *Journal of the American Chemical Society*, 135(34):12608–12611, 2013. PMID: 23947580.

[47] Y. Zhong, G. Tian, Z. Gu, Y. Yang, L. Gu, Y. Zhao, Y. Ma, and J. Yao. Elimination of photon quenching by a transition layer to fabricate a quenching-shield sandwich structure for 800 nm excited upconversion luminescence of Nd^{3+}-sensitized nanoparticles. *Advanced Materials*, 26(18):2831–2837, 2014.

[48] X. Li, R. Wang, F. Zhang, L. Zhou, D. Shen, C. Yao, and D. Zhao. Nd^{3+} sensitized up/down converting dual-mode nanomaterials for efficient in-vitro and in-vivo bioimaging excited at 800 nm. *Scientific reports*, 3:3536, December 2013.

[49] N. Estebanez Bloem, J. Ferrera González, L. Francés-Soriano, R. Arenal, M. González-Béjar, and J. Pérez-Prieto. Breaking the Nd^{3+}-sensitized upconversion nanoparticles myth about the need of onion-layered structures. *Nanoscale*, 10, 06 2018.

[50] S. L. Steven L Jacques. Optical properties of biological tissues: a review. *Physics in Medicine and Biology*, 58(11):R37–R61, may 2013.

[51] L. M. Wiesholler, F. Frenzel, B. Grauel, C. Würth, U. Resch-Genger, and T. Hirsch. Yb,Nd,Er-doped upconversion nanoparticles: 980 nm versus 808 nm excitation. *Nanoscale*, 11:13440–13449, 2019.

[52] L. Mackenzie, J. Goode, A. Vakurov, P. Nampi, S. Saha, G. Jose, and P. Millner. The theoretical molecular weight of $NaYF_4$:RE upconversion nanoparticles. *Scientific Reports*, 8, 01 2018.

[53] T. Bhutta, D. Shepherd, C. Serrano, and E. Daran. Nd:LaF_3 channel waveguide lasers fabricated by molecular beam epitaxy. *Filtration Industry Analyst*, 01 2000.

[54] B. del Rosal, A. Perez, E. Carrasco, D. Jovanovic, M. Dramicanin, G. Dražić, A. Juarranz, F. Sanz-Rodriguez, and D. Jaque. Neodymium-based stoichiometric ultrasmall nanoparticles for multifunctional deep-tissue photothermal therapy. *Advanced Optical Materials*, pages n/a–n/a, 03 2016.

[55] V. Lupei, A. Lupei, and A. Ikesue. Transparent Nd and (Nd, Yb)-doped Sc_2O_3 ceramics as potential new laser materials. *Applied Physics Letters*, 86:111118–111118, 03 2005.

[56] Y.-F. Wang, G.-Y. Liu, L.-D. Sun, J. Xiao, J.-C. Zhou, and C.-H. Yan. Nd^{3+}-sensitized upconversion nanophosphors: Efficient in vivo bioimaging probes with minimized heating effect. *ACS nano*, 7, 07 2013.

[57] V. Lupei, A. Lupei, C. Gheorghe, and A. Ikesue. Sensitized Yb^{3+} emission in (Nd, Yb):$Y_3Al_5O_{12}$ transparent ceramics. *Journal of Applied Physics*, 108:123112–123112, 12 2010.

[58] T. Főrster. 10th spiers memorial lecture. transfer mechanisms of electronic excitation. *Discuss. Faraday Soc.*, 27:7–17, 1959.

[59] J. Jackson. *Classical electrodynamics*. 2004.

[60] T. Kaudse. Diplomarbeit - Erweiterung eines einzelmolekuel-FRET-spektrometers um alternierende laseranregung und charakterisierung des systems, 2009.

[61] I. Medintz and N. Hildebrandt. *FRET - Förster Resonance Energy Transfer: From Theory to Applications*. 2013.

[62] C. Zhang, L. Sun, Y. Zhang, and C. Yan. Rare earth upconversion nanophosphors: synthesis, functionalization and application as biolabels and energy transfer donors. *Journal of Rare Earths*, 28(6):807–819, 2010.

[63] J. Lakowicz. *Principles of Fluorescence Spectroscopy*, volume 1. 01 2006.

[64] Y. Fu, X. Chen, X. Mou, Z. Ren, X. Li, and G. Han. A dual-color luminescent localized drug delivery system with ratiometric-monitored doxorubicin release functionalities. *ACS Biomaterials Science & Engineering*, 2(4):652–661, 2016. PMID: 33465865.

[65] N. Hildebrandt, C. M. Spillmann, W. R. Algar, T. Pons, M. H. Stewart, E. Oh, K. Susumu, S. A. Díaz, J. B. Delehanty, and I. L. Medintz. Energy transfer with semiconductor quantum dot bioconjugates: A versatile platform for biosensing, energy harvesting, and other developing applications. *Chemical Reviews*, 117(2):536–711, 2017. PMID: 27359326.

[66] V. Muhr, C. Würth, M. Kraft, M. Buchner, A. J. Baeumner, U. Resch-Genger, and T. Hirsch. Particle-size-dependent förster resonance energy transfer from upconversion nanoparticles to organic dyes. *Analytical Chemistry*, 89(9):4868–4874, 2017. PMID: 28325045.

[67] M. I. Saleh, I. D. Panas, F. Frenzel, C. Würth, B. Rühle, Y. L. Slominskii, A. Demchenko, and U. Resch-Genger. Sensitization of upconverting nanoparticles with a NIR-emissive cyanine dye using a micellar encapsulation approach. *Methods and Applications in Fluorescence*, 7(1):014003, jan 2019.

[68] S. Bhuckory, E. Hemmer, Y.-T. Wu, A. Yahia, F. Vetrone, and N. Hildebrandt. Core or shell? Er^{3+} FRET donors in upconversion nanoparticles. *European Journal of Inorganic Chemistry*, 2017, 08 2017.

[69] C. L. C. Smith, N. Stenger, A. Kristensen, N. A. Mortensen, and S. I. Bozhevolnyi. Gap and channeled plasmons in tapered grooves: a review. *Nanoscale*, 7:9355–9386, 2015.

[70] W. R. Erwin, H. F. Zarick, E. M. Talbert, and R. Bardhan. Light trapping in mesoporous solar cells with plasmonic nanostructures. *Energy Environ. Sci.*, 9:1577–1601, 2016.

[71] T. D. Barrett, T. H. Doherty, and A. Kuhn. Pushing Purcell enhancement beyond its limits. *New Journal of Physics*, 22(6):063013, jun 2020.

[72] K. A. Willets and R. P. Van Duyne. Localized surface plasmon resonance spectroscopy and sensing. *Annual Review of Physical Chemistry*, 58(1):267–297, 2007. PMID: 17067281.

[73] J.-X. Liu, H. He, D. Xiao, S. Yin, W. Ji, S. Jiang, D. N. Luo, B. Wang, and Y. Liu. Recent advances of plasmonic nanoparticles and their applications. *Materials*, 11, 2018.

[74] K. Park, M. Park, H. Jang, J. Park, J. Kim, Y. Cho, I. Han, D. Byun, and H. Ko. Highly secure plasmonic encryption keys combined with upconversion luminescence nanocrystals. *Advanced Functional Materials*, 28, 04 2018.

[75] P. Anger, P. Bharadwaj, and L. Novotny. Enhancement and quenching of single-molecule fluorescence. *Phys. Rev. Lett.*, 96:113002, Mar 2006.

[76] W. Park, D. Lu, and S. Ahn. Plasmon enhancement of luminescence upconversion. *Chem. Soc. Rev.*, 44:2940–2962, 2015.

[77] S. Schietinger, T. Aichele, H. Wang, T. Nann, and O. Benson. Plasmon-enhanced upconversion in single $NaYF_4$:Yb^{3+}/Er^{3+} codoped nanocrystals. *Nano Letters*, 10(1):134–138, 2010. PMID: 20020691.

[78] N. J. Greybush, M. Saboktakin, X. Ye, C. Della Giovampaola, S. J. Oh, N. E. Berry, N. Engheta, C. B. Murray, and C. R. Kagan. Plasmon-enhanced upconversion luminescence in single nanophosphor–nanorod heterodimers formed through template-assisted self-assembly. *ACS Nano*, 8(9):9482–9491, 2014. PMID: 25182662.

[79] D. Piatkowski, N. Hartmann, T. Macabelli, M. Nyk, S. Mackowski, and A. Hartschuh. Silver nanowires as receiving-radiating nanoantennas in plasmon-enhanced upconversion processes. *Nanoscale*, 7:1479–1484, 2015.

[80] K. Green, J. Wirth, and S. Shuang Fang Lim. Optical investigation of gold shell enhanced 25 nm diameter upconverted fluorescence emission. *Nanotechnology*, 27(13):135201, feb 2016.

[81] A. Alizadehkhaledi, A. L. Frencken, M. K. Dezfouli, S. Hughes, F. C. J. M. van Veggel, and R. Gordon. Cascaded plasmon-enhanced emission from a single upconverting nanocrystal. *ACS Photonics*, 6(5):1125–1131, 2019.

[82] A. Das, C. Mao, S. Cho, K. Kim, and W. Park. Over 1000-fold enhancement of upconversion luminescence using water-dispersible metal-insulator-metal nanostructures. *Nature Communications*, 9, 12 2018.

[83] W. Zhang, F. Ding, and S. Y. Chou. Large enhancement of upconversion luminescence of $NaYF_4$:Yb^{3+}/Er^{3+} nanocrystal by 3D plasmonic nano-antennas. *Advanced Materials*, 24(35):OP236–OP241, 2012.

[84] H. P. Paudel, L. Zhong, K. Bayat, M. F. Baroughi, S. Smith, C. Lin, C. Jiang, M. T. Berry, and P. S. May. Enhancement of near-infrared-to-visible upconversion luminescence using engineered plasmonic gold surfaces. *The Journal of Physical Chemistry C*, 115(39):19028–19036, 2011.

[85] M. Saboktakin, X. Ye, U. K. Chettiar, N. Engheta, C. B. Murray, and C. R. Kagan. Plasmonic enhancement of nanophosphor upconversion luminescence in Au nanohole arrays. *ACS Nano*, 7(8):7186–7192, 2013. PMID: 23909608.

[86] Q. Sun, H. Mundoor, J. C. Ribot, V. Singh, I. I. Smalyukh, and P. Nagpal. Plasmon-enhanced energy transfer for improved upconversion of infrared radiation in doped-lanthanide nanocrystals. *Nano Letters*, 14(1):101–106, 2014. PMID: 24279776.

[87] A. Chu, H. He, Z. Yin, R. Peng, H. Yang, X. Gao, D. Luo, R. Chen, G. Xing, and Y. J. Liu. Plasmonically enhanced upconversion luminescence via holographically formed silver nanogratings. *ACS Applied Materials & Interfaces*, 12(1):1292–1298, 2020. PMID: 31820628.

[88] I. L. Rasskazov, L. Wang, C. J. Murphy, R. Bhargava, and P. S. Carney. Plasmon-enhanced upconversion: engineering enhancement and quenching at nano and macro scales. *Opt. Mater. Express*, 8(12):3787–3804, Dec 2018.

[89] T. Som and B. Karmakar. Enhancement of Er^{3+} upconverted luminescence in Er^{3+}: Au-antimony glass dichroic nanocomposites containing hexagonal Au nanoparticles. *J. Opt. Soc. Am. B*, 26(12):B21–B27, Dec 2009.

[90] H. K. Dan, D. Zhou, R. Wang, Q. Jiao, Z. Yang, Z. Song, X. Yu, and J. Qiu. Effects of gold nanoparticles on the enhancement of upconversion and near-infrared emission in Er^{3+}/Yb^{3+} co-doped transparent glass–ceramics containing BaF_2 nanocrystals. *Ceramics International*, 41(2, Part B):2648 – 2653, 2015.

[91] D. Mendez-Gonzalez, S. Melle, O. G. Calderón, M. Laurenti, E. Cabrera-Granado, A. Egatz-Gómez, E. López-Cabarcos, J. Rubio-Retama, and E. Díaz. Control of upconversion luminescence by gold nanoparticle size: from quenching to enhancement. *Nanoscale*, 11:13832–13844, 2019.

[92] D. M. da Silva, L. R. P. Kassab, S. R. Lüthi, C. B. de Araújo, A. S. L. Gomes, and M. J. V. Bell. Frequency upconversion in Er^{3+} doped PbO–GeO_2 glasses containing metallic nanoparticles. *Applied Physics Letters*, 90(8):081913, 2007.

[93] S. Tirtha and K. Basudeb. Nano Au enhanced upconversion in dichroic Nd^{3+}:Au–antimony glass nanocomposites. *Solid State Sciences*, 11(5):1044–1051, 2009. E-MRS symposium N and R.

[94] J. Ueda, S. Tanabe, and A. Ishida. Surface plasmon excited infrared-to-visible upconversion in Er^{3+}-doped transparent glass ceramics. *Journal of Non-Crystalline Solids*, 355(37):1912–1915, 2009. Non-Oxide and New Optical Glasses 16.

[95] S. K. S. K. Singh, N. K. Giri, D. K. Rai, and S. B. Rai. Enhanced upconversion emission in Er^{3+}-doped tellurite glass containing silver nanoparticles. *Solid State Sciences*, 12(8):1480–1483, 2010.

[96] Z. Pan, A. Ueda, R. Aga, A. Burger, R. Mu, and S. H. Morgan. Spectroscopic studies of Er^{3+} doped Ge-Ga-S glass containing silver nanoparticles. *Journal of Non-Crystalline Solids*, 356(23):1097–1101, 2010.

[97] Sahar M. R. Amjad R. J. et al. Reza Dousti, M. Enhanced frequency upconversion in Er^{3+}-doped sodium lead tellurite glass containing silver nanoparticles. *Eur. Phys. J.*, 66(237), 2012.

[98] R. J. Amjad, M .R. Sahar, S .K. Ghoshal, M. R. Dousti, S. Riaz, and B. A. Tahir. Enhanced infrared to visible upconversion emission in Er^{3+} doped phosphate glass: Role of silver nanoparticles. *Journal of Luminescence*, 132(10):2714–2718, 2012.

[99] X. Jia, M. Xia, Y. Xu, L. Yang, Y. Zhang, M. Li, and S. Dai. Silver nanoparticle enhanced 2.7 μm luminescence in Er^{3+}-doped bismuth germanate glasses. *Opt. Mater. Express*, 8(6):1625–1632, Jun 2018.

[100] L. Meng. *Thermal and optical-gain effects in nanophotonics with applications to sensing and perfect absorption.* PhD thesis, ICFO - The Institute of Photonic Sciences and UPC - Universitat Politècnica de Catalunya, 2018.

[101] M. Kraft. *Spectroscopic characterization of upconversion nanomaterials with systematically varied material composition and surface chemistry.* PhD thesis, Humboldt-Universität zu Berlin, Mathematisch-Naturwissenschaftliche Fakultät, 2019.

[102] M. Kaiser, C. Würth, M. Kraft, I. Hyppänen, T. Soukka, and U. Resch-Genger. Power-dependent upconversion quantum yield of $NaYF_4$:Yb^{3+},Er^{3+} nano- and micrometer-sized particles – measurements and simulations. *Nanoscale*, 9:10051–10058, 2017.

[103] M. Kraft, C. Würth, V. Muhr, T. Hirsch, and U. Resch-Genger. Particle-size-dependent upconversion luminescence of $NaYF_4$: Yb, Er nanoparticles in organic solvents and water at different excitation power densities. *Nano Research*, 08 2018.

[104] M. S. Meijer, P. A. Rojas-Gutierrez, D. Busko, I. A. Howard, F. Frenzel, C. Würth, U. Resch-Genger, B. S. Richards, A. Turshatov, J. A. Capobianco, and S. Bonnet. Absolute upconversion quantum yields of blue-emitting $LiYF_4$:Yb^{3+},Tm^{3+} upconverting nanoparticles. *Phys. Chem. Chem. Phys.*, 20:22556–22562, 2018.

[105] J. Kalisz. Review of methods for time interval measurements with picosecond resolution. *METROLOGIA Metrologia*, 41:17–32, 02 2004.

[106] W. Yu, W. Xu, H. Song, and S. Zhang. Temperature-dependent upconversion luminescence and dynamics of $NaYF_4$:Yb^{3+}/Er^{3+} nanocrystals: influence of particle size and crystalline phase. *Dalton Trans.*, 43:6139–6147, 2014.

[107] F. Frenzel, C. Würth, O. Dukhno, F. Przybilla, L. M. Wiesholler, V. Muhr, T. Hirsch, Y. Mély, and U. Resch-Genger. Multiband emission from single β-$NaYF_4$(Yb,Er) nanoparticles at high excitation power densities and comparison to ensemble studies. *Nano Research*, 2021.

[108] E. Bayati, S. Zhan, A.and Colburn, and A. Majumdar. Role of refractive index in metalens performance. *Applied Optics*, 58:1460, 02 2019.

[109] O. Hollrichter and W. Ibach. *High-Resolution Optical and Confocal Microscopy*, volume 158 of *Springer Series in Optical Sciences*. Springer-Verlag Berlin Heidelberg, 2010.

[110] S. Hell. Far-field optical nanoscopy. volume 316, pages 3–4, 11 2010.

[111] V. Ntziachristos. Fluorescence molecular imaging. *Annual review of biomedical engineering*, 8:1–33, 02 2006.

[112] S. Wilhelm, B. Gröbler, M. Gluch, and M. Heinz. Grundlagen: Die konfokale laser scanning mikroskopie. Technical report, Carl Zeiss.

[113] F. Weigert. *Characterization of Photo-Physical Properties of Semiconductor Quantum Dots at the Ensemble and Single Particle Level*. PhD thesis, Technische Universität Berlin, Mathematisch-Naturwissenschaftliche Fakultät, 2021.

[114] S. Wilhelm, M. Kaiser, C. Würth, J. Heiland, C. Carrillo-Carrion, V. Muhr, O. S. Wolfbeis, W. J. Parak, U. Resch-Genger, and T. Hirsch. Water dispersible upconverting nanoparticles: effects of surface modification on their luminescence and colloidal stability. *Nanoscale*, 7:1403–1410, 2015.

[115] V. Muhr. *Design, Synthesis and Surface Modification of Lanthanide-Doped Nanoparticles for FRET-Based Biosensing Applications*. PhD thesis, Universität Regensburg, Fakultät Chemie und Pharmazie, 2017.

[116] M. Kaiser, C. Würth, M. Kraft, T. Soukka, and U. Resch-Genger. Explaining the influence of dopant concentration and excitation power density on the luminescence and brightness of $NaYF_4$:Yb^{3+},Er^{3+} nanoparticles: Measurements and simulations. *Nano Research*, 06 2019.

[117] F. Wang, J. Wang, and X. Liu. Direct evidence of a surface quenching effect on size-dependent luminescence of upconversion nanoparticles. *Angewandte Chemie International Edition*, 49(41):7456–7460, 2010.

[118] S. Fischer, N. Johnson, J. Pichaandi, J. C. Goldschmidt, and F. Veggel. Upconverting core-shell nanocrystals with high quantum yield under low irradiance: On the role of isotropic and thick shells. *Journal of Applied Physics*, 118:193105, 11 2015.

[119] G. Yao, C. Lin, Q. Meng, S. M. May, and M. T. Berry. Calculation of Judd-Ofelt parameters for Er^{3+} in β-$NaYF_4$: Yb^{3+}, Er^{3+} from emission intensity ratios and diffuse reflectance spectra. *Journal of Luminescence*, 160:276 – 281, 2015.

[120] D. Sardar, J. Gruber, B. Zandi, J. Hutchinson, and C. Trussell. Judd-Ofelt analysis of the Er^{3+}($4f^{11}$) absorption intensities in phosphate glass: Er^{3+}, Yb^{3+}. *Journal of Applied Physics*, 93:2041 – 2046, 03 2003.

[121] R. Wegh, E. van Loef, G. Burdick, and A. Meijerink. Luminescence spectroscopy of high-energy $4f^{11}$ levels of Er^{3+} in fluorides. *Molecular Physics*, 101:1047–1056, 04 2003.

[122] O'Shea, D. G., Ward, J. M., Shortt, B. J., Mortier, M., Féron, P., and Chormaic, S. N. Upconversion channels in Er^{3+}:ZBLALiP fluoride glass microspheres. *Eur. Phys. J. Appl. Phys.*, 40(2):181–188, 2007.

[123] X. Chen, E. Ma, and G. Liu. Energy levels and optical spectroscopy of Er^{3+} in Gd_2O_3 nanocrystals. *The Journal of Physical Chemistry C*, 111(28):10404–10411, 2007.

[124] Z. X. Cheng, S. J. Zhang, F. Song, H. C. Guo, J. R. Han, and H. C. Chen. Optical spectroscopy of Yb/Er codoped $NaY(WO_4)_2$ crystal. *Journal of Physics and Chemistry of Solids*, 63(11):2011–2017, nov 2002.

[125] L. Marciniak, K. Waszniewska, A. Bednarkiewicz, D. Hreniak, and W. Strek. Sensitivity of a nanocrystalline luminescent thermometer in high and low excitation density regimes. *The Journal of Physical Chemistry C*, 120(16):8877–8882, 2016.

[126] N. Bhiri, M. Dammak, M. Aguiló, F. Díaz, J. Carvajal, and M. Pujol. Stokes and anti-stokes operating conditions dependent luminescence thermometric performance of Er^{3+}-doped and Er^{3+}, Yb^{3+} co-doped $GdVO_4$ microparticles in the non-saturation regime. *Journal of Alloys and Compounds*, 814:152197, 09 2019.

[127] M. T. Berry and P. S. May. Disputed mechanism for NIR-to-red upconversion luminescence in $NaYF_4$:Yb^{3+},Er^{3+}. *The Journal of Physical Chemistry A*, 119(38):9805–9811, 2015. PMID: 26325357.

[128] M. Yuan, R. Wang, C. Zhang, Z. Yang, W. Cui, X. Yang, N. Xiao, H. Wang, and X. Xu. Exploiting the silent upconversion emissions from a single β-$NaYF_4$:Yb/Er microcrystal via saturated excitation. *J. Mater. Chem. C*, 6:10226–10232, 2018.

[129] Y. Cho, S. W. Song, S. Y. Lim, J. H. Kim, C. R. Park, and H. M. Kim. Spectral evidence for multi-pathway contribution to the upconversion pathway in $NaYF_4$:Yb^{3+},Er^{3+} phosphors. *Phys. Chem. Chem. Phys.*, 19:7326–7332, 2017.

[130] F. T. Rabouw, P. T. Prins, P. Villanueva-Delgado, M. Castelijns, R. G. Geitenbeek, and A. Meijerink. Quenching pathways in $NaYF_4$:Er^{3+},Yb^{3+} upconversion nanocrystals. *ACS Nano*, 12(5):4812–4823, 2018. PMID: 29648802.

[131] R. Mauricio, Z. Carlos, M. Jaume, and D. Francisco. Optical absorption of Er^{3+} in $RbTiOPO_4$ and $KTiOPO_4$. *Journal of Physics-Condensed Matter*, 10113:10101–10113, 1998.

[132] X. Mateos, R. Solé, J. Gavaldà, M. Aguiló, F. Díaz, and J. Massons. Ultraviolet and visible emissions of Er^{3+} in $KY(WO_4)_2$ single crystals co-doped with Yb^{3+} ions. *Journal of Luminescence*, 115(3):131 – 137, 2005.

[133] A. A. Lyapin, S. V. Gushchin, A. S. Ermakov, S. V. Kuznetsov, P. A. Ryabochkina, V. Yu. Proydakova, V. V. Voronov, P. P. Fedorov, and M. V. Chernov. Mechanisms and absolute quantum yield of upconversion luminescence of fluoride phosphors. *Chin. Opt. Lett.*, 16(9):091901, Sep 2018.

[134] F. Vetrone, R. Naccache, A. Zamarrón, A. Juarranz de la Fuente, F. Sanz-Rodríguez, L. Martinez Maestro, E. Martín Rodriguez, D. Jaque, J. García Solé, and J. A. Capobianco. Temperature sensing using fluorescent nanothermometers. *ACS Nano*, 4(6):3254–3258, 2010. PMID: 20441184.

[135] J. Bergstrand, Q. Liu, B. Huang, X. Peng, C. Würth, U. Resch-Genger, Q. Zhan, J. Widengren, H. Ågren, and H. Liu. On the decay time of upconversion luminescence. *Nanoscale*, 11:4959–4969, 2019.

[136] F. Vetrone, J.-C. Boyer, J. A. Capobianco, A. Speghini, and M. Bettinelli. Significance of Yb^{3+} concentration on the upconversion mechanisms in codoped Y_2O_3:Er^{3+}, Yb^{3+} nanocrystals. *Journal of Applied Physics*, 96(1):661–667, 2004.

[137] E. M. Chan, E. S. Levy, and B. E. Cohen. Rationally designed energy transfer in upconverting nanoparticles. *Adv Mater*, 27(38):5753–61, 2015.

[138] B. Chen and F. Wang. Combating concentration quenching in upconversion nanoparticles. *Accounts of Chemical Research*, 53(2):358–367, 2020. PMID: 31633900.

[139] A. Podhorodecki, B. Krajnik, L. W. Golacki, U. Kostiv, G. Pawlik, M. Kaczmarek, and D. Horák. Percolation limited emission intensity from upconverting $NaYF_4$:Yb^{3+},Er^{3+} nanocrystals – a single nanocrystal optical study. *Nanoscale*, 10:21186–21196, 2018.

[140] R. Arppe, I. Hyppänen, N. Perälä, R. Peltomaa, M. Kaiser, C. Würth, S. Christ, U. Resch-Genger, M. Schäferling, and T. Soukka. Quenching of the upconversion luminescence of $NaYF_4$:Yb^{3+},Er^{3+} and $NaYF_4$:Yb^{3+},Tm^{3+} nanophosphors by water: the role of the sensitizer Yb^{3+} in non-radiative relaxation. *Nanoscale*, 7:11746–11757, 2015.

[141] J. Wang, R. Deng, M. A. MacDonald, B. Chen, J. Yuan, F. Wang, D. Chi, T. Andy Hor, P. Zhang, G. Liu, Y. Han, and X. Liu. Enhancing multiphoton upconversion through energy clustering at sublattice level. *Nature Materials*, 13(2):157–162, 2014.

[142] L. Sun, R. Gao, T. Pan, X.-C. Ai, L. Fu, and J.-P. Zhang. Concentration-regulated photon upconversion and quenching in $NaYF_4$:Yb^{3+},Er^{3+} nanocrystals: nonexponentiality revisited. *Nanoscale*, 11:18150–18158, 2019.

[143] W. Wei, Y. Zhang, R. Chen, J. Goggi, N. Ren, L. Huang, K. K. Bhakoo, H. Sun, and T. T. Y. Tan. Cross relaxation induced pure red upconversion in activator- and sensitizer-rich lanthanide nanoparticles. *Chemistry of Materials*, 26(18):5183–5186, 2014.

[144] C. Würth, S. Fischer, B. Grauel, A. P. Alivisatos, and U. Resch-Genger. Quantum yields, surface quenching, and passivation efficiency for ultrasmall core/shell upconverting nanoparticles. *Journal of the American Chemical Society*, 140(14):4922–4928, 2018.

[145] R. B. Anderson, S. J. Smith, P. S. May, and M. T. Berry. Revisiting the NIR-to-visible upconversion mechanism in β-$NaYF_4$:Yb^{3+},Er^{3+}. *The Journal of Physical Chemistry Letters*, 5(1):36–42, 2014. PMID: 26276178.

[146] B. Grauel. *$NaYF_4$:Yb,Er-Upconversion-Nanopartikel: Aufklärung von Energieverlustprozessen zur systematischen Erhöhung der Lumineszenzeffizienz.* PhD thesis, Humboldt-Universität zu Berlin, Mathematisch-Naturwissenschaftliche Fakultät, 2021.

[147] W.M. Haynes, D. Lide, and T. Bruno. *Handbook of Chemistry and Physics.* CRC Press, Taylor and Francis Group, 6000 Broken Sound Parkway NW, Suite 300, Boca Raton, 95 edition, 2014. ISBN 978-1-4822-0868-9.

[148] C. Würth, B. Grauel, M. Pons, F. Frenzel, P. Rissiek, K. Rücker, U. Resch-Genger, and M. Haase. The upconversion luminescence quantum yield of highly doped $NaYF_4$:Yb,Er/$NaYF_4$:Lu core/shell nanocrystals. *submitted to Angewandte Chemie International Edition*, 2021.

[149] B. Grauel, C. Würth, C. Homann, L. Krukewitt, E. Andresen, J. Roik, S. Recknagel, M. Haase, and U. Resch-Genger. Volume and surface effects on two-photonic and three-photonic processes in dry co-doped upconversion nanocrystals. *Nano Research*, 08 2021.

[150] Y. Cen, Y.-M. Wu, X.-J. Kong, S. Wu, R.-Q. Yu, and X. Chu. Phospholipid-modified upconversion nanoprobe for ratiometric fluorescence detection and imaging of phospholipase d in cell lysate and in living cells. *Analytical Chemistry*, 86(14):7119–7127, 2014. PMID: 24939283.

[151] C. Kembuan. *Synthesis and characterization of gold shell nanoparticles for controlled enhancement of photon upconversion process.* PhD thesis, Freie Universität Berlin, Department of Biology, Chemistry and Pharmacy, 2019.

[152] S. Maysoon. *Upconversion Nanoparticles: Stability, Surface Modification and Dye Sensitization.* PhD thesis, Freie Universität Berlin, Department of Biology, Chemistry and Pharmacy, 2021.

[153] Q. Liu, W. Feng, T. Yang, T. Yi, and F. Li. Upconversion luminescence imaging of cells and small animals. *Nature protocols*, 8:2033–44, 10 2013.

[154] Q. Zhan, J. Qian, H. Liang, G. Somesfalean, D. Wang, S. He, Z. Zhang, and S. Andersson-Engels. Using 915 nm laser excited Tm^{3+}/Er^{3+}/Ho^{3+}-doped $NaYbF_4$ upconversion nanoparticles for in vitro and deeper in vivo bioimaging without overheating irradiation. *ACS Nano*, 5(5):3744–3757, 2011. PMID: 21513307.

[155] M. Kochanowicz, J. Zmojda, A. Baranowska, P. Miluski, M. Lesniak, M. Kuwik, J. Pisarska, W. A. Pisarski, J. Dorosz, and D. Dorosz. Near-IR and mid-IR luminescence

and energy transfer in fluoroindate glasses co-doped with Er^{3+}/Tm^{3+}. *Opt. Mater. Express*, 9(12):4772–4781, Dec 2019.

[156] D. Jaque and F. Vetrone. Luminescence nanothermometry. *Nanoscale*, 4:4301–4326, 2012.

[157] X. Wang, X. Kong, Y. Yu, Y. Sun, and H. Zhang. Effect of annealing on upconversion luminescence of $ZnO:Er^{3+}$ nanocrystals and high thermal sensitivity. *The Journal of Physical Chemistry C*, 111(41):15119–15124, 2007.

[158] M. Runowski, P. Woźny, N. Stopikowska, I. R. Martín, V. Lavín, and S. Lis. Luminescent nanothermometer operating at very high temperature—sensing up to 1000 K with upconverting nanoparticles (Yb^{3+}/Tm^{3+}). *ACS Applied Materials & Interfaces*, 12(39):43933–43941, 2020. PMID: 32869638.

A Appendix

A.1. Chapter 3 - Experimental basis

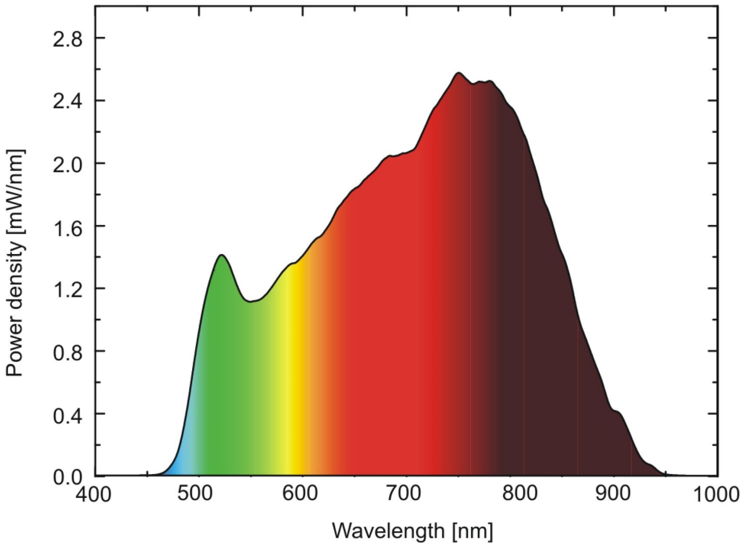

Figure A.1. Spectral dependent laser output power of the SOLEA Supercontinuum Laser from PicoQuant covering the vis range from about 480 to 850 nm. Taken from the PicoQuant Solea Datasheet.

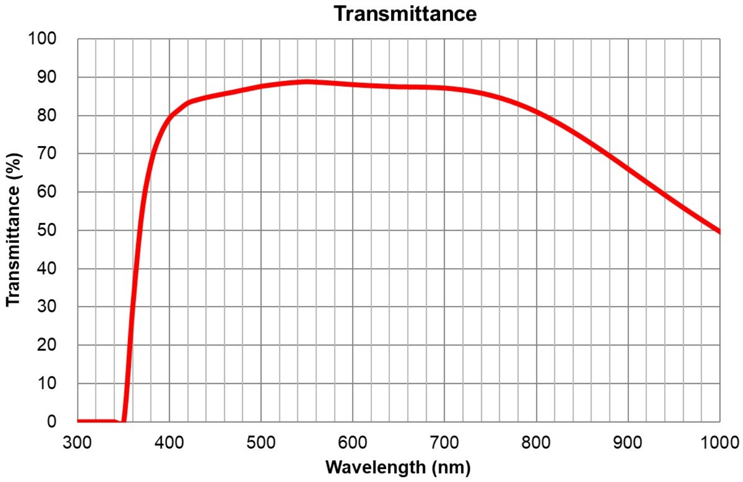

Figure A.2. Transmission behaviour of UPLSAPO100XO Plan Apochromat objective from Olympus with 100x magnification, 1.4 NA and working distance of 0.013 mm. Taken from the Olympus UPLSAPO100XO Datasheet.

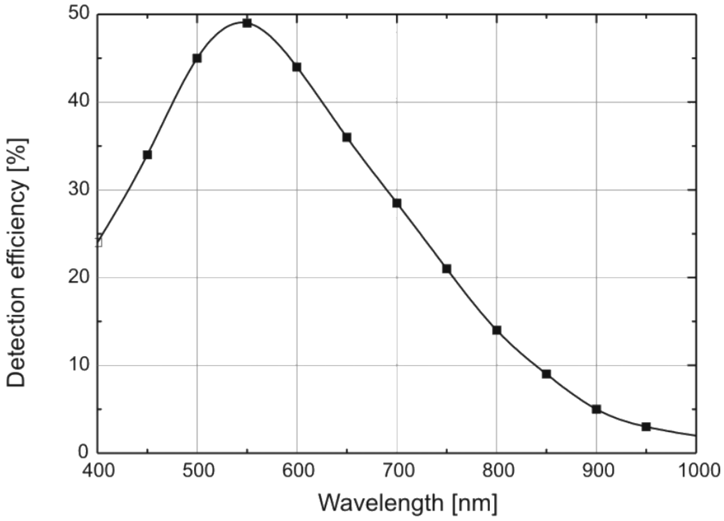

Figure A.3. Spectral detection efficiency of the Single Photon Avalanche Diodes APD, model "MPD-100-CTB" of the PDM series from PicoQuant, Germany.

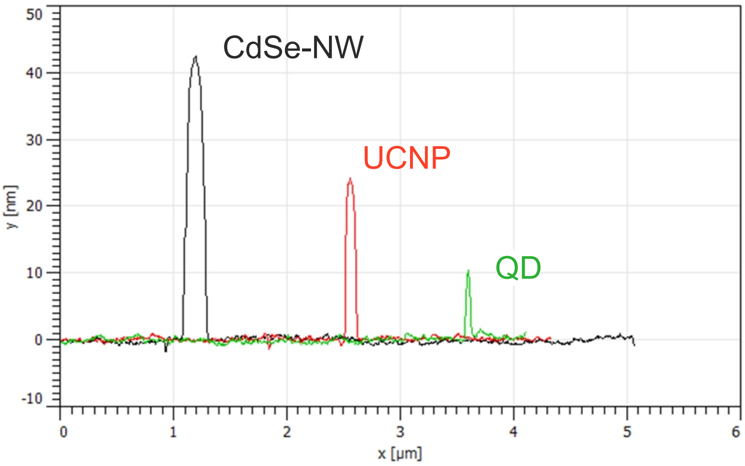

Figure A.4. Height profiles of one CdSe-nanowire (NW), one UCNP and one QD illustrating the possibility of clear differentiation of the three material systems from AFM topographic information. Taken from [113].

A.2. Chapter 4 - Yb/Er UC materials

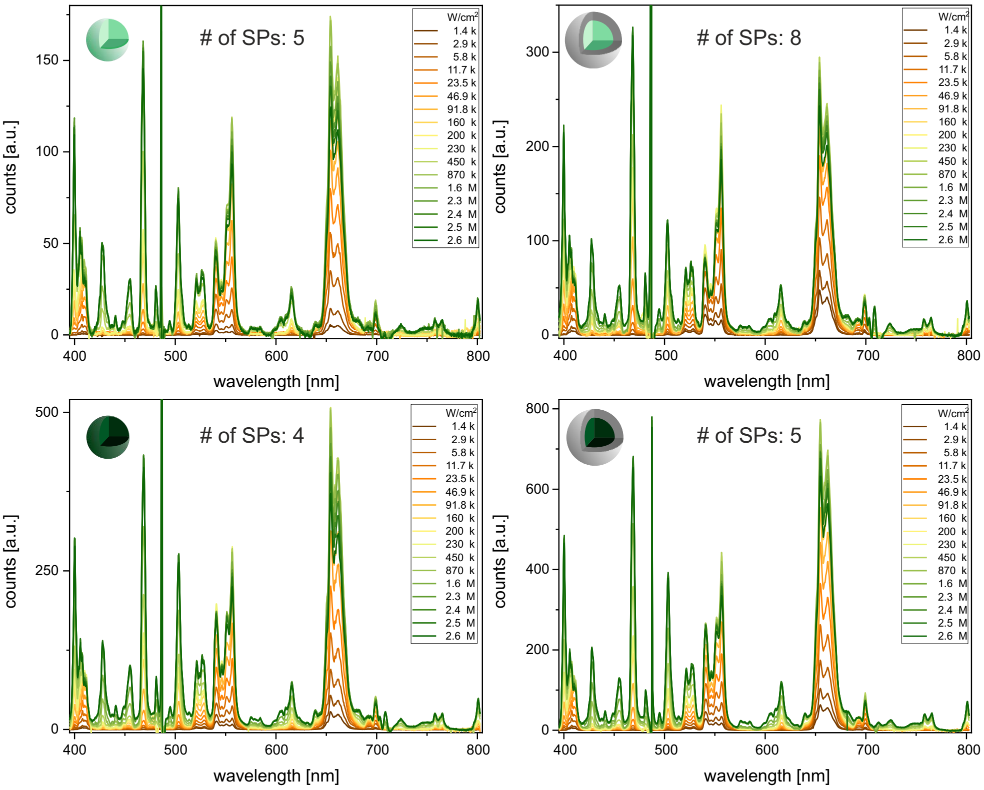

Figure A.5. *P*-dependent spectra of core and core-shell NPs with 1% Er^{3+} (upper plots) and 3% Er^{3+} (bottom plots) doping taken in the *P* range of 1.4 kW/cm^2 - 2.6 MW/cm^2. These spectra are averaged results from individual emission spectra of 5, 8, 4 and 5 single particles of the corresponding NP system and cover a spectral range from 390 to 810 nm. Taken and modified from own publication [107].

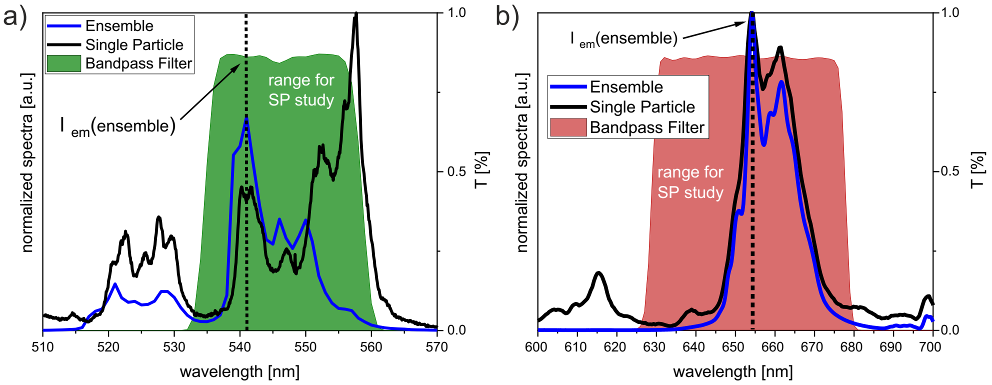

Figure A.6. Comparison of the spectral regions of the ensemble (blue) and the SP UC emission (black) using different detection methods, a monochromator for the ensemble and a bandpass-filter for SP studies: a) Green emission band with the 541 ±1 nm peak cut out with the monochromator for ensemble studies and the transmissive spectral region from 533-557 nm for the SP studies. b) Red emission band with the 654 ±1 nm peak cut out with the monochromator for ensemble studies and the transmissive spectral region from 635-675 nm for the SP studies. This illustrating the contribution of the 556 nm and the 639 nm emission bands to the green and red decay kinetic measurements of SPs at high *P*. Taken and modified from own publication [107].

A.3. Chapter 5 - High variation in Yb and Er doping

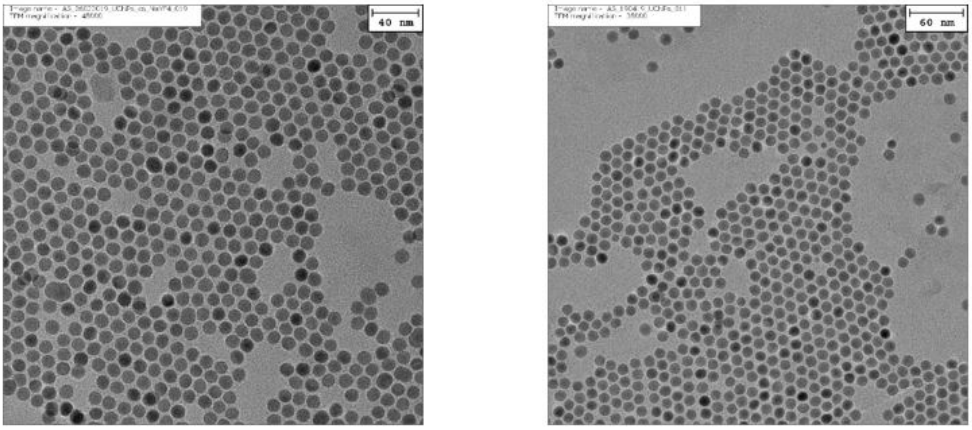

β-NaYF$_4$(20%Yb,2%Er)@NaYF$_4$
core-shell: 12.3 ± 1.2 nm
corresponding core: 8.5 ± 0.8 nm

β-NaYbF$_4$(20%Er)@NaYF$_4$
core-shell: 12.8 ± 0.9 nm
corresponding core: 8.4 ± 0.5 nm

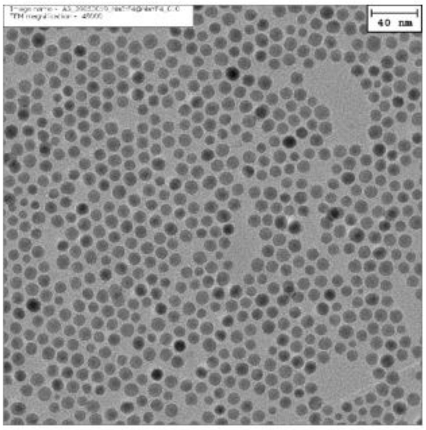

β-NaErF$_4$@NaYF$_4$
core-shell: 11.2 ± 1.4 nm
corresponding core: 6.0 ± 0.4 nm

Figure A.7. TEM images of core-shell NPs and corresponding size distribution of core and core-shell NPs of the three samples with Yb/Er ratios of 10/02, 80/20 and 0/100. The measurements and size analysis has been performed by Alexandra Schroter from the Hirsch group (Regensburg).

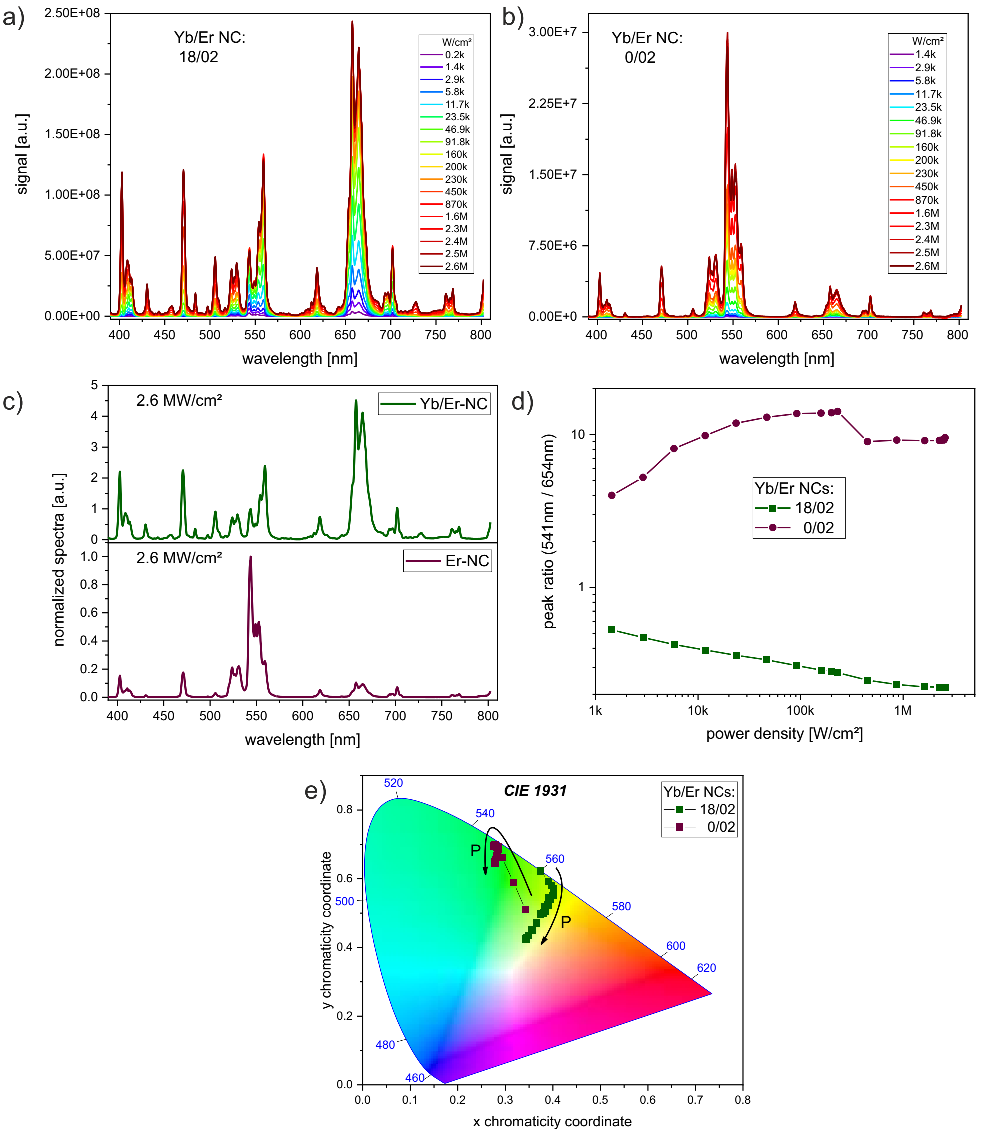

Figure A.8. *P*-dependent optical behaviour of μm-sized UCNCs with Yb/Er ratios of 18/02 (Yb/Er-NC) from K. Kramer (University of Bern) and 0/02 (Er-NC) provided from Th. Jüstl (FH Münster): a) and b) *P*-dependent spectra of the two samples measured on the CLSM covering a *P* range from 1 kW/cm^2 to 2.6 MW/cm^2. c) Normalized spectra comparison of the two samples taken at maximal *P* of 2.6 MW/cm^2. d) 541 nm to 654 nm peak ratios. e) CIE diagram for illustration of the overall emission colours changing with *P*.

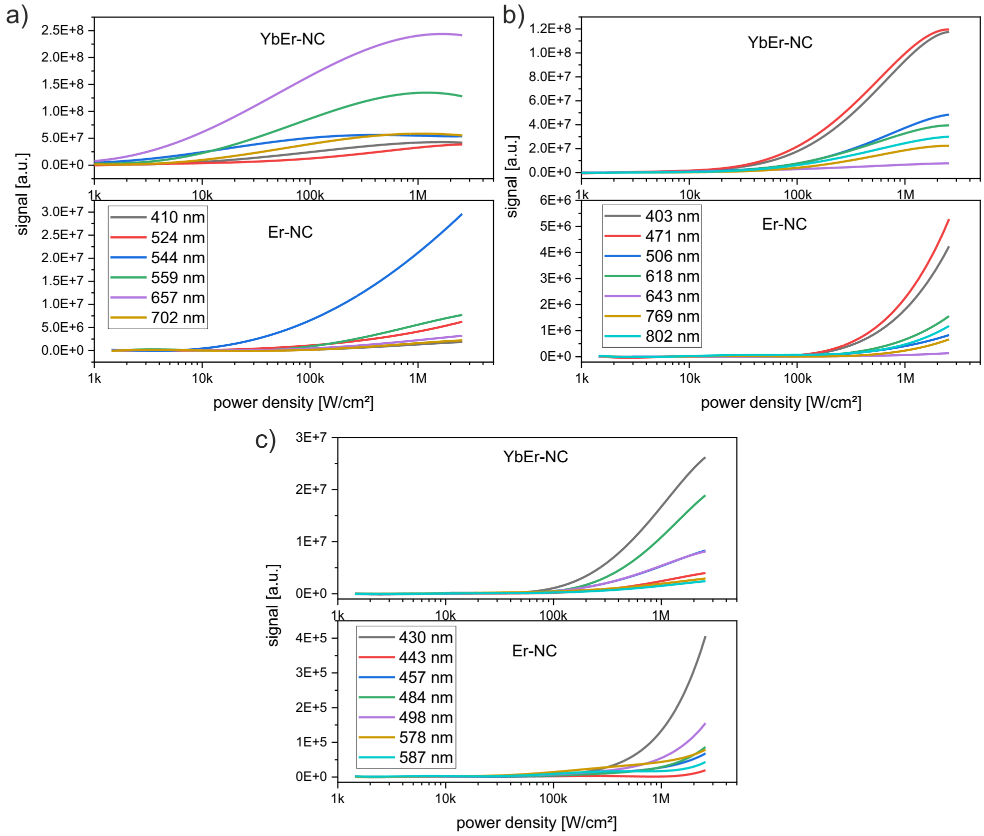

Figure A.9. P-dependent optical behaviour of μm-sized UCNCs with Yb/Er ratios of 18/02 (Yb/Er-NC) from K. Kramer (University of Bern) and 0/02 (Er-NC) provided from Th. Jüstl (FH Münster): a)-c) Classification of the main emission bands into three groups corresponding to 2–3, 3–4 and 4 photonic processes as described in [107].

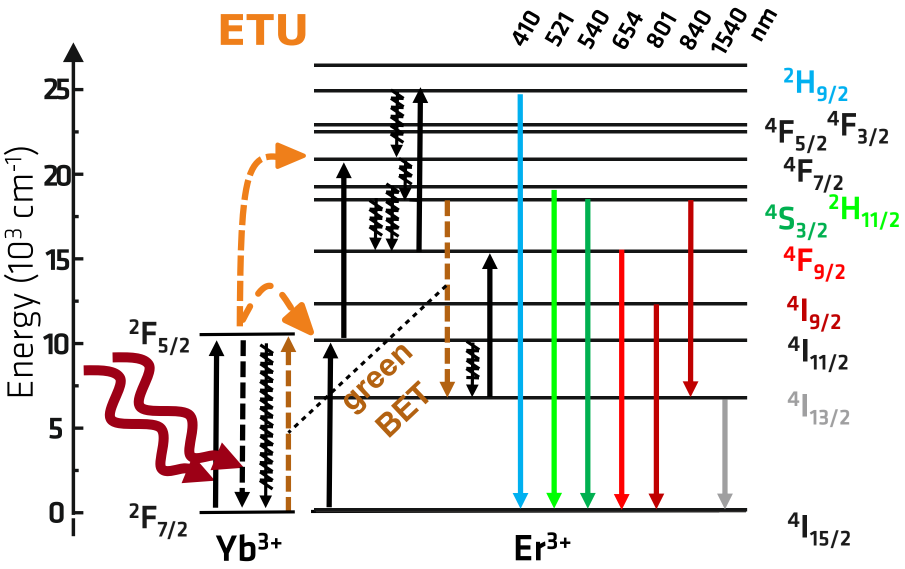

Figure A.10. Dieke diagram of Yb-Er interacting ions illustrating the "green BET", which is an Er-Yb back-energy transfer and was proposed for NaYbF$_4$:2% Er UCNPs by [141].

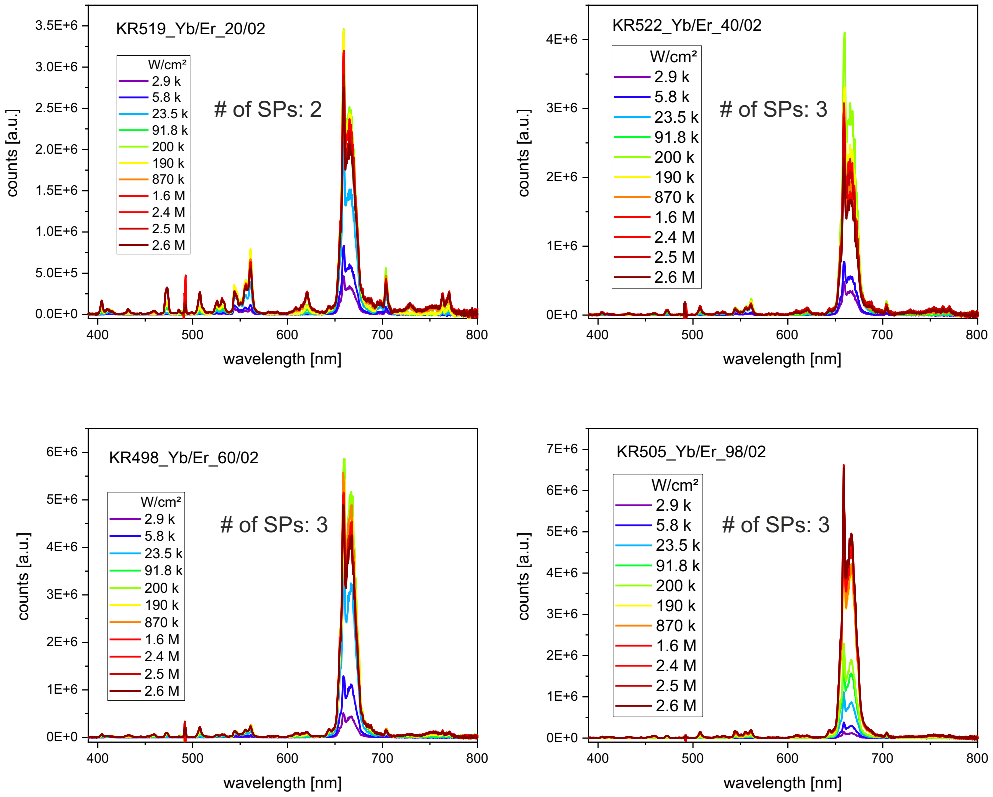

Figure A.11. *P*-dependent emission spectra in range from 1 kW/cm^2 to 2.6 MW/cm^2 of the Yb series synthesized by Haase group (Osnabrück) following the synthesis protocol described in [37], with the Yb/Er ratios of 20/02, 40/02, 60/02 and 98/02. These spectra are averaged results from individual emission spectra of 2 and 3 single particles of the corresponding NP system.

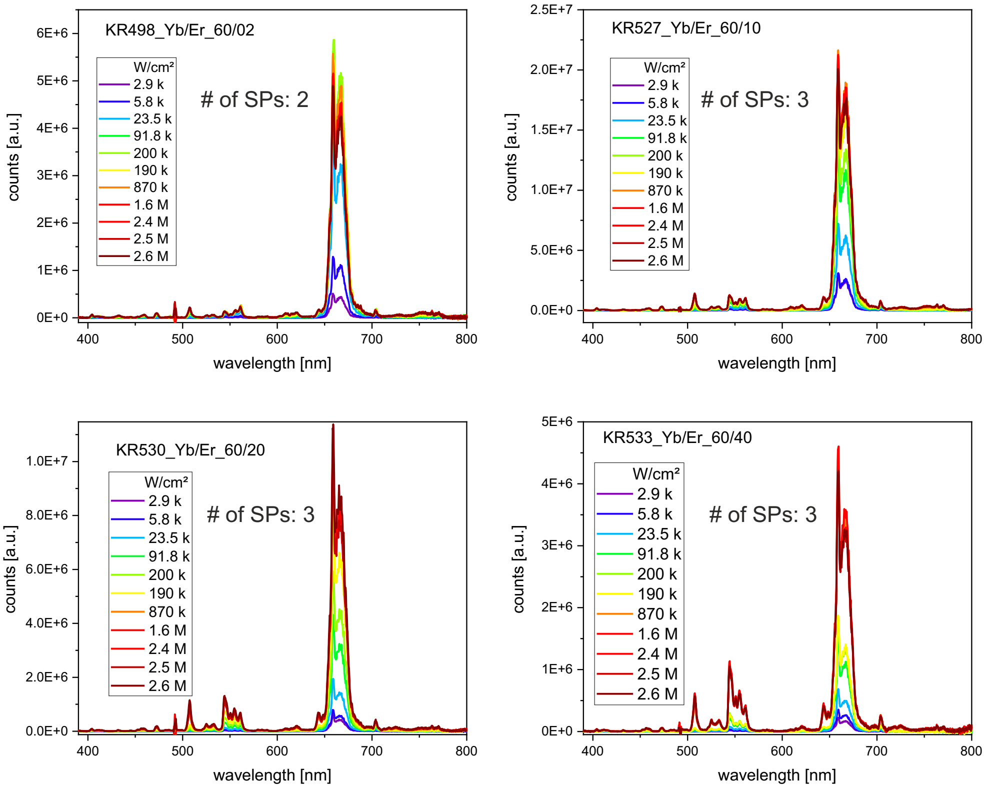

Figure A.12. P-dependent emission spectra in range from 1 kW/cm^2 to 2.6 MW/cm^2 of the Er series synthesized by Haase group (Osnabrück) following the synthesis protocol described in [37], with the Yb/Er ratios of 60/02, 60/10, 60/20 and 60/40. These spectra are averaged results from individual emission spectra of 2 and 3 single particles of the corresponding NP system.

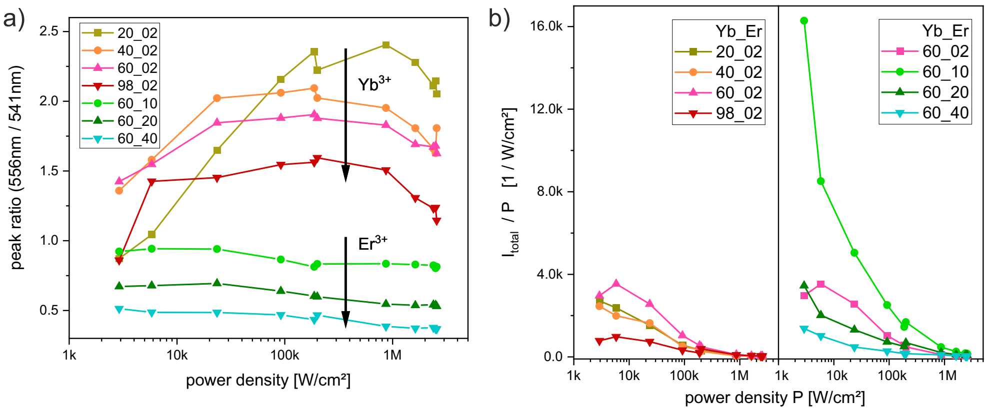

Figure A.13. P-dependent emission trends of the Yb and Er series synthesized by the Haase group (Osnabrück): a) 556 nm to 541 nm peak ratio demonstrating the ratio of 3 to 2 photonic absorption processes in the green emission range. It is important for data interpretation of green decay studies with their photon accumulation in the 545 ± 12.5 nm spectral range. b) Integrated intensities I_{total} over P, reflecting the change of UCL per P unit and can be used as measure, scaling with the optical QYs.

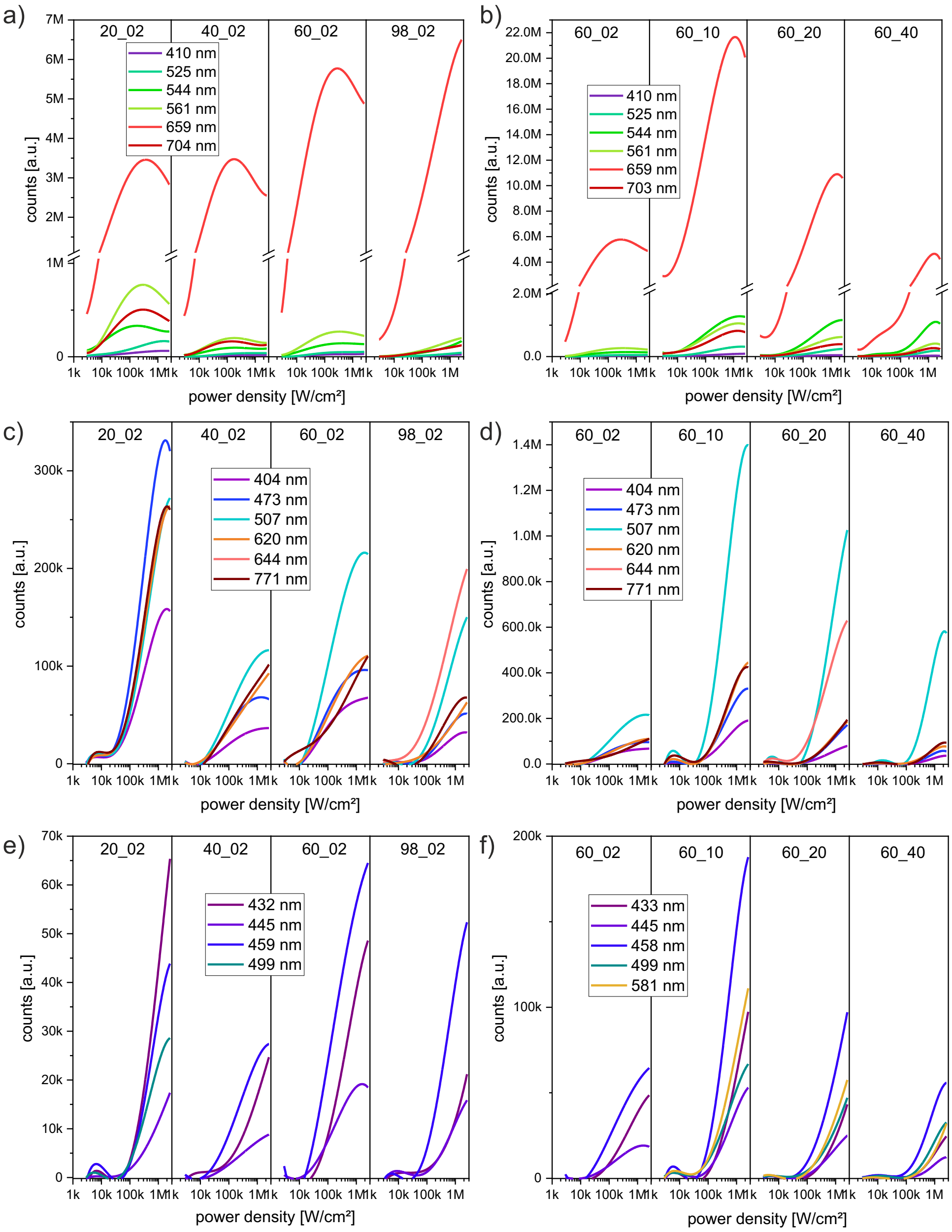

Figure A.14. *P*-dependent trends of main emission bands of both, the core-shell Yb series (20/02, 40/02, 60/02 and 98/02 Yb/Er ratios) and core-shell Er series (60/02, 60/10, 60/20 and 60/40 Yb/Er ratios), synthesized by Haase group (Osnabrück) following the synthesis protocol described in [37]: Classification of the main emission bands into three groups corresponding to 2–3 (a and b), 3–4 (c and d) and 4 (e and f) photonic processes as described in [107] with a), c), e) for the Yb series and with b), d), f) for the Er series.

A.4. Chapter 6 - Yb vs. Nd excitation

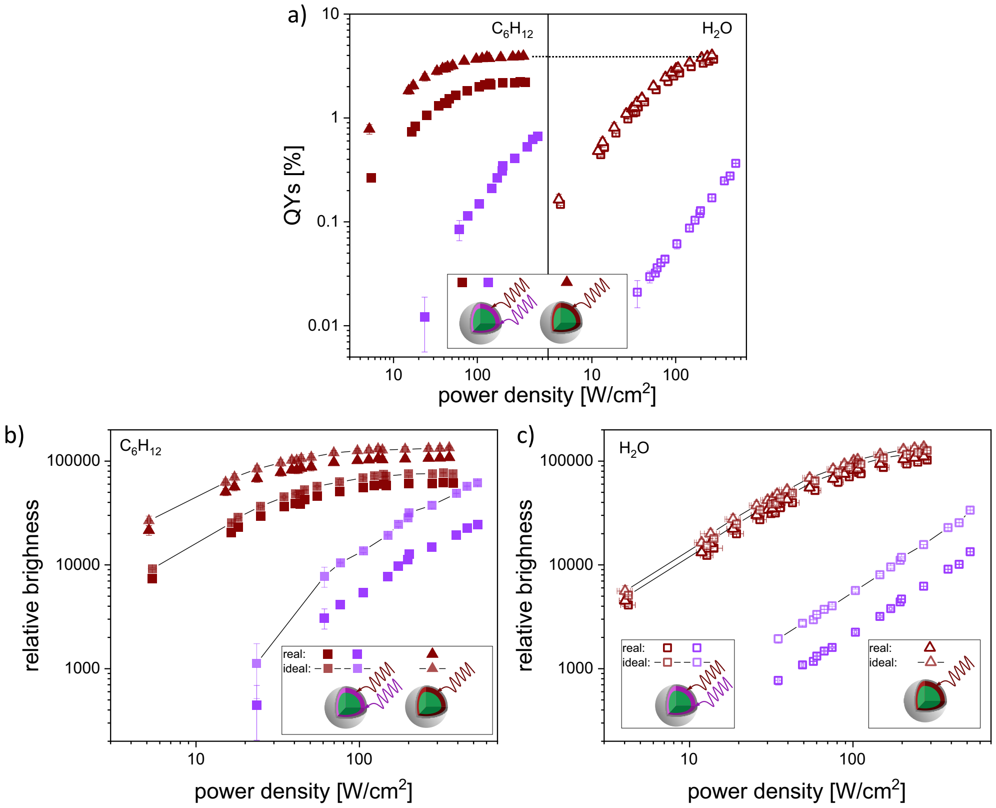

Figure A.15. *P*-dependent QYs and relative brightness values under Nd- and Yb-excitation of (Yb@Yb,Nd)^{is}) NPs and Yb-excitation of (Yb@Yb)^{is}) NPs in different solvents in ensemble: a) QYs in cyclohexane and water. b) and c) Relative brightness in cyclohexane and water. Taken and modified from own publication [51].

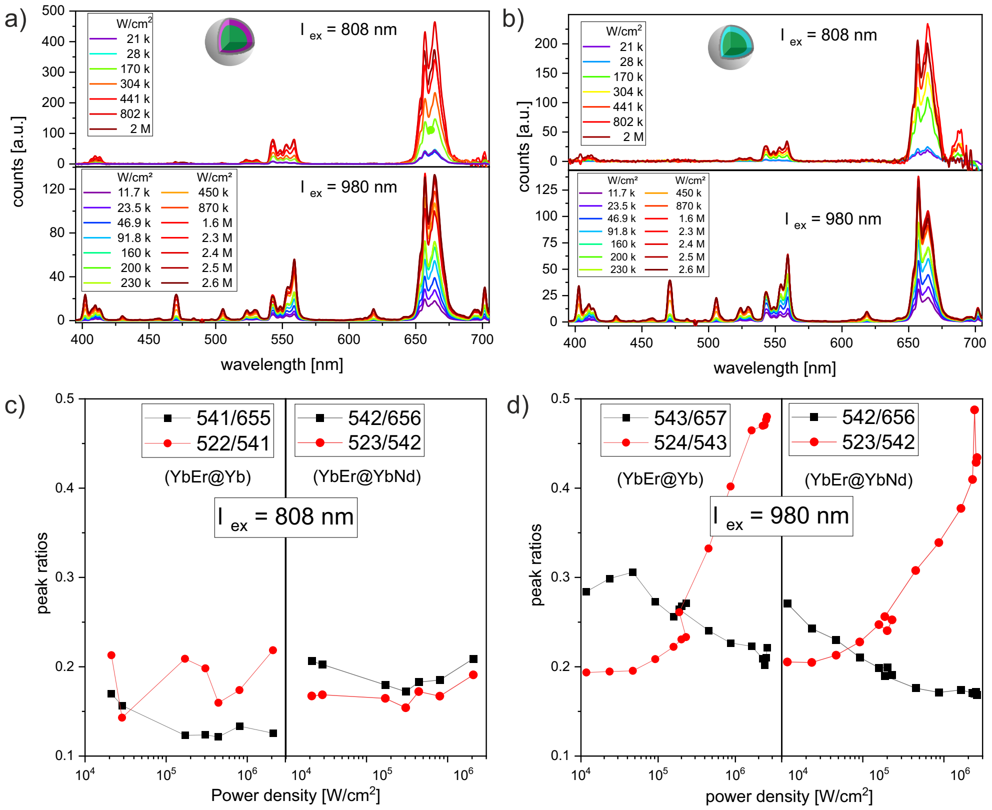

Figure A.16. P-dependent spectra and peak ratios of (Yb@Yb,Nd)^{is} and (Yb@Yb)^{is} SPs in the P range from kW/cm^2 up to MW/cm^2: a) Nd- and Yb-excitation (808 and 980 nm) of (Yb@Yb,Nd)^{is} SPs. b) Nd- and Yb-excitation of (Yb@Yb)^{is} SPs. c) and d) Green-to-red (G/R) and green-to-green (G/G) peak ratios under 808 nm (c) and 980 nm (d) excitation.

A.5. Chapter 7 - LRET and plasmonic studies

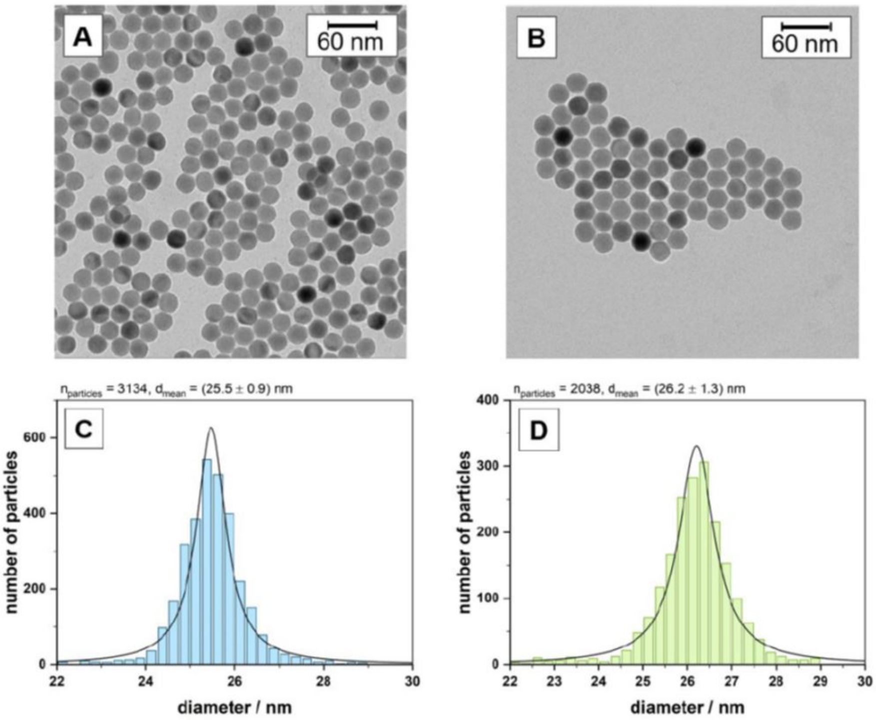

Figure A.17. TEM images (A, B) and histograms showing size distribution (C, D) of oleate capped, core-only NaYF$_4$:20% Yb^{3+}, 2% Er^{3+}) UCNPs (A, D) and core-shell UCNPs. The mean diameter d$_{mean}$ and the standard deviation were calculated based on the size distribution by Markus Buchner (TU Regensburg).

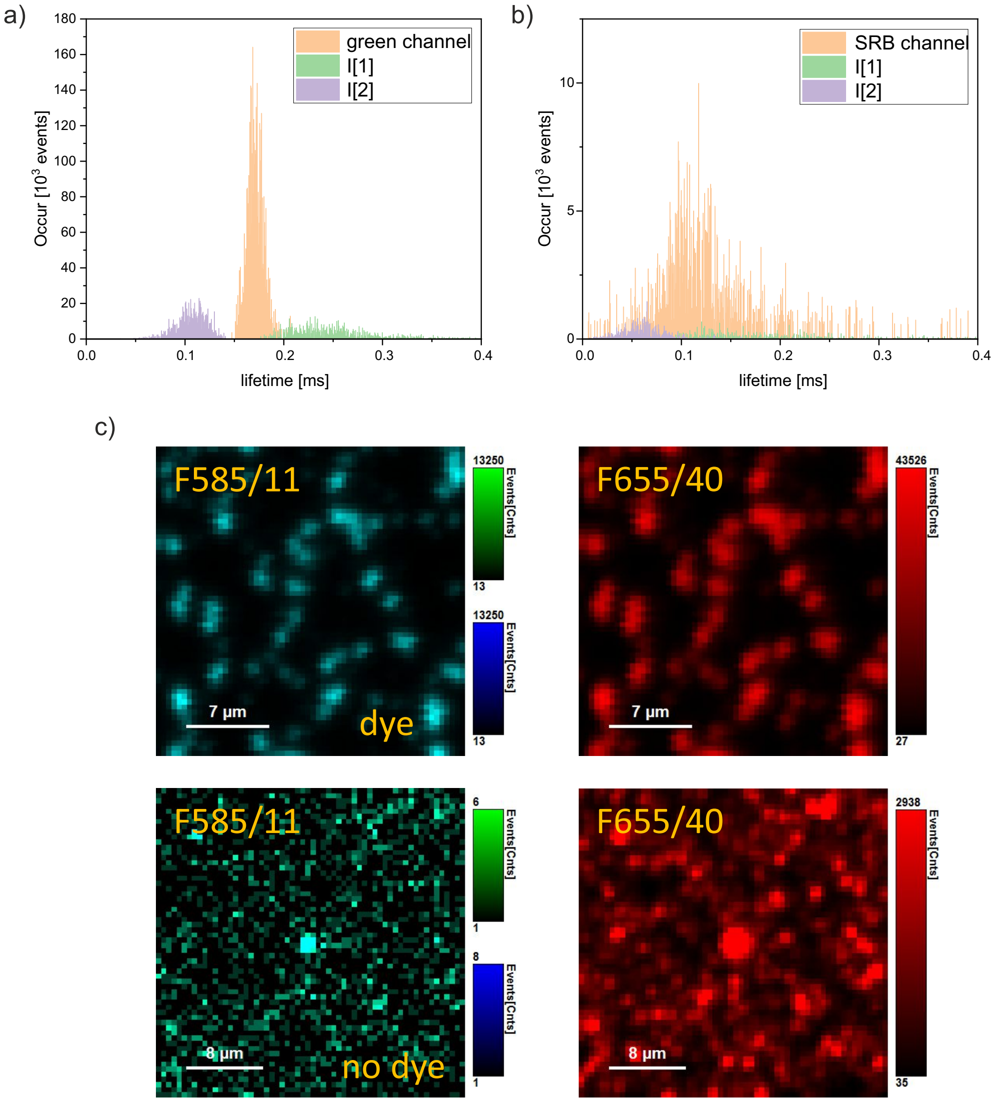

Figure A.18. LRET studies on CLSM: a) and b) LT distributions (short, long component and intensity-weighted averaged LT) of FLIM images (Fig. 7.3 a) and b)) of the donor (green) and the acceptor (SRB) channels. c) Performance of the bandpass filter F585/11 (SRB channel) tested for SRB-loaded UCNPs (upper plots) and for SRB-free UCNPS (bottom plots) with high blocking quality of the UC emission bands. The scans on the right show the red channel (655/40 nm) as reference.

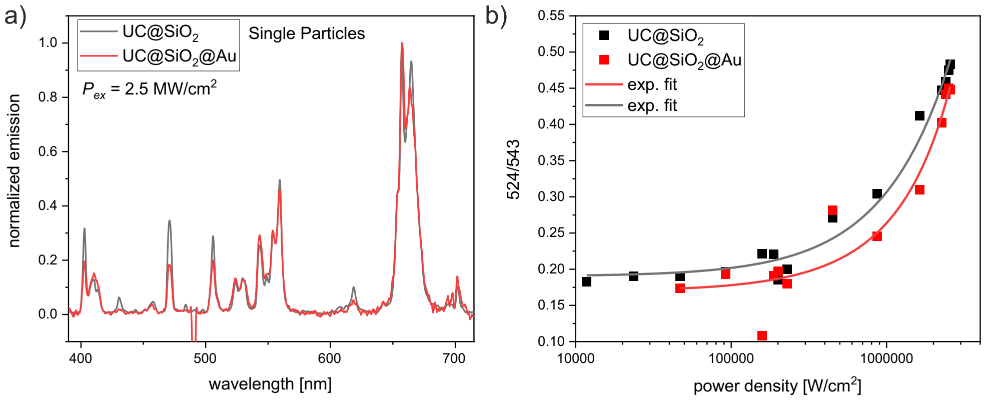

Figure A.19. Comparison of optical behaviour of single UC@SiO$_2$ NPs with and without Au-shell: a) Red band normalized spectra of both NP conditions obtaining the quenching influences of the additional Au-shell at *P* of about 2.5 MW/cm^2. b) *P*-dependent green-to-green band ratios (524 nm/543 nm) revealing the local, laser induced heating of the both NP systems.

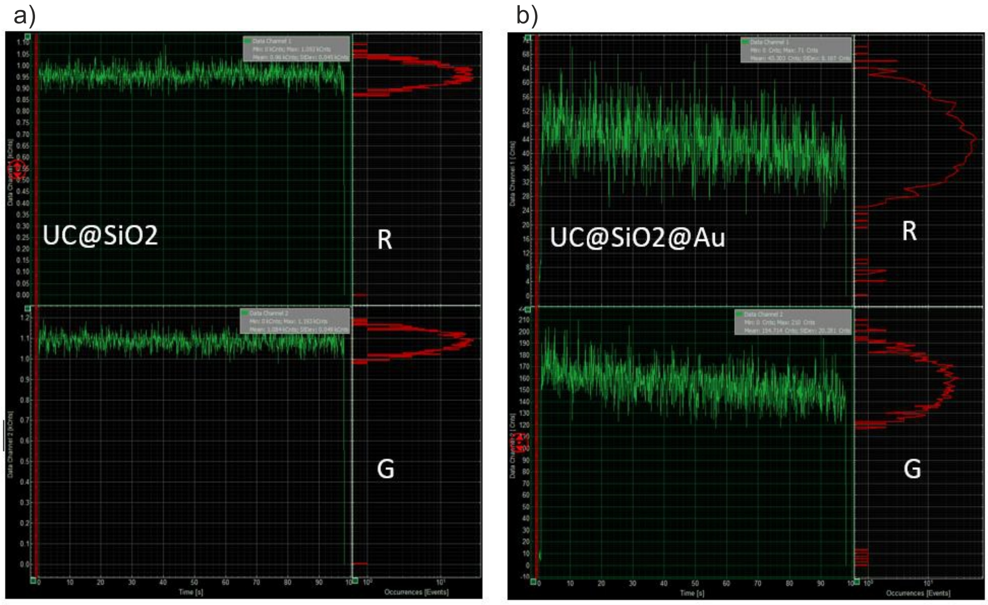

Figure A.20. Time-traces of the red (R) and green (G) channels on 980 nm excited NPs to illustrate the stability of the NPs and the measurement condition of the first 100 s: a) Stable conditions of the single UC@SiO$_2$ NP without additional Au-shell and b) decreasing intensities in both channels of the single UC@SiO$_2$ NP with Au-shell obtaining no stable condition, which might be caused by Au-melting effects due to laser-induced heating.

Danksagungen

An dieser Stelle möchte ich mich bei allen bedanken, die mich in den letzten Jahren auf die eine oder andere Art unterstützt haben, und ohne die der Abschluss dieser Arbeit nicht möglich gewesen wäre. Mein besonderer Dank geht an meinen Doktorvater Prof. Oliver Benson für die Betreuung an der HU Berlin und die Begutachtung meiner Arbeit. Für die Übernahme der weiteren Gutachten möchte ich mich bei PD Dr. Kirstein von der HU Berlin und bei Prof. Ilko Bald von der Universität Potsdam bedanken, sowie bei Prof. Norbert Koch für den Vorsitz der Kommission.

Mein ganz besonderer Dank geht an Dr. Ute Resch-Genger, für die Themenbereitstellung, für die fruchtbaren Diskussionen, für die offene, herzliche und direkte Art der Kommunikation und für die vielen spannenden Nebenprojekte, von denen überraschend viele in diese Arbeit eingeflossen sind.

Für die wissenschaftliche Betreuung vor Ort in den Laboren, der konstruktiven Diskussionen beim Erstellen der Publikationen, der Planung und Umsetzung bei den optischen Aufbauten und der Unterstützung bei der Entwirrung und Zuordnung dutzender neu entdeckter strahlender Er-Emissionen auf die passenden Energieniveaus möchte ich mich bei Dr. Christian Würth bedanken.

Mein herzlicher Dank gilt auch meinen Kooperationspartnern, die in den verschiedenen Projekten, die theoretischen Berechnungen, die Expertise an Messgeräten und die Proben bereitgestellt haben. Hier besonderer Dank an Dr. Thomas Hirsch und seiner Gruppe aus Regensburg für die Synthesen der Proben durch Lisa, Verena, Alexandra, Angelina, Susanne, Markus und John. Für die plasmonischen Berechnungen danke ich Lijun und Prof. Javier Garcìa de Abajo und für die Probenherstellung Maysoon und Cynthia, sowie Prof. Christina Graf. Für die Gastfreundschaft und den Messmarathon in Straßbourg möchte ich mich bei Prof. Yvès Mély, Frédéric und Oleksii bedanken. Für die Proben aus Osnabrück geht mein Dank an Prof. Markus Haase, Kerstin, Christian und Hennig.

Dank geht an Saskia, David, Florian und Martin für das fachliche Probelesen ausgewählter Abschnitte der Arbeit nach jeweiliger Expertise.

Für die Unterstützung bei der Planung, dem Aufbau und dem Kalibrieren unseres Einzelpartikelmessplatzes möchte ich mich besonders bei Christian, Arne und Florian bedanken.

Dank für die Unterstützung beim Bewältigen des einen oder anderen Messmarathons gehen an Bettina, Monica, Katrin und Robert.

Für das harmonische und freundschafliche Büroleben mit dem Spirit eines WG-Wohnzimmers, in dem auch private Gespräche nicht zu kurz kamen gilt mein Dank Bettina, Melissa, Lisa, Maysoon, Saskia und Eugeny.

Für die gute Arbeitsatmosphäre, die gemeinsamen Mensagänge und die motivierenden Kafferunden, die über wissenschafliche Durststrecken geholfen haben, möchte ich mich bei meinen Freunden Bettina, Cui, Elina, Melissa, Lorena, Monica, Maysoon, Marco, Florian, Daniel, Bastian und Gerado bedanken.

Dank geht auch an Katrin, Jutta, Daniel, David und Bastian für die Beantwortung chemischer Fragen, die kreativen Beiträge bei den Doktorhüten und für die Synthese von Proben.

Darüber hinaus geht mein Dank an alle Kollegen der Biophotonik Gruppe, die mich in den letzten Jahren unterstützt haben.

Zu guter Letzt möchte ich mich bei meinen Eltern, meiner Schwester und besonders meiner Freundin Wanda für die anhaltende Unterstützung bedanken, die Rückendeckung, das Verständnis für lange und späte Arbeitsstunden und die Motivation mit Blick nach vorne.

Publication List

List of scientific publications in peer-reviewed journals as a result of the work in this thesis and the cooperations maintained throughout the thesis's time.

1. C. Homann, L. Krukewitt, *F. Frenzel*, B. Grauel, C. Würth, U. Resch-Genger, and M. Haase. **$NaYF_4$:Yb,Er/$NaYF_4$ core/shell nanocrystals with high upconversion luminescence quantum yield**. *Angewandte Chemie International Edition*, 57(28): 8765–8769, 2018
   My contribution: Parts of decay and *P*-dependent QY measurements

2. R. Tietze, R. Panzer, T. Starzynski, C. Guhrenz, *F. Frenzel*, C. Würth, U. Resch-Genger, J. J. Weigand, and A. Eychmüller. **Synthesis of NIR-emtting InAs-based core/shell quantum dots with the use of Tripyrazolylarsane as Arsenic precursor**. *Particle & Particle Systems Characterization*, 35(9):1800175, 2018
   My contribution: QY measurements and analysis

3. M. S. Meijer, P. A. Rojas-Gutierrez, D. Busko, I. A. Howard, *F. Frenzel*, C. Würth, U. Resch-Genger, B. S. Richards, A. Turshatov, J. A. Capobianco and S. Bonnet. **Absolute upconversion quantum yields of blue-emitting $LiYF_4$:Yb^{3+},Tm^{3+} upconverting nanoparticles**. *Phys. Chem. Chem. Phys.*, 20:22556–22562, 2018
   My contribution: *P*-dependent QY measurements and analysis

4. M. I. Saleh*, I. D. Panas*, *F. Frenzel**, C. Würth, B. Rühle, Y. L. Slominskii, A. Demchenko and U. Resch-Genger. **Sensitization of upconverting nanoparticles with a NIR-emissive cyanine dye using a micellar encapsulation approach**. *Methods and Applications in Fluorescence*, 7(1):014003, 2019
   My contribution: Steady-state measurements and analysis

5. L. M. Wiesholler*, *F. Frenzel**, B. Grauel, C. Würth, U. Resch-Genger and T. Hirsch. **Yb,Nd,Er-doped upconversion nanoparticles: 980 nm versus 808 nm excitation**. *Nanoscale*, 11:13440–13449, 2019
   My contribution: *P*-dependent QY measurements and analysis; calculation of cross-sections and brightness values; theoretical modelling of enhanced ion doping concentration

* means equal contributing author

6. *F. Frenzel*, C. Würth, O. Dukhno, F. Przybilla, L. M. Wiesholler, V. Muhr, T. Hirsch, Y. Mély and U. Resch-Genger. **Multiband emission from single β-NaYF$_4$(Yb,Er) nanoparticles at high excitation power densities and comparison to ensemble studies**. *Nano Research*, 2021
   My contribution: Design of the study; decay and P-dependent measurements at ensemble and single particle level; lifetime determination and analysis
7. R. Xu, W. Teich, *F. Frenzel*, K. Hoffmann, J. Radke, J. Rösler, K. Faust, A. Blank, S. Brandenburg, M. Misch, P. Vajkoczy, J. Onken, and U. Resch-Genger. **Optical characterization of sodium fluorescein in vitro and ex vivo**. *Frontiers in Oncology*, 11:1439, 2021
   My contribution: Measurements on the CLSM and analysis
8. C. Würth, B. Grauel, M. Pons, *F. Frenzel*, P. Rissiek, K. Rücker, U. Resch-Genger and M. Haase. **The upconversion luminescence quantum yield of highly doped NaYF$_4$:Yb,Er/NaYF$_4$:Lu core/shell nanocrystals** *submitted to Angew. Chem. Int. Ed.*, 2021
   My contribution: Single particle measurements and analysis

Scientific Contributions

Poster

Power dependent optical properties of hexagonal β-NaYF$_4$: x% Er^{3+}, 20% Yb^{3+} core/ core-shell upconversion nanoparticles in cyclohexane and water

F. Frenzel, C. Würth, V. Muhr, T. Hirsch and U. Resch-Genger

- Summer School ”Exciting nanostructures”, Bad Honnef, Germany, 2017
- PhD Day, BAM Berlin, Germany, 2017
- UPCON 2018 Conference, Valencia, 2018

Multiband Emission from Single β-NaYF$_4$(Yb,Er) NPs at High P and Comparison to Ensemble Studies

F. Frenzel, C. Würth, O. Dukhno, F. Przybilla, L. M. Wiesholler, V. Muhr, T. Hirsch, Y. Mély, and U. Resch-Genger

- UPCON 2021 Conference, online, 2021

List of Figures